Biaxial Dynamic Fatigue Tests of Wind Turbine Blades

Von der Fakultät für Bauingenieurwesen und Geodäsie
der Gottfried Wilhelm Leibniz Universität Hannover
zur Erlangung des Grades

Doktor der Ingenieurwissenschaften
– Dr.-Ing. –

genehmigte Dissertation von

Dipl.-Ing. Falko Bürkner
geboren am 14.02.1976 in Bochum, Deutschland

2020

Referent:	**Prof. Dr.-Ing. Andreas Reuter** Gottfried Wilhelm Leibniz Universität Hannover Institut für Windenergiesysteme
Korreferent:	**Prof. Henrik Stang** Technical University of Denmark Department of Civil Engineering
Kommissionsmitglied:	**Prof. Dr.-Ing. Raimund Rolfes** Gottfried Wilhelm Leibniz Universität Hannover Institut für Statik und Dynamik
Vorsitz:	**Prof. Dr.-Ing. Martin Achmus** Gottfried Wilhelm Leibniz Universität Hannover Institut für Geotechnik

Tag der Promotion: **30. October 2020**

Eigenständigkeitserklärung

Hiermit erkläre ich folgendes:

- Die Regeln der geltenden Promotionsordnung sind mir bekannt und wurden eingehalten. Mit einer Prüfung nach den Bestimmungen der Promotionsordnung bin ich einverstanden.
- Die Dissertation habe ich selbst verfasst (Selbständigkeitserklärung), ich habe keine Textabschnitte von Dritten oder eigener Prüfungsarbeiten ohne Kennzeichnung übernommen und alle benutzten Hilfsmittel und Quellen in meiner Arbeit angegeben.
- Dritten habe ich weder unmittelbar noch mittelbar geldwerte Leistungen für Vermittlungstätigkeiten oder für die inhaltliche Ausarbeitung der Dissertation erbracht. Das heißt; die wissenschaftliche Arbeit ist weder in Teilen noch in Gänze von Dritten gegen Entgelt oder sonstige Gegenleistung erworben oder vermittelt worden.
- Die Dissertation habe ich noch nicht als Prüfungsarbeit für eine staatliche oder andere wissenschaftliche Prüfung eingereicht.
- Ich habe keine gleiche oder eine in wesentlichen Teilen ähnliche Arbeit bei einer anderen Hochschule als Dissertation eingereicht. Weiterhin habe ich keine andere Abhandlung als Dissertation eingereicht.
- Ich bin damit einverstanden, dass die Dissertation zum Zwecke der überprüfung der Einhaltung allgemein geltender wissenschaftlicher Standards genutzt wird. Dies gilt insbesondere auch unter Verwendung elektronischer Datenverarbeitungsprogramme.

Bremen, den 08.06.2020,

F. Bühner

Executive Summary

Over the last 30 years, wind energy has become an established industry and one of the most important sources of renewable energies. However, energy cost have still to be reduced further to stay competitive with other energy sources. Especially the extremely loaded rotor blades are to be optimized using modern design methods, highly utilized materials and serial production. In view of the manually driven manufacturing, the design must be verified carefully for these components, but common dynamically loaded full-scale fatigue tests are rather inaccurate. Only limited areas of the blade are realistically tested using a time-consuming test method. Hence, this work focuses on improving these subjects.

The most important fatigue loads of blades are stochastic wind loads and deterministic gravity loads caused by the rotor rotation. To test blades for fatigue, two separate oscillations with over one million load cycles are performed at the 1$^{\mathrm{st}}$ and 2$^{\mathrm{nd}}$ natural frequency of the blade. A static calibration loading prior to the fatigue test is used to determine the test amplitude by comparing the strains of the calibration loading with the strains measured during the test.

Caused by the high slope values of S/N curves from common glass and carbon fiber materials used for blades, even very small errors when determining the test amplitude will lead to extremely faulty levels of introduced damages and test results, respectively. Hence, two optimization methods using only a minimal number of additional measurements were developed to reduce errors in the test load determination by a factor of four. In addition, local nonlinear behavior of measured strains over global bending moments will occasionally lead to significantly incorrect calibrations. A method to locate these areas and to eliminate these errors by measuring and calculating the nonlinear behavior was developed using only a minimum of additional measurements. Herewith, even for biaxial blade tests an acceptable level of accuracy is achieved for the determination of the test load.

With today's common two uniaxial test directions, approximately only half of the blade cross-sectional areas can be loaded adequately. To achieve a more representative test loading, all areas of the cross-sections have to be loaded adequately. Both uniaxial test oscillations have to be excited at the same time and need to have the same frequency. The resulting elliptic movement of the blade would lead to an ideal test and reduces the overall testing time by 20% to 30%. No realizable test mechanism is available to achieve such elliptic movement combined with dynamic loading for an optimized load distribution along the blade span. The blade's natural frequencies of both directions are different; hence, an excitation of both will result in complex Lissajous figures instead of an ellipse. With attaching masses to the blade, the 2$^{\mathrm{nd}}$ natural frequency of the blade can be decreased to be equal to the 1$^{\mathrm{st}}$ natural frequency of the pure blade. To avoid that the attached masses also reduce this frequency, a method was developed to eliminate the influence of the attached masses only in this direction. Only in this way, an elliptical oscillation combined with

a dynamic loading is possible. The excitation can be performed with a realizable test mechanism using only two servo-hydraulic actuators.

A transient finite element simulation was performed to compare the new method with common tests for the applied test loading and testing time. The simulation was validated with uniaxial and biaxial full-scale blade tests. With biaxial test loadings performed on a modern 40m blade, additionally it was shown that a controlled and predictable movement is possible with the control-system used for the servo-hydraulic actuators.

Future work should be performed to validate the intended optimization methods for calibration tests and the simulation of the projected biaxial test method. Automated tools to determine optimized test setups in terms of blade loading and test geometry should be developed.

Zusammenfassung

Während der letzten 30 Jahre hat sich die Windenergie zu einer etablierten Industrie entwickelt und ist die wichtigste erneuerbare Energiequelle zur Stromerzeugung. Trotzdem ist eine weitere Reduktion der Stromentstehungskosten notwendig, um mit anderen Formen der Energieerzeugung langfristig konkurrenzfähig zu sein. Gerade die extrem belasteten Rotorblätter müssen weiterhin mit modernen Konstruktionsmethoden, höherer Materialausnutzung und verbesserter Serienproduktion optimiert werden. Auch aufgrund der noch immer stark manuell geprägten Herstellung sollten Rotorblätter mit größter Sorgfalt validiert werden. Gerade die heute üblichen Ermüdungsversuche von Blättern sind noch sehr ungenau. Ideale Testlasten werden bei weitem nicht in allen Bereichen erzeugt. Darüber hinaus sind die momentanen Tests immer noch sehr zeitaufwändig. Der Fokus der Arbeit liegt daher auf der Verbesserung dieser Themen.

Die Ermüdungsbelastung von Rotorblättern setzt sich überwiegend aus stochastischen Windlasten und deterministischen Eigengewichtslasten zusammen. Um Blätter auf Ermüdung zu testen, werden daher zwei separate zyklische Tests mit jeweils mehr als einer Million Zyklen durchgeführt. Die Belastung erfolgt hierbei mit Hilfe von Resonanzschwingungen in der ersten und zweiten Eigenfrequenz. Mit vorab durchgeführten Kalibrierungstests, in welchen das Verhältnis von Dehnung zu Biegemoment ermittelt wird, wird später die Biegebelastung in den dynamischen Ermüdungsversuchen bestimmt.

Durch den flachen Verlauf der Wöhlerkurven von Glas- und Kohlefaser-Materialien, welche in Rotorblättern zum Einsatz kommen, wirken sich kleinste Ungenauigkeiten der Testamplituden extrem stark hinsichtlich der erzeugten Materialschädigungen im Test und somit auch auf das Testergebnis aus. Aus diesem Grund werden zwei Optimierungsmethoden vorgeschlagen, um die Ungenauigkeiten der Testlastermittlung mit einfachen und daher in der Praxis umsetzbaren Messungen in etwa auf ein Viertel zu reduzieren. Zusätzlich kann in lokalen Bereichen der Blätter ein nichtlineares Verhalten von Dehnung zu Biegebelastung zu stark verfälschten Ergebnissen der Kalibiertests führen. Es wurde eine Methode zur Lokalisierung dieser Bereiche sowie zur Messung und Korrektur des nichtlinearen Verhaltens entwickelt, wobei nur wenige zusätzliche Messungen notwendig werden. Durch die Entwicklung dieser Methoden wird auch die Bestimmung der Testbelastung bei dynamischen biaxialen Blatttests mit ausreichender Genauigkeit möglich.

Mit den heute üblichen separaten Ermüdungstests in zwei Richtungen kann nur in etwa die Hälfte aller Bereiche eines Blattquerschnitts repräsentativ belastet werden. Um einen repräsentativeren Test zu erreichen, müssen alle Bereiche der Blattquerschnitte ideal belastet werden. Hierfür müssen die beiden uniaxialen Schwingungen gleichzeitig und mit gleicher Frequenz ausgeführt werden. Die hieraus resultierende elliptische Schwingung des Blattes würde einen idealen Test darstellen und zusätzlich die gesamte Testzeit um 20% bis 30% verringern. Bisher ist keine praxistaugliche Mechanik bekannt, um diese elliptische Bewegung mit einer Eigenfrequenzschwingung auszuführen.

Dies rührt daher, dass die Eigenfrequenzen der Blätter in beiden benötigten Testrichtungen unterschiedlich sind. Bei einer Anregung beider Frequenzen entsteht somit eine komplexe Lissajous-Figur, aber keine Ellipse. Durch das Befestigen von zusätzliche Massen am Blatt kann die zweite Eigenfrequenz auf die erste Eigenfrequenz des reinen Blattes abgesenkt werden. Um jedoch zu vermeiden, dass die Zusatzmassen auch die erste Eigenfrequenz absenken, wurde eine Methode entwickelt, die den Einfluss der Massen nur in dieser Richtung verhindert. Nur hierdurch wird eine elliptische Bewegung kombiniert mit einer dynamischen Belastung möglich. Die Anregung des Blattes kann trotzdem mit nur zwei Hydraulikzylindern und unter Verwendung einer praxistauglichen Mechanik durchgeführt werden.

Transiente Finite-Elemente-Berechnungen wurden durchgeführt, um die neue Methode mit herkömmlichen Tests in Bezug auf die Blattbelastung und Testzeit zu vergleichen. Die Berechnungen wurden mit uni- und biaxialen Ganzblatttests validiert. Zusätzlich wurde mit Hilfe von biaxialen Testbelastungen an einem 40m langen Rotorblatt gezeigt, dass eine kontrollierte Bewegung mit servo-hydraulischen Zylindern regelbar ist.

Weitere Arbeit sollte in die Validierung der vorgestellten Optimierungsmethoden für Kalibriertest und die Simulation der neuen Belastungsmethode für Biaxialtests investiert werden. Außerdem sollten automatisierte Berechnungen zur Optimierung der Mechanik in Bezug auf die Blattbelastung und die Testgeometrie entwickelt werden.

Acknowledgements

I would like to thank Prof. Dr.-Ing. Andreas Reuter for his scientific advice and for giving me scientific space throughout this work. Prof. Henrik Stang is acknowledged for his very valuable scientific advice.

All IWES colleagues shall be acknowledged for creating a friendly and supportive working environment throughout my whole time at Fraunhofer IWES. Especially acknowledged shall be Dr.-Ing. Arno van Wingerde for many discussions on the topic and for proof-reading the thesis as well as Dipl.-Ing Willi Wroblewski for supporting the testing and organization.

For endless discussions, valuable ideas and comments on rotor blade testing I would like to express my gratitude to Dr. Nathan Post, one of the greatest engineers and scientists I have worked with. In the same sense I would like to thank M.Sc. Eric Putnam for an exceptional working relationship at Fraunhofer IWES.

Designing the rotor blade test-rigs was a necessary preparation for all following developments on testing concepts. For the creative, friendly and very constructive working atmosphere during these special years in my career, I would like to thank a few of the very first employees of Fraunhofer CWMT (former Fraunhofer IWES). Prof. Dr. rer. nat. Hans-Gerd Busmann for his support and his trust, my friends Dr.-Ing. Fabian Vorpahl, Dr.-Ing. Florian Sayer, Dr.-Ing. Holger Huhn and Dipl.-Ing. Hendric Schäfer for an exceptional time.

Acknowledged shall be Dipl.-Ing. Uwe Helmke (Enercon) for his support and the opportunity to proceed my work on blade testing topics, as well as Dipl.-Ing. Urs Wihlfahrt and M.Sc. Wojciech Popko for a very appreciated support on editorial issues.

I would like to thank my parents Karin and Dr.-Ing. Karl-Ernst Bürkner for giving me a creative and inquisitive engineering mindset on my way and last but not least my wife Saskia for an extraordinary support.

Parts of the work were carried out with the financial support of the German Federal Ministry of Nature Conservation and Nuclear Safety (BMU) in the frame of the Better Blade project (FKZ 0325169).

List of Figures

List of Tables

List of Symbols

Latin symbols

Symbol	Unit	Description
A	$-$	coefficient in calibration matrix (11, 13, 14)
A	$-$	blade cross-sectional area to calculate the drag force due to air damping at location i (81)
Amp_{1st}	mm	amplitude at the 1st eigenmode (16–18, 20–22, 69, 70)
Amp_{2nd}	mm	amplitude at the 2nd eigenmode (16–18, 20–22, 69, 70)
C_d	$-$	drag coefficient for air damping at location i (81–84, 91–93)
C	$-$	finite element damping matrix (80, 81)
E	$-$	bending moment difference of calibration tests comparing the loading of an undeformed blade (and a loading perpendicular to the pitch axis) with an deformed blade (and the actual load direction) (43, 51, 52, 54–56, 122, 123, 129–131)
EI	N/mm^2	bending stiffness of the root-wise end of an element (124, 126–129)
E_{Lc_z}	$-$	error E at the loading location of the blade (50–52, 122)
E_{root}	$-$	error E at the root of the blade (50–52, 122)
F	N	calibration force (11, 45, 46, 48, 51, 54, 126, 127, 130)
F_d	$-$	drag force due to air damping at location i (81)
u_{el}	mm	deflection of the tip-wise node of an element (X_{IEC}-Z_{IEC} plane) (124–128)
f_{1st}	$1/s$	frequency of the 1st eigenmode (16, 18–22, 59, 63, 69–71)
f_{2nd}	$1/s$	frequency of the 2nd eigenmode (16–22, 59, 63, 69–71)
F_{num}	N	force used in the numeric calculation of OM-II (126–128, 130)
F_{el}	$-$	flap-wise force perpendicular to each element (124–126)
K	$-$	finite element stiffness matrix (80, 81)
L	mm	distance between calibration load coordinate Lc_z and the strain gauge coordinate in Z_{IEC} direction Lsg_z (11, 12)
l_{el}	mm	length of element (124, 126–128)

Symbol	**Unit**	**Description**
Lb	mm	blade length or tip coordinate in Z_{IEC} direction (45, 67, 68, 136, 137)
Lc_x	mm	location (coordinate) of the calibration load attachment location in X_{IEC} direction (51, 52, 54–56, 122, 130)
Lc_z	mm	location (coordinate) of the calibration load attachment location in Z_{IEC} direction (43–48, 50–53, 55, 56, 122–124, 126–130)
Ln_x	mm	location (coordinate) of a node in X_{IEC} direction (124, 127, 128, 130, 131)
Ln_z	mm	location (coordinate) of a node in Z_{IEC} direction (55, 124, 127–130)
M	–	finite element mass matrix (80, 81)
M	Nmm	bending moment (14, 49, 50, 130)
M_y	–	flap-wise bending moment (rotor coordinate system) (127)
M_{el}	–	flap-wise bending moment of an element (124–126)
S	$\mu m/m$	strain signal (11, 14, 15)
s	–	type A uncertainty (53)
T_{1st}	s	period of the 1st eigenmode (16)
T_{2nd}	s	period of the 2nd eigenmode (17)
t	s	time (16, 17)
u	–	type B uncertainty (53)
u_x	mm	deflection in X_{IEC} direction (122, 130)
u_y	mm	deflection in Y_{IEC} direction (123)
u_z	mm	deflection in Z_{IEC} direction (51, 52, 122, 123, 130)
v	–	velocity of the blade at location i (81)
x	mm	coordinate in X_{IEC} direction (16)
X_{IEC}	–	X-axis according to IEC-61400-23 (2014) or described in Appendix A (15–18, 20–22, 43, 45, 48, 49, 53, 67–70, 92, 93, 100, 124, 129, 130)
Y_{IEC}	–	Y-axis according to IEC-61400-23 (2014) or described in Appendix A (15–18, 20–22, 43, 48, 49, 67–70, 92, 93, 100)
Z_{IEC}	–	Z-axis according to IEC-61400-23 (2014) or described in Appendix A (15, 17, 44, 46, 124)

Greek symbols

Symbol	Unit	Description
α_{damp}	–	mass matrix multiplier for damping (80, 81)
β	deg	rotation of the blade to the pitch axis (51, 52, 54, 55, 122–124, 126–129)
β_{el}	deg	rotation of the tip end of an element around the Y_{IEC} axis (124–127)
β_{damp}	–	stiffness matrix multiplier for damping (80, 81)
θ	deg	calibration load to blade chord (0° is in flap-wise direction) (47, 48, 50)
Γ	deg	calibration load orthogonal to the pitch axis (54, 56, 130)
γ	deg	calibration load to vertical (51, 52, 122, 123, 130)
ω_{1st}	$1/s$	angular frequency of the 1^{st} eigenmode (16, 17)
ω_{2nd}	$1/s$	angular frequency of the 2^{nd} eigenmode (17)
ω_i	$1/s$	angular frequency of eigenmode i (81)
φ_{1st}	deg	phase shift of the 1^{st} eigenmode (16–18, 20–22, 69–71)
φ_{2nd}	deg	phase shift of the 2^{nd} eigenmode (17)
ψ_{1st}	deg	rotation of the 1^{st} eigenmode around Z_{IEC} (16–18, 20–22, 69–71)
ψ_{2nd}	deg	rotation of the 2^{nd} eigenmode around Z_{IEC} (16–18, 20–22, 69–71)
ρ	kg/m^3	air density (81)
ξ_i	–	material damping ratio at eigenmode i (81–84, 91, 92)

Indices and special characters

Symbol	Description
$\square^c$	calibration-test
$\square_i$	radii span-wise
$\square_{prebend}$	parameters describing the undeformed geometry of a prebend blade
$\square^t$	fatigue-test
$\square_x$	x direction
$\square_y$	y direction
$\square_z$	z direction

List of Acronyms

AMC	active mass compensation (xiii, 74, 76, 78, 79, 84–88, 96, 101, 103, 135–137, 139)
BEDEX	biaxial elliptical dynamic excitation (75–79, 84, 89, 92, 94–101, 103, 105, 106, 139)
DEL	damage equivalent load (7, 10, 18, 25, 70)
FE	finite element (8, 34, 40, 42, 43, 56, 78–80, 82–87, 89–92, 94, 95, 98, 105, 106, 124, 137–139)
FPW	flap-wise (15, 16, 18, 20–22, 92, 93, 98, 100)
FTW	flat-wise (124, 126–128)
LE	leading edge (14, 121)
LLW	lead-lag-wise (15, 16, 18, 20–22, 81, 92, 93, 98, 100)
NF	natural frequency (86)
OEM	original equipment manufacturer (2, 59, 72, 103)
OM-I	optimization method I (51–54, 56, 57, 83, 104, 105, 122, 123)
OM-II	optimization method II (54–57, 104–106, 126, 129)
PS	pressure side (14, 121)
SS	suction side (14, 121)
TE	trailing edge (14, 121)

Contents

Chapter 1

Introduction

1.1 Background and Motivation

Wind energy is one of the major opportunities to achieve the necessary reduction of CO_2 emission to slow down global warming. Having become one of the most promising renewable energy sources, an established industry has been developed over the past 30 years delivering a large number of turbines. Large multinational companies took over the market with financial strength and optimized production capacities. The cost of energy has been reduced to become competitive with all other energy sources.

During the last decade, generally no new turbine concepts for decreasing the cost of energy for onshore and offshore wind turbines were presented. The three bladed up-wind turbine is still the most efficient concept. Instead the costs are reduced by improved modern design methods, a higher utilization of the material and automated or optimized manufacturing processes. Installation, operation and maintenance costs are reduced by installing less turbines with a larger rated power.

During a turbine's life time of 20 to 30 years, the blades are heavily loaded. Extreme turbulent wind gusts or wind speeds cause large extreme loads. High fatigue loads are introduced with up to $2.0{*}10^8$ rotations of the rotor causing deterministic fatigue loads due to the alternating gravity loads. Aditionally, stochastic wind fatigue loads appear in orthogonal direction. To withstand these fatigue loads, blades have to be well designed and well built. Material such as glass- or carbon-fiber reinforced plastic is used especially because of its durable behavior against fatigue degradation combined with its low weight. Even thought a large number of blades is produced, the manufacturing of blades is still manually driven resulting in varying quality. Hence, a careful verification of the design and the manufacturing is important.

According to IEC-61400-23 (2014), full-scale rotor blade tests include measurements of the dead weight and eigenfrequencies as well as extreme load and fatigue tests. Only one prototype blade has to be tested. Hence, a statistical information of the test is not possible. Instead of testing load cases which are present at the actual turbine, the tests focus on *testing the design assumptions*.

To test blades for fatigue, a test load is determined which generates a material damage equal to combining all fatigue loads of the turbine's life time. An accelerated test is used by increasing the load amplitude compared to real turbine loads. Because the blade material generally performs extremely well for fatigue degradation, the testing becomes especially tough. The immense fatigue loading in terms of energy has to be reproduced during the short testing time. The most common test method is to fix the blade with the blade root to a rigid test rig and to excite the blade to a natural frequency oscillation. Herewith, the test load cycles are applied rather fast and without needing much energy. Additionally, the test loading at such oscillation usually fits the ideal loading quite nicely. For a typical test, the blade is separately excited at the 1^{st} and 2^{nd} natural frequency. A constant amplitude oscillation with one to five million cycles is usually used, needing one to sometimes four months per test direction. Even though it is still discussed how realistic full-scale fatigue tests of rotor blades represent reality, major problems of the blade design or the manufacturing process are often found already at an early stage of the fatigue test campaigns. Failures of blades at the turbine often occur after some months at the earliest. With having hundreds of blades in operation at this time, the replacement of blades and the resulting bad reputation of the original equipment manufacturer (OEM) can be disastrous for every company.

Even though the industry has grown larger over the last 30 years, common fatigue tests of blades are quite inaccurate regarding the determination of the test load amplitude. In combination with the high slopes of the S/N curves describing the blade material in terms of fatigue degradation over load cycles, the applied damage to the material and therefore the results of the tests easily become extremely faulty. At the same time, the realistically tested areas of the blade are rather small, because the usual used two separate fatigue tests still do not load all areas of the blade cross-sections. Only areas with a very large distance to the neutral axis at the bent blade are loaded with a significant strain amplitude to achieve adequate damage to the material. Keeping in mind that smaller test amplitudes lead to extremely low applied damages, roughly only half of the cross-sections is tested using this approach. Furthermore, the rather long fatigue tests are problematic to achieve fast innovation loops necessary to stay competitive. Significantly improving blade fatigue tests is the motivation for the work presented in this thesis.

1.2 Blade Design

In this section, typical blade materials, constructions, production methods and loads are described. Even though this work focuses on loading mechanisms for blade fatigue tests, it is beneficial to have a fundamental understanding of the test specimen.

Most of today's blades are manufactured from glass- or carbon-fiber reinforced plastic, because these materials are very light, stiff and resistant against extreme and fatigue loads at the same time. Intensive material testing was performed to analyze the material parameters starting with Mandell and Samborsky (1997) or Jansen et al. (2006). The matrix consists of thermoset or polyester materials. In Sayer et al. (2009) or Sayer et al. (2013), it was shown that on one of the first built glass-fiber reinforced plastic blades, a critical degradation of the material could hardly be found after 18 years of service life.

In general, many different designs are present today. Still, on a broader view, most designs do have an I-beam or double I-beam construction to achieve a high stiffness for tower clearance. A typical

Figure 1.1: Left: Typical blade cross-section. **Right:** Trailing and leading edge detail.

blade cross-section is shown in Figure 1.1[1]. The large dark green areas in the left picture show the spar caps consisting of unidirectional glass fiber materials. The I-beam is built by connecting the spar caps with the sandwich shear web (beige) using bonding paste (light green). The pictures on the right show the trailing- and leading edge bonding connection (light green) of the suction and compression side sandwich shells made of balsa wood and glass fiber. Since great efforts are put into automating the manufacturing process of blades, the blade design will most likely change in the future to be optimized for this type of production.

---

[1] In this thesis, the nomenclature of IEC-61400-23 (2014) will be used. Hence, at the bottom of the left picture the leading edge and at the top the trailing edge of the profile is located, defining the edge-wise direction. Orthogonal is the flat-wise direction with the suction side on the left and the compression side on the right. Taking the rotor plane and not the profile as reference, the two directions become the lead-lag-wise and flap-wise directions.

Usually all main blade components are built prior to assembly. Spar caps, suction and compression side shells as well as shear webs are produced in moulds by vacuum infusion technology after placing multiple glass- or carbon fiber fabrics and core materials carefully in the molds by hand. With closing the two moulds, all parts are glued together to build up the load-carrying structure. After curing in the mould, the aerodynamic shape is optimized by filling and sanding irregularities to achieve a smooth surface. At last, a coating is applied to protect against UV radiation.

Typical extreme loads are turbulent gusts, wind shear or special load cases like emergency stops. Fatigue loads can be split into stochastic wind loads in flap-wise and deterministic gravity loads in lead-lag-wise direction. With about 1 to 2×10^8 rotations in 20 to 30 years of service life, the lead-lag-wise gravity loads are rather uncritical for blade lengths of less than 30m. At around 55m to 60m, the loads get equal to the flap-wise fatigue loads and for blades of 80m or more, the lead-lag-wise fatigue loading is typically much higher and more critical for the structure. Where this loading can only be reduced with lighter blades, today efforts are made to reduce the flap-wise fatigue loads especially for very long blades using passive and active flaps or swept blades (Aagaard Madsen and Løgstrup Andersen (2015) and Castaignet et al. (2014), Ashwill (2010), Paquette, Laird, Griffith, and Rip (2006) and Paquette, van Dam, and Hughes (2007)). Hence, combined with the tendency towards longer blades, lead-lag-wise tests become more challenging for blades.

1.3 History of Fatigue Tests

Modern three bladed up-wind turbines firstly evolved in the early 1980s. At the same time, static tests were performed for example at RISØ[2] (Nielsen, Berring, Pavese, and Branner (2013)), TU Delft[3] or the DLR[4]. Besides static tests (Figure 1.2), one of the first fatigue test of a glass-fiber epoxy blade was performed with a test blade of the DEBRA-25 turbine (Böhnisch (1988)) at the DLR. Sandbags were stacked on the compression side of the blade to load the blade quasi-statically[5] in flap-wise direction. To achieve cyclic loading, the opposite direction was loaded using a servo-hydraulic actuator in combination with a whiffletree structure (Figure 1.3). Like today, the test was already an accelerated life time test due to lifted amplitudes determined by using the Palmgren Miner rule. To keep the testing time moderate, the test was performed with only 40,000 cycles[6].

---

[2] RISØ National Laboratory, Roskilde Denmark

[3] Delft University of Technology (WMC-Group and later Knowledge Center WMC), Delft Netherlands

[4] German Aerospace Center DLR, Stuttgart Germany

[5] The loading of the blade is at a frequency much lower than the natural frequency of the blade.

[6] Even though highly accelerated tests as performed in Kristensen and Jørgensen (2003) do often not show a change of the critical loading areas of a blade, the usual cycle numbers of nowadays tests are with over one million cycles in flap-wise direction and over 1.5 million cycles in lead-lag-wise direction much higher. It is still quite unknown, whether the failure mode will be similar when having higher amplitudes at the fatigue test.

Figure 1.2: Static test in flap-wise direction of the DEBRA-25 blade, carried out in 1983/84. Four load frames and a whiffletree structure were used in combination with a hydraulic actuator.

Figure 1.3: Fatigue test in flap-wise direction of the DEBRA-25 blade, carried out in 1983/84. Four load frames and a whiffletree structure were used in combination with a hydraulic actuator to lift the blade up. Sandbags were used to apply the specified loading when unloading the actuator. 40,000 cycles were applied at different amplitudes.

Later uniaxial blade tests with quasi-static loading were performed at TU Delft by connecting an actuator directly to the blade at around mid-span or slightly further outboards. With using this loading method but two orthogonal oriented actuators, even biaxial tests were possible, as the blade could be moved in an ellipse with operating the flap- and lead-lag-wise actuator at the same time and at the same frequency (D. White (2004)).

Dynamically loaded[7] fatigue tests were evolved to reduce the high amount of energy needed for quasi-static tests and to enlarge the tested area in span-wise direction. The blades were uniaxially excited at their 1st or 2nd natural frequencies using electric exciters or hydraulic shakers.

This technique was also used for the flap-wise direction of biaxially loaded blades in combination with a quasi-static loading in lead-lag-wise direction. Mechanisms are described in D. White, Musial, and Engberg (2005) (Hughes (2008) and Hughes (2010)), Malhotra (2010) and Williamson (2012).

Since 2009, actuators were coupled directly between blade and strong floor to uniaxially excite the blade in its natural frequency (Bürkner and van Wingerde (2012)) at Fraunhofer IWES[8]. This excitation method was later used by WTTC[9], ORE Catapult[10] and Enercon[11].

Different approaches for dynamically loaded fatigue tests were tested since then. Descriptions of most methods are presented in Section 2.3 and Section 2.4.

Recently, research was performed on testing blades in segments, e.g. testing an inner blade part with 0-60% and the outer part separately (Ha, Bätge, Melcher, and Czichon (2019)). Uni- and biaxial approaches were analysed including spring elements to adjust the loading over blade length. Efforts are started to take this development even further by testing even smaller parts (components) of the blade (Rosemeier, Basters, and Antoniou (2018)).

1.4 The Ideal Fatigue Test

To explain general constrains for today's full-scale blade testing, today's test method is explained starting from a theoretically ideal test.

The purpose of structural fatigue prototype blade tests is to lower the risk that blades from serial production show problems when running at the turbines. Throughout the whole life time unexpected losses in energy production as well as cost intensive repairs must be avoided.

---

[7] A dynamic loading is an excited oscillation in or near the natural frequency of the blade with attached tuning masses.

[8] Fraunhofer Institute for Wind Energy and Energy System Technology (IWES), Bremerhaven Germany

[9] Wind Technology Testing Center (WTTC) of the Massachusetts Clean Energy Center, Boston MA US

[10] Offshore Renewable Energy Catapult (ORE Catapult), Blyth UK

[11] WRD GmbH, Aurich Germany

The most perfect fatigue test (most thorough test) would load the blade comparable to the turbine with regard to load amplitudes, ranges, cycle numbers and load history, but by adding the safety margins to consider variations of wind load, manufacturing tolerances, etc. Because such test would require the turbine's life time, an *accelerated* fatigue test has to be used.

A slight reduction of the testing time can be achieved by omitting all small load cycles with negligible damage to the material. For a significant reduction of the testing time, the turbine loads have to be transferred by the Palmgren Miner rule into a damage equivalent load (DEL). For this reason, the load history information of the real loads is not considered any more.

Including commercial aspects like testing time and testing costs, the ideal fatigue test would have a *constant amplitude loading* to achieve the determined DEL as fast as possible. The loading would be applied by a *dynamic oscillation* of the blade to reduce the loading energy as much as possible. To test the blade as thoroughly as possible at the same time, it is necessary to achieve an ideally distributed test loading for each cross section by loading the blade in a *biaxial elliptical* movement as much as possible.

1.5 Scope

The work performed in this thesis shall help to improve the validity of full-scale *fatigue* tests of wind turbine rotor blades *without increasing testing time and costs*. Not included are full-scale *static* tests (extreme load tests). Besides scientific research testing, most blade tests are performed to achieve a blade certification according to the European Standard IEC-61400-23 (2014). Hence, the focus of this work will be on this certification testing.

The first part of the thesis focuses on methods to significantly increase the accuracy and decrease the uncertainty of the fatigue test load determination with *practical* methods. This becomes especially important for the developed combined dynamic *and* biaxial loading methods.

To show, that such movement is possible with using hydraulic actuators directly attached to the blade, in the second part of the thesis a full-scale biaxial fatigue test of a 40m long blade is analyzed.

Ideally the same damage is applied to the material at blade fatigue tests compared to the real turbine operation. To apply this damage in the shortest possible time using a minimal load amplitude a dynamic biaxial *elliptic* movement of the blade is beneficial. Hence, the third part of the thesis elaborates on a realizable mechanism to load the blade in such elliptic motion.

1.6 Structure of the Thesis

A short **Executive Summary** of all chapters can be found at the beginning of the thesis. After explaining the motivation, the history and the scope in **Chapter 1**, different calibration test methods and state-of-the-art fatigue test methods are presented in **Chapter 2**. The identified needs for research and the methodology of the work are described in **Chapter 2.6**, including the thematic transition to this thesis. In **Chapter 3**, the main inaccuracies of present calibration tests are listed, analyzed and discussed. Two methods to improve the accuracy of calibration tests are presented. In **Chapter 4**, a biaxial dynamic fatigue test of a 40m long blade is described to shown that such test is possible in reality with using servo-hydraulic actuators. In **Chapter 5**, a new biaxial blade excitation method is presented to achieve a biaxial, elliptical and dynamic oscillation of the blade. The new excitation method is simulated with a validated finite element (FE) model. The conclusions with contribution to the state-of-the-art, recommendations and future work are described in **Chapter 6**.

Chapter 2

State-of-the-Art Fatigue Tests

In this section, an overview of mechanisms to load blades for *fatigue* testing is described, leading towards state-of-the-art biaxial tests. All tests are classified into uniaxial and biaxial tests described in Section 2.3 and Section 2.4 with sub-sections for quasi-static, dynamic and combined loadings.

Almost all tests are performed with the blade root fixed rigidly to a test rig foundation and the blade tip pointing upwards at 0° to 15° to the horizontal. A high stiffness of the foundation is beneficial to avoid any movement of the blade root, resulting in a decreased test frequency and therefore longer testing time.

Most blade tests are performed to achieve a blade certification according to the international standard IEC-61400-23 (2014). The main aspect of IEC-61400-23 (2014) is *to evaluate the integrity of a certain blade type and population respectively to confirm the design assumptions with a certain probability*. With regard to fatigue, the term design assumption means the comparison of the calculated material damage to allowed material damage. The turbine loads simulated for the life time (according to IEC-61400-1 (2005)) in combination with the material data yields the material damage which is compared with the allowed values. To test these assumptions, a test load is generated to achieve the same material damage in a much shorter period of time compared to the turbine life time (accelerated fatigue test). The applied damage to the blade material after the test has to be equal or larger than the calculated damage. Nevertheless, the purpose of the test can be fulfilled *without* loading the blade at amplitudes directly comparable to amplitudes occurring at the turbine[12].

2.1 Calibration Testing to Determine the Loading of Dynamic Tests

Present calibration test methods to determine the applied test loading of dynamic fatigue tests are quite inaccurate. New optimization methods will be described in Section 3. In this section, current

---

[12] Alternatively a simplified approach to determine test loads from a design load spectrum is presented in Freebury and Musial (2000).

calibration test methods are evaluated regarding their accuracy. General calculation approaches for all calibration methods are described in Section 2.1.1 and Section 2.1.2. Two ways to perform calibration tests will be described (comparable to IEC-61400-13 (2001)). Both described methods will only use a flap- and lead-lag-wise bending moment calibration test but not a torsional or shearforce calibration test, because in Papadopoulos et al. (1998) and Papadopoulos, Morfiadakis, Philippidis, and Lekou (2000) it was shown that the influences of these loads are much smaller and might be neglected.

To test the design assumptions of blades with regard to fatigue loads, the challenge of the testing laboratory is to perform the measurement of the blade loading during testing as precise as possible, because minor inaccuracies cause major changes of the test DEL. If a blade is loaded with a quasi-static loading for a fatigue test, the applied bending moments can be directly calculated by multiplying the actuator force by the lever arm (distance to where the actuator is attached). Because the stroke of the actuators is limited, non-geometric effects due to large deflection are rather limited leading to a quite accurate calculation of the bending moments. But for most current fatigue tests, a dynamic loading by oscillating the blade at natural frequencies is used. The force of the actuator cannot be used to directly determine the blade loading by force times lever arm. Instead, the bending moments have to be determined by correlating the measured strains throughout the testing with measured strains of previously performed quasi-static calibration loadings. The accuracy of these calibration tests therefore determines the accuracy of the load determination at the fatigue test [13]. Alternative analytical methods to measure the loading were analyzed in Lekou and Mouzakis (2009). Because of the large inaccuracies of the results, it is concluded that they are not recommended for composite materials.

Because IEC-61400-13 (2001) is focused on measuring the bending moments at the blade root and not for the whole blade length (like at fatigue tests), the issues arising when using the same calibration technique for blade tests (and therefore for the whole blade length) will be listed in Section 2.1.1 and discussed in Section 3.

2.1.1 Loading in One Direction

Prior to uniaxial flap- or lead-lag-wise fatigue tests, a quasi-static calibration loading has to be performed at least in the direction of the later test. In Figure 2.1, the quasi-static loading of the blade is shown in principle. The blade is horizontally oriented and fixed with the root to a test rig. The rotation of the blade in the test rig usually makes that the pressure side faces upwards. It is loaded vertically downwards at the tip to calibrate the flap-wise direction. The lead-lag-wise direction is calibrated separately with an horizontal loading.

---

[13] In IEC-61400-23 (2001), a calibration test is mentioned in Annex D. In IEC-61400-23 (2014), a calibration test is not mentioned any more but left to the testing laboratory.

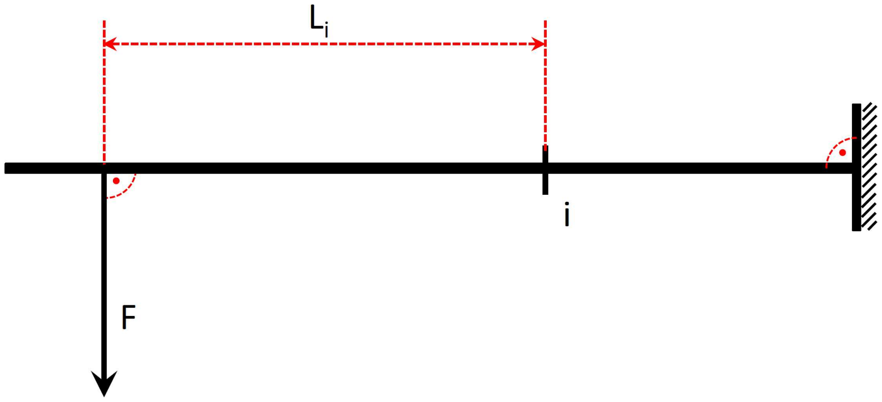

Figure 2.1: Calibration test setup: The blade's root is fixed to a rigid structure. Close to the tip, force F is applied rectangular to the blade pitch axis. The bending moment at location i is calculated using lever arm L_i.

When measuring the force and the lever arms between the span-wise loading location and the radial locations of each specific strain gauge at these tests, the quotient of strain versus lever arm times force yields the calibration factor for each strain gauge:

$$A_i = \frac{S_i^c}{L_i \times F} \tag{2.1}$$

A_i**:** Calibration factor at location i

S_i^c**:** Strain at location i at the calibration test

L_i**:** Distance between load F and strain gauge at location i

F**:** Calibration force

Dividing the strain readings during the actual fatigue test by the calibration factors results in the test bending moments:

$$M_i^t = \frac{S_i^t}{A_i} \tag{2.2}$$

M_i^t**:** Test bending moment at location i

S_i^t**:** Strain at location i during a fatigue test

This basic method to evaluate the test loading is often used, although it is quite inaccurate in reality. Looking closer to the method shows that many requirements have to be met to achieve precise results. The most important constraints and their related problems are listed below:

1. Each strain gauge has to be exactly on the neutral axis of the cross-section of the *unloaded* test direction. Otherwise strains introduced by a minor movement of the blade in that direction are measured additionally, leading to erroneous results [14].
2. The deflection in the quasi-static calibration test needs to be very small to avoid nonlinear effects. But to measure proper calibration factors, at the same time the strains measured at a calibration test need to exceed a certain level. To achieve this level for strain gauges located close to the root, where the bending stiffness is high, the calibration loading needs to be quite high as well. But when applying such high loading to the blade, large deflections will occur resulting in varying loading angles throughout the increasing deflection. E.g. a realistic setup is shown in Figure 2.2. Additionally, the distance L shown in Figure 2.1 decreases with larger deflections compared to the undeformed situation.
3. In reality, torsional loading is present at dynamic fatigue loadings[15]. The strain values to determine the flap- and lead-lag-wise bending moments are therefore slightly different, as there is always axial strain due to torsion (even though it is on a minor scale). With adding additional calibration factors for torsion this issue can be solved.
4. The loading of calibration tests is many times smaller than at the actual dynamic fatigue test. The determination of the test bending moments when using the calibration factors does therefore depend on a large linear extrapolation. In reality, local effects like buckling can lead to a nonlinear strain-to-bending moment relation, which leads to an incorrect determination of the test bending moment.

Because it is impossible to comply with all these assumptions, better methods need to be used to achieve more precise results. In Section 2.1.2, a method is described with which the flap- and lead-lag-wise test loading can be calculated at once (according to IEC-61400-13 (2001)). At least the assumption that strain gauges need to be exactly on the neutral axis is repealed with this approach (item one of above list).

2.1.2 Loading in Two Directions

As discussed in Section 2.1.1, if using only one calibration (in the actual test direction), each strain gauge has to be applied exactly on the neutral axis of the blade in the orthogonal direction of the test. Figure 2.3 shows exemplarily strain gauge positions and their distance to the neutral axis in reality. With the blade e.g. moving mainly in flap-wise direction and with only a minor

---

[14] For example, if the blade moves in flap-wise direction, all spar-cap sensors have to read zero strain when moving the blade in the lead-lag-wise direction (and vice versa). In reality, the neutral axis varies from the calculated position, making an ideal positioning impossible. Furthermore, the strain sensors are very often supposed to be located exactly in the middle of the spar cap, and therefore they cannot be exactly on the neutral axis.

[15] Prebend blades and dead weight deflections can be the reason for lead-lag-wise tests. For flap-wise tests, torsional loading often occurs because the center of gravity of tuning masses does not sit exactly in the shear center of the blade.

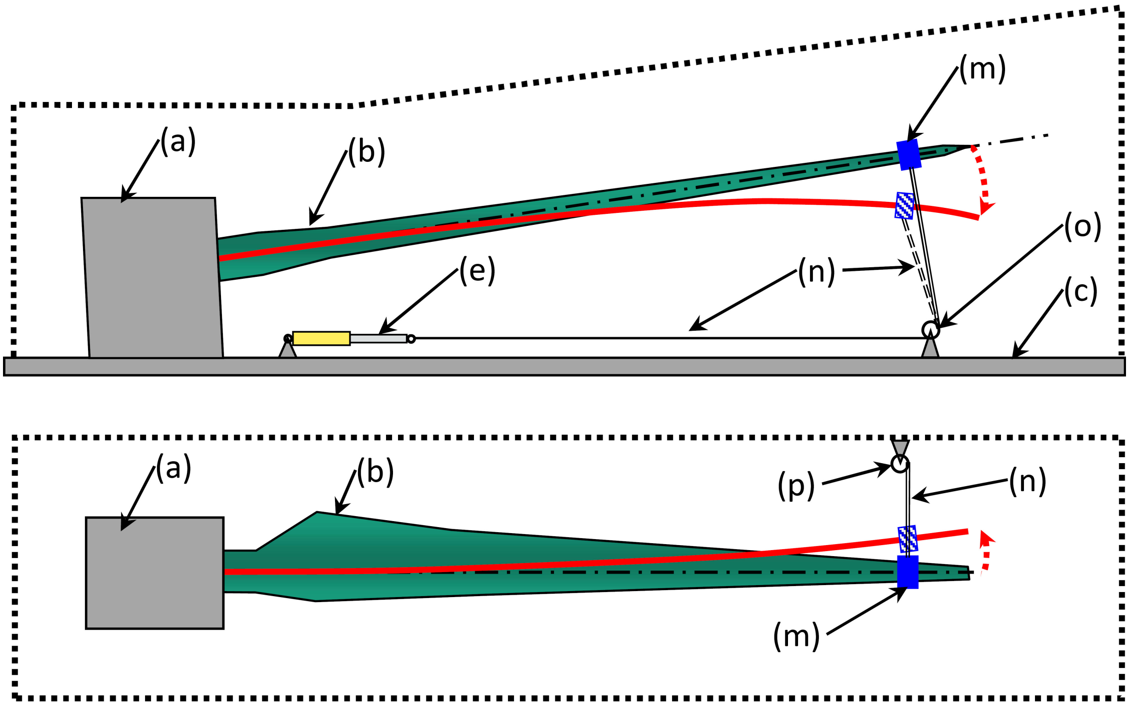

Figure 2.2: Test setup of a flap- and lead-lag-wise calibration test. Side view: Flap-wise test. Top view: Lead-lag-wise test. (a) Test rig; (b) Blade; (c) Strong floor; (e) Actuator; (m) Load frame; (n) Loading cable; (o) Turning block; (p) Winch/chain hoist

movement in lead-lag-wise direction, still the strain reading of the sensors on the spar caps is influenced by this small movement.

To be able to measure flap- and lead-lag-wise bending moments in parallel and to take care of the issue that the strain gauges are not located on the neutral axis, more calibration factors are needed. Not only the direct flap-wise and lead-lag-wise factors are needed but also the cross-talk factors for each sensor, e.g. the calibration factor of a spar cap strain gauge at edge-wise calibration loading and vice versa. In addition to the list of assumptions in Section 2.1.1, it is necessary that the two sensors to measure the flap- and lead-lag-wise bending moment have to be on *exactly* the same radius. The general method is described in IEC-61400-13 (2001) for the purpose of measuring the blade root bending moment at the turbine in use. The local blade axis (flat-wise and edge-wise) is used to define the equations. For blade tests, it is more important to know the bending moments in the flap- and lead-lag-wise direction; hence, the equations are changed accordingly.

Equation 2.3 describes the relation of the strains and bending moments for each direction. The four necessary calibration factors A_1 to A_4 for each radius can be calculated with Equation 2.1.

To be able to use equation Equation 2.1, it is necessary that calibration tests are performed *only* in the flap-wise or *only* in the lead-lag-wise direction[16].

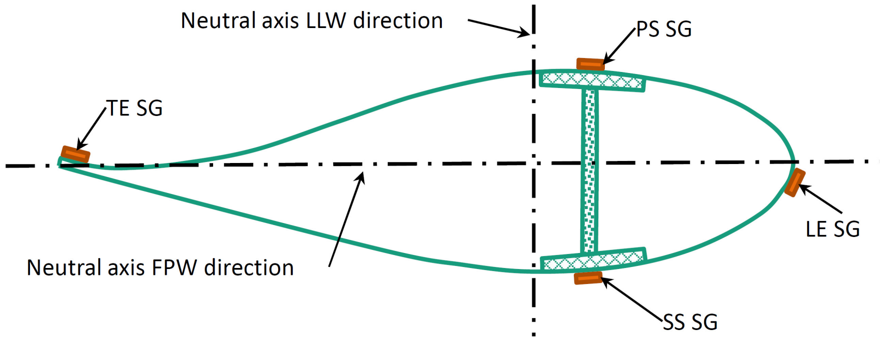

Figure 2.3: Typical strain gauge (SG) positions at calibration tests. Strain gauges are located close to the leading edge (LE) and trailing edge (TE) as well as in the middle of the spar caps on the pressure side (PS) and suction side (SS).

$$\begin{bmatrix} S^c_{SC} \\ S^c_{TE} \end{bmatrix} = \begin{bmatrix} A_1 & A_2 \\ A_3 & A_4 \end{bmatrix} \times \begin{bmatrix} M^c_{FPW} \\ M^c_{LLW} \end{bmatrix} \tag{2.3}$$

S^c_{SC}, S^c_{TE}: Strains of spar cap and trailing edge sensors due to the flap- and lead-lag-wise calibration loading

A_{1-4}: Calibration factors for flap-wise calibration A_1 and lead-lag-wise calibration A_4 as well as the related cross-talk values A_2 and A_3

M^c_{FPW}, M^c_{LLW}: Bending moments of the flap- and lead-lag-wise calibration loadings

Where Equation 2.3 describes the strains resulting from various bending moments, once the calibration matrix is known, it can be used to calculate the bending moments in the actual fatigue test by inverting the matrix (Equation 2.4).

$$\begin{bmatrix} M^t_{FPW} \\ M^t_{LLW} \end{bmatrix} = \begin{bmatrix} A_1 & A_2 \\ A_3 & A_4 \end{bmatrix}^{-1} \times \begin{bmatrix} S^t_{SC} \\ S^t_{TE} \end{bmatrix} \tag{2.4}$$

M^t_{FPW}, M^t_{LLW}: Flap- and lead-lag-wise fatigue test bending moments

---

[16] Another option is to perform two loadings in random directions but to measure the load directions exactly with a special measuring device (Greaves et al. (2016). In this case, Equation 2.3 need to be set up twice for both calibration tests, resulting in fore equations and fore calibration factors (unknowns).

S^t_{SC}, S^t_{TE}: Strains of edge and flat sensors at the fatigue test

As an example, in Appendix C a blade was analyzed by using calibration tests in flap- and lead-lag-wise direction to determine the loads of a dynamic fatigue test with and without using the cross-talk terms of Equation 2.4. The scatter of all possible bending moments of each cross-section becomes significantly smaller when using the cross-talk terms and the results will therefore be more precise and reliable.

2.2 Blade Movement of Biaxial Dynamic Fatigue Tests

In this section, the theoretical movement of blades at biaxial tests will be described in preparation for the new biaxial loading purposed in Chapter 5. At uniaxial dynamic fatigue tests, the blade is excited in the first *or* in the second eigenmode in case of flap- or lead-lag-wise dynamic fatigue tests. The eigenmodes are defined by the oscillating system which is not only the blade, but also additional masses like tuning weights or the engines to excite the system. If both eigenmodes are excited *at the same time*, the test can be called a biaxial dynamic fatigue test.

For simplification the analyzed blade in this section shall not be prebend in any direction. Furthermore, no dead weight deflection is assumed. The tip is therefore on the pitch axis or Z_{IEC}. In case of prebend blades and dead weight deflections, offsets would have to be added. For the following calculations it is assumed that the blade is fixed horizontally to the test rig.

The tip movement will be described, using the equations of harmonic oscillators in the flap- and lead-lag-wise coordinate system of IEC-61400-23 (2014). Even though it is a damped harmonic oscillation, in all tests the damping rate will be compensated with different exciter systems by introducing additional energy into the system. Hence, the damping terms are left out, as the oscillation is at a constant amplitude for the whole test. When looking at the linearity of the spring (blade) over displacement, it is known form experience that blades do behave linear. This is still valid, if smaller sections of the blade do behave nonlinear as described in Section 3.2.

2.2.1 Tip Movement of Uniaxial Dynamic Tests

To start with a simple system first, the structural twist is set to zero. The minimum stiffness is in the direction of Y_{IEC} (Section A) and defining the flap-wise behavior of the blade. The maximum stiffness is in the direction of X_{IEC} and defining the lead-lag-wise behavior of the blade accordingly. Hence, the 1st eigenmode is oriented in flap-wise (FPW) and the 2nd eigenmode in lead-lag-wise (LLW) direction. At this point, the oscillation of the tip can be described by equations Equation 2.5 and Equation 2.6. The movement of the 1st and 2nd eigenmode is visualized in Figure 2.4(left)[17].

---

[17] All following diagrams are oriented accordingly. View from root to tip.

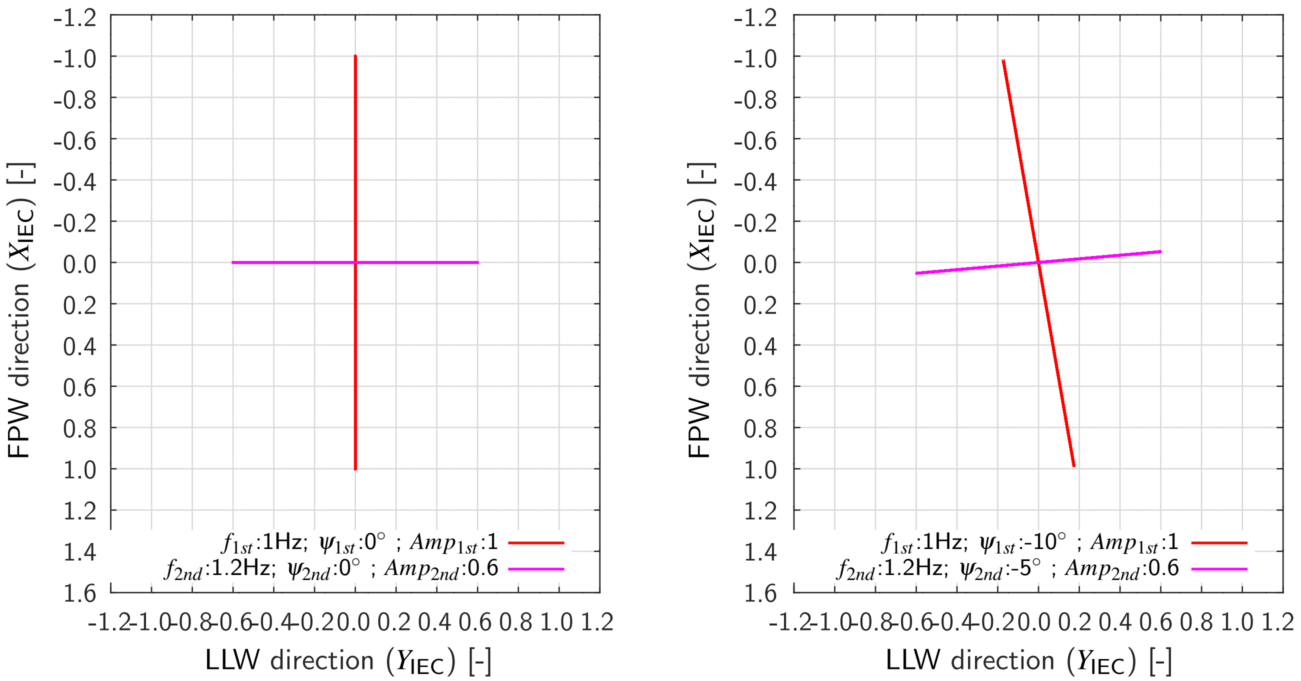

Figure 2.4: Movement of the blade tip for a blade **without** (left) and **with** (right) structural twist. Blade without prebend or dead weight deflection.

flap-wise (vertical) movement:

$$\begin{gathered} x_{1\text{st}}(t) = Amp_{1st} \times \sin(\omega_{1st} \times t + \varphi_{1st}) \\ \omega_{1st} = \frac{2 \times \pi}{T_{1st}}, \qquad f_{1st} = \frac{1}{T_{1st}} \end{gathered} \tag{2.5}$$

x**:** Coordinate in X_{IEC} direction

t**:** Time

Amp_{1st}**:** Amplitude at the 1st eigenmode

ω_{1st}**:** Angular frequency of the 1st eigenmode

φ_{1st}**:** Phase shift of the 1st eigenmode

T_{1st}**:** Period of the 1st eigenmode

f_{1st}**:** Frequency of the 1st eigenmode

lead-lag-wise (horizontal) movement:

$$\begin{aligned} y_{\mathrm{2nd}}(t) &= Amp_{2nd} \times \sin\left(\omega_{2nd} \times t + \varphi_{2nd}\right) \\ \omega_{2nd} &= \frac{2 \times \pi}{T_{2nd}}, \qquad f_{2nd} = \frac{1}{T_{2nd}} \end{aligned} \tag{2.6}$$

To include the structural twist, the directions of the oscillations have to be rotated around the Z_{IEC}-axis. The angles are defined as ψ_{1st} and ψ_{2nd} with the right-handrule to the Z_{IEC}-axis. The resulting coordinates in the X_{IEC} and Y_{IEC} directions are according to Equation 2.7 and Equation 2.8. The movement of the 1st and 2nd eigenmode is visualized in Figure 2.4(right) for exemplary rotations of both directions[18].

1st eigenmode movement:(usually described as flap-wise or vertical movement)

$$\begin{aligned} x_{\mathrm{1st}}(t) &= \quad \cos\left(\psi_{1st}\right) \times Amp_{1st} \times \sin\left(\omega_{1st} \times t + \varphi_{1st}\right) \\ y_{\mathrm{1st}}(t) &= -\sin\left(\psi_{1st}\right) \times Amp_{1st} \times \sin\left(\omega_{1st} \times t + \varphi_{1st}\right) \end{aligned} \tag{2.7}$$

2nd eigenmode movement:(usually described as lead-lag-wise or horizontal movement)

$$\begin{aligned} x_{\mathrm{2nd}}(t) &= \quad \sin\left(\psi_{2nd}\right) \times Amp_{2nd} \times \sin\left(\omega_{2nd} \times t + \varphi_{2nd}\right) \\ y_{\mathrm{2nd}}(t) &= \quad \cos\left(\psi_{2nd}\right) \times Amp_{2nd} \times \sin\left(\omega_{2nd} \times t + \varphi_{2nd}\right) \end{aligned} \tag{2.8}$$

2.2.2 Tip Movement of Biaxial Dynamic Tests

For a biaxial dynamic fatigue test, the 1st and 2nd eigenmode is excited at the same time. With given natural frequencies of both modes, the only parameter which is possible to adjust is the phase φ_{1st} and φ_{2nd}. In any case, the sinusoidal movement is repeated after a certain period so that in all further calculations only φ_{1st} is used to define the phase. To classify all generally different movements, three categories were chosen. It is not intended to classify the curves in a mathematical way, but to describe principally different blade test options.

1.) Equal frequencies:

Almost all blades have different natural frequencies for the 1st and 2nd eigenmode. To achieve equal frequencies, the blades have to be tuned with extra masses and extra mechanical systems as described in Section 5. The blade will move in an ellipse in this case. When changing the phase

---

[18] The angle ψ_{1st} and ψ_{2nd} is not necessarily identical or negative. Both are dependent on the distribution of the structural twist and the mass distribution in span-wise direction.

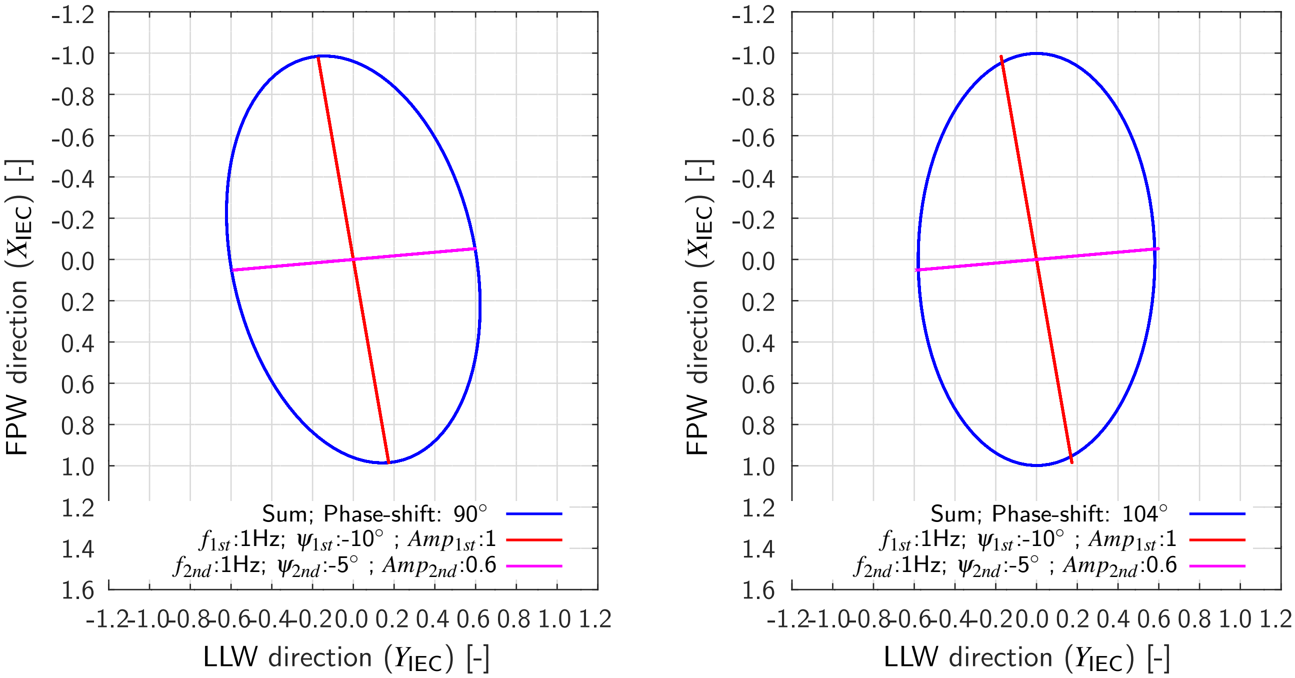

Figure 2.5: Movement of the blade tip at a phase shift of 90° (left) and 104° (right). Blade **with** structural twist and without prebend or dead weight deflection.

the shape of the ellipse can be manipulated. In Figure 2.5(left), the biaxial movement is shown with the rotation angles and amplitudes of Figure 2.4(right) but equal frequencies and a phase of φ_{1st} is 90°.

To control the loading of a blade in such a test, the amplitudes (Amp_{1st}, Amp_{2nd}) and the phase (φ_{1st}) can be adjusted. An example is shown in Figure 2.5 (right), where the phase was tuned to 104°. In this case, the maximum deflection in flap- and lead-lag-wise direction is at a time with no loading in the secondary direction. Many other shapes are possible. As described in D. White (2004), ideally not only one phase angle but most likely a variety of angles shall be used to achieve the best possible DEL in comparison with the real turbine loading. If one phase is used for simplification, in D. White (2004) an angle of 72° was estimated to be ideal for the analysed turbine.

2.) Certain quotients of both frequencies:

Many options are possible how two harmonic oscillations might be combined with regard to the frequencies and phases. Simple curves occur, if the quotient of both frequencies is for example 1:2, 2:3, 3:4 or 4:5. Using 1:2 and 3:4 as examples and assuming that the rotation angles ψ_{1st} and ψ_{2nd} are zero, an exemplary blade tip movement is shown in Figure 2.6(top). The flap- and lead-lag-wise movement of the blade tip for all setups of Figure 2.6(top) is shown in Figure 2.6(bottom). A constant amplitude fatigue test would be performed. In this sense, these dynamic fatigue tests are comparable when performing two uniaxial dynamic fatigue tests in flap- and lead-lag-wise direction separately. The performed cycle numbers in both directions (in a specific time period) are fixed to the quotient of the 1^{st} and 2^{nd} natural frequency.

Using the above examples (1:2, 3:4) again, but including the usual structural twist of a blade, rotation of the flap- and lead-lag-wise movement occurs. The blade tip movement is shown in Figure 2.7(top). In Figure 2.7(bottom) the flap- and lead-lag-wise movement of the blade tip is plotted over time. In this case, the direction of the 1^{st} and 2^{nd} eigenmode is *not* identical with the flap- and lead-lag-wise direction. In comparison to Figure 2.6(bottom), for the flap- and lead-lag-wise direction, a constant amplitude test is *not* given any more, because each half cycle has a different size. This behavior was also described by Beckwith, White, and Barsotti (2013) and will later be discussed in Section 4.3.

3.) Arbitrary quotients:

The higher the natural numbers of the quotient of the 1^{st} and 2^{nd} natural frequencies, the longer the period at which the movement is repeated. In Figure 2.8, the movement of the blade tip is exemplary shown for f_{1st} over f_{2nd} is 25:28 or $f_{1st} = 1$Hz and $f_{2nd} = 1.12$Hz. In Figure 2.9, the movement of the blade in flap- and lead-lag-wise direction is shown. No constant amplitude test is possible. The more complex the movement of the blade tip gets, the more steps are present in the resulting load spectrum of the flap- and lead-lag-wise direction.

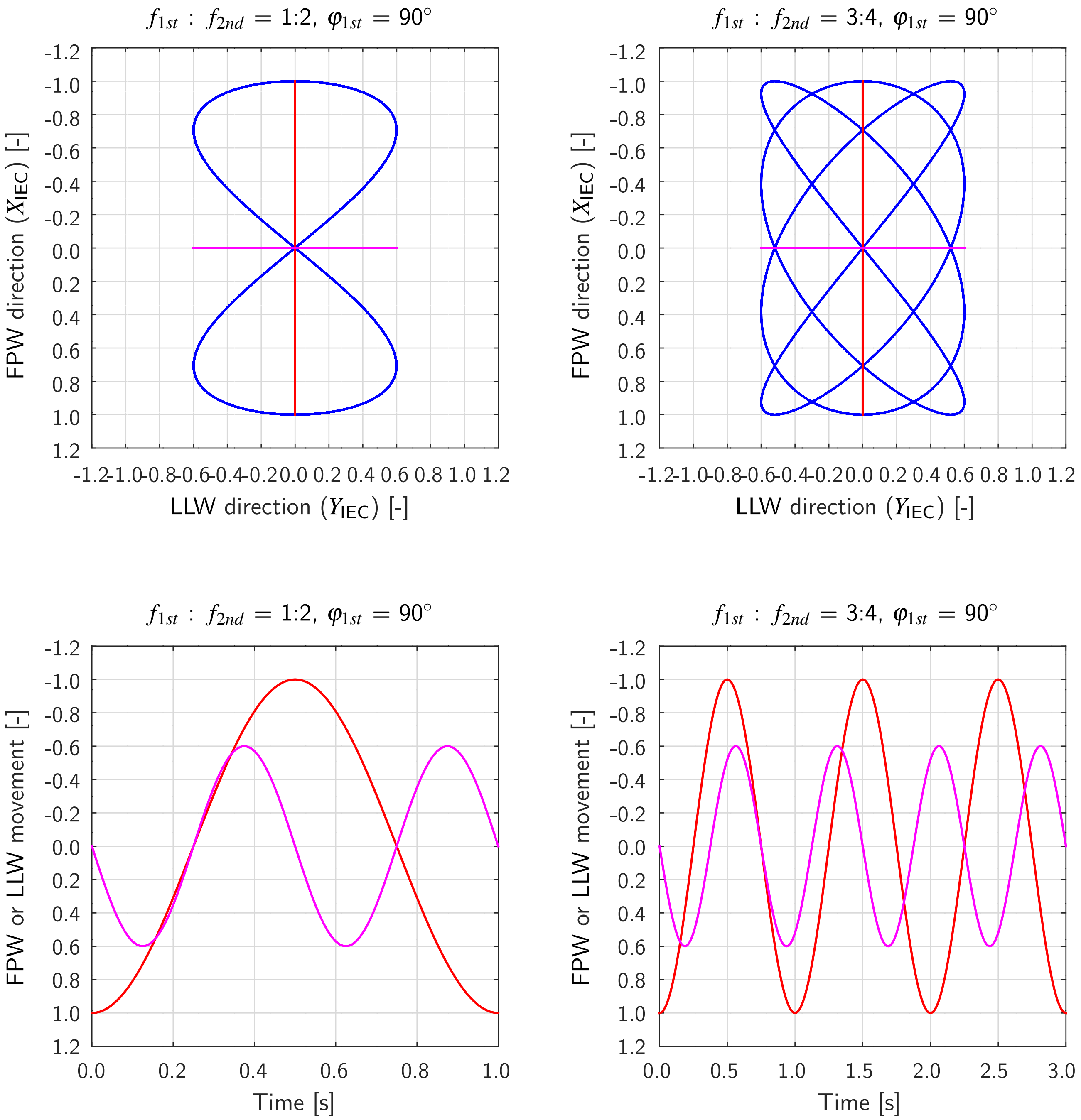

Figure 2.6: Two different biaxial movements of the blade tip. Blade **without** structural twist. **Top:** In blue: Biaxial movement of the blade tip. Amplitudes (Amp_{1st}=1.0 Amp_{1st}=0.6). Blade without prebend or dead weight deflection (Offset=0). In red: If Amp_{2nd}=0. In magenta: If Amp_{1st}=0. **Bottom:** Movement of the blade tip. In red: Movement of the blade tip in flap-wise direction. In magenta: Movement of the blade tip in lead-lag-wise direction. Because structural twist **is not** present (ψ_{1st}=0° , ψ_{2nd}=0°), the direction of the 1^{st} and 2^{nd} eigenmode **is** equal to the flap- and lead-lag-wise direction.

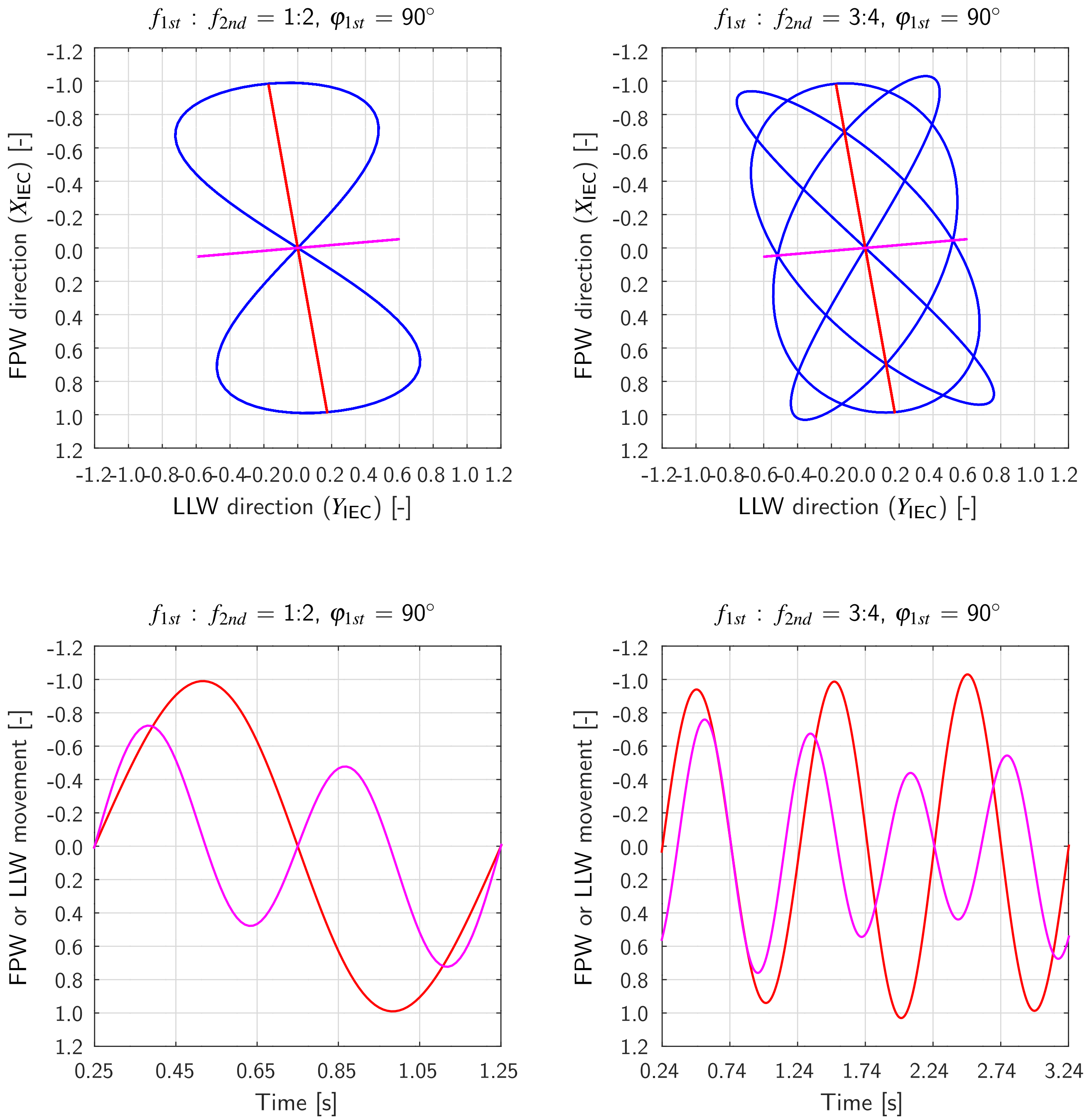

Figure 2.7: Two different biaxial movements of the blade tip. Blade **with** structural twist. **Top:** In blue: Biaxial movement of the blade tip. A blade with structural twist (ψ_{1st}=-10° , ψ_{2nd}=-5°). Amplitudes (Amp_{1st}=1.0 Amp_{1st}=0.6). Blade without prebend or dead weight deflection (Offset = 0). In red: If Amp_{2nd}=0. In magenta: If Amp_{1st}=0. **Bottom:** Movement of the blade tip. In red: Movement of the blade tip in flap-wise direction. In magenta: Movement of the blade tip in lead-lag-wise direction. Because structural twist **is** present, the direction of the 1st and 2nd eigenmode **is not** equal to the flap-wise and lead-lag-wise direction.

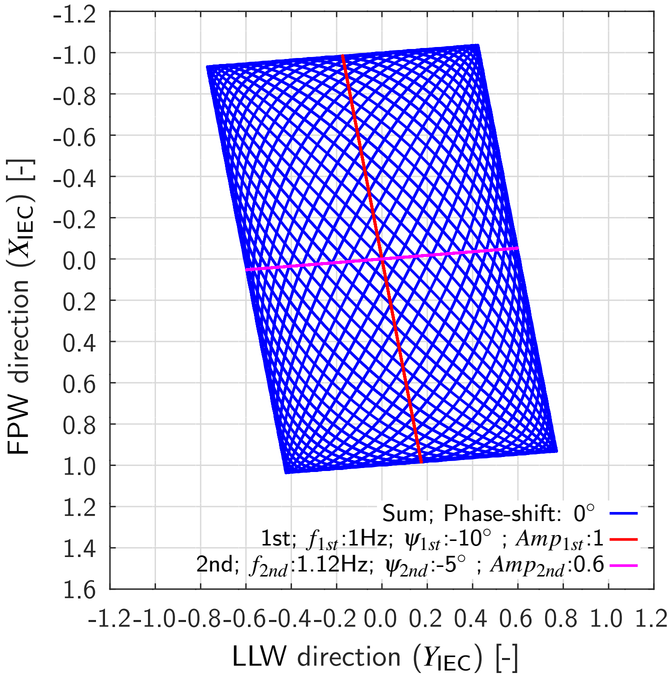

Figure 2.8: Blade movement **with** structural twist. f_{1st} over f_{2nd} is 25:28. In blue: Biaxial movement of the blade tip. Without prebend or dead weight deflection in the 1st and 2nd eigenmode (Offset = 0). In red: If $Amp_{2nd} = 0$. In magenta: If $Amp_{1st} = 0$. Time plotted from 0 to 40s

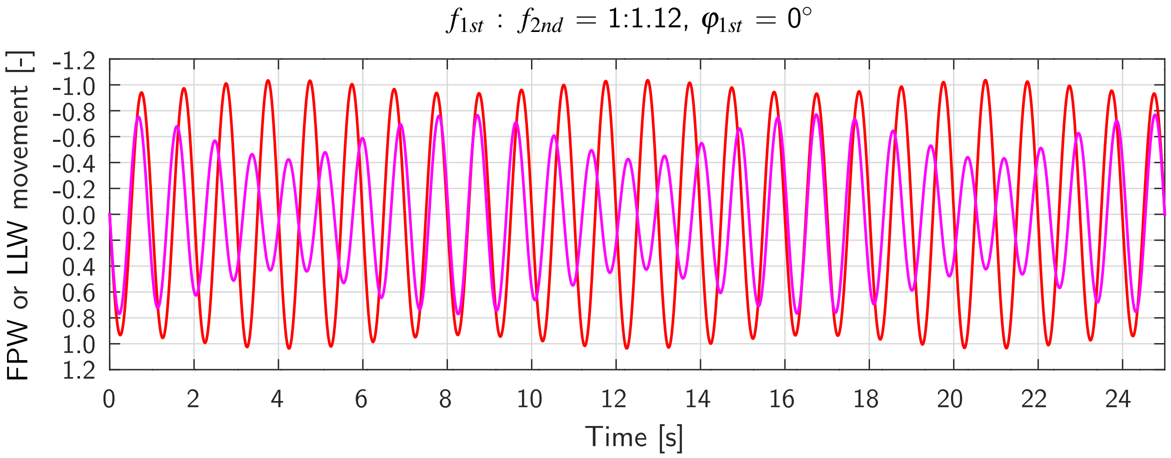

Figure 2.9: Movement of the blade tip for each axis. Blade **with** structural twist. f_{1st} over f_{2nd} is 25:28. In red: Movement of the blade tip in the flap-wise direction. In magenta: Movement of the blade tip in the lead-lag-wise direction. Because structural twist **is** present, the direction of the 1st and 2nd eigenmode is **not** equal with the flap-wise and lead-lag-wise direction.

2.3 Loading Mechanisms for Uniaxial Fatigue Tests

2.3.1 Uniaxial Quasi-static Tests

At uniaxial tests, the blade is loaded in flap- and lead-lag-wise direction separately. Quasi-static means that the frequency of the cyclic load to move the blade is significantly lower than the natural frequency of that direction. In Figure 2.10, the responding amplitudes of a forced excitation are given in relation to the excitation frequency over the natural frequency for different damping coefficients. Already at 50% of the natural frequency combined with small damping values of 0.1, the dynamic loading is down to 0.2 to 0.3 of the static loading. Combining the same damping ratio with an excitation at the natural frequency, the dynamic loading is already 5.0 times higher than the static loading.

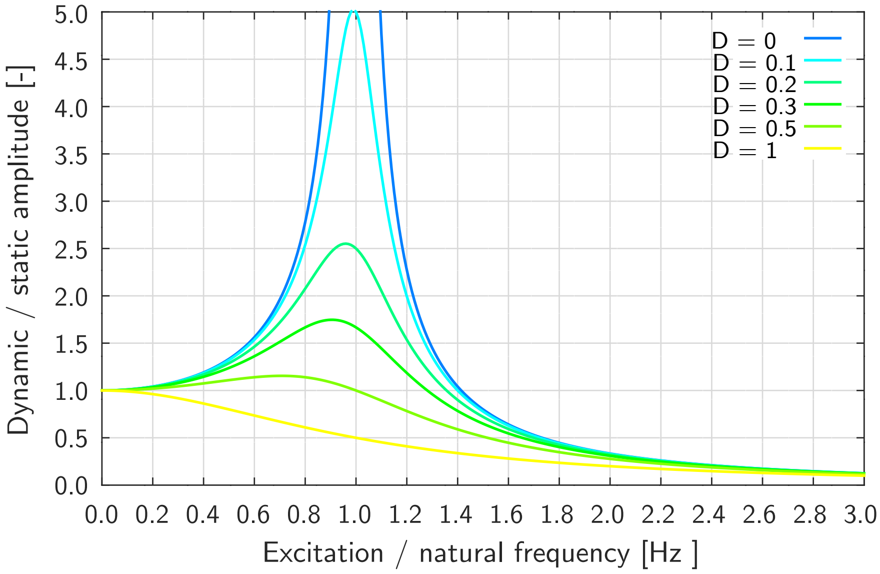

Figure 2.10: Resulting amplitudes of a forced excitation of a spring mass damper system plotted over the excitation frequency (for different damping coefficients).

An exemplary test setup for a uniaxial quasi-static test is shown in Figure 2.11. At around 70% of the blade length, a servo-hydraulic actuator is connected to the blade. The blade is loaded with a cyclic, sinusoidal movement of the actuator. In span-wise direction the bending moment increases linearly from the actuator position towards the blade root. Outboard of the load introduction location, no loading can be applied. Hence, blade tips where often cut to reduce the required space.

Because the ideal bending moment distribution is usually not linear but exponential, a second actuator can be fixed to the blade at around 30 - 40% radius (IEC-61400-23 (2001) Annex D). With a simultaneous loading of both actuators a bi-linear load distribution is achieved for a better load fitting.

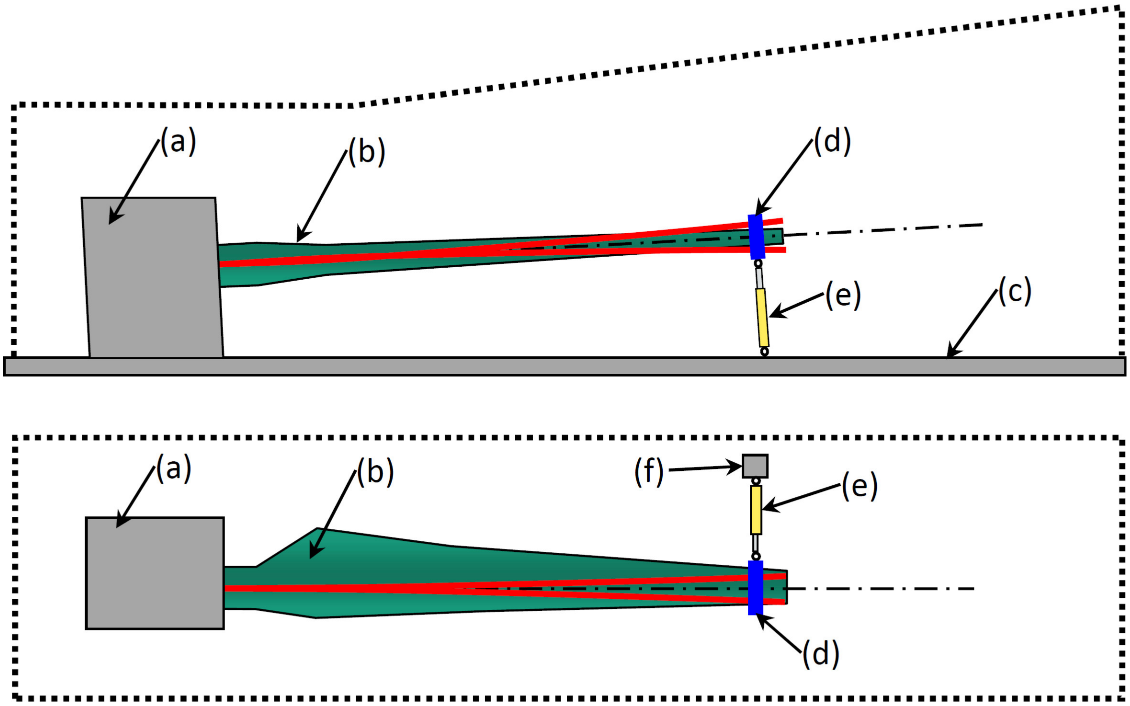

Figure 2.11: Test setups of two quasi-static uniaxial fatigue tests loaded with directly attached servo-hydraulic actuators. Side view: Flap-wise test. Top view: Lead-lag-wise test. (a) Test rig; (b) Blade; (c) Strong floor; (d) Load frame; (e) Vertical or horizontal actuator; (f) Support of horizontal actuator.

The energy consumption of these tests is very high. The large actuator forces combined with the large deflections require a high amount of energy. Test frequencies are limited due to the capacity of the expensive hydraulic system, hence the testing time is usually long.

2.3.2 Uniaxial Dynamic Tests

In a *dynamic* fatigue test, the cyclic loading of the blade is created by the oscillating structure itself. The blade is excited to a natural frequency oscillation with only adding a little amount of energy to compensate the air and material damping. The energy in the system changes every quarter cycle from pure kinetic energy only to pure elastic energy only.

Dynamic tests are performed with the suction side of the blade facing downwards. Hence, the flap-wise loading is applied by deflecting the blade vertically. Herewith, the average wind load is represented by the dead weight of the blade (test mean load). The lead-lag-wise loading is applied by deflecting the blade horizontally, because having no mean load is more representative compared to the turbine loading[19]. A comparable test load to real loads appears to be logical, but because certification tests focus on testing the design assumptions (IEC-61400-23 (2014)) and test loads are purely mathematically determined by using the Palmgren Miner rule (DEL), comparable loads to reality are not necessary. Especially if using a material model taking the meanload properly into account, this influence is already included in the test load determination (Sutherland and Mandell (2004a), Sutherland and Mandell (2004b), Sutherland and Mandell (2005) or Nijssen (2006)). Still, if possible, flap-wise tests are performed vertically and lead-lag-wise tests horizontally. Most likely because it is still questionable how accurate such material models represent reality and if the failure mode of the structure will be comparable.

A uniaxial dynamic test setup using eccentric electric motors is sketched in Figure 2.12. Also servo-hydraulic shakers are often used instead. For both methods, the excitation system is attached to the blade and moves together with the oscillating blade to compensate the air damping. Most likely additional extra weights are attached to the blade to adjust the bending moment curve to fit the desired distribution.

In lead-lag-wise direction the air damping is rather small, therefore excitation systems with a low mass can be used. Compared to the pure blade oscillation, the influence on the oscillation due to the exciter mass is small. In flap-wise direction the air damping is significantly higher resulting in a much heavier exciter mass. The natural frequencies of the oscillating systems are still decreased to an extent that the blade part's outboard of the exciter location is not loaded adequately.

Generally at least in flap-wise direction, the loading is dominated by the acceleration forces of the exciter mass, resulting in a rather unfitting load distribution, which again has to be improved using attached masses decreasing the test frequency further.

Large exciter masses can be avoided, if the drag coefficient can be reduced with aerodynamic optimizations at the blade tip, but the effort to build these structures, the limited possibility for inspecting the blades and the complicated maintenance of sensors in this region is disadvantageous.

Ghorashi and Moetakef-Imani (2016) describe how to introduce more energy into the blade without increasing the masses of the excitation system attached to the blade. A blade is excited with an electrically driven eccentric engine. The exciter is connected by a stiff cable to the blade to introduce the excitation force by using a specialised control algorithm. The testing was performed on rather small blades. It is concluded that up scaling to large blades will be quite challenging.

Another method to excite a blade to a natural frequency oscillation is to directly couple a servo-hydraulic actuator between blade and strong floor as shown in Figure 2.13. On the contrary to eccentric exciters, it is much easier to apply large mechanical energy to the blade. Hence, usually no aerodynamic optimization is necessary. The oscillation can often be performed without having extra masses on the blade but with already achieving an appropriate loading. The resulting high test frequency leads to a short overall testing time. In case additional masses are needed for an adequate loading, they *can* be placed at any location on the blade such that the tested area is

---

[19] The load to drive the generator is of course present, but usually not taken into account.

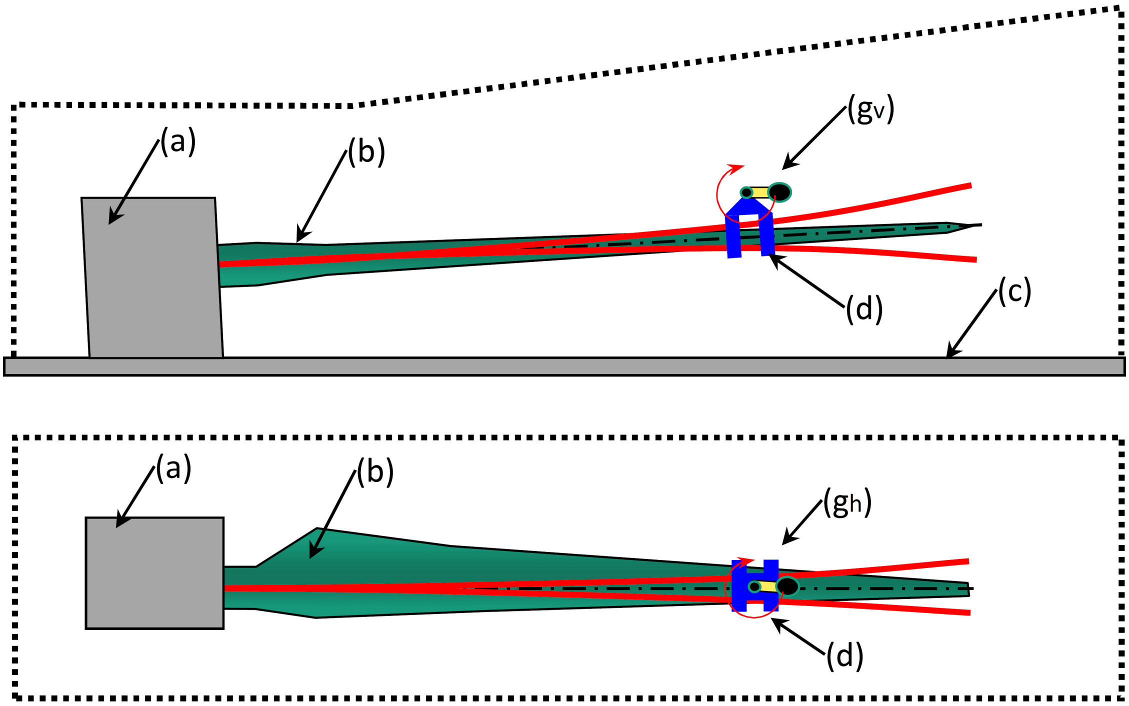

Figure 2.12: Test setups of two uniaxial dynamic fatigue tests loaded with eccentric motors. Side view: Flap-wise test. Top view: Lead-lag-wise test direction. (a) Test rig; (b) Blade; (c) Strong floor; (d) Load frame; (g_v) Vertical eccentric motor; (g_h) Horizontal eccentric motor

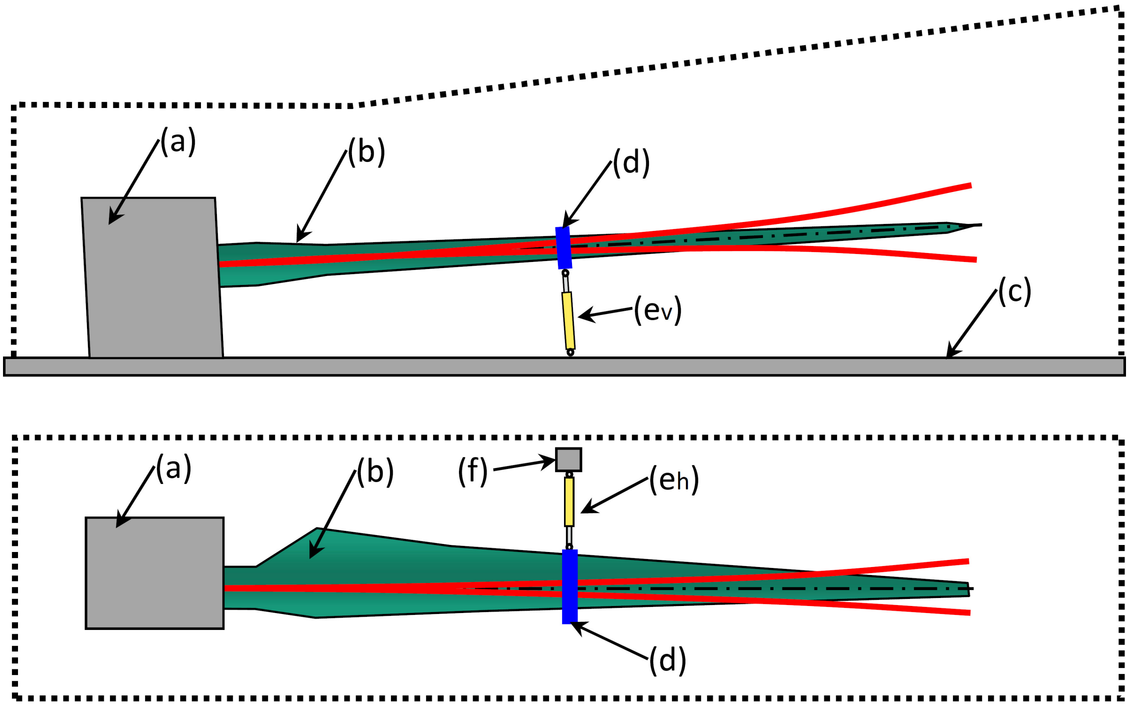

Figure 2.13: Test setups of two dynamic uniaxial fatigue tests loaded with directly attached servo-hydraulic actuators. Side view: Flap-wise test. Top view: Lead-lag-wise test. (a) Test rig; (b) Blade; (c) Strong floor; (d) Load frame; (e_v) Vertical actuator; (e_h) Horizontal actuator; (f) Support of horizontal actuator.

usually larger contrary to eccentric exciters. With lowering the excitation frequency in very small steps, starting at the blade natural frequency, the span-wise loading distribution changes, allowing a fast and precise tuning of the test load. Disadvantageous is the high amount of energy needed for such tests. A sinusoidally moved hydraulic actuator can only transfer a part of the applied hydraulic energy to mechanical energy (because the cross-section of the actuator requires the same volume of oil at any force and stroke).

Recently, the IABG[20] and R&D [21] have presented electric direct/gear drive approaches to excite blades for fatigue. With using a bell crank mechanism in combination with high-torque electric motors, the disadvantage of hydraulic systems regarding the high energy consumption might be reduced. Contrary to electric eccentric exciters, the system does not oscillate with the blade, avoiding the discussed disadvantages of such approaches.

2.4 Loading Mechanisms for Biaxial Fatigue Tests

2.4.1 Biaxial Quasi-static Tests

The uniaxial quasi static tests described in Section 2.3.1 can be performed in both directions of the blade simultaneously (flap- and lead-lag-wise). An exemplary test setup is shown in Figure 2.14. In D. White (2004) and D. L. White and Musial (2004), the relation of flap- and lead-lag-wise loads at the actual turbine were analyzed to find an ideal phase angle for such tests at an elliptic motion of the blade cross-wise to the pitch axis. The kinematics of necessary test structures were analyzed in Hughes, Musial, and Stensland (1999), D. White (2004) and Malhotra (2010). A test setup is also shown in Westphal (2010).

Again the high energy consumption in comparison with two uniaxial quasi-static tests is disadvantageous (as described in Section 2.3.1, IEC-61400-23 (2014) or D. White (2004)). Aditionally the test time is rather long due to the very low test frequency, even though both uniaxial tests are performed in parallel which already halves the test time. Also disadvantageous is the limited tested length in span-wise direction, as discussed in Section 2.3.1. An advantage is that because of the elliptic motion a larger part of the cross-sections is loaded realistically compared to uniaxial tests.

2.4.2 Biaxial Quasi-static and Dynamic Combined Tests

To reduce the energy of biaxial quasi-static tests and to enlarge the tested areas in span-wise direction, the beneficial elliptic motion of the blade can also be achieved with a dynamic loading

---

[20] Industrieanlagen-Betriebsgesellschaft mbH (IABG), Ottobrunn Germany

[21] R&D Engineering A/S, Hinnerup Denmark

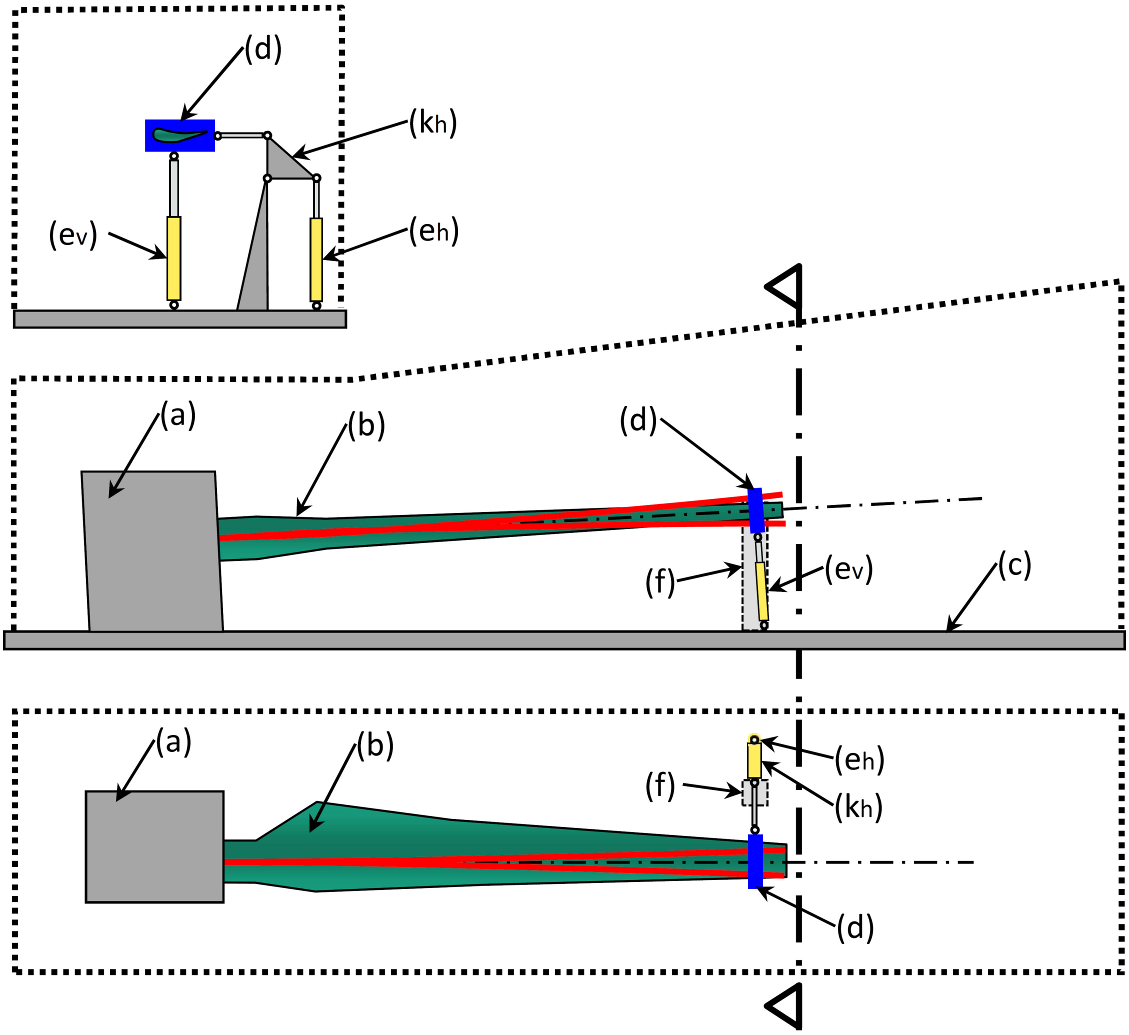

Figure 2.14: Test setup of a quasi-static biaxial fatigue test loaded with directly attached servo-hydraulic actuators. Side view: Flap-wise test. Top view: Lead-lag-wise test. (a) Test rig; (b) Blade; (c) Strong floor; (d) Load frame; (e_v) Vertical actuator; (e_h) Horizontal actuator; (f) Support of bell crank; (k_h) Horizontal bell crank mechanism.

in one direction. One approach is, that the flap-wise direction can be loaded dynamically at its natural frequency and the lead-lag-wise direction can be loaded quasi-statically in parallel (at the same frequency as the flap-wise direction).

In Figure 2.15, such setup is shown using a hydraulic shaker system in combination with a hydraulic actuator and bell crank mechanism. The test method is analyzed in Hughes et al. (1999), D. White (2004), D. White et al. (2005) and Borst (2012).

A major disadvantage is that because of the large displacement of the blade tip in flap-wise direction the quasi-static loading of the tip region in lead-lag-wise direction is almost impossible. Long horizontal bellcrank mechanisms combined with a very low mass would be needed. The

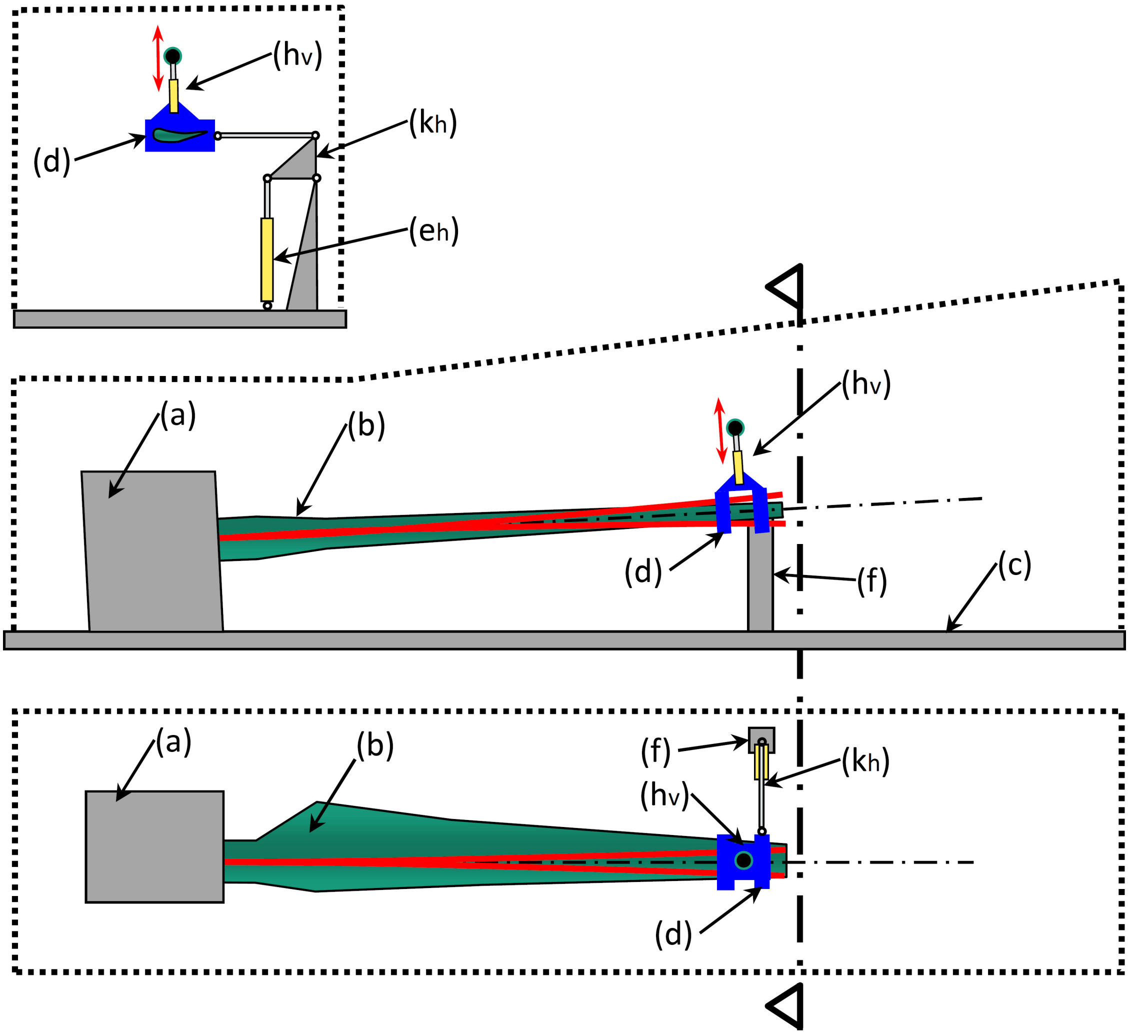

Figure 2.15: Test setup of a dynamic and quasi-static combined biaxial fatigue test loaded with a linear shaker in flap-wise direction (dynamic) and a directly attached servo-hydraulic actuator in lead-lag-wise direction (quasi-static). Side view: Flap-wise test. Top view: Lead-lag-wise test. (a) Test rig; (b) Blade; (c) Strong floor; (d) Load frame; (e_h) Horizontal actuator; (h_v) Vertical linear shaker; (f) Support of bell crank; (k_h) Horizontal bell crank mechanism.

result is a rather far inboard positioned loading location in lead-lag-wise direction. Hence, a large part of the outboard blade cannot be loaded (Borst (2012)).

Another approach to achieve an elliptical motion of the blade is shown in Figure 2.16 and described in D. White, Desmond, Gowharji, Beckwith, and Meierjurgen (2011) and Beckwith et al. (2013). Instead of reducing the lead-lag-wise to the flap-wise frequency, the opposite was performed. Where the lead-lag-wise direction was run in its natural frequency using a hydraulic shaker system on the blade, in the flap-wise direction the blade was loaded at the lead-lag-wise natural frequency. A hydraulic actuator was coupled between blade and strong floor to force the blade beyond the natural frequency in that direction. In lead-lag-wise direction, a hydraulic mass shaker system was

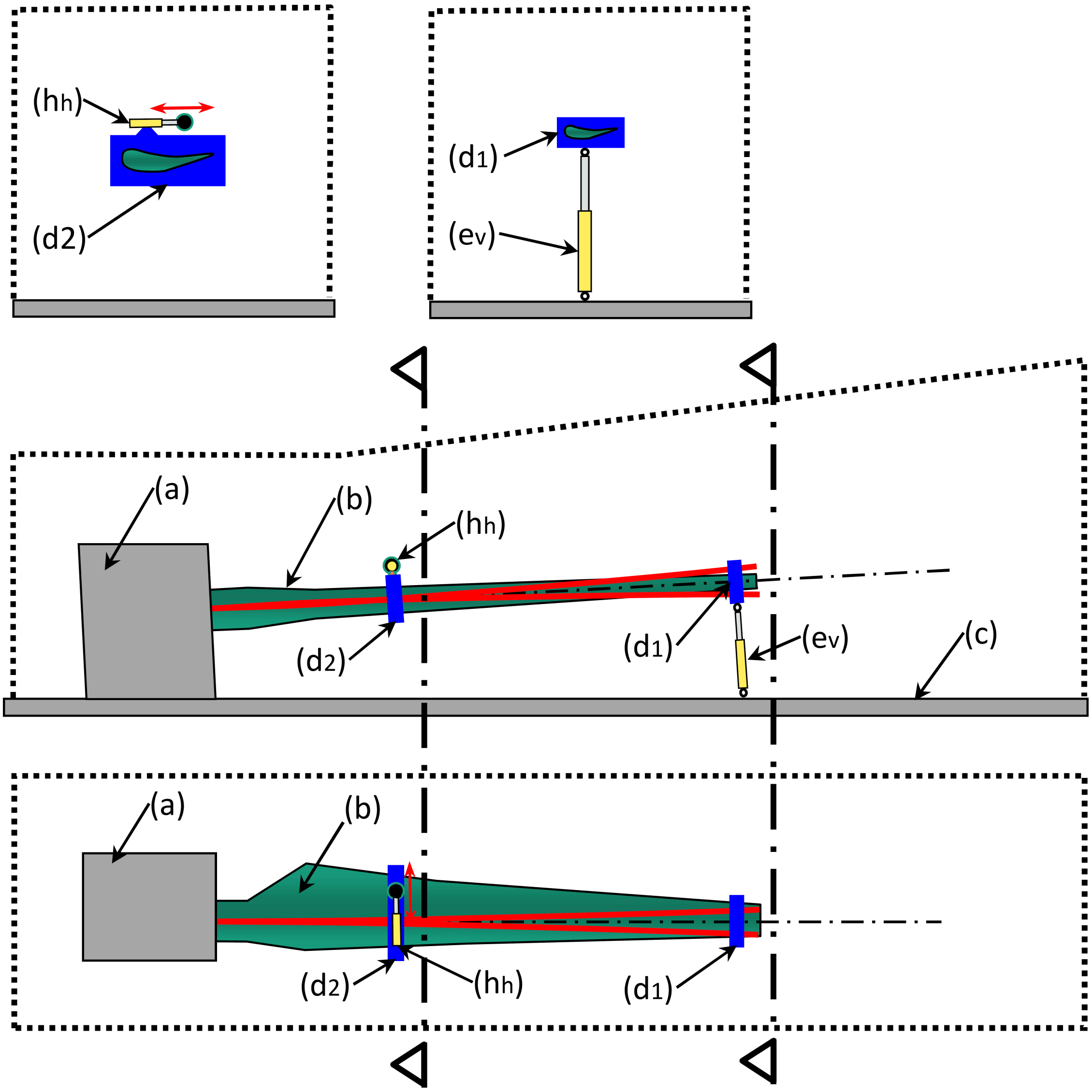

Figure 2.16: Test setup of a dynamic and quasi-static combined biaxial fatigue test loaded with a linear shaker in lead-lag-wise direction (dynamic) and a directly attached servo-hydraulic actuator in flap-wise direction (quasi-static). Side view: Flap-wise test. Top view: Lead-lag-wise test. (a) Test rig; (b) Blade; (c) Strong floor; (d$_{1+2}$) Load frames; (e$_v$) Vertical actuator; (h$_h$) Horizontal linear shaker.

used. Where it was possible to simulate such a test setup in theory, in Beckwith et al. (2013) was concluded that it is unrealistic to use it for certification tests of multi-megawatt turbines.

2.4.3 Biaxial Dynamic Tests

Trying to achieve all benefits of biaxial tests, like a more realistic loading and a fast test in combination with a large tested area in span-wise direction and a reduced energy, at the same time, the dynamic excitation methods described in Section 2.3.2 were combined to excite the blade the first two natural frequencies in flap- as well as in lead-lag-wise direction simultaneously.

A test setup using mass shakers is shown in Figure 2.17 and presented in Snowberg, Dana, Hughes, and Berling (2014). Another approach is described in Chapter 4 using servo-hydraulic actuators to excite both directions (Figure 4.1 and Figure 4.2).

Because the blade can only be excited exactly in its two first natural frequencies, the movement of the blade produces a rather complex Lissajous figure which is additionally rotated because of the rotating structural twist of the blade along the span. The movements are described Section 2.2. It was found that especially a short testing time is only achievable, if the blade can be excited in an elliptical motion instead, for which equal frequencies in flap- and lead-lag-wise direction are necessary (Beckwith et al. (2013)).

Mechanisms to achieve such elliptic motion (equal frequencies) are shown in Melcher, Bätge, and Neßlinger (2019), Greaves (2013), Westphal (2010) and Borst (2012). Masses are attached to only influence the lead-lag-wise direction in order to decrease the lead-lag-wise natural frequency exactly to the flap-wise natural frequency. The mechanism sketched in Figure 2.18 uses masses on roller tables sideways to the blade. The masses have to be connected with very lightweight push rods to the blade. The excitation can be performed with any type of actuator, shaker or eccentric motor. Because of the large hall space necessary, a realization for common certification tests is unlikely (Greaves (2013)). The mechanism sketched in Borst (2012) uses large bell-crank mechanisms instead. It needs less hall space but testing the outboard regions of the blade is still hardly possible because of the high flap-wise deflections. In Melcher et al. (2019) also spring elements were purposed to adjust for an optimized bending moment distribution in span-wise direction. According to Melcher et al. (2019), Greaves, Dominy, Ingram, Long, et al. (2011), D. White (2004) or IEC-61400-23 (2014), advantages are that the biaxial elliptical loading of the blade leads to a thoroughly tested blade (at the span-wise areas which can be loaded).

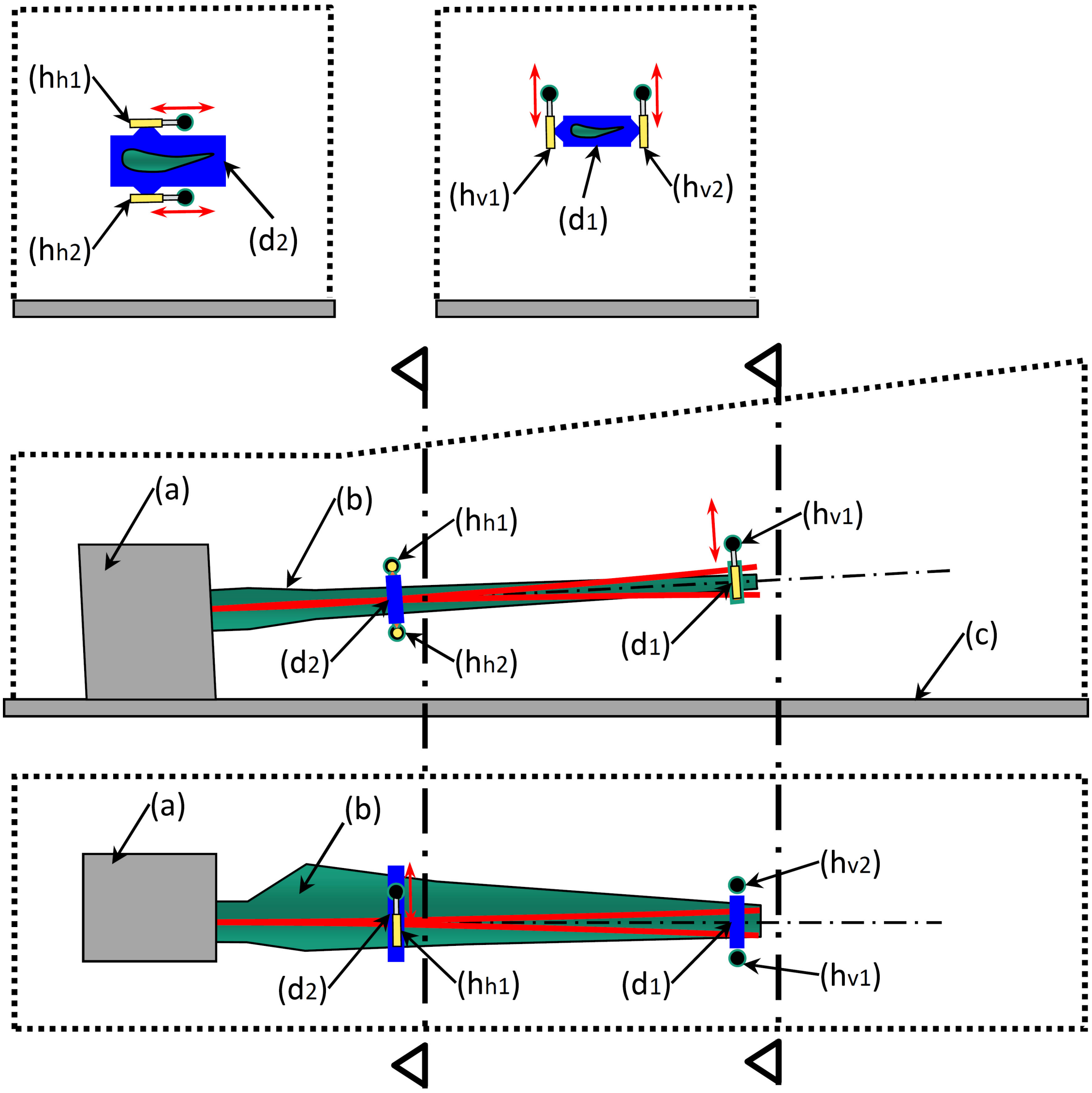

Figure 2.17: Test setup of a dynamic biaxial fatigue test loaded with linear shakers in flap- and lead-lag-wise direction (dynamic). Side view: Flap-wise test. Top view: Lead-lag-wise test. (a) Test rig; (b) Blade; (c) Strong floor; (d_{1+2}) Load frame; (h_{h1+2}) Horizontal linear shakers; (h_{v1+2}) Vertical linear shakers.

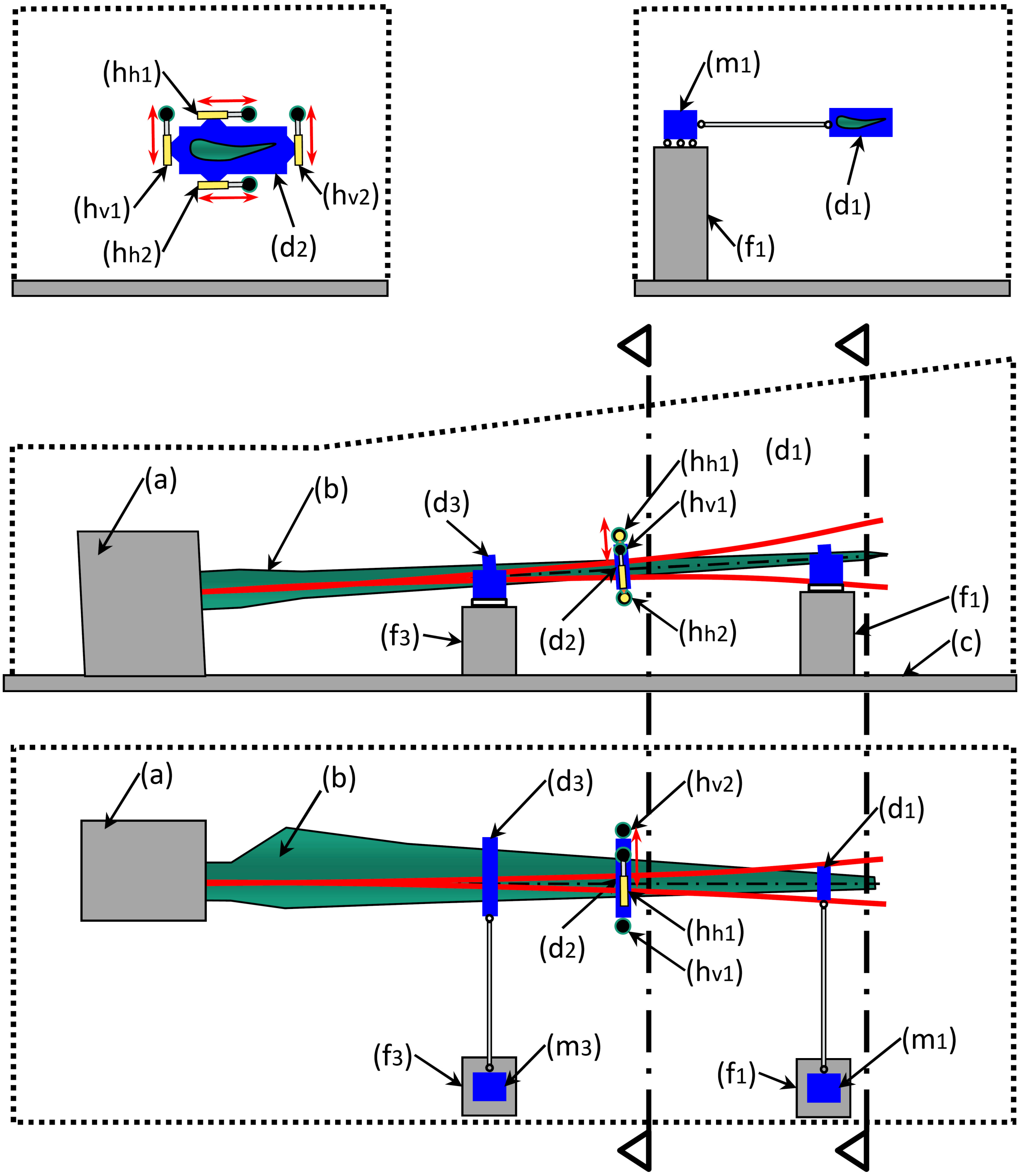

Figure 2.18: Test setup of a dynamic biaxial fatigue test. Tuning masses are attached in the lead-lag-wise direction only to reduce this natural frequency in the flap-wise direction. Loaded with linear shakers in flap- and lead-lag-wise direction (dynamic). Side view: Flap-wise test. Top view: Lead-lag-wise test. (a) Test rig; (b) Blade; (c) Strong floor; (d_{1+2+3}) Load frames; (h_{h1+2}) Horizontal linear shakers; (h_{v1+2}) Vertical linear shakers; (m_{h1+3}) Tuning masses on rollers; (f_{1+3}) Support of tuning masses.

2.5 Conclusions of State-of-the-Art Fatigue Tests

Testing blades in fatigue requires significant strain amplitudes and a large cycle number to achieve damage equivalent loading compared to reality. Only with a dynamic loading, the energy to load the blade and the testing time will stay at an acceptable level.

To determine the test load at dynamic loadings, the measured strains of a precisely known loading of the blade (calibration test) are compared with the strains during the blade test. Ideally at least a calibration loading in flap-wise *and* lead-lag-wise direction is used for the calculation to achieve accurate results.

Usually separate uniaxial dynamic fatigue tests are used in flap- and lead-lag-wise direction. For a more realistic loading of the blade a simultaneous (biaxial) loading of the flap- and lead-lag-wise direction is beneficial. Furthermore, a shortening of the testing time is only possible, if the biaxial movement is an ellipse and not a Lissajous figure of a higher order. Wherever test setups are described in literature to achieve a dynamic *and* elliptical movement, they are impractical because of their large dimensions and dead weights, if also the outboard regions of blades shall be loaded.

2.6 Development Needs and Methodology

Even with using calibration test in flap-wise *and* lead-lag-wise direction, the determination of the blade loading can be very inaccurate. Large deflection effects or uncertain position measurement of sensors are exemplary reasons. Where scientific approaches with cost intensive optical measurement systems are possible, accurate but *practical* solutions need to be developed.

Therefore inaccuracies and uncertainties of large deflection effects of calibration test or erroneous sensor positioning are systematically analysed by parameter variation. The methodology for developing new calibration test methods, will be based on using only a limited amount of simple and cheap sensors. Additionally, a simple post processing shall be mandatory. The developed concepts will be validated with either test data or a FE simulation.

Assuming that a dynamic *and* elliptical movement would be the fastest way of testing, loading mechanisms need to be developed to achieve this motion. Because of their large dimensions, test set-ups described in literature are quite impractical, especially if the more outboard regions of the blade shall be tested as well. Hence, a loading method is needed which can be realistically used for biaxial elliptical and dynamic certification testing.

After developing a mechanism fulfilling this needs, performing a full-scale blade test at IWES was not possible at that time. Therefore another methodology had to be used for this work to verify the method. Instead, an FE simulation is used to simulate the concept and to compare the blade loading with common uniaxial tests. A uniaxial full-scale blade test of a 65m long blade and a biaxial but *non*-elliptic full-scale blade test of a 40m long blade is used to validate different aspects of the FE simulation and to demonstrate, that such complex blade movement can be controlled using servo-hydraulic actuators with bell-crank mechanisms directly attached to the blade.

Chapter 3

Calibration Tests

In this chapter, critical uncertainties and inaccuracies of the test load determination when performing dynamic fatigue tests are analyzed with the goal to measure the blade loading more exactly[22]. An additional goal is to keep the effort of the calibration test and the post-processing to an acceptable level, because it is rather unlikely that a complex 3D measurement system (Greaves et al. (2016)) is available for all tests. Hence, the challenge is to improve the accuracy by using *standard* measurement devices, loading mechanisms and post-processing methods. IEC-61400-13 (2001) describes a calibration test method to determine the blade root bending moment with the blade being installed at the turbine. Where this method is adequate to determine the blade root bending moment precisely, in a full-scale blade test the bending moments along almost the whole blade span are needed. Additional issues need to be analyzed in this case (compare Section 2.1). In this chapter, it is tried to identify the most critical uncertainties and inaccuracies with the goal to determine the loading of a dynamic fatigue test with an acceptable accuracy. Uncertainties of measurement devices (Section 3.1.1, Section 3.1.2), local nonlinear deformations of the blade (Section 3.2) and large deformations leading to nonlinear geometric effects (Section 3.3) were analyzed. After having added all analyzed effects conservatively, uncertain bending moments of up to -17% to +4% compared to the correct value were found (Figure 3.15). Because the applied damage to glass-fiber composites is related to the 10th power of the amplitude (according to GL-2015), the fatigue damage is reduced by a factor of about 6 in comparison to the defined test damage respectively load. For carbon, the ratio between intended and applied fatigue damage increases to 13 and is therefore even larger, because the applied damage is related to the 14th power of the amplitude. Therefore, applying the load accurately is important for an effective blade test.

Optimization methods are developed to significantly decrease the inaccuracies which are caused by the global and local nonlinearities (Section 3.2) and by misaligned calibration loadings (Section 3.4.1 and Section 3.4.2).

---

[22] The exactness of the results is defined by the *uncertainty* and the *inaccuracy* of the results. The *uncertainty* describes the bandwidth of the results. This type usually describes the effect of measuring equipment on the result. The bandwidth is calculated at a certain probability. The *inaccuracy* describes phenomenons which cause principally different results in relation to the ideal value. For example, an incorrect theoretic approach to calculate results of measured values can lead to results being principally too high or too low.

As discussed in Papadopoulos et al. (2000) a torsional calibration should be performed. Shear forces and axial forces might not be taken into account, as their influence is rather small. Also not analyzed is the behavior of the strain measurement over time. Many different parameters influence the electrical strain gauge measurement and need to be analyzed for each testing laboratory differently (Papadopoulos et al. (2000)). Certification tests usually only run for some days without interruption between calibration tests. A rather stable temperature can be assumed for an inside test during this time period. In this case, temperature effects are on a minor scale to other inaccuracies.

3.1 Measurement Uncertainties

3.1.1 Strain Measurement Using Electrical Strain Gauges

Measuring strains of fiber-composite materials is rather complex. Influences are summarized in Papadopoulos et al. (1998) and Papadopoulos et al. (2000). As mentioned in Lekou and Mouzakis (2009) and IEC-61400-13 (2001), in case of measuring absolute strains on fiber composites using electrical strain gauges for an analytical calibration, the measurement uncertainty is usually unacceptable. In IEC-61400-13 (2001) this method is only allowed for homogeneous materials like steel in combination with simple cross-sections. The advantage of a calibration test according to Section 2.1 is that a *relative* strain measurement instead of an *absolute* strain measurement is needed to determine the test load. Hence, in this thesis repetitive tests of the actual calibration test setup are purposed to avoid a detailed analysis of all issues influencing the measurement. In this case the whole measurement chain is analyzed in total. At the same time, the uncertainty of the specific test setup is determined instead of an uncertainty of a measurement device only.

Ten calibration tests (blade 1 of Table B.1) were carried out according to the loading shown in Figure 3.1. The uncertainties of each strain gauge is shown in Figure 3.2 over the maximum strain reached at full calibration load. Above a strain level of approximately $300\,{}^{\mu m}/_{m}$, the uncertainty can be neglected because of values lower than 0.1%. When analyzing the data like described in Figure 3.1, methods c) and d) can be recommended (Calculating the calibration factors as the quotient of zero load and the 50% (respectively 100%) plateau, using two defined load situations). The nonlinearities of the large deformation of the blade can be corrected at the two locations to achieve results which are much more precise (Section 3.4.2). On the contrary, methods a) and b) use data at all deflected situations of the blade (from *Start* to *End* shown in Figure 3.1). If this needs to be corrected for the nonlinear geometric behavior, a precise calculation of the bending moment would have to be performed at any time throughout the test and not only at full load, which would be much more complex[23].

---

[23] Method b) would avoid latge deflection effects due to the small loading, but the small strains would lead to large uncertainties again.

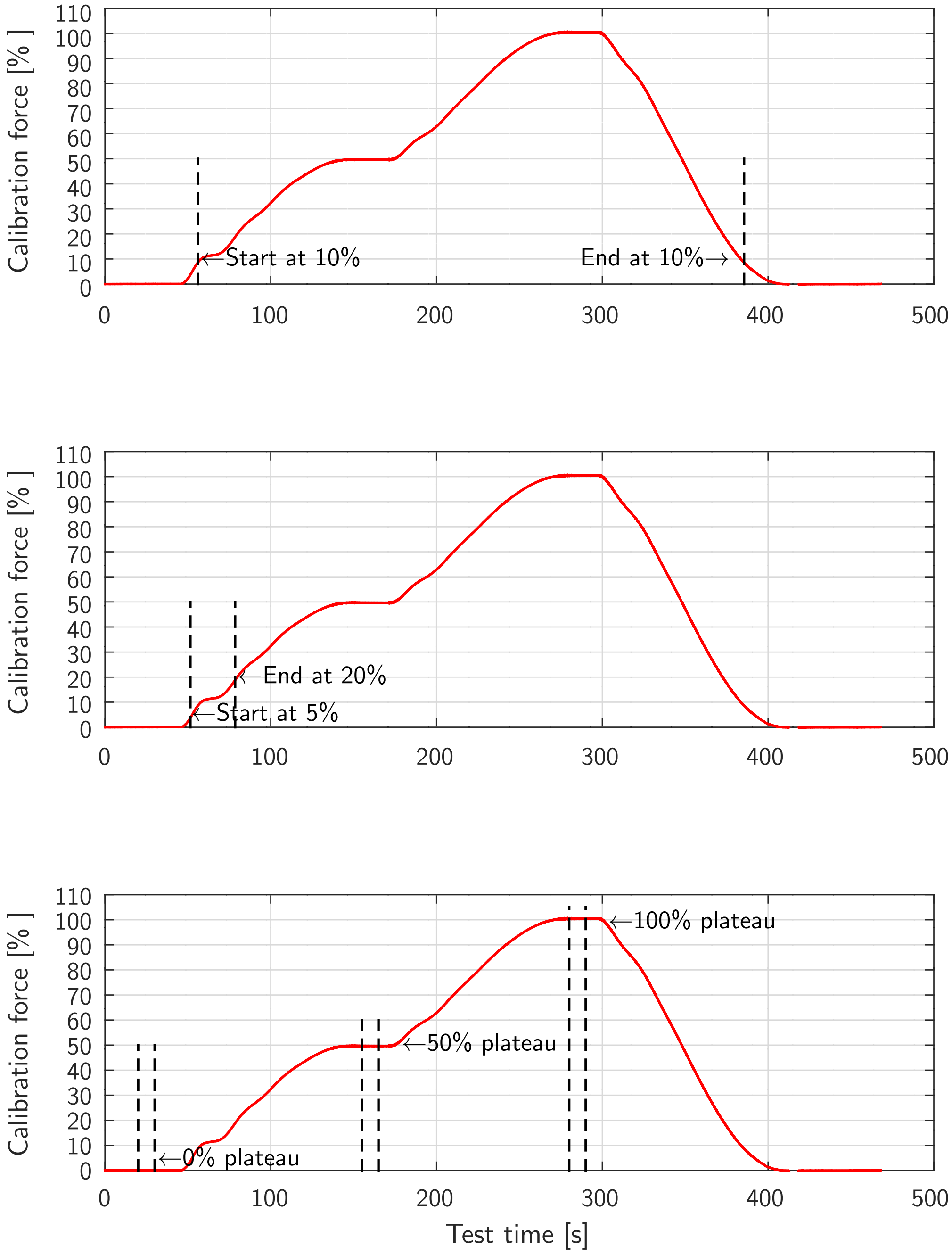

Figure 3.1: Load over time for a calibration test loading. Different options to determine calibration factors: Top figure: a) Least-squares fit method of all values between 10% at loading and unloading, Central figure: b) Least-squares fit method of all values between 5% and 20% at loading, Bottom figure: c) Difference between 0% and 50% and d) Difference between 0% and 100%

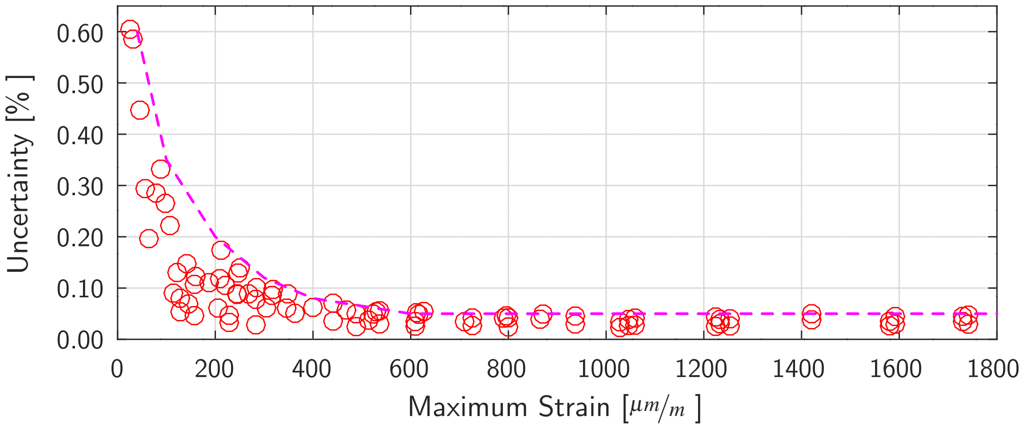

Figure 3.2: Uncertainty of all strain gauge measurements vs. the maximum strain of the data used to evaluate the calibration factors. The dashed magenta line represents a fitted envelope.

3.1.2 Location Measurement of Strain Gauges and Loading Location

At a calibration test, the determination of the distance between strain gauges and loading location has a direct influence on the calculation of the applied bending moments, the calibration factors and thus on the determined test loading. For only measuring the root bending moment of blades at the turbine, in Papadopoulos et al. (1998)[Page 40], the uncertainty of this distance measurement is listed besides others. The mathematical method to determine the uncertainty is laid down in IEC-61400-13 (2001) as well. To determine the load for a dynamic fatigue test, it is necessary to determine the bending moments along the whole blade span. This shortens the distance between strain gauge and loading location which increases the uncertainty of the results significantly, because the distance is usually calculated by a subtraction of the rather large span-wise distance of the two locations towards the blade root.

In case the strain gauge is not applied to the correct span-wise location, firstly, the distance between strain gauge and loading location (lever arm) is incorrect and secondly, the bending moment is determined at an incorrect radius of the blade. As the test bending moment decrease fast from root to tip, an incorrect bending moment is measured which is higher if the strain gauge sits closer to the root and lower if it is closer towards the tip. For an incorrect strain gauge location, the two phenomenons (lever arm and bending moment) fortunately counteract each other, so that the impact is therefore moderate.

The impact of an incorrect loading location has always a fully negative dependency. It is therefore beneficial to use a measurement tool with high accuracy to determine this location.

To show the addition of the uncertainties of these two effects, caused by a measuring uncertainty of 1/500 of the blade length, 8 different blades, which were tested at Fraunhofer IWES, have been

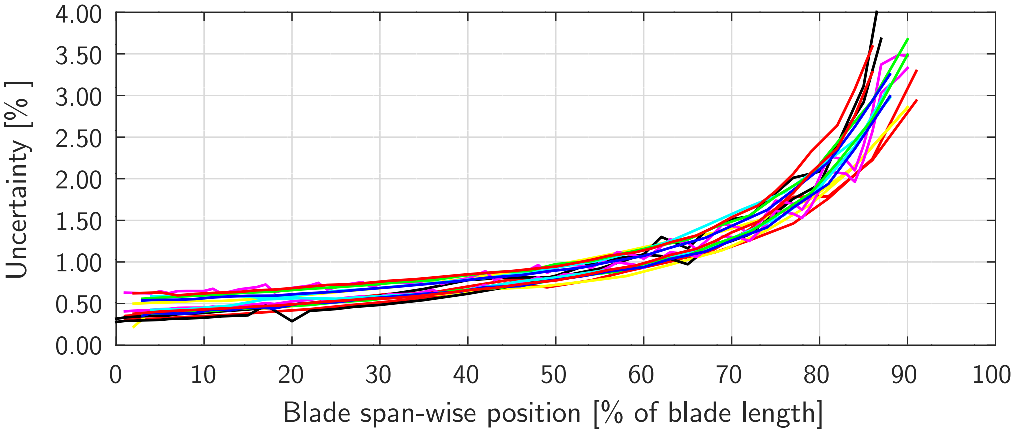

Figure 3.3: Uncertainty of the desired test bending moment with a span-wise measurement uncertainty of the strain gauge position of ±1/500 of the blade length, analyzed for eight different blades. The blades are loaded at 90% of the blade length

analyzed[24] (blade 1-2, 4-7, 9-10 of Table B.1). The results are shown in Figure 3.3. Because the bending moment distribution of most blades is quite similar, the bandwidth of the uncertainties of all blades is rather small and the results are almost equal for every blade.

Up to 60% of the blade length, the uncertainty is ≤±1% and might be within an acceptable range. Beyond this radius, towards the tip, the uncertainty is at an unacceptable level of up to ±4% . At least in this area, the measurement accuracy of the sensor and loading location position needs to be increased.

3.2 Nonlinear Strain vs. Displacement Behaviour

Whereas the blade root section is a circle, going outboard the cross-section gradually changes to a typical aerodynamic profile at maximum chord and keeps this shape until the tip. These outboard part behaves quite linearly during typical dynamic fatigue test loadings. But at the inner part of the blade (transition area), nonlinearities regarding the strain to bending moment relation are often present. One reason is the S-type curvature of the trailing edge in that region in combination with high axial loads. Another example is the *Brazier effect* of blade cross-sections. Intensive work was performed on flap-wise loadings of box girders to measure the Brazier effect and to find stiffeners to increase the ultimate strength (F. M. Jensen, Falzon, Ankersen, and Stang (2006),

---

[24] An uncertainty of 1/500 seems possible to be reached for present measurement devices, but other influences are present as well. For example, prebend blades need to be taken into account. Additionally to the prebend, the strain gauges on the pressure side and suction side need to be placed perpendicularly to the local blade axis. At the same time, the blade is usually bent due to its dead weight when sitting in the hall on only two support structures. Adding all uncertainties, staying underneath 1/500 is already challenging.

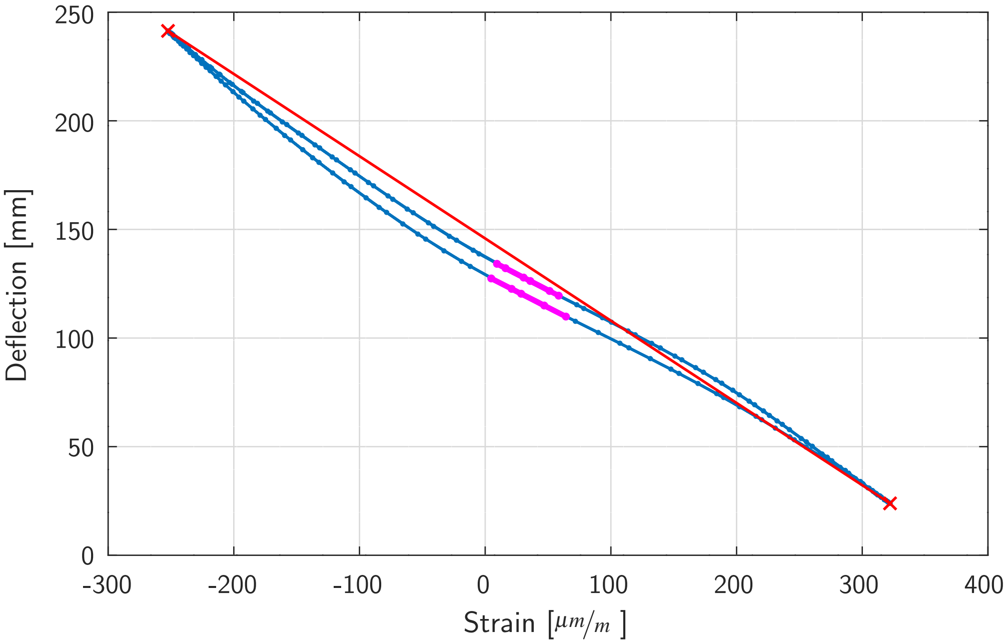

Figure 3.4: Trailing-edge strain gauge at 1.4% blade length. In blue: Displacement over strain. In red: Straight line between maximum and minimum strain values. In magenta: Displacement over strain in the region where the calibration test was performed.

F. M. Jensen (2008), F. Jensen et al. (2008a), F. Jensen et al. (2008b), F. M. Jensen, Puri, Dear, Branner, and Morris (2011), F. M. Jensen, Weaver, Cecchini, Stang, and Nielsen (2012)). Tests of buckling spar caps and the related nonlinear strain response is also described by Jørgensen et al. (2004) and analyzed in Rosemeier, Berring, and Branner (2015) by using geometric nonlinear FE simulations including imperfections. In addition, the buckling of flat back profiles at the trailing edge region under compression can cause this local nonlinear behavior (Eder et al. (2015)).

When determining the bending moments of dynamic fatigue tests with calibration tests, a nonlinear behavior of the measured strain in relation to the bending moment of that cross-section will lead to incorrect results. The reason for this is that the calibration test loading is performed only at a few percent of the dynamic fatigue test loading. But according to the theory described in Section 2.1.2, a linear extrapolation is needed.

In Figure 3.4, Figure 3.5 and Figure 3.6, the displacement is plotted over strain at three different strain gauge locations for one cycle of a lead-lag-wise dynamic fatigue test (blade 7 of Table B.1). In case the relation is not linear, as shown Figure 3.4, a correction of the calibration factor can be carried out. The idea is based on the assumption that the relation between blade deflection and bending moment is linear at a natural frequency oscillation, even though this local areas of the blade structure behave nonlinearly. The displacement signal of the hydraulic actuator (or a separate displacement sensor) is used to be plotted over the strain signals. In Figure 3.4, Figure 3.5 and Figure 3.6, this is shown by the blue curves. The correction factor to be used

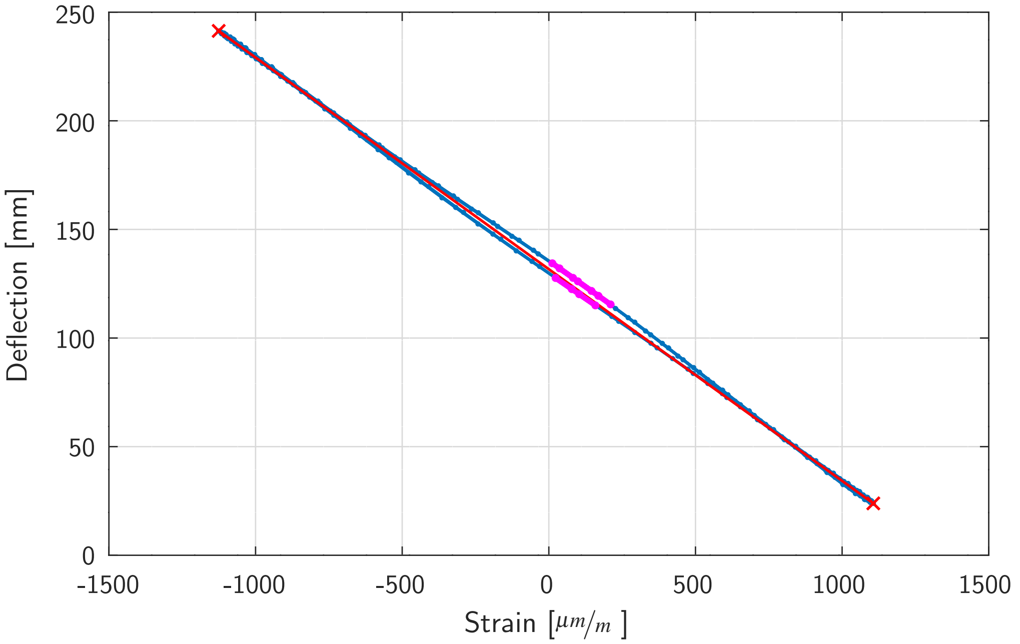

Figure 3.5: Trailing-edge strain gauge at 14.3% blade length. In blue: Displacement over strain. In red: Straight line between maximum and minimum strain values. In magenta: Displacement over strain in the region where the calibration test was performed.

on the calibration factor is the ratio between the slope of the red line (connecting the extreme loads) and the average of the two slopes (magenta lines) representing the strains versus the blade displacement during the calibration test (at the calibration test load level). Since the strains during calibration are small, the relationship between strains and blade displacement is assumed to be linear at this small load.

In case large regions of a blade behave in a nonlinear way, the assumption that bending moments over deflections behave linearly might be incorrect, because the general linearity between amplitude and bending moment might be influenced. For the blade analyzed in this thesis, this behavior was not detected, as the majority of all strain gauges showed a linear behavior, as exemplarily shown in Figure 3.5 or Figure 3.6. In case a whole section of the blade would behave nonlinearly, at least all strain gauges located outboard of that region should show a nonlinear behavior as well. This can easily be verified by analyzing the outboard strain gauges. A verification of the method is presented in Appendix D.

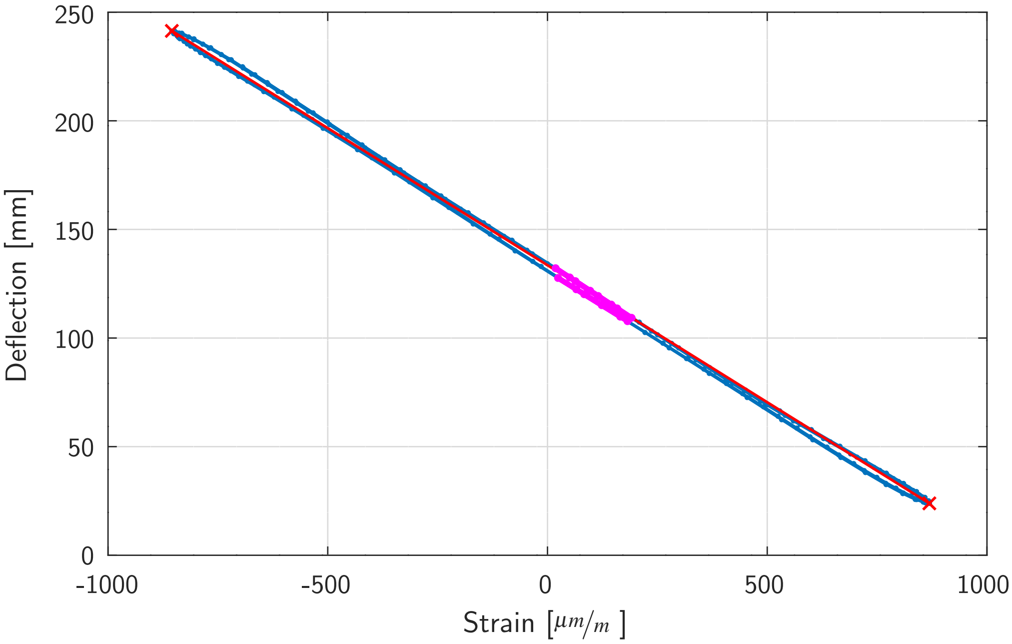

Figure 3.6: Trailing-edge strain gauge at 25.1% blade length. In blue: Displacement over strain. In red: Straight line between maximum and minimum strain values. In magenta: Displacement over strain in the region where the calibration test was performed.

3.3 Geometric Nonlinear Behavior

The calibration test method described in IEC-61400-13 (2001) is used to determine the blade root bending moment only. Geometric nonlinear effects when loading the blade at the tip or with its dead weight are rather small. But if such a calibration test is used to determine the calibration factors along most of the blade span, nonlinear geometric effects due to the large deflections at the tip cause significant changes of the applied bending moments especially in the tip region.

In this section, the difference between calculating the bending moments at a calibration test with an undeformed blade compared to a large deformed blade will be analyzed using FE simulations. Different locations to where the load cable is directed during the calibration loading are simulated to systematically analyze the impact on the applied bending moment. In each subsection of this chapter, the pulling location is moved only in one specific direction. (Section 3.3.1: vertical direction, Section 3.3.2: span-wise direction, Section 3.3.3: side-wise direction). In Section 3.4.1 and Section 3.4.2, two different methods to avoid inaccuracies due to these geometric nonlinear effects will be shown.

For all analyses, the blade was considered to be fixed horizontally to a rigid support with the pressure side upwards. The location to load the blade was at 95% of the blade length. Because often the bending moments are calculated without taking geometric nonlinearities into account, the results for all simulations are the difference of the applied bending moment of the deformed blade compared with the undeformed situation and a perpendicular loading (with or without geometric nonlinear effects)[25]. In Figure 2.2, the general setup is shown, using a hydraulic actuator connected to the rope to load the blade for calibration.

3.3.1 Blade Loading - Moving the Pulling Location Vertically

In this section, the influence on the calibration test load is exemplarily analyzed when moving the pulling location in vertical direction (changing the length of the loading cable) [26]. The bending moment calculated with the undeformed blade is compared with the deformed situation. The difference is always described as *error* E in this work. Five different blades with lengths of around 40m to 90m were analyzed (blade 1,3,8,9,12 of Table B.1)[27]. For all blades, the prebend in flap-wise and lead-lag-wise direction was set to zero to achieve comparable results. The exemplary test geometry is shown in Figure 3.7. The pulling location on the strong floor was varied between two different distances to the blade. In both cases, the pulling location was located rectangular to the pitch axis underneath the blade at a span-wise location of 95% of the blade length (Lc_z), at which the load cable was attached to the blade. As the closest location, P1 is located at a vertical distance to the undeformed blade of $1/10 \times Lc_z$ first. Secondly, P2 is located at $1 \times Lc_z$ to analyze a very large distance.

In Figure 3.8, the flap-wise results are exemplary shown for a deflection of $1/15 \times Lc_z$. The five lower curves (solid lines) represent the results of the pulling location being $1/10 \times Lc_z$ underneath the blade (P1) and upper curves (dashed lines) of $1 \times Lc_z$ underneath the blade (P2).

With more than -14%, large inaccuracies were found for the flap-wise direction. Even though these values were determined with a small distance of the pulling location to the blade, significant inaccuracies were also found for more conservative parameters. The result of this analysis is part of the motivation to determine the optimization methods described in Section 3.4.1 and Section 3.4.2.

The same five blades were analyzed for the lead-lag-wise direction (comparable to the results of Figure 3.8 for the flap-wise direction). With $1/80 \times Lc_z$, the deflection for the lead-lag-wise direction was defined much smaller in comparison to the flap-wise direction, because the greater stiffness of the blade in this direction leads to higher strains at already low deflections. The smaller deflection reduces the nonlinear effects. Hence, the maximum change in bending moment was less than -0.15% and therefore negligible.

---

[25] The FE software package ANSYS Mechanical 15.0 was used for the simulation. Because the result needs to be a bending moment distribution along the blade span and not the strains of the shell, a beam model instead of a shell model was used to discretize the blade. Around 30 BEAM188 elements were used to describe the blades. The rope to load the blade for example with a winch or hydraulic actuator was described by a LINK11 element. Due to the large deflection of the blade, the NLGEOM option was enabled for the calculation.

[26] X_{IEC} direction for the flap-wise and Y_{IEC} for the lead-lag-wise direction.

[27] Exemplarily for the FE calculations performed to analyse calibration testing, the FE code for blade 3 is shown in Appendix K.1.

3.3.2 Blade Loading - Moving the Pulling Location Span-wise

In this section, the influence on the calibration test load is analyzed when moving the pulling location in span-wise direction (Z_{IEC} direction).

Blade 1 of Figure 3.8 (red curve) was used as an example for this simulation (blade 8 of Table B.1), because it showed the largest effect of the change in the bending moment due to an incorrect loading angle. In Figure 3.9 the geometry of the simulation for the flap-wise calibration test is shown. A similar geometry compared to Section 3.3.1 is used. Nine different locations of the pulling location were analyzed, starting at the same radius like the attachment of the loading cable at the blade (Lc_z). For each analysis, the pulling location is moved by $1/300 \times Lc_z$ inboard. The results are shown in Figure 3.10. Each curve in this figure represents the relative change in the bending moment at specific radii (blue lines). The radii were almost equally distributed along the whole blade span, starting at the blade root with the red line with circles and ending at 93% of the blade length with the red line with squares.

It can be seen that moving the pulling location P1 inboard reduces the error of the bending moment at the tip location (magenta line with squares in Figure 3.10), but after moving more than 1% inboard, the error for the bending moment at the blade root starts to increase (red line with circles in Figure 3.10). An overall minimum is reached for the bending moments, if the pulling position is shifted inboard $4/300 \times Lc_z$ (at location P5).

For the lead-lag-wise calibration test, a similar geometry to the flap-wise direction was simulated. Only the deflection was reduced to $1/80 \times Lc_z$ which is assumed to be the largest deflection possible in this direction. The behavior is quite similar to the flap-wise direction, but the magnitude of uncertainties is roughly only 10% of the flap-wise direction, so less critical. A minimum is reached for the bending moments at all radii, if the pulling position is shifted inboard $1/300 \times Lc_z$.

By changing the position of the pulling location, the maximum error of the actual applied loading in comparison to a perpendicular loading of the undeformed blade could be reduced by a factor of almost ten. This behavior was used to determine the ideal pulling angle (or pulling location) as described in Section 3.4.1.

3.3.3 Blade Loading - Moving the Pulling Location Side-wise

In this section, the influence on the calibration test load is analyzed when moving the pulling location in sidewise direction or when the blade moves sidewise due to its structural twist.

The geometric situation is shown in Figure 3.11. At the top, a side view of a flap-wise calibration test is shown. The undeformed blade is the solid black line with the load frame (LF*) for loading the blade. The dashed line shows the fully deflected blade (LF). The pulling location of the rope is at P1 as already defined in the previous sections. Two phenomenons can occur which lead to a loading which is not vertical any more but rotates around the Z_{IEC} axis. Firstly, a misalignment is easily given by an incorrect position of the pulling location P1, as shown in the left bottom sketch of Figure 3.11. Secondly the blade might move perpendicular to the test direction due

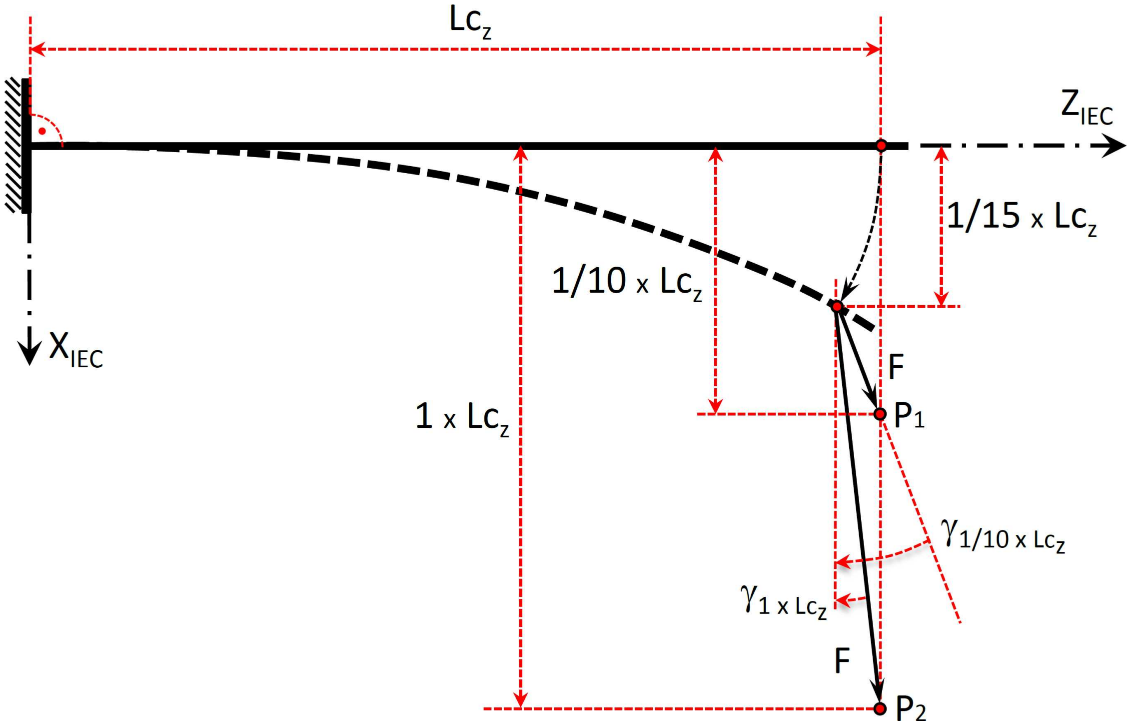

Figure 3.7: Geometry of a flap-wise calibration test setup with two different distances between the pulling locations (P1 or P2) and the blade (X_{IEC}). The distance of P1 is $1/10 \times Lc_z$ and for P2 it is $1 \times Lc_z$. The pulling location is oriented perpendicular to the pitch axis at 95% of Lb (Lc_z) towards the suction side. The applied load F leads to a deflection (dashed line) of $1/15 \times Lc_z$.

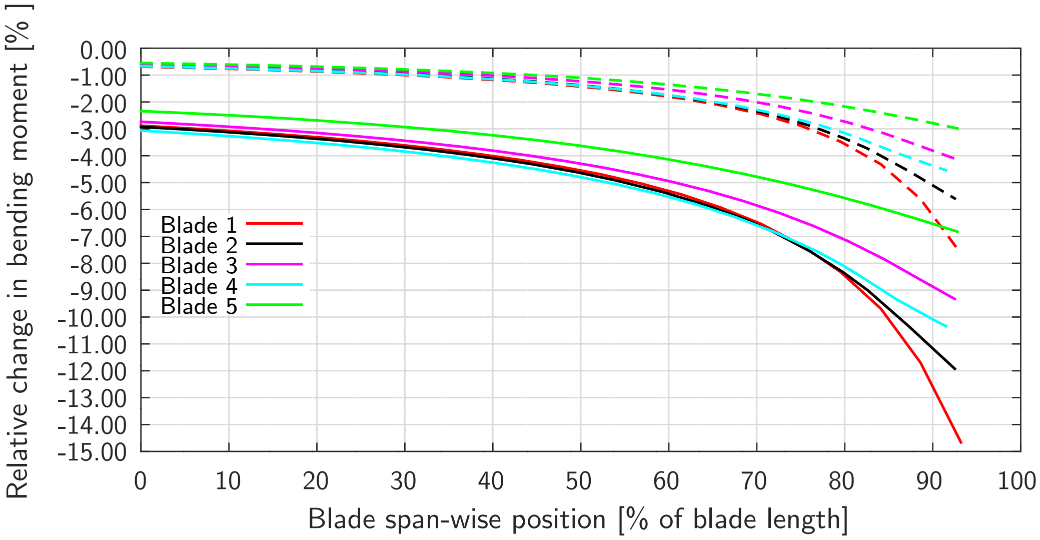

Figure 3.8: Relative change in the bending moment of five blades in a flap-wise calibration test for two pulling locations in X_{IEC} direction. Comparing the loading of an undeformed blade with a deformed blade of $1/15 \times Lc_z$. The distance of the pulling location to the blade is $1/10 \times Lc_z$ for the solid lines (P1) and $1 \times Lc_z$ for the dotted lines (P2). The pulling location is oriented perpendicular to the pitch axis at 95% of Lb (Lc_z) towards the suction side.

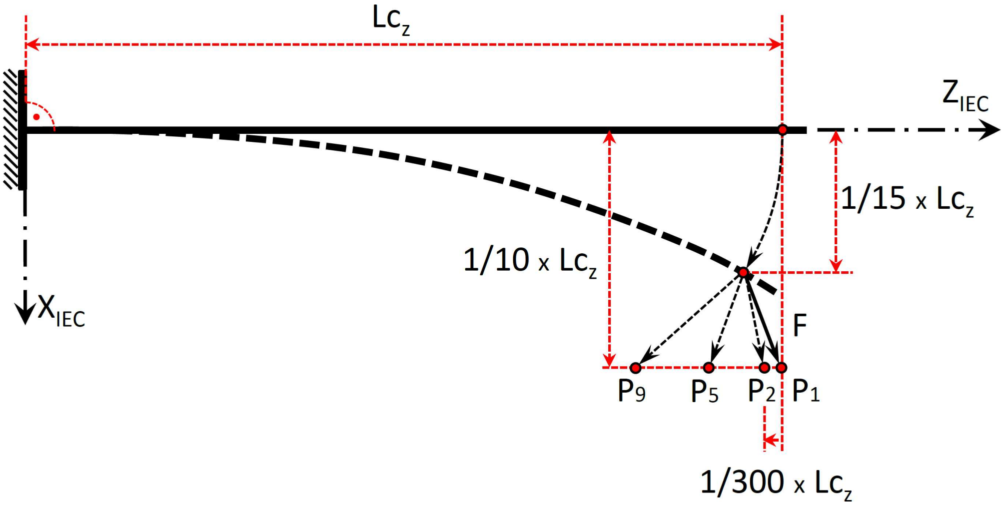

Figure 3.9: Geometry of a flap-wise calibration test with nine different pulling locations (P1 to P9) in span-wise direction (Z_{IEC}). The position of P1 is $1/10 \times Lc_z$ perpendicular to the undeformed blade. From P1, P2, P3. . . to P9, the pulling location is moved inboard in steps of $1/300 \times Lc_z$. P5 shows the ideal pulling location. The applied load F leads to a deflection (dashed line) of $1/15 \times Lc_z$.

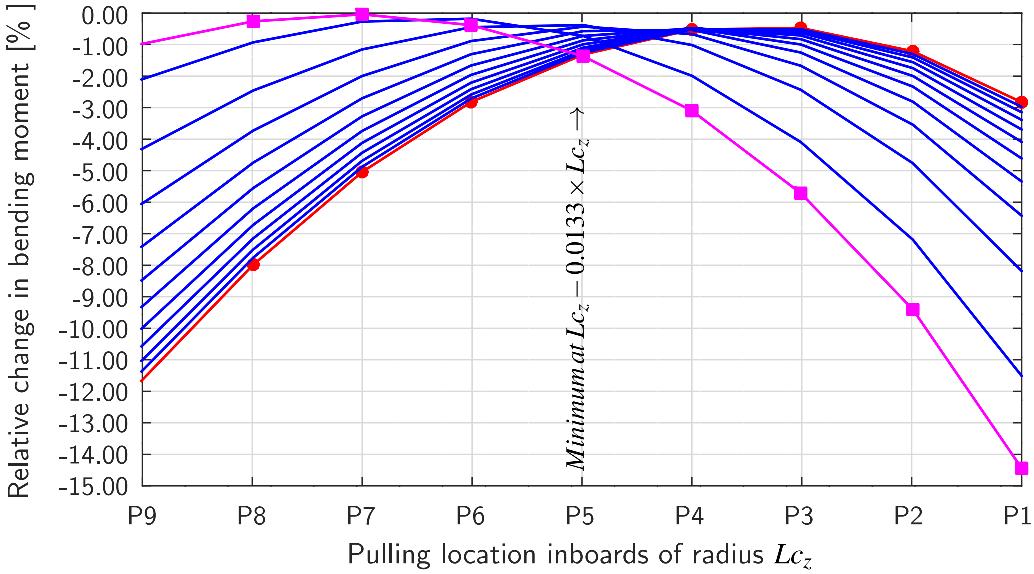

Figure 3.10: Relative change in the bending of blade 1 in a flap-wise calibration test, comparing the loading of an undeformed blade and a perpendicular loading to the pitch axis with a deformed blade of $1/15 \times Lc_z$ at different pulling locations in Z_{IEC} direction and the actual load direction. The distance of the pulling location to the blade is $1/10 \times Lc_z$ towards the suction side. The pulling location is oriented perpendicular to the pitch axis at 95% of the blade length (Lc_z). For each analysis, the pulling location is moved inboard from location P1 to P9, starting from Lc_z in steps of $1/300 \times Lc_z$.

to the rotation of the main stiffness axis of the blade, as shown in the right bottom sketch of Figure 3.11. In both cases the force misalignment can by described with an angle θ, which is ideally 0° for a calibration test.

The estimation of angle θ is rather complex, as both described phenomenons can occur at the same time. Additionally, each phenomenon can be reduced automatically again, because the blade is principally pulled back in case of a rising angle θ throughout the loading. Firstly the magnitude of θ resulting from an incorrect position of the pulling location was estimated exemplarily by shifting the pulling location 15cm sideways with the blade being at 5m distance to the pulling location. At full calibration loading, θ becomes 1.7°. Secondly, the magnitude of θ resulting from the typical movements of the blade perpendicularly to the calibration test direction was evaluated by analyzing the five blades already used before. By loading the blades in purely flap- and lead-lag-wise direction, to a deflection of $1/15 \times Lc_z$, a maximum θ of 3° was determined for the flap-wise direction and of 1.5° for the lead-lag-wise direction.

As described before, both angles do not have to be added, because the load component perpendicular to the calibration test direction decreases θ automatically again. To use a realistic and non-conservative value, an angle of 1.5° was exemplarily used to calculate the impact on the determination of the test bending moment, taking both effects into account.

The research performed in Papadopoulos et al. (1998) and Papadopoulos et al. (2000) focused on the determination of the blade root bending moment using calibration tests. In this case, it was adequate to only decrease the calibration load with the cosine of θ to determine the uncertainties. The sine component of θ can be neglected, because the strain gauges of the blade root cross-section can be located quite exactly on the neutral axis of a perpendicular axis to the test direction. Therefore, the influences of a perpendicular loading (sine component) is negligible. For a calibration test used to determine the load of a dynamic fatigue test, this is not comparable, because often it is not possible to place the strain gauges on the neutral axis of the different cross-sections, as shown in Figure 2.3. In this case, the sine component has to be taken into account to determine precise calibration factors, as the cross-talk terms of Equation 2.4 can have a significant influence.

To calculate exemplary uncertainties, angle θ of 1.5° is used as defined above on the five blades of Figure 3.8 (blade 1,3,8,9,12 of Table B.1). The worst-case of pressure side or suction side and trailing edge or leading edge strain gauges is used[28]. In Figure 3.12, the resulting uncertainties of the test bending moments are shown for the flap-wise direction and in Figure 3.13 for the lead-lag-wise direction. With 2% in flap-wise and up to 5% in lead-lag-wise direction (at 70% blade length), the uncertainties are quite high. The envelopes shown in Figure 3.12 and Figure 3.13 will be later used for an analysis where all inaccuracies and uncertainties of a calibration test will be added.

---

[28] Determined with the quotient of the calibration factors of each strain gauge given by a flap- and lead-lag-wise loading.

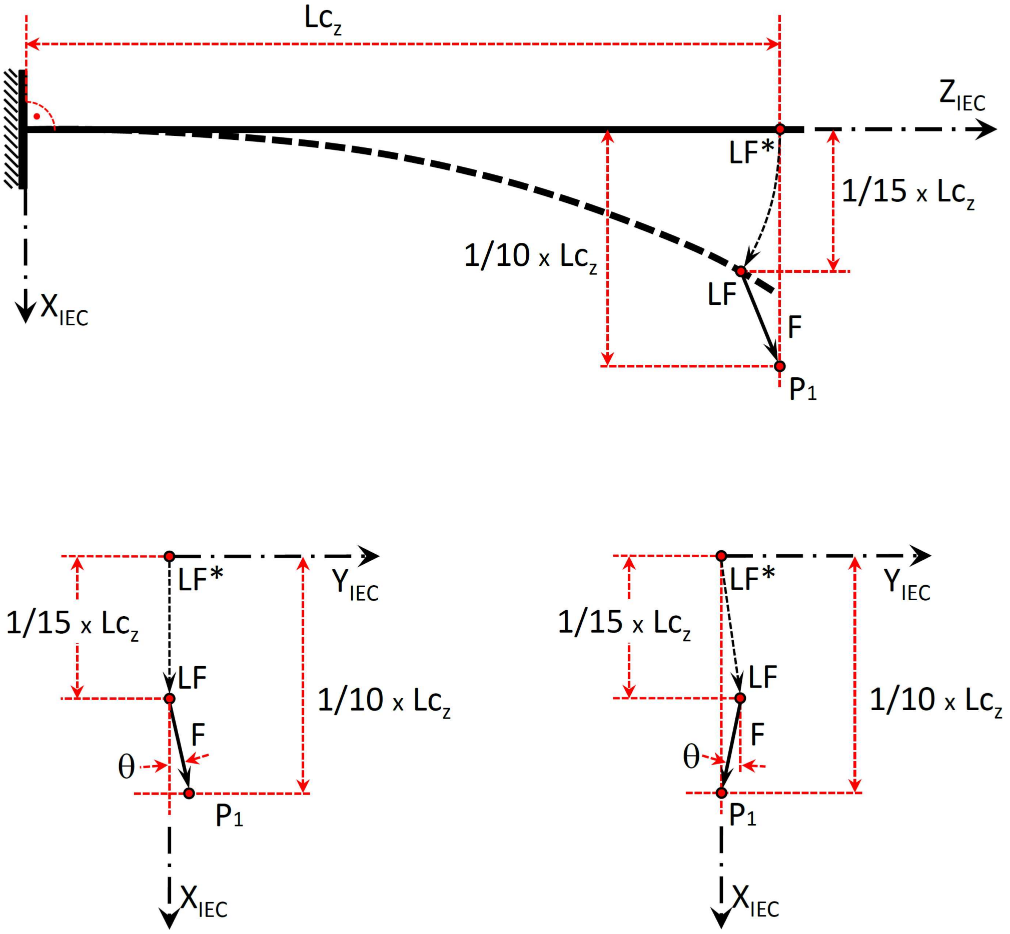

Figure 3.11: Geometry of a flap-wise calibration test with different pulling locations in side-wise direction (Y_{IEC}). At top: With force F, the blade is loaded at the load frame (LF). The pulling location P1 is $1/10 \times Lc_z$ perpendicular to the undeformed blade. The deflection (dashed line) is $1/15 \times Lc_z$. At bottom left: View from blade tip to root. P1 is located in positive X_{IEC} direction and the blade moves vertically downwards. At bottom right: View from blade tip to root. P1 is located vertically underneath the undeformed blade. The blade moves in positive X_{IEC} direction with increasing loading.

Figure 3.12 shows, that the influence of the sine component of θ often becomes critical in the transition area for a flap-wise calibration test. The tip region of the blade is critical for a lead-lag-wise calibration test, as shown in Figure 3.13. It was found out that especially at the tip region the calibration factors of the leading edge strain gauges often have 1.5 to 2 times higher absolute strain readings at a flap-wise bending moment in comparison to a lead-lag-wise bending moment of the same amount. As shown in Figure 2.3, it is often not possible to apply strain gauges right on the leading edge. Even when using the closest possible location towards the spar caps, the strain gauge is already far away from the flap-wise neutral axis of the profile.

If not measuring θ throughout the loading, to include the sine and cosine effects into the determination of the calibration factors, the inaccuracy is equal to sin(θ) and cos(θ)-1. The sine

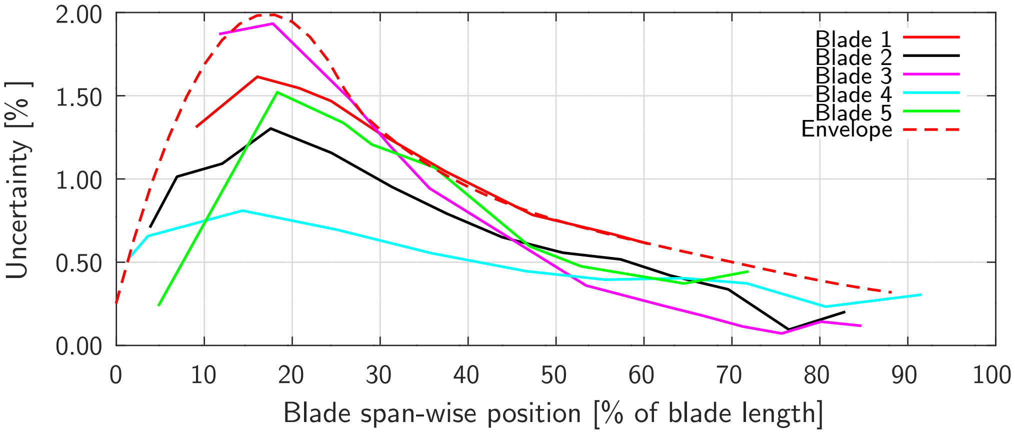

Figure 3.12: Uncertainty of the dynamic fatigue test bending moment M^t due to an incorrect positioning or measurement of the pulling location in Y_{IEC} direction at a vertical flap-wise calibration test. An incorrect angle of 1.5° is used. Five modern blades (with lengths between 40m and 70m) were analyzed to determine an envelope as a worst-case scenario.

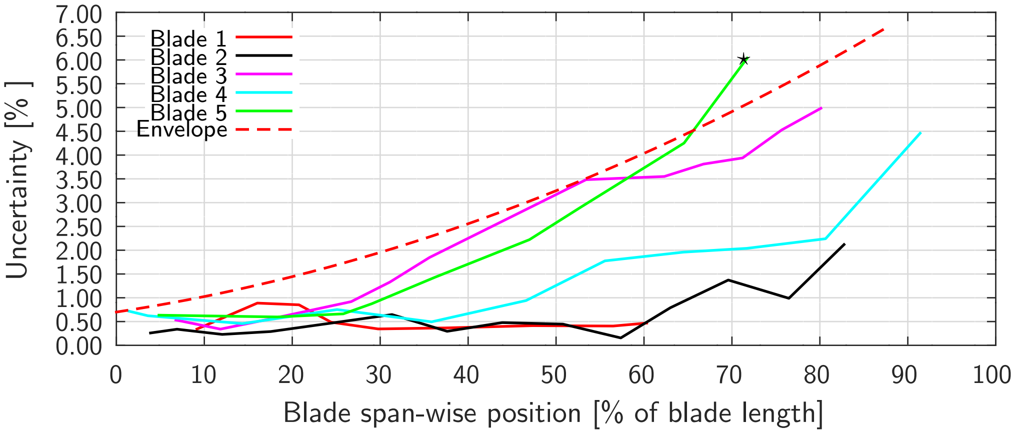

Figure 3.13: Uncertainty of the dynamic fatigue test bending moment M^t due to an incorrect positioning or measurement of the pulling location in X_{IEC} direction at a horizontal lead-lag-wise calibration test. An incorrect angle of 1.5° is used. Five modern blades (with lengths between 40m and 70m) were analyzed to determine an envelope as a worst-case scenario (* one value was treated as an outlier, hence it is accepted to be outside of the envelope).

effect is therefore much higher in comparison to the inaccuracy caused by the cosine. Hence, both load components need to be used in Equation 2.3 to achieve proper results.

A first conclusion is that the determination of the calibration factor is more exact when measuring θ at least at the 100% load level of each calibration test. Knowing θ, the sine and cosine load component can be calculated and used in Equation 2.3 to determine precise calibration factors and therefore precise bending moments of the dynamic fatigue test. A second conclusion is that the ideal test with regard to a misaligned loading is carried out by attaching a dead weight to the blade. Automatically a pure flap-wise loading is given[29]. This approach is used for the optimization method described in Section 3.4.2.

3.4 Optimization Methods

3.4.1 Optimized Pulling Direction

In Section 3.3, the inaccuracies were described, when calculating the bending moment at calibration loadings without taking the large deflection of the blade into account. Figure 3.10 shows that with adjusting the load angle in span-wise direction to a specific value reduces the inaccuracies significantly. The ideal angle is found, if the errors at the blade root (E_{root}) and at the loading location (E_{Lc_z}) are equal after the optimization (Figure 3.10). Only a minimum of measurement data shall be necessary for the method to keep the test setup simple. The method requires a loading system allowing a positioning of the turning block or winch at any location on the strong floor (in span-wise direction). E_{root} and E_{Lc_z} can be calculated according to Equation 3.1 and Equation 3.2.

$$E_{root} = \frac{M_{root,deformed\,blade}}{M_{root,undeformed\,blade}} - 1 \tag{3.1}$$

$$E_{Lc_z} = \frac{M_{Lc_z,deformed\,blade}}{M_{Lc_z,undeformed\,blade}} - 1 \tag{3.2}$$

---

[29] Asuming that the blade can be oriented accurately in the test-rig with the flap-wise direction being vertically

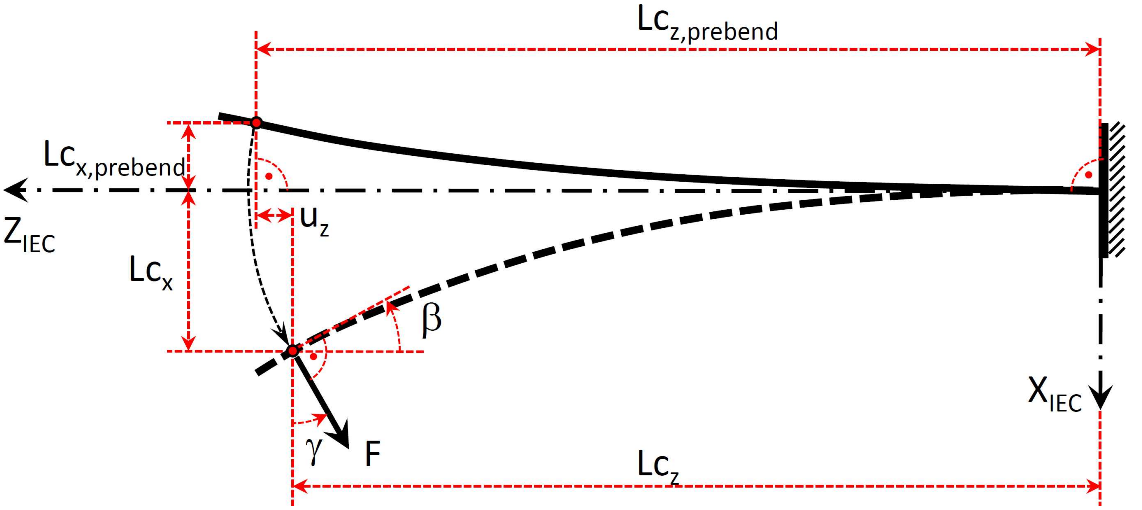

Figure 3.14: Geometry of a calibration test using optimization method I (OM-I)

In Figure 3.14, the values used to derive E_{root} and E_{Lc_z} with Equation 3.4 and Equation 3.5 are sketched (deflection u_z has a negative sign).

$$E_{root} = \frac{F \times \cos\gamma \times (Lc_{z,prebend} + u_z) + F \times \sin\gamma \times Lc_x}{F \times Lc_{z,prebend}} - 1 \tag{3.3}$$

or:

$$E_{root} = \cos\gamma \times \frac{Lc_{z,prebend} + u_z}{Lc_{z,prebend}} + \sin\gamma \times \frac{Lc_x}{Lc_{z,prebend}} - 1 \tag{3.4}$$

With the goal to use only parameters which can be easily measured at the test rig, E_{Lc_z} is calculated by only using the load angle to vertical and the local blade angle at the loading location Lc_z to horizontal:

$$E_{Lc_z} = \frac{F \times \cos(\beta - \gamma)}{F} - 1 = \cos(\beta - \gamma) - 1 \tag{3.5}$$

Equation 3.4 being equal to Equation 3.5 yields:

$$\cos\gamma \times \frac{Lc_{z,prebend} + u_z}{Lc_{z,prebend}} + \sin\gamma \times \frac{Lc_x}{Lc_{z,prebend}} - 1 = \cos(\beta - \gamma) - 1 \tag{3.6}$$

By solving Equation 3.6 to γ, the optimized angle gamma can be calculated according to Equation 3.7[30]:

$$\gamma = \arccos\left[+ \sqrt{\frac{\left(\frac{Lc_x}{Lc_{z,prebend}} - \sin\beta\right)^2}{\left(\frac{Lc_{z,prebend}+u_z}{Lc_{z,prebend}}\right)^2 + \left(\frac{Lc_x}{Lc_{z,prebend}-\sin\beta}\right)^2}}\right] \tag{3.7}$$

OM-I needs iterative steps to achieve the ideal load angle[31]:

1. Estimation of all values needed to calculate γ at 100% load level and calculation of γ according to Equation 3.7.
2. Performing the calibration test with the estimated values of step 1 and measuring at 100% load level.
3. Repeat step 2 and 3 as long as E_{root} and E_{Lc_z} are not acceptable.

The simulation performed in Section 3.3 is used to evaluate the sensitivity of E_{root} and E_{Lc_z} when using OM-I, with the goal to determine the usability of the method. By using Equation 3.4 and Equation 3.5, E_{root} and E_{Lc_z} were calculated for different values of γ. At a difference of $\pm 2^\circ$ to the ideal angle, E increases in the flap-wise calibration test by 0.66% and in the lead-lag-wise calibration test by 0.13% only. The absolute values are not representative for all blades, but the tendency of the difference is the same, as the deflections in flap-wise and lead-lag-wise direction are generally quite different. It can be concluded that the dependency on the result having an incorrect angle γ is moderate. A sensitivity analysis of all other input values is shown in Appendix E.

As mentioned at the beginning of Chapter 3, the dimensions of inaccuracies and uncertainties can be rather large, if the aspects analyzed in this work are not taken into account. A full uncertainty analysis always relates to a specific blade, test geometry and measurement system. How to take different kinds of uncertainties of such tests into account was analyzed in Papadopoulos et al. (1998) and Papadopoulos et al. (2000) and summarized in IEC-61400-13 (2001) for measuring the blade root bending moment. To show the magnitude of inaccuracies and uncertainties when measuring the bending moments along the whole blade span, two blades were chosen as examples

---

[30] To evaluate which result of Equation 3.7 is valid (plus or minus), the simulation results of blade 1 (Section 3.3) were compared with the analytically calculated results of Equation 3.7.

[31] If the tilt angle of the test rig is adjustable, using a dead weight loading for the calibration test in combination with OM-I to evaluate the ideal load angle (by adjusting the tilt angle to the evaluated load angle), the accuracy of the calibration test or the determination of the test bending moment can be increased significantly. There is even a good chance that the test rig tilt angle does already lead to acceptable inaccuracies without adjusting it. The error at the root and the loading location at a certain tilt angle can be calculated according to Equation 3.4 and Equation 3.5.

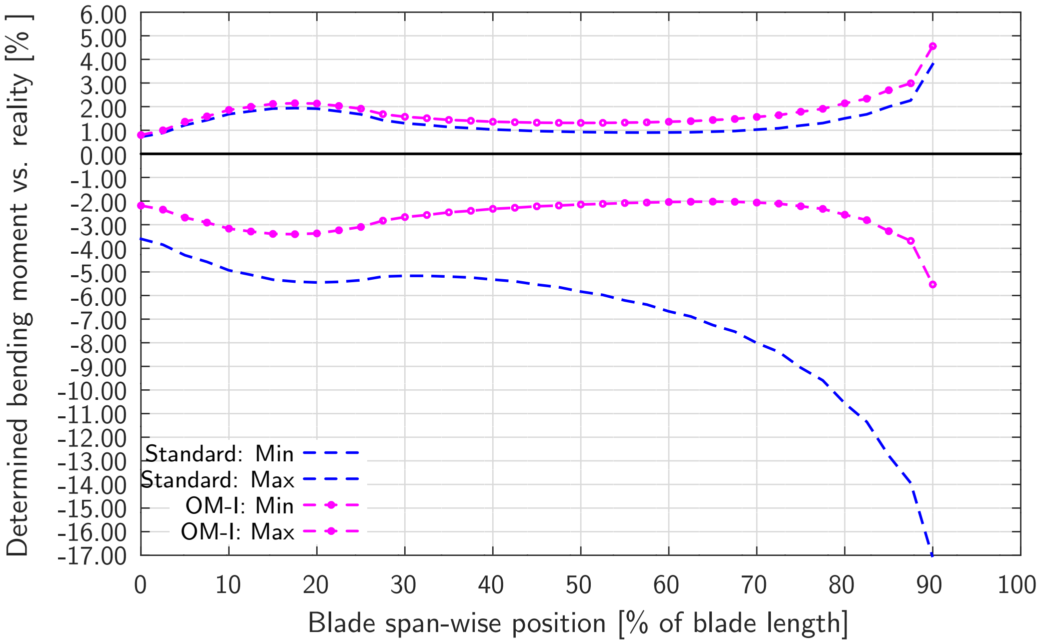

Figure 3.15: Bandwidth of inaccuracies and uncertainties over the blade span for a *standard* calibration test and with using optimization method OM-I.

for the highest and the lowest inaccuracy of all available blades. The results *without* and *with* taking OM-I into account were compared[32].

In Figure 3.15, the blue dotted line shows the sum of uncertainties and inaccuracies for a *standard* test. When using OM-I, the bandwidth of inaccuracies plus or minus the uncertainties are shown for the two analyzed blades as the magenta dotted lines with squares. The largest reduction of the inaccuracy and uncertainty when using OM-I is possible at the tip region.

---

[32] Assumptions for the calculations: Pulling location at 95% of the blade length. To use realistic numbers the bandwidth of the blades analyzed in Section 3.3 was used (Figure 3.8). The pulling location is assumed to be $1/10 \times Lc_z$ underneath the blade (in X_{IEC} direction). The deflection of the blade at the calibration test is $1/15 \times Lc_z$. For the minimum error, the pulling location is placed $1 \times Lc_z$ underneath the blade (in X_{IEC} direction) and a loading to only 50% of the deflection $1/15 \times Lc_z$ is used. According to Section 3.1.1, an uncertainty of 1/500 of the blade length is assumed. For the measurement tool, the uncertainty used for the calculation is according to the maximum of all lines of Figure 3.3. According to the example calculated in Section 3.3.3, a sideways misalignment of 1.5° of the ideal load direction is assumed. The uncertainty used for the calculation is according to the red dotted line of Figure 3.12. The uncertainty of the load cell is set to ±0.5% . All uncertainties were combined according to IEC-61400-13 (2001) with $u = \sqrt{s_i^2 + u_i^2}$.

3.4.2 Optimized Deflection Calculation

When using OM-I, the incorrect determination of the blade bending moment was reduced by a factor of almost 10 for the example shown in Figure 3.10. Still at some areas of the blade, the determined bending moment is generally ≈1.5% too low. Furthermore, uncertainties due to a misaligned calibration load will occur, as for OM-I, the load angle needs to be manually adjusted and sideways misalignments are still possible. To further increase the accuracy, a more accurate optimization method II (OM-II) was developed. Firstly, the loading of the calibration test is performed with a dead weight hanging to the blade, resulting in an absolutely predictable loading direction eliminating all uncertainties due to misalignments (Section 3.3). When knowing the loading direction precisely, secondly the deflected geometry of the blade needs to be known to be able to calculate the exact loading along the blade span.

Because the test rig position and orientation is accurately known, this also applies for the position and the rotation of the blade root. Additionally, the blade rotation and deflection at the loading location can be determined using standard measurements. By knowing the exact deflection and rotation of the blade at these two locations, the deflection curve in between is estimated using an iterative deflection calculation to fit the blade deflection and rotation to these two locations.

If precise displacement measurements were performed along the whole blade span at the test, the applied bending moment could be exactly determined using the measured curvature of the large deflected blade. Still, full-scale tests of wind turbine blades are performed on a low-budget level, in comparison to tests for example in aerospace industry. Expensive 3D deformation measurement devices are usually not available. Therefore, another goal of OM-II was to achieve accurate results with a minimum of standard measurements necessary, but also with a simple post-processing. It is beneficial that the high geometric nonlinear behavior due to the large flap-wise deflection is in the vertical direction, because a dead weight loading can be easily applied in this direction.

Once the blade deformation is known, the exact applied bending moment can be calculated. To be comparable to the previous results, in this thesis the difference to the undeformed (and perpendicularly loaded) situation is calculated (error E). Therefore, the results of OM-II are used to *compensate* the inaccuracies shown in Figure 3.8.

After performing the calibration loading and recording the measurement data at 100% load level, error E can be directly calculated. The geometry of the unloaded and fully loaded situation is shown in Figure 3.16. Necessary data of the blade are the prebend coordinates and the estimated flap-wise stiffness distribution. Because the tilt angle of the test rig is known with high precision, the load angle Γ is also precisely known. The required measurement data when performing the test is Lc_x, β (at the loading location), F and all necessary strains. The calibration factors have to be calculated with the quotient of the fully loaded to the unloaded situation[33].

---

[33] Sometimes, slope functions are used to determine the calibration factors using the data during the whole loading process. This leads to incorrect results, because the geometry changes throughout the loading. With OM-II, only the exact loading at 100% calibration load is calculated and should therefore be used for the determination of the calibration factors (Section 3.1.1).

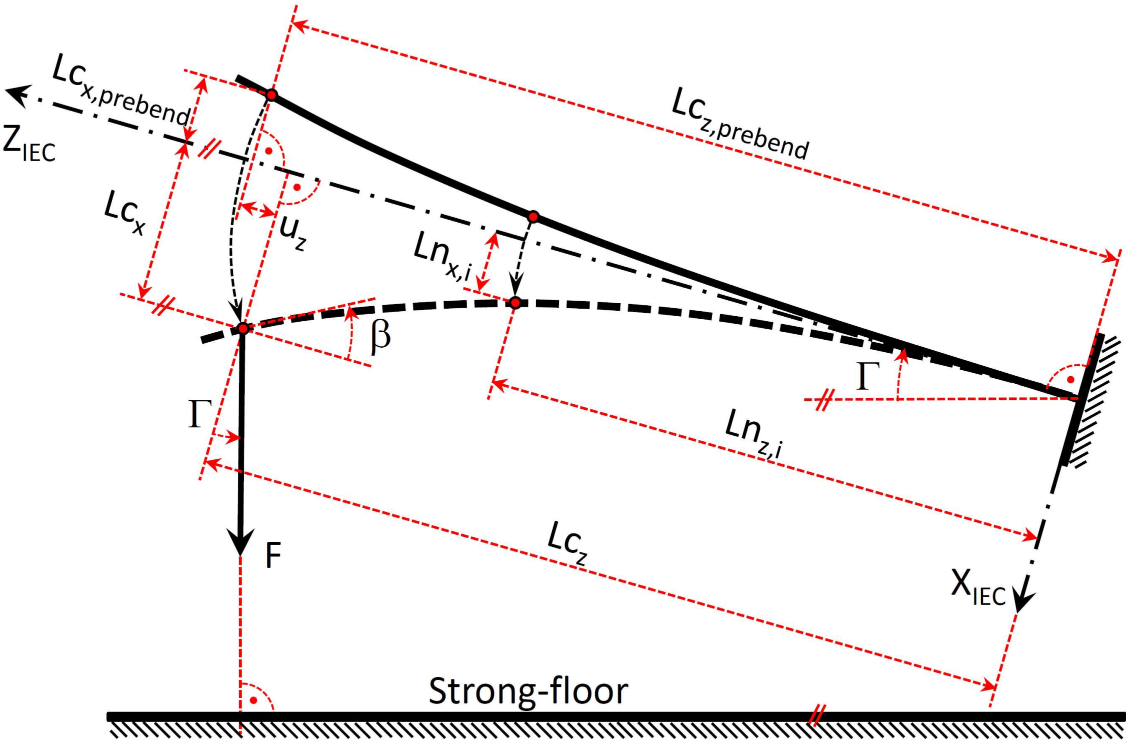

Figure 3.16: Geometry of an calibration test using OM-II

The deflection curve of the blade between root and loading location is then calculated with a very simple numeric blade model using for example an Excel sheet. Without using the measured load at the calibration test, only by changing the *numeric load* in the spread sheet, the deflection of the numeric blade model at the loading location is iteratively adjusted to the deflection measured during the calibration test (Lc_x). Additionally the deflection of the numeric blade model, the local blade angle β at the loading location (Lc_z) is also iteratively adjusted to the measured angle from the calibration test. The angle of the numeric calculation can be adjusted by changing the distribution of the blade stiffness in span-wise direction[34]. Now the numerically determined deflection curve has exactly the same deflection and rotation at the root and at the loading location in comparison to the measured values. The stiffness distribution is *only* used to estimate the deflection curve as precisely as possible in between these two locations. The geometry of the deflected blade and the exact loading direction is now known. The real applied bending moment distribution at the calibration test can now be calculated using the *measured* force. With this data, error E can be calculated with the quotient of the bending moment resulting from the numeric model and the bending moment of an undeformed blade at a perpendicular loading[35]. The

---

[34] Multiplying the stiffness at every position with the same factor does not change the deflection curve and therefore does not change the angle. As a distribution, for example a curve of $(Ln_{zi}/Lc_z)^5$ can be used. Other power terms work as well but were not considered.

[35] Instead of calculating error E, the corrected bending moments can be used directly to determine the calibration factors.

calibration factors can be corrected according to the determined error E. The numeric calculation is described in Section F.

Using the estimated stiffness of the blade to determine the loading of the blade in the calibration tests seems to be in contrast to the test purpose of design verification. But the stiffness data is only used for a correction of the measured data. Furthermore, the exact stiffness is not even needed, but only the general distribution along the blade span.

A verification of OM-II is performed by comparing the simplified calculation results with full FE blade simulations. The verification was performed with four modern blades, two of around 40m and two of around 60m length. All blades were analyzed with ANSYS 15.0 Mechanical APDL. Up to 144 calculations were performed for straight and prebend blades, deflections Lc_x of 25%, 50%, 75% or 100% (of $1/15 \times Lc_z$) and pulling directions of 0° to 16° (tilt angle Γ of the blade). For all analyses, the pulling location was at 95% of the blade length. The uncertainty of OM-II for large deflection effects was limited to $+0.35\%$ to -0.3% for all calculations, assuming that the FE analysis precisely represents reality.

With OM-II, an uncertainty analysis was performed comparable to OM-I of Section 3.4.1. Principally, the same assumptions were used for the calculation. Because the inaccuracy due to large deflection is corrected with OM-II, the analysis of two blades representing a minimum and maximum inaccuracy was not necessary any more. This leaves only the uncertainty of the method. In comparison to OM-I, a dead weight loading was used, so that the uncertainty due to a misaligned loading could be set to zero. According to the verification described above, an overall uncertainty of $\pm 0.5\%$ is conservatively used for large deflection effects (originally $+0.35\%$ to -0.3%).

In Figure 3.17, the uncertainty of a standard calibration test is shown as dotted blue lines and when using OM-I as magenta dotted lines with circles. The uncertainty when using OM-II is shown as red dotted lines with squares, only the uncertainty caused by measuring the strain gauge locations according to Section 3.1.1 (Figure 3.3) still causes significant uncertainties in the tip region.

It can be concluded that a verification using FE models was possible. As no validation against real tests was performed, this task has to be addressed in future work (Section 6.3).

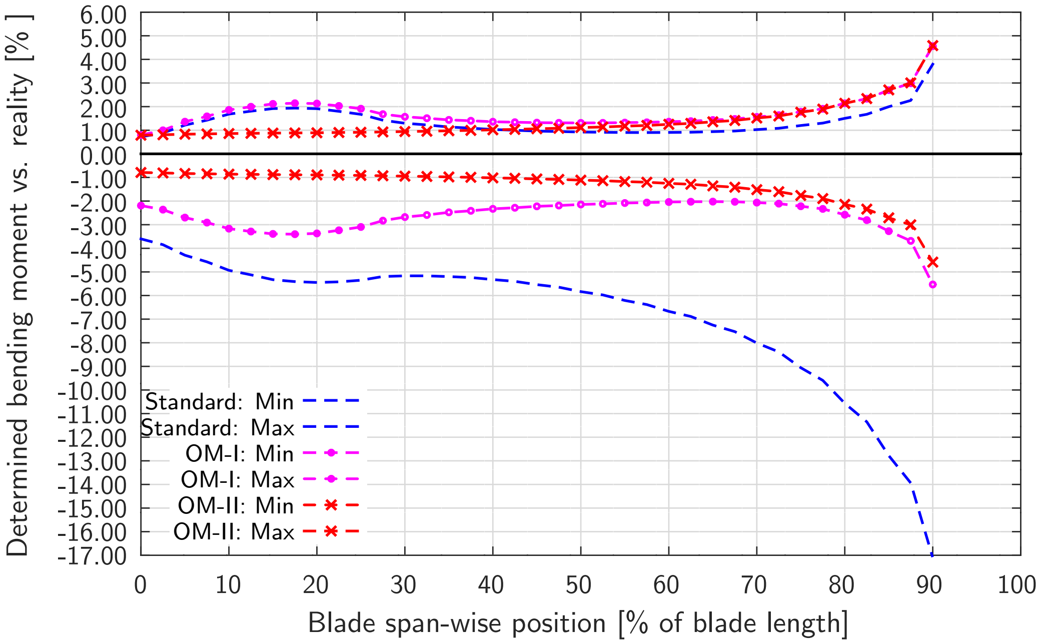

Figure 3.17: Bandwidth of inaccuracies and uncertainties over the blade span for a *standard* calibration test and with using optimization methods OM-I or OM-II.

3.5 Conclusions of Calibration Test

Compared to the correct values, the determined bending moments of present dynamic fatigue tests lay in practice between -8% to +2% for the inner 70% of the blade length and for further outboard regions up to -17% to +4% . The reasons are inaccuracies and uncertainties caused by the measurement uncertainty of the strain gauges and their locations and the geometric nonlinear behavior of typical calibration tests. It was found out that by using the optimization methods described in this chapter, the inaccuracy and uncertainty of the test bending moment determination can be reduced to ±1.5% without using complex measurement devices for the inner 70% of the blade length and ±3% up to 85% of the blade length.

Inaccurately determined test bending moments of more than 25% are found at small blade areas especially at the root region. Different types of local nonlinear behaviors are the reason. A method to correct such errors is presented, with the advantage that no additional test effort is necessary.

Chapter 4

Biaxial Dynamic Excitations of a 40m Blade

In Chapter 2, it was concluded that a biaxial movement in flap-wise *and* lead-lag-wise direction at the same time will generally lead to a more realistic loading of the blade, but a biaxial excitation of the blade using hydraulic actuators was not performed. With previously performed tests at Fraunhofer IWES it was shown that at least the separate excitation of blades in their flap-wise *or* lead-lag-wise natural frequency can be achieved with special control algorithms[36]. To show that a biaxial dynamic loading is also possible, a test on a 40m long blade was performed at the Fraunhofer IWES test rig and will be described in this chapter (blade 2 of Table B.1). Measurements were analyzed to determine, if the test can be performed in a controlled manner.

The methods described in Chapter 3 were developed *after* the biaxial full-scale test described in this chapter was performed. Hence it was unfortunately not possible to use the methods for the blade test.

In Chapter 5, a new method to move rotor blades biaxially, dynamically and *elliptically* during a fatigue test will be numerically simulated and described. The excitation of the blade is also performed with directly attached hydraulic actuators. Because the invention of this method was made after the test on the 40m long blade was performed, the results of this test shall be used to prove that such an elliptic excitation is possible, because besides an elliptic motion, rather complex excitations, like a Lissajous figure with a frequency quotient of f_{1st}:f_{2nd} = 3:4, were successfully performed with the 40m test blade[37].

Before the biaxial excitation was conducted, a full certification test program was performed on the 40mblade including a flap- and lead-lag-wise uniaxial dynamic fatigue test. To compare the uniaxial and biaxial test methods, the OEM of the blade has numerically calculated the damage of

---

[36] The flap- and lead-lag-wise natural frequency is technically spoken wrong, as a system has only a 1st, 2nd,... natural frequency. But because the mode-shape of almost every blade of the 1st natural frequency is oriented mainly in flap-wise direction, and the 2nd natural frequency mainly in lead-lag-wise direction, they are often called the flap-wise natural frequency and lead-lag-wise natural frequency.

[37] Due to the limited number of test rigs with such special equipment, it was not possible to occupy a test rig. Furthermore, the significant test budget was not available at that time.

Figure 4.1: Test setup of the biaxial dynamic fatigue test. View from the blade tip.

the material for both tests as described in Bürkner and Antoniou (2014). The test was supported by a project funded by the *Federal Ministry for the Environment, Nature Conservation and Nuclear Safety* and is described in Bürkner and van Wingerde (2011) and Bürkner and Antoniou (2014). The results will be discussed in Section 4.3.

4.1 Test Setup

The blade has a length of 40m and is attached with the blade root to the test rig at a height of 4.5m. The pitch axis points upwards with an angle of 10° and the pressure side facing upwards. The test setup is shown in Figure 4.1 and Figure 4.2. At 18m from the root, a load frame is fixed to the blade to which the actuators are connected for exciting the blade. As sketched in Figure 4.3, the 1st natural frequency (flap-wise) is excited by actuator 1 which is directly attached between the load frame and a support structure fixed to the strong floor. Actuator 1 is oriented perpendicular to the local pitch axis in span-wise direction. In sideways direction, it is also oriented

Figure 4.2: Test setup of the biaxial dynamic fatigue test. View from the blade root.

vertically. To excite the 2nd natural frequency (lead-lag-wise), a bell crank structure is used[38]. The joints used at the actuators, the bell crank and the push rod are pre-stressed to eliminate any movement. From measurements performed when testing significantly larger blades, it can be assumed that the stiffness of the test rig is infinite. Any limitation of force, stroke, velocity or acceleration of the actuators, which might influence the test results, were not detected for the performed tests.

During each test run the strains, forces and displacements were recorded. To be able to measure the large tip deflection, a new optical measurement system was used as described in Bürkner and Antoniou (2014). The measurement setup is described in Appendix G.

---

[38] This was beneficial because of the following reasons: 1.) By using a push rod, the distance between load frame and the upper joint of the bell crank structure can be adjusted easily. To reduce the disturbance of the push rod force in the direction of the 1st eigenmode, this distance should be as big as possible (D. White (2004), Malhotra (2010)). 2.) The actuator could be positioned almost vertically for reduced shear forces in the piston. 3.) Due to the relations of the two lever arms of the bell crank, the stroke of the actuator can be smaller than the stroke of the push rod which is beneficial for the actuator design.

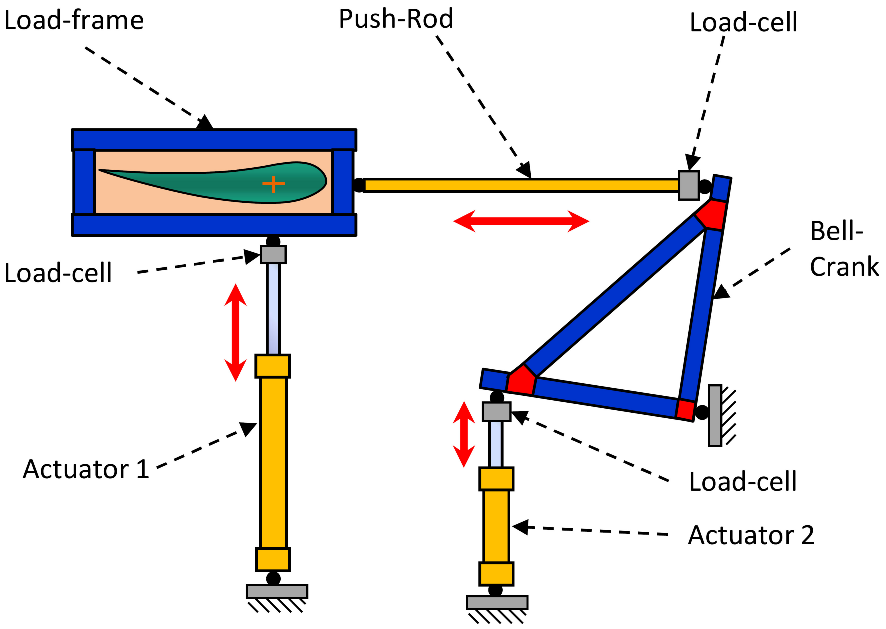

Figure 4.3: Mechanics of the test setup of the biaxial dynamic fatigue test to excite the 1st and 2nd natural frequency with servo-hydraulic actuators. View from the blade root.

4.2 Tests Performed

Different loadings were performed to analyze the behavior of the blade and the test setup:

- Uniaxial movements in flap- and lead-lag-wise direction, with different amplitudes and different excitation frequencies.
- Biaxial tests near the flap- and lead-lag-wise natural frequencies. A quotient of the flap-wise over lead-lag-wise frequencies of exactly 3:4 was used. The amplitudes and the phase were varied.
- Biaxial tests in exactly the flap- and lead-lag-wise natural frequency of the blade. Performed at different amplitudes.

4.2.1 Flap-wise and Lead-lag-wise Movement Separately Excited with One Actuator

To analyze the behavior of the blade for each direction separately, either the push rod of the actuator 2 bell crank mechanism or the piston rod of actuator 1 was unattached from the load frame (Figure 4.3).

Variation of the Amplitude

In flap-wise direction, the test was ramped up step-wise to 85-90% of the desired certification test load. In Figure 4.4, the quotient of the achieved test bending moment over the target bending moment from the specification is given for each span-wise position and each load step. Using a stable control algorithm for the servo-hydraulic actuators, the general behavior of the oscillating system is not expected to change with increasing amplitudes. To visualize this assumption, in Figure 4.5, all curves of Figure 4.4 were scaled linearly to be 1 at 31% of the blade length. It appears that the behavior of the oscillating system is identical for different amplitudes up to the specified range.

Comparable to the flap-wise direction, the lead-lag-wise direction was excited only up to 60-70% of the desired test load, not to damage the blade occasionally. The results are shown in Figure 4.6 and Figure 4.7. Again the behavior appears to be identical for the test amplitudes.

Based on the results of Figure 4.5 and Figure 4.7, it is shown that a variation of the amplitude will not lead to different test bending moment distributions. A stable and reproducible oscillation can be achieved in both directions.

Variation of the Excitation Frequency

To visualize the behavior of the oscillating system when changing the excitation frequency, in Figure 4.8 and Figure 4.9 the resulting quotients of applied test bending moment over the target bending moment from the test specification are shown for the flap- and lead-lag-wise direction. All curves are scaled to be 1 at 7% of the blade length for comparison. Starting with the red line, showing the results for an excitation in the pure 1^{st} or 2^{nd} natural frequency of the blade, the frequency was lowered step-wise. It can be observed that the tip loading decreases relative to the root with decreasing excitation frequency. The bending moment distributions themselves do look similar from step to step which indicates a stable control algorithm for the servo-hydraulic actuators. Comparable to the outcome of the previous section, the excitation is performed in a stable, reproducible way when changing the excitation frequency.

4.2.2 Biaxial Test with 1^{st}:2^{nd} Frequency Equaling 3:4, Different Load Levels and Phase Shifts

In this section, the behavior of blade, test setup and control algorithm of the two actuators attached to the blade, shall be analyzed for a biaxial loading. The goal is, to show a stable, repeatable and precise excitation using directly coupled servo-hydraulic actuators. The excitation frequencies of the flap-wise over lead-lag-wise direction are set to a quotient of 3:4. The goal was to excite a Lissajous figure as shown in Figure 2.7 (f_{1st}:f_{2nd} = 3:4). In order to achieve this exact ratio, the flap-wise direction was excited at 97.4% of the 1^{st} natural frequency of the blade and the lead-lag-wise directions at 96.1% of the 2^{nd} natural frequency of the blade.

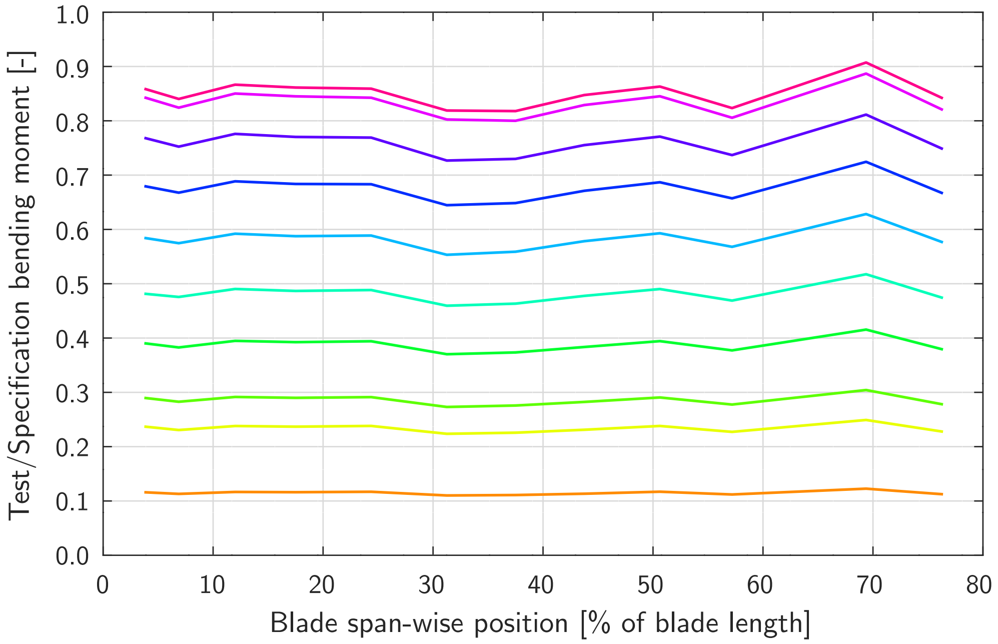

Figure 4.4: For a step-wise increased amplitude of a flap-wise dynamic fatigue test, the quotient of the achieved test bending moment over the target bending moment from the specification is given for each span-wise position. Each curve represents one excitation amplitude.

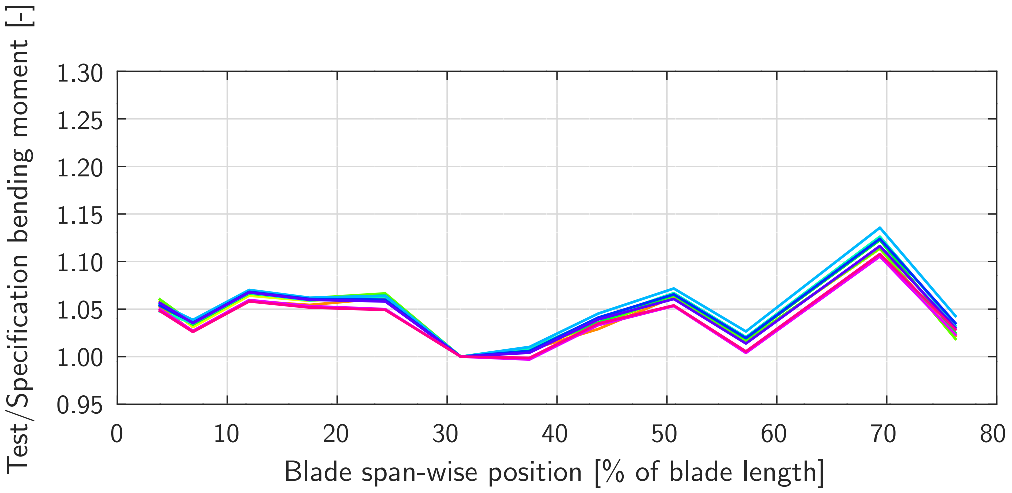

Figure 4.5: To be comparable, all curves of Figure 4.4 were scaled linearly to be 1 at 31% of the blade length. The deviations of up to 4% at 70% of the blade length are likely caused by aerodynamic drag forces

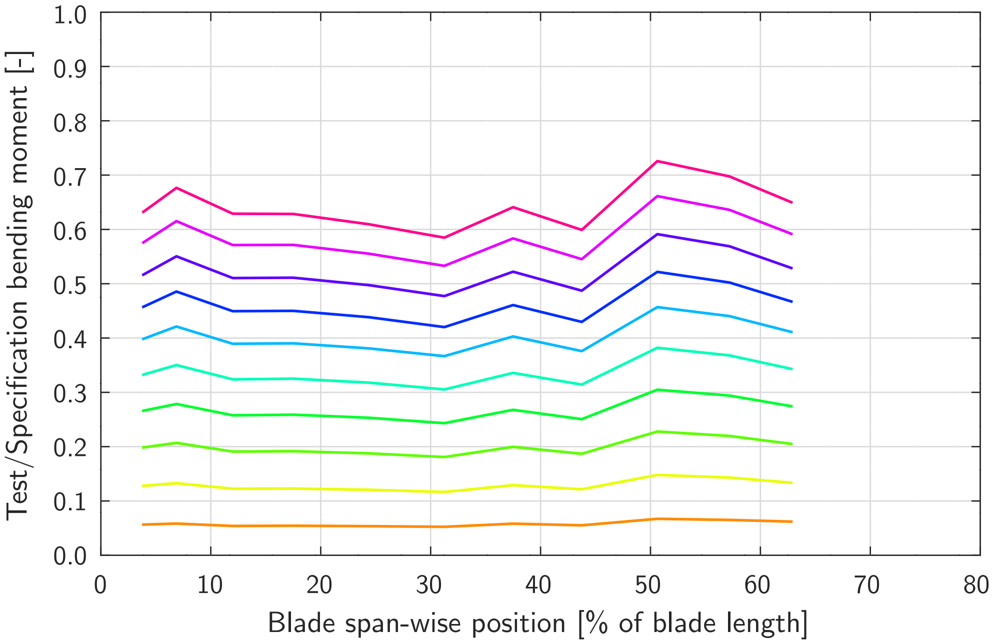

Figure 4.6: For a step-wise increased amplitude of a lead-lag-wise dynamic fatigue test, the quotient of the achieved test bending moment over the target bending moment from the specification is given for each span-wise position. Each curve represents one excitation amplitude.

Figure 4.7: To be comparable, all curves of Figure 4.6 were scaled linearly to be 1 at 31% of the blade length. The deviations of up to 6% at 60% to 70% of the blade length are likely caused by aerodynamic drag forces.

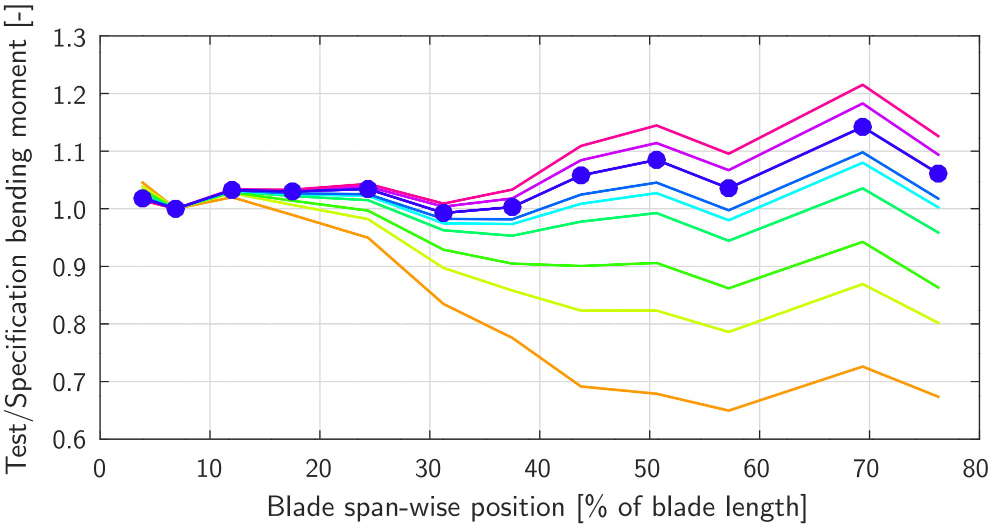

Figure 4.8: For a step-wise decreased excitation frequency of a flap-wise dynamic fatigue test, the quotient of the achieved test bending moment over the target bending moment from the specification is given for each span-wise position. Each curve represents one excitation frequency. Starting at the pure 1st blade natural frequency in red, the excitation frequency was reduced with the following steps in percent: 100, 99.5, 99, 98.5, 98, 97.5, 96, 94, 90. To be comparable, all curves were scaled to be 1 at 7% of the blade length. The most probable frequency for a certification test is highlighted with markers.

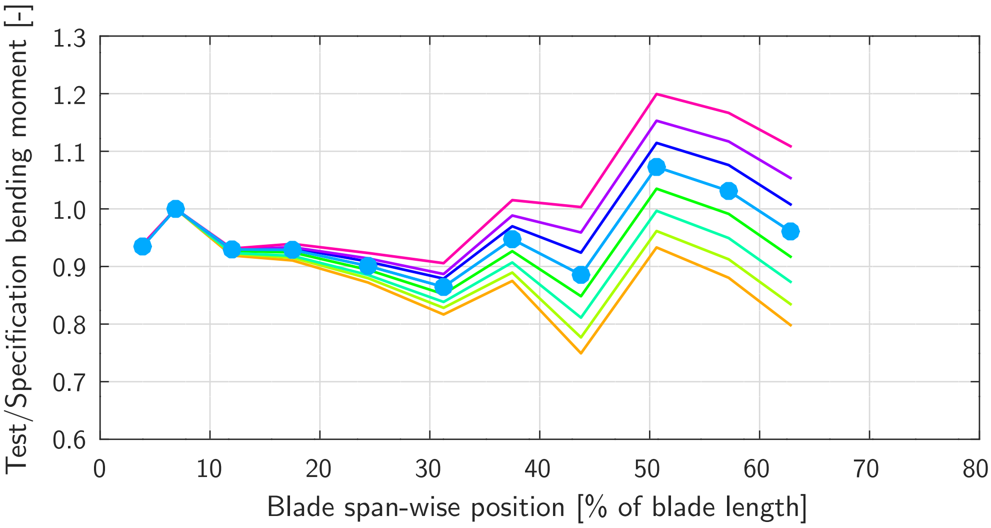

Figure 4.9: For a step-wise decreased excitation frequency of a lead-lag-wise dynamic fatigue test, the quotient of the achieved test bending moment over the target bending moment from the specification is given for each span-wise position. Each curve represents one excitation frequency. Starting at the pure 1st blade natural frequency in red, the excitation frequency was reduced with the following steps in percent: 100, 99, 98, 97, 96, 95, 94, 93. To be comparable, all curves were scaled to be 1 at 7% of the blade length. The most probable frequency for a certification test is highlighted with markers.

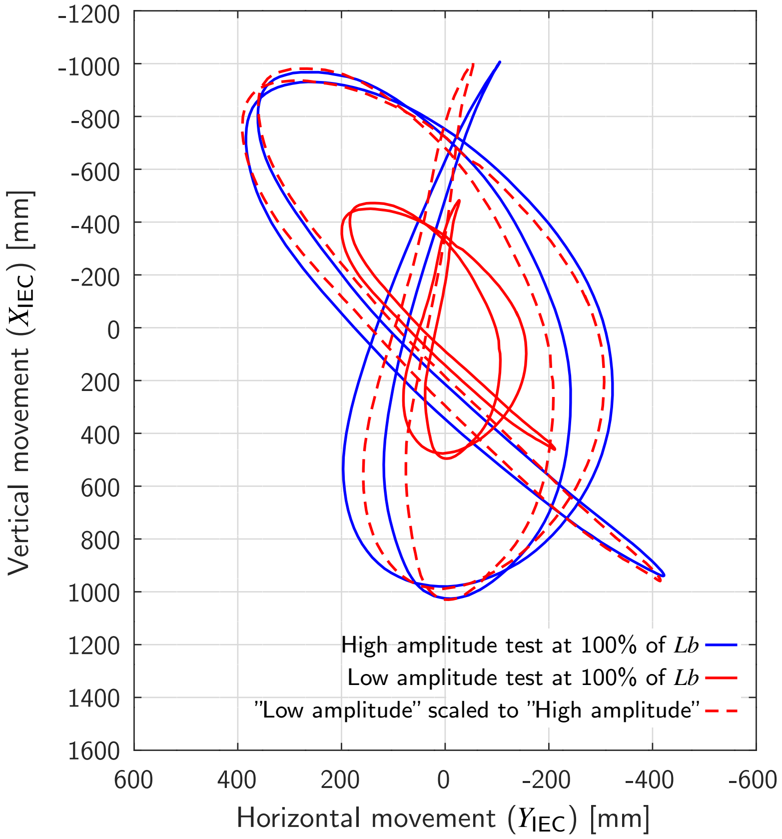

Figure 4.10: Movement of the tip at different amplitudes with an excitation of flap-wise over lead-lag-wise frequency is 3:4. The *high amplitude* level represents a deflection of ≈50% of an usual uniaxial dynamic fatigue test at the maximum deflection locations of the movement.

Similarity of the Movement for an Excitation at Different Amplitudes

As performed for the excitation of only the flap-wise *or* lead-lag-wise direction (shown in Section 4.2.1), the blade was loaded at amplitudes in the flap-wise *and* lead-lag-wise direction at the same time. All other parameters like the excitation frequencies and the phase were kept the same. As the tip is the most sensitive part of the excited system, it was used to analyze the movement by comparing the displacement. The coordinates of the tip were measured with the optical prototype measurement system from AICON as described in Appendix G.

In Figure 4.10, the movement of the blade tip is plotted. A visual comparison of the curves shows, that the behavior of the system is almost identical when exciting the system at different amplitudes. The shape of the movement and the phase is almost the same. A difference will occur due to changing load angles of the push rod at higher flap-wise amplitudes.

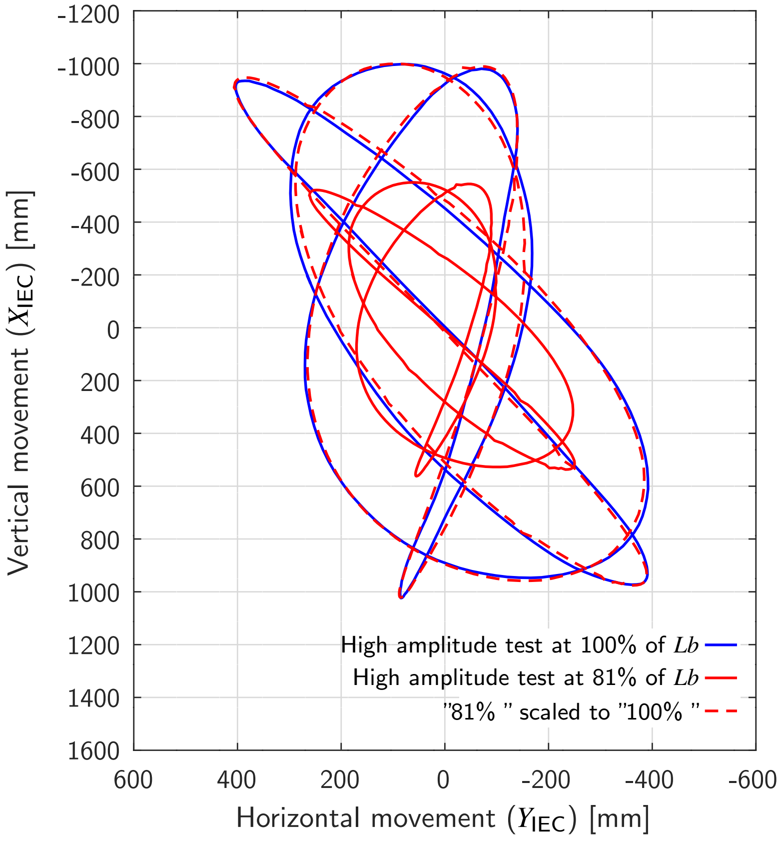

Figure 4.11: Movement of the tip at different span-wise locations with an excitation of flap-wise over lead-lag-wise frequency is 3:4. The *high amplitude* level represents a deflection of ≈50% of a usual uniaxial dynamic fatigue test at the maximum deflection locations of the movement.

Similarity of the Movement at different span-wise Locations of the Blade

The movement of the blade was also measured at two different span-wise locations. In Figure 4.11, the movement of the blade tip is plotted to see the comparability of the movement with regard to different span-wise locations (100% of the blade length and 81% of the blade length).

By visually comparing the scaled movement at 81% of the blade length with the tip movement, both curves can be described as identical. This shows that the blade movement is without vibrations at higher frequencies or other disturbing effects, but precisely at the 3:4 curvature at the specific phase.

In Figure 4.10 and Figure 4.11, two different phases are shown. Principally, all theoretical phases can be chosen. Tests were performed by varying the phase in steps of 25° without noticing any unstable or problematic behavior of the system.

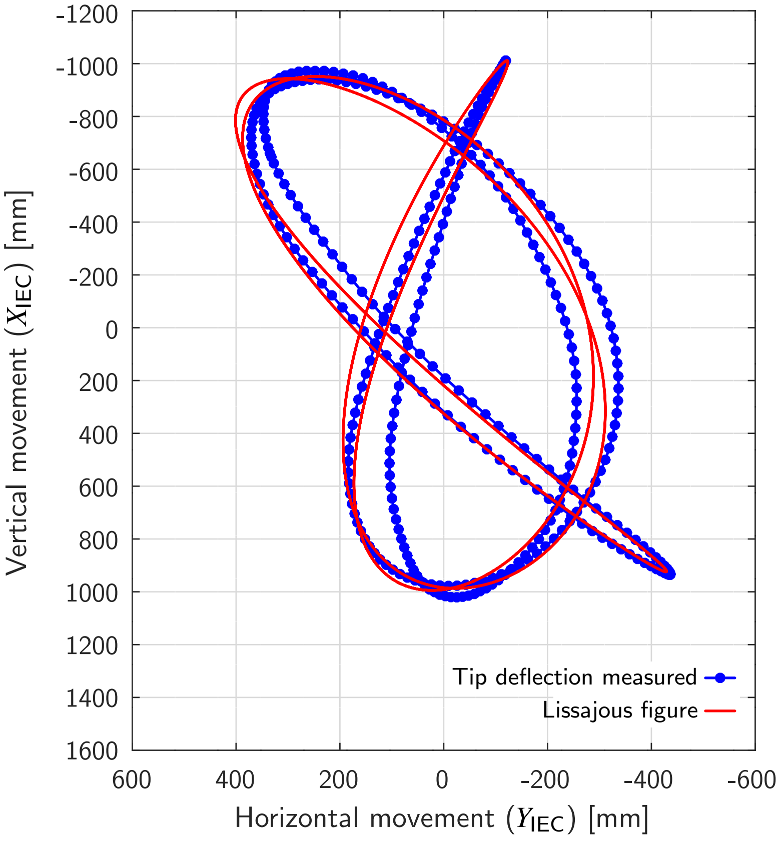

Figure 4.12: Movement of the tip compared to an adjusted Lissajous figure with an excitation of flap-wise over lead-lag-wise frequency is 3:4.

Comparison of the Theoretical Movement with the Measured Movement

To visualize the precision of the biaxial movement according to a theoretical Lissajous figure, in Figure 4.12, both options are plotted. For the test movement, the excitation shown in Figure 4.10 is used (tip movement of an excitation of the flap-wise *and* lead-lag-wise direction having a frequency quotient of flap-wise : lead-lag-wise = 3:4). The Lissajous figure is calculated according to Section 2.2.1 and Section 2.2.2 by adjusting the parameters Amp_{1st}, Amp_{2nd}, φ_{1st}, ψ_{1st} and ψ_{2nd}. The frequencies f_{1st} and f_{2nd} were equal to the test frequencies.

The goal is to visualize how close the movement is to a best-fit adjusted theoretical curve. Analyzing Figure 4.12 under this respect, it becomes clear that some disturbances are present. For example, the whole excitation mechanism will have some influence. Still, the curves are quite equal, so that an excitation according to a theoretical Lissajous figure is accomplished. The change of the accumulated damage is negligible when comparing both curves in a fatigue calculation of a blade.

4.2.3 Biaxial Test Exactly at 1^{st} and 2^{nd} Natural Frequency

The blade was additionally excited at its 1st and 2nd natural frequency at the same time to prove that a stable oscillation is also possible with such setup.

The movement of the tip is plotted in Figure 4.13. After ramping-up, the test was runn for 175s. According to Section 2.2.2 or Figure 2.8, the shape of the movement seems to be comparable. For a better comparison, the movement was calculated with sine curves of exactly same frequencies f_{1st} and f_{2nd} and with the previously estimated rotations ψ_{1st} and ψ_{2nd}. As the phase has no influence on the shape, φ_{1st} was set to zero. The amplitudes Amp_{1st} and Amp_{2nd} were adjusted to fit the measured movement. Furthermore, the sine curves of the flap- and lead-lag-wise wise direction were each overlaid with another sine curve. To the flap-wise sine curve, a sine curve was added defined by the lead-lag-wise natural frequency. The amplitudes and phases of that curves were adjusted. This theoretic movement is now identical to the measured movement shown in Figure 4.13.

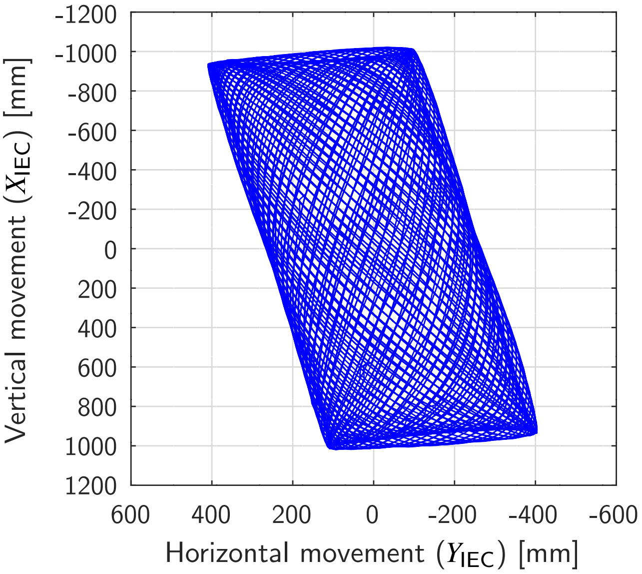

Figure 4.13: Movement of the tip at an excitation of both natural frequencies for 175s. View from blade root to blade tip.

Even though it was not further evaluated, the reason why parts of the perpendicular oscillation were found in the movement could be that the excitation mechanism (Figure 4.3) introduces for example lead-lag-wise loads in flap-wise direction due to the angle of the push rod and vice versa. In case the push rod is not parallel to the lead-lag-wise movement at the load frame location any more, flap-wise loads are introduced with the sine of the angle times the push rod force.

Having such influences does not mean that the blade oscillates in an uncontrolled way, but it is necessary to record every cycle with the data acquisition system to be able to calculate the correct DEL of the test (by summing up the DELs of each cycle).

4.3 Comparison of the Damage Distribution for Uni- and Biaxial Tests

In this section, the advantages and disadvantages of the biaxial tests in comparison to usual uniaxial tests will be described. Firstly, the applied damage per cycle will be discussed and secondly, the damage distribution of blade cross-sections.

To analyze the impact on the applied damages, an example will be used with a biaxial dynamic fatigue test at a ratio of f_{1st}:f_{2nd}=3:4 (phase φ_{1st}=90° , structural twist of ψ_{1st}=-10° and ψ_{2nd}=-5°). The maximum amplitude shall be 1.0 in flap- and 0.6 in lead-lag-wise direction (Figure 2.6 and Figure 2.7 bottom right). In case of a uniaxial test, the maxima and minima of a flap- and lead-lag-wise movement over time are all on a constant level (Figure 2.6). For a biaxial test, alternating levels are present (Figure 2.7). Using rainflow counting, the flap- and lead-lag-wise curves of the biaxial test according to ASTM (1997) were analyzed. A variable amplitude with three respectively four levels can be found. In flap-wise direction, the three different amplitudes are 1.0, 0.968 and 0.933. In lead-lag-wise direction, the four different amplitudes are 0.6, 0.520, 0.392 and 0.286. Because the applied damage is dependent on the amplitudes, the applied damage of such biaxial tests is much smaller, if the number of applied cycles stays the same. In comparison to a uniaxial test with constant amplitudes of one, the applied damage for the flap-wise direction is 74.1% using an S-N slope of 10 representing glass-fiber materials. In case of carbon-fiber materials with an S-N slope of 15, the applied damage drops to 65.6%. For the lead-lag-wise direction, the effect is even bigger. For an S-N slope of 10, the applied damage is 31.3% and for an S-N slope of 15, it is 28%. The result of this examination is that when limiting the maximum amplitudes to the same level for the uniaxial and the 3:4 biaxial test and additionally loading the blade with the same cycle number, the applied damage at the biaxial test is significantly smaller. Hence, the cycle number or testing time would have to be extended.

With regard to the damage distribution of blade cross-sections, three different accumulated damage distributions should be compared: 1) Damage sum calculated by a numerical simulation of the whole turbine life. 2) Damage sum applied by the two uniaxial tests in flap- and lead-lag-wise direction. 3) Damage applied by the biaxial test.

The following results were achieved within the scope of the project *Better Blade* (Bürkner and Antoniou (2014)). The uni- and biaxial loadings were measured in the laboratory and provided to the manufacturer of the test blade. Because the numerical model of the blade could not be provided due to commercial reasons, the detailed analysis of the blade structure had to be performed by the manufacturer.

- Biaxial dynamic fatigue tests performed exactly at the first two natural frequencies of the blade or at certain Lissajous figures are possible for certifying a blade. The applied damage distribution leads to are more thoroughly tested blade compared to the sum of two uniaxial dynamic fatigue tests.
- If an ideal phase (φ_{1st}) is used for the biaxial dynamic fatigue test, the regions between pressure side, suction side, leading edge and trailing edge can be tested more accurately,

because the applied damage in these regions is much higher than for uniaxial loads. For this reason, the damage is closer to the numerically determined damage of the turbine's life time, i.e the test is more realistic. A similar conclusion was described in Greaves et al. (2011) and Beckwith et al. (2013).

- With assuming an equal testing time for uni- and biaxial tests the following was found: 1) The maximum amplitude in flap-wise direction can be slightly reduced in comparison with the uniaxial setup 2). The maximum amplitude in lead-lag-wise direction has to be increased by +15% in comparison to the uniaxial setup.

Increasing the amplitude of the lead-lag-wise direction like described in item three is very critical, because the test amplitudes are already much higher than at load cycles at the real turbine to achieve an accelerated fatigue test. When using the Palmgren Miner rule, theoretically the same damage is applied. But since it is questionable that this theoretical approach represents reality above certain test amplitudes, almost all OEMs try to keep the maximum test amplitude beneath a certain level. Hence, for every test a compromise between low amplitudes and long testing time or high amplitudes with a short testing time has to be determined. Most likely, an increased amplitude of +15% will not be accepted, but if reducing the amplitude and increasing the cycle number, the advantage of a shorter test is obsolete.

Using biaxial testing concepts leading to a variable amplitude fatigue test is therefore not ideal for certification tests, even though a more thorough test is possible. Other test methods avoiding this problem need to be developed to achieve a realistic loading and also a shortening of the testing time. A new idea how to achieve this goal is described, analyzed and discussed in Chapter 5.

4.4 Conclusions of Biaxial Test

It can be concluded that it is possible to excite a modern blade of 40m length with servo-hydraulic actuators (directly coupled to the blade) in a very controlled biaxial motion. Excitations in the 1^{st} and 2^{nd} natural frequency or biaxial excitations close to the 1^{st} and 2^{nd} natural frequency are possible. When using the described bell crank mechanism and actuator length, no significant divergence to the theoretically movement was detected.

When comparing the applied excitation of uniaxial and biaxial tests (excited at the 1^{st} and 2^{nd} natural frequencies), the flap-wise and lead-lag-wise loading of the biaxial test results in variable amplitudes. With the same maximum amplitude compared to the uni- and biaxial test, the applied damage at the biaxial test is much smaller. A comparable applied damage can only be achieved using a biaxial motion which results in constant amplitude tests, as described in the next chapter.

Chapter 5

Biaxial Elliptical Dynamic Excitation (BEDEX)

In Section 2.5 and Section 4.3, it was concluded that saving testing time with a biaxial test without increasing the test amplitude in comparison to uniaxial tests is only possible, if the blade can be loaded in a biaxial *elliptical* movement. Therefore, in this chapter a test setup is described to excite a blade in a biaxial *elliptical and dynamic* excitation to test the blade in fatigue.

5.1 Description of the Method

Because the natural frequencies of blades in flap- and lead-lag-wise direction are different, an elliptical loading cannot be applied dynamically. For the method described in this chapter, the lead-lag-wise frequencies will be tuned by using additional masses, so that they are equal to the flap-wise frequency without these masses. To achieve such movement, an active movement of these masses attached to the blade is pursued in flap-wise direction, in order to neglect their influence on the flap-wise natural frequency.

5.1.1 Approach

The common practice of how to perform dynamic fatigue tests is described in Section 2.3.2. The excitation mechanisms can be divided in two groups: 1) Excitation systems only connected to the blade, like eccentric motors or linear shakers. 2) Excitation systems connected to the blade *and* the test rig (strong floor).

Category 1) test setups have specific natural frequencies in flap- and lead-lag-wise direction, defined by the stiffness and mass of the blade as well as the mass of the exciter system. By adding tuning masses to the blade, always all natural frequencies will be changed. Hence, tuning equal frequencies only with extra masses is impossible.

Considering category 2) test setups, the blade plus extra masses plus the excitation mechanisms has no precisely defined natural frequencies. This is because the actuator connects the blade to the strong floor in a way, which cannot be described with a spring or a spring damper description. To better understand the behavior of these systems in terms of their natural frequencies, the following setup shall be imagined: All actuators do have zero friction and can run freely. In this case, the blade with attached masses like the mass of the excitation mechanisms, the joint between load frame and piston rod of the actuator and the mass of the piston rod itself has precisely defined natural frequencies. This setup will be called *the system* having *the system's natural frequencies*. The mass of the barrel of the actuator is not considered, as it will not move when oscillating the blade.

The advantage of category 2) systems is that the actuators can be moved sinusoidally at any frequency chosen and by applying high forces to the blade at the same time. This results in a major advantage: By moving the actuator sinusoidally at specific frequencies, all masses attached to the blade at the span-wise position of the actuator can be reduced or even neutralized in the direction of the specific mode shape. The method will be explained in Section 5.3. In case bell crank mechanisms are used, the direction of the push rod (Figure 4.3) connecting the bell crank to the blade is essential. The neutralization can be generated not only with one actuator, but at any location where an actuator is connected. Two actuators in span-wise direction (and with the same direction) will also be simulated in Section 5.3. By neutralizing these masses, the blade loading is comparable to the situation without these attached masses.

Because additional energy is needed to move the added masses by the actuators, the method can be described as an *active* mass compensation (AMC). An algorithm of how to control actuators to achieve such active mass compensation while having a stable oscillation at the same time was developed at Fraunhofer IWES (Bürkner (2014)).

As an example, the system shown in Figure 2.13 (top sketch) shall be considered: Only one actuator is connected to the blade to excite an oscillation in the flap-wise direction. Attached masses are the load frame, the joint construction and the piston rod. When moving the actuator in the system's natural frequency in flap-wise direction, the dynamic loading of the blade is given by the oscillation of *the system*. The blade will therefore be loaded dynamically by its own mass plus the attached masses. A totally different loading can be applied when moving the actuator exactly at the 1st natural frequency of the pure blade. In this case, all attached masses will be actively compensated. The blade will oscillate and will be dynamically loaded, as if it oscillates without any attached mass.

Coming back to the goal of moving the blade biaxially, dynamically and elliptically, the 1st an 2nd natural frequencies of the system have to be almost identical. By comparing the system to a simple spring-mass oscillator, it becomes clear that either the stiffness or the mass of the system has to be changed to tune both frequencies to be identical. Because the stiffness of the system cannot be changed and adding passive masses only results in a decrease of *all* the system's natural frequencies, masses have to be added *only* in the lead-lag-wise direction to decrease the 2nd natural frequency to the 1st natural frequency. To be able to reduce the influence of masses to only one direction, the idea has to be combined with the previously mentioned possibility of compensating masses in one direction by using the AMC method. Having the 1st and 2nd natural

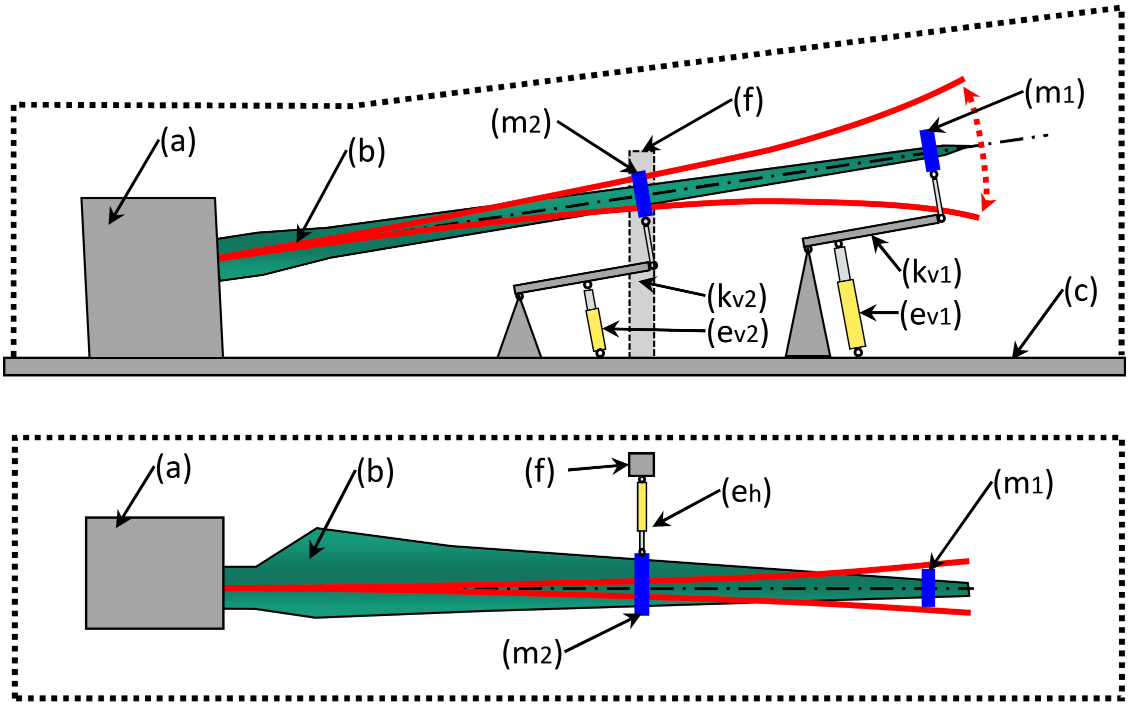

Figure 5.1: Test setup of a biaxial dynamic fatigue test (BEDEX). Loaded with directly attached servo-hydraulic actuators using bell crank mechanisms. Side view: Flap-wise test direction. Top view: Lead-lag-wise test direction. (a) Test rig; (b) Blade; (c) Strong floor; (e_h) Horizontal actuator; (e_v1 and e_v2) Vertical actuators; (f) Support of horizontal actuator; (k_v1 and k_v2) Vertical bell crank systems; (m_1) Tuning mass 1; (m_2) Tuning mass 2

frequency tuned very close to each other, the blade can be biaxially, elliptically and dynamically excited at any phase (biaxial elliptical dynamic excitation (BEDEX)).

5.1.2 Basic Setup

In Figure 5.1, a BEDEX test setup is shown with a side view and a top view. The blade (b) is rigidly fixed to the test rig (a). The test rig is fixed to the strong floor (c). The two tuning masses 1 (m_1) and 2 (m_2) are fixed to the blade at different span-wise positions. They are used to tune the natural frequency of the lead-lag-wise direction to the flap-wise natural frequency of the blade. In order to match the achieved test bending moment properly with the ideal test bending moment (usually defined in each test specification), it is assumed that at least two masses are necessary to achieve a mainly bilinear bending moment distribution.

The horizontal actuator (e_h) which is fixed to a support (f) is attached to mass 2. The blade plus the masses 1 and 2 plus the joint and the piston rod of the horizontal actuator can be roughly seen as the oscillator for the lead-lag-wise direction (they need to have the same natural frequency as the *pure* blade in flap-wise direction). The vertical actuators 1 and 2 (e_v1 and e_v2) are included in the vertical bell crank mechanisms 1 and 2 (k$_v1$ and k$_v2$), in order to increase the movement of the vertical actuators to meet to the large deflections appearing at the blade tip in flap-wise direction[39]. The push rods of the bell crank mechanisms are located perpendicular underneath the masses 1 and 2.

As explained above, all three actuators will be moved in the 1st or flap-wise natural frequency of the pure blade. Hence, the masses 1 and 2 will be fully neutralized in flap-wise direction by AMC and the blade will be oscillated and loaded as without attached masses in this direction. In lead-lag-wise direction, the loading of the blade is defined by the dynamic blade mass and the masses 1 and 2.

By moving the actuators at the same frequency, an elliptic motion of the blade occurs. By adapting the amplitudes and the phase between the horizontal and vertical actuators, the shape of the ellipse can be manipulated to adjust the fatigue test loading.

5.1.3 Setup with Electric Shaker

For saving energy, a BEDEX test setup is possible, where the horizontal actuator (e$_h$) like shown in Figure 5.1 is substituted by a horizontal eccentric motor to excite the lead-lag-wise oscillation in order to save energy (comparable to (g$_h$) Figure 2.12). Because the test frequency in lead-lag-wise direction is on the system's natural frequency, the necessary excitation energy is moderate. Hence, using an eccentric motor becomes feasible.

The advantage of using such a system is the lower amount of electrical energy needed to achieve the necessary mechanical energy for exciting the blade in this direction. Electrically driven eccentric motors can convert electrical energy into mechanical energy at a high rate, because the loss of the motor or the gearbox is rather small. On the contrary, a hydraulic actuator does need approximately a two times higher electrical energy input (hydraulic pumps) than the available output of mechanical energy to excite the blade. The reason is the *sinusoidal* force that is necessary to excite a system in its natural frequency and the fact that the energy needed to drive an actuator at a certain velocity but with different forces cannot be adjusted automatically.

A disadvantage would be that a tuning in lead-lag-wise direction using the AMC method is not possible any more (adjusting the frequency). Applying a significant extra force with an eccentric motor would lead to unacceptably high masses of the exciter.

---

[39] Actuators with a very large stroke are expensive to manufacture, sensitive in terms of the handling and critical in terms of the velocity of the piston rod, even in case hydrostatic bearings are used. Bell crank systems are well-known and do work reliably. The leverage of the bell crank can be designed for actuators with a moderate piston rod velocity to use cheap actuators with slide sealings. The increasing force of the actuator, having a bell crank with a big transmission, is not critical, because actuators can be easily designed for large forces.

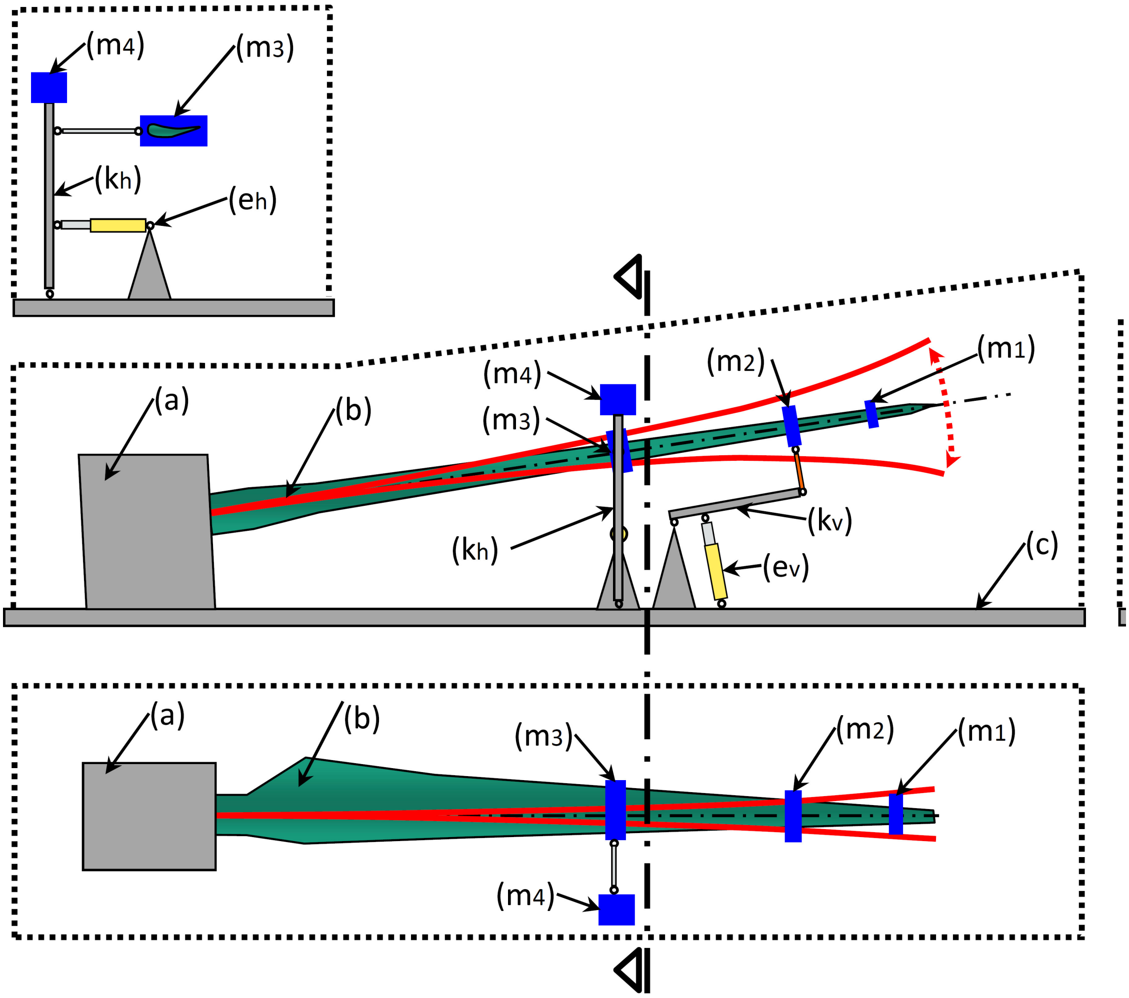

Figure 5.2: Test setup of a biaxial dynamic fatigue test (BEDEX). Loaded with directly attached servo-hydraulic actuators using one vertical and one horizontal bell crank system. Cross-section as marked. Side view: Flap-wise test direction. Top view: Lead-lag-wise test direction. (a) Test rig; (b) Blade; (c) Strong floor; (e_h) Horizontal actuator; (e_v) Vertical actuator 1; (k_h) Bell crank system for horizontal loading; (k_v) Bell crank system for vertical loading; (m_1) to (m_4) Tuning masses

5.1.4 Setups with Reduced Number of Actuators

A setup is possible which combines the advantages of a flexible tuning of the test with the minimum number of necessary actuators. In this way, costs can be reduced, as less hardware has to be installed and less energy is needed. The setup is shown in Figure 5.2. In this case, a bell crank mechanism is also used for the horizontal loading (k_h). The advantage is that a mass (m_4) can be attached to the horizontal bell crank (k_h) without having an influence on the flap-wise direction and without the need for a vertical actuator to compensate the mass in flap-wise direction.

The oscillation in flap-wise direction is at a frequency given by the natural frequency of the blade plus masses (m_1) and (m_3). The masses can be used to tune the bending moment curve to fit the specification in flap-wise direction. The mass (m_2) is compensated by the bell crank (k_v) and therefore has no influence on the flap-wise direction. At the same time, the bell crank (k_v) loads the blade in flap-wise direction. Because mass (m_4) is located *on* the bell crank (k_h), it has no influence on the flap-wise direction.

The oscillation in lead-lag-wise direction is exactly at a frequency given by the flap-wise direction. The natural frequency of the system in lead-lag-wise direction is given by the blade plus masses (m_1) to (m_4). After masses (m_1) and (m_3) are defined by the tuning of the flap-wise direction, only masses (m_2) and (m_4) can be used to tune the bending moment curve in lead-lag-wise direction to fit the specification. The tuning of a BEDEX test will be explained in Section 5.5.3.

With this setup, only two bell crank mechanisms are needed for the test. In comparison to this, separate flap- and lead-lag-wise tests need almost the same hardware. Applying four masses does need a certain effort, but masses are rather cheap hardware components. Time and costs of such tests are analyzed in Section 5.5.5.

5.1.5 Validation Approach

For the lack availability of a test hall and a test budget, a real test of the BEDEX method has not been possible yet. Hence, to analyze the method, a full transient FE simulation is performed in Section 5.5. All critical aspects to perform this simulation were individually validated and analyzed to achieve representative results.

1. To prove that the AMC idea is represented correctly with this FE simulation, a validation of the FE model is performed in Section 5.2, using a test of a 60m blade. The validated model is later used to simulate the AMC (Section 5.3).
2. To prove that a biaxial movement can be adequately simulated, in Section 5.4, the excitation of complex Lissajous figures was compared with simulation results. The measurement data of the biaxial test described in Chapter 4 is used for this validation. The BEDEX method is later described in Section 5.5 using this validated FE simulation.
3. The servo-hydraulic control system is *not* included in the simulations. The tests described in Chapter 4 were performed to prove that a servo-hydraulic excitation system is capable

of moving the blade biaxially. It was shown that even complex Lissajous figures can be achieved in a stable and repeatable way. Because the BEDEX method only needs a rather simple elliptical movement, it is assumed that an elliptical motion for a BEDEX test can be excited without difficulty.

5.2 FE Analysis of a Uniaxially Loaded Blade

In this section, the FE approach to simulate the AMC method (Section 5.3) is validated with a uniaxial dynamic fatigue test (blade 9 of Table B.1). The test setup is shown in Figure 5.3. A blade of approx. 65m length (b) is fixed to a stiff test rig (a) at an angle of 7.5° to horizontal above the strong floor (c). The pressure side of the blade faces upwards. At ≈50% blade length, an actuator (e_v) is attached to the load frame (mass m_2). To tune the bending moment distribution, an additional mass (m_1) is attached at the tip region of the blade.

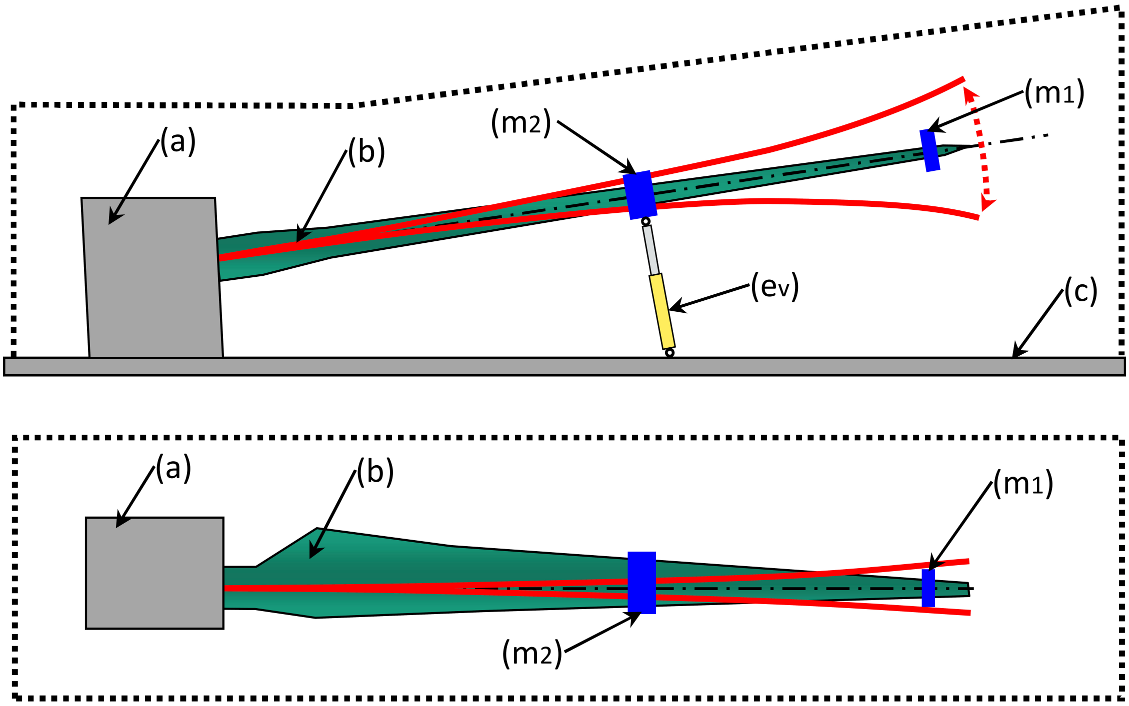

Figure 5.3: Test setup used to validate the simulation approach for demonstrating the AMC method. The blade is loaded with one directly attached servo-hydraulic actuator. Side view and top view. (a) Test rig; (b) Blade; (c) Strong floor; (e_v) Vertical actuator; (m_1) and (m_2) Masses

5.2.1 FE Model

The FE software package ANSYS Mechanical 15.0[40] was used for the simulations. As the result of the analysis is a bending moment distribution along the blade span, a beam model was taken for the blade discretization. The blade was discretized with over 50 BEAM189 elements. The FE model with integrated damper elements is shown in Figure J.1[41]. The mass and the moment of inertia of the different cross-sections are integrated by MASS21 elements. All attached masses were also discretized as point masses using MASS21 elements. For the actuators, LINK11 elements were used as well. The air (drag) damping of the blade is simulated by attaching 50m long COMBIN14 elements in flap- and lead-lag-wise direction. The FE code is shown in Appendix K.2.

The goal is to simulate the behavior of the blade during oscillation, including the loading of the actuator, extra weights, material damping and air damping. Because the damping of the material, the test-rig as well as the joints of the excitation mechanic are unknown, they are summarized in the material damping. The simulation of the pure hydraulic system, such as pump valve actuator and control interaction, is not part of the analysis.

Any loading of the blade before starting the oscillation will *only* change the mean loading of the blade at the dynamic fatigue test. As this load does not change the range value of bending moments significantly, zero gravity acceleration was used in this simulation to simplify the analysis. For each simulation, a transient FE analysis was performed for 60s in time steps of 0.025s. The large deflection option was enabled. The blade root was rigidly fixed at all six degrees of freedom. Sinusoidal forces were applied to the actuator element.

5.2.2 Damping

Material and air damping (caused by the large deflection and high tip speeds) were discretized in the FE model. The material damping is included with a Rayleigh damping approach, shown in Equation 5.1 and Equation 5.2[42].

$$[C] = \alpha_{damp} * [M] + \beta_{damp} * [K] \tag{5.1}$$

The damping matrix (C) is determined by multiplying the coefficient α_{damp} (representing a frictional damping) with the mass matrix (M) and multiplying β_{damp} (representing a material damping) by the stiffness matrix (K). Because no frictional damping is used, α_{damp} can be set to

---

[40] http://www.cadfem.de/, CADFEM GmbH

[41] The lead-lag-wise excitation structure is not used in this case.

[42] ANSYS Documentation - Mechanical APDL - Structural Analysis Guide - Alpha and Beta Damping (Rayleigh Damping)

zero. After converting Equation 5.2, β_{damp} can be determined directly with the usually known modal damping ratio ξ_i.

$$\xi_i = \frac{\alpha_{damp}}{2 * \omega_i} + \frac{\beta_{damp} * \omega_i}{2} \quad \Rightarrow \quad \beta_{damp} = \frac{2 * \xi_i}{\omega_i} \tag{5.2}$$

C: finite element damping matrix

M: finite element mass matrix

K: finite element stiffness matrix

α_{damp}: Mass matrix multiplier for damping

β_{damp}: Stiffness matrix multiplier for damping

ξ_i: Material damping ratio at eigenmode i

ω_i: Angular frequency of eigenmode i

The drag forces (F_d) due to air damping on the blade are calculated according to the Morison equation (Equation 5.3).

$$F_d = \frac{1}{2} * \rho * A * C_d * v^2 \tag{5.3}$$

F_d: Drag force due to air damping at location i

ρ: Air density

A: Blade cross-sectional area to calculate the drag force due to air damping at location i (cord length for flap-wise and height of profile for LLW direction)

C_d: Drag coefficient for air damping at location i

v: Velocity of the blade at location i

To apply these forces to the blade elements, a row of COMBIN14 elements was attached to the blade, for loading the flap- and lead-lag-wise direction separately (Figure J.1). To calculated the cross-wise area of the blade (A) the cord length was used for the flap-wise direction and the height of profile for the lead-lag-wise direction.

5.2.3 Validation of the FE Simulation

After adjusting the blade model [43], the discretization of the rest of the real test setup was added to the FE model. This includes two tuning masses which were attached to the real blade, the actuator to excite the flap-wise oscillation and the damping elements. The LINK11 element, representative for the actuator, was attached to the blade at ≈50% span-wise position. The simulation was performed for 60s. Three parameters were tuned:

1. The amplitude of the oscillation was iteratively adjusted, so that the flap-wise bending moment at 10% span-wise position was identical when comparing the real blade test bending moments with the FE analysis results.
2. The test excitation frequency was adjusted to fit the test bending moment distribution with as much accuracy as possible.
3. The material damping (ξ_i) was adjusted, so that the actuator force is comparable with reality.

The resulting range of bending moments in relation to the specified bending moments for the test is shown in Figure 5.4.

Which values for C_d and ξ_i are adequate is still not fully known. In Greaves (2013), a CFD analysis was performed for the flap-wise oscillation of a 1m wide blade at 1Hz and an amplitude of ±1m and ±2m . It was found that a quasi-steady condition was not given. C_ds of 5.3 and 4.45 were estimated for these unsteady conditions. For example, wake effects were given as a reason, because the blade moves back and forth, always hitting its own wake.

Because the test simulated in this work has a much higher amplitude and a lower frequency, generally lower C_d values were assumed in comparison to Greaves (2013), as the blade hits its own wake much later in time. Hence, in this work, two scenarios were calculated. For both scenarios, the material damping ξ_i was *not* used from measurements, but it was adjusted in such a way that the actuator force is comparable with reality. Where it is not clear what type of damping is present to what extent, the energy given by the measured actuator force has to be applied to the oscillating system and therefore has to be damped during the stable motion. Hence, a comparable amplitude of the sinusoidal force has to be reached in the FE analysis in comparison to reality as well.

---

[43] To adjust the FE discretization described in Section 5.3.1 with measurement data from a real natural frequency test, the mass of the pure blade model was adjusted by less than 1%, so that the first two flap-wise natural frequencies of the FE model and the real blade are similar to 1/10000Hz. The lead-lag-wise stiffness was linearly scaled, so that the first lead-lag-wise natural frequency of the FE model and the real blade are similar to 1/100Hz and the second lead-lag-wise natural frequency of the FE model and the real blade are similar to 3/100Hz.

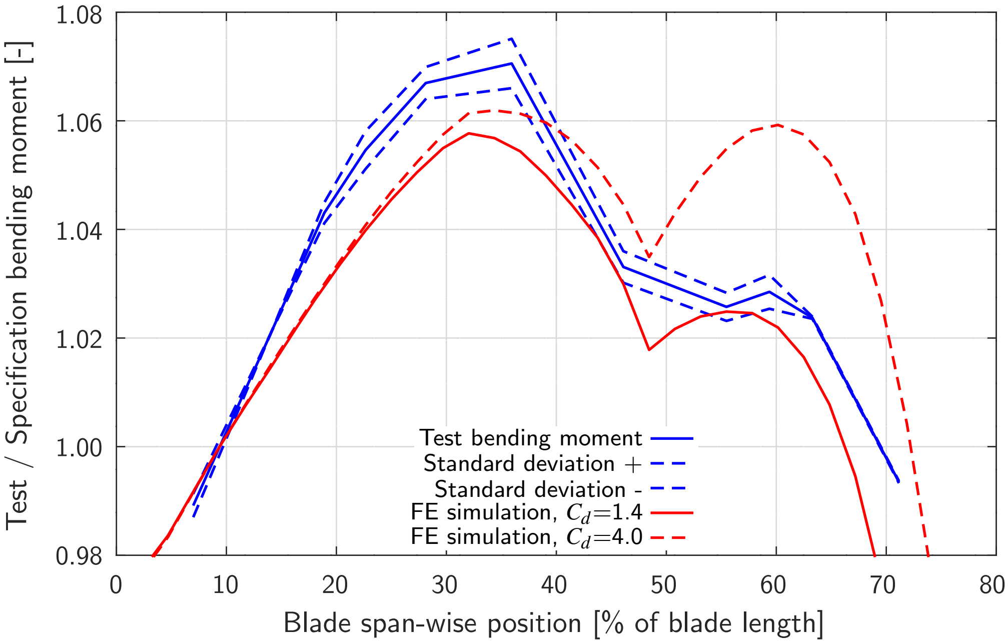

Figure 5.4: Comparison of a flap-wise bending moment measured at a real uniaxial dynamic fatigue test with the FE analysis of that test. The calibration test to determine the test bending moment was performed according to OM-I. The given standard deviation shows the deviation of four bending moment curves calculated by using different combinations of sensors (compare to Section C). The standard deviation is with $\leq$0.4% in the test region (abscissa $\geq$1) rather small.

Scenarios:

1. The aerodynamic damping is comparable to quasi-steady conditions. Usual blade C_d values were used. For the flap-wise direction, $C_d = 1.4$ was used and for the lead-lag-wise direction, $C_d = 0.2$ was used. The resulting bending moment is shown in Figure 5.4 "*FE simulation, C_d=1.4*".
2. The aerodynamic damping is slightly lower than determined in Greaves (2013) for unsteady conditions. For the flap- and lead-lag-wise direction, $C_d = 4.0$ was used. The resulting bending moment is shown in Figure 5.4 "*FE simulation, C_d=4.0*".

As shown in Figure 5.4, using $C_d = 1.4$ corresponds better to reality (difference in bending moment for $C_d = 1.4$ is $\leq$1.6% and $C_d = 4.0$ is $\leq$3.0%). But to achieve enough damping in order to have actuator forces that are comparable to the real test, a material damping ratio of $\xi_i = 0.0224$ had to be used for this calculation. In Lee and Park (2014), Lee and Park (2015), D. White (2004) and Chaviaropoulos et al. (2006) damping rations of 0.01 to 0.024 were found for a flap-wise blade fatigue test *including* air-damping. Still, when determining ξ_i with a free vibration test at small amplitudes, for the 1st flap-wise mode, $\xi_i = 0.0015$ (or lower) is typically measured for pure material damping, being ten times smaller than at the simulation. Hence other damping componants like the test-rig itself or the joints of the excitation mechanism must have a significant influence.

In case of $C_d = 4.0$, the actuator force is comparable using a ratio of $\xi_i = 0.0045$. This is still a significantly larger value than the one measured in free vibration tests. A better knowledge of drag coefficients related to blade shapes, test frequencies and test amplitudes seems necessary for planning tests more accurately, but has to be addressed in future work (Section 6.3). As a result, $C_d = 1.4$ and $\xi_i = 0.0224$ will be used for the simulation of the AMC method.

Coming back to the goal of achieving an accurate FE approach, only an absolute difference of $\leq$1.5% is observed in the test region (abscissa $\geq$1) when using $C_d = 1.4$.

Hence, a stable and reliable FE model is used because of the following two reasons: 1) Only very small changes of the blade model were necessary to hit the measured mass and flap-wise natural frequencies. 2) After including the loading mechanism elements in the first place (according to the measured geometry and the measured masses from the real test), no tuning of the setup was necessary to achieve the comparable results presented in Figure 5.4.

With less than 1.6% difference in bending moment it is concluded, that the FE model represents reality sufficiently to achieve reliable results when performing the following AMC simulations.

5.3 Active Mass Compensation (AMC)

In Section 5.1, the BEDEX method was explained. The major idea is to use the AMC method on one or more added weights (like load frames). The goal is to actively move the load frames sinusoidally parallel to the oscillating blade, so that the mass of the load frame will not influence the oscillation of the pure blade in that direction (fist described as *Virtual Mass* in Post and Bürkner (2019).

An FE simulation is used to demonstrate the AMC method (blade 9 of Table B.1). The FE model was validated in Section 5.2 and will be explained in Section 5.3.1. Simulation results will be discussed in Section 5.3.2.

5.3.1 Mechanical Setup and FE Model for AMC Simulations

Five different mechanical setups will be used to simulate the AMC method (setup 1 to 5). In Figure 5.5, all components of all setups are shown. A blade (b) of more than 60m length is fixed to a stiff test rig (a) at an angle of 7.5° to horizontal above the strong floor (c). The pressure side of the blade is facing upwards. Two bell crank mechanisms are attached to the blade at $\approx$50% and $\approx$90% of the blade in span-wise position. Each bell crank mechanism (k_v1 and k_v2) consists of a load frame, a push rod connecting the load frame and the lever arm, an actuator (e_v1 and e_v2) and a solid fixture of the lever arm at the end. The masses of the bell crank structures are located at the load frames (m_1 and m_2) and at the push rod end of the lever arm (m_3).

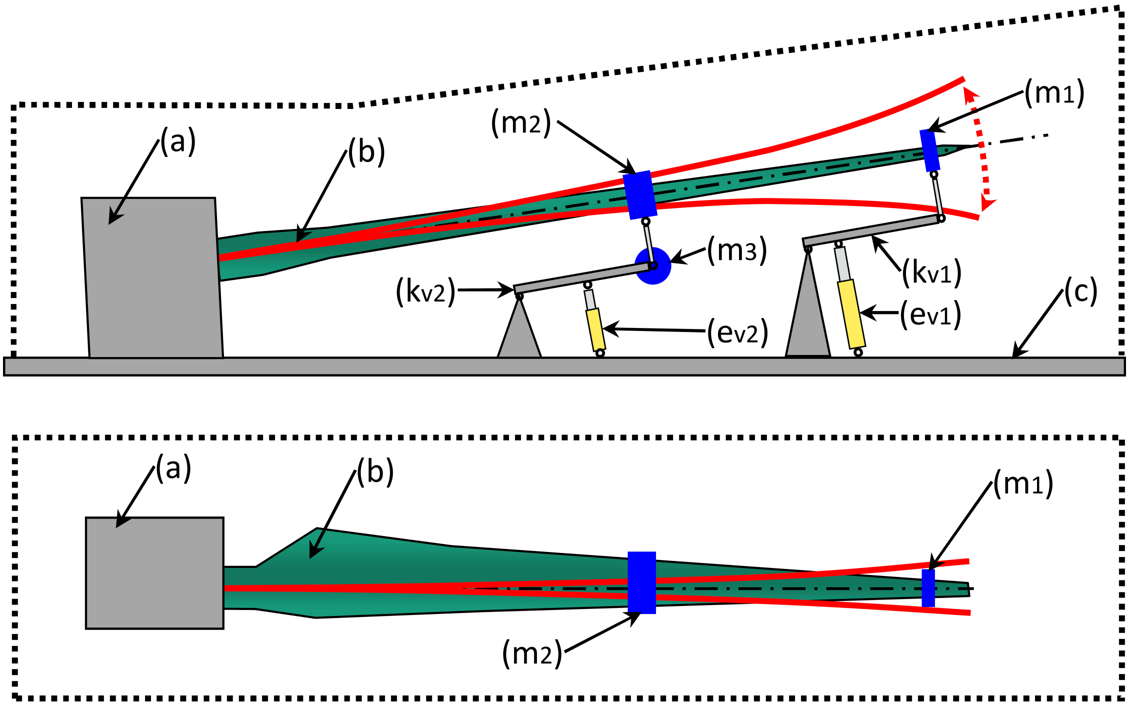

Figure 5.5: Test setup used to demonstrate the AMC method for the flap-wise test direction. The blade is loaded with one or two directly attached servo-hydraulic actuators using vertical bell crank mechanisms. Side view and top view. (a) Test rig; (b) Blade; (c) Strong floor; (e$_v$1) and (e$_v$2) Vertical actuators; (k$_v$1) and (k$_v$2) Bell crank systems for vertical loading; (m$_1$) to (m$_3$) Masses

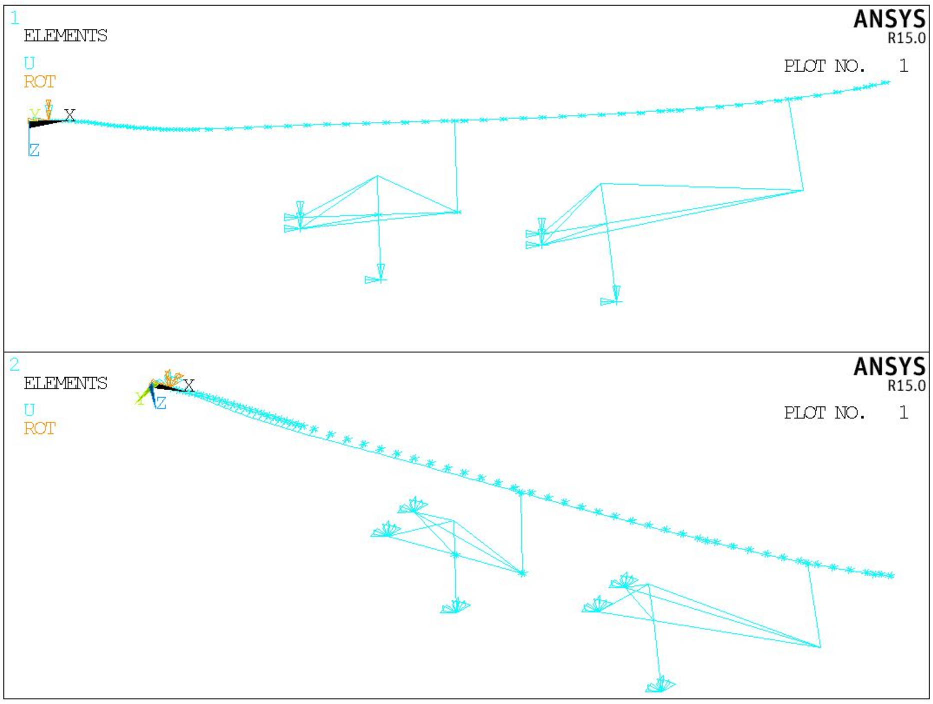

Figure 5.6: FEs model and boundary conditions of the blade and the excitation mechanisms. Top: Side view; Bottom: Overview.

The basic system is modeled according to the FE model described and validated in Section 5.2 including the damping approach. Additionally, the bell crank structures are modeled using very stiff LINK11 elements building an open-web girder and MPC184 elements for the joints (Figure 5.6 and Figure J.2). Secondary influences like friction of the bell crank joints or bending of the bell crank parts are not included in the analysis. The two pivot points of each bell crank structure and the base of the actuators were constrained against translational displacement but not against rotations. The FE code is exemplarily shown in Appendix K.3.

Sinusoidal forces were applied to the actuator element of the first bell crank, and a sinusoidal displacement was applied to the second bell crank. After a smooth ramp-up of the sinusoidal load for 50s, the oscillation was kept 10s at a constant amplitude for stabilization. Longer simulations were performed, but no significant change of the results was observed.

5.3.2 FE Simulations of AMC

As mentioned before, five different mechanical setups were used to simulate the AMC method (setup 1 to 5). All components of all setups are shown in Figure 5.5. The masses and natural frequencies for each mechanically different setup and each simulation are shown in Table 5.1. All setups are mechanically different. They are numbered from 1 to 5. Different simulations on each setup are numbered from a to d.

Table 5.1: Overview of different mechanical setups and FE analysis of the AMC method. The 1^{st} (flap-wise) natural frequency (NF) and the test or excitation frequency is given in relation to the natural frequency of setup 1. In the column 'Comment', the excitation frequency is specified (e.g. NF of 1 means the natural frequency of setup one).

Setup [-]	**Bell crank** [-]	**Mass 1** [kg]	**Mass 2** [kg]	**Mass 3** [kg]	**NF** [-]	**Test freq.** [-]	**Comment** [-]
1a	**2**	667	0	0	1.0	1.0	NF of 1
2a	**2**	667	900	0	0.993	0.993	NF of 2
2b	**2**	667	900	0	0.993	1.0	NF of 1
3a	**2**	667	900	900	0.9859	0.9859	NF of 3
3b	**2**	667	900	900	0.9859	0.993	NF of 2
3c	**2**	667	900	900	0.9859	1.0	NF of 1
3d	**2**	667	900	900	0.9859	0.9691	$\leq$NF of 3
4a	**1 and 2**	1167	900	900	0.8555	0.8555	NF of 4
4b	**1 and 2**	1167	900	900	0.8555	0.9859	NF of 3
5a	**1 and 2**	1167	1800	900	0.8512	0.9859	NF of 3

The goal of the analysis is to show that mass added at the location of an actuator can be compensated by the actuator in the way that the added mass has no influence on the loading of

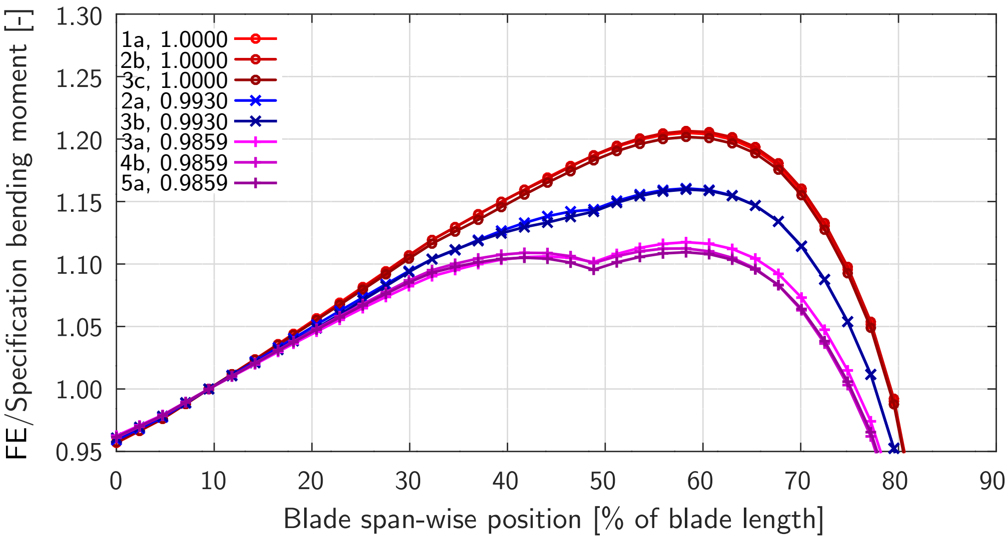

Figure 5.7: Resulting bending moment in relation to the specified bending moment. Simulations performed at the natural frequencies of setups 1, 2 and 3. In the legend, the number of the simulation and each specific test excitation frequency is given.

the blade in the actuator direction (AMC). The methodology is to compare the resulting bending moment distribution of dynamic fatigue tests using mechanically different systems but equal test excitation frequencies. The AMC concept is confirmed, provided that the loadings of those systems are identical.

Different mechanical systems - same frequencies - equal loading of the blade

All simulations shall have equal results in terms of the achieved test bending moment, if the same test excitation frequency is used, even with different mechanical setups. After completion of all transient analyses, the maximum and minimum bending moment of one cycle was read out for each node. The bending moment range was calculated for each node to be compared to the specification value at this span-wise position. The span-wise bending moment distributions of the specification and the FE analysis were scaled to 1 at 10% of the span-wise position[44].

In Figure 5.7, the bending moments of the FE analysis in relation to the specified bending moment are plotted for all simulations which were performed at the natural frequencies of setups 1, 2 and 3. Using the AMC method should lead to the same curves when using the same excitation frequency. With minor deviations of $\leq$1% , all curves for each excitation frequency can be considered as equal.

---

[44] The specified test load cannot be published. For this calculation, this is no drawback, as loadings of the blade will only be compared to each other. Using the difference of the test load to the specified load, the variations of loadings can be much better visualized.

For example, simulation 1a includes the blade and a mass of 667kg at ≈90% span-wise position. The excitation frequency is exactly at the natural frequency of the system (blade and mass). Simulation 2b was performed with an additional mass of 900kg at ≈50% span-wise position and simulation 3c with another 900kg at the same position. But as the excitation frequency was exactly like in simulation 2b, the additional masses were moved by the actuator parallel to the oscillation, not influencing the loading of the blade. The same behavior can be observed comparing simulation 4b and 5a. In this case, two locations with an AMC are present. The bending moment distribution is still comparable and no interaction between the two actuators loading the blade in the same direction was detected.

To move these extra masses sinusoidally, an additional force is needed in comparison to a pure natural frequency oscillation. But when comparing the actuator or push rod forces of the different simulations, the amplitudes are only slightly increased. The reason is, that the sinusoidal force to compensate masses is at around 90° phase shift to the sinusoidal force that is necessary to oscillate the blade against the air damping. When overlaying these two curves, the result is a sinusoidal curve with an only slightly increased amplitude. Hence, the compensation of at least small masses requires only slightly higher actuator forces in comparison to a test at pure natural frequency of the system. In Appendix H this phenomena is described with an example. To quantify the results of the simulations, the actuator an push-rod forces are discussed in Appendix I.

Same mechanical systems - different frequencies - different loading of the blade

Contrary to Figure 5.7, in Figure 5.8, the resulting bending moments of different mechanical systems excited at each natural frequency are shown (except for 3d). No AMC is used. This is shown to demonstrate how added masses usually influence the bending moment distribution of a blade at a dynamic fatigue test. In addition, the advantage of using a directly attached actuator in comparison to shaker systems shall be shown with simulation 3d.

Starting with 4a, the influence of the large weight at ≈90% of the blade length exceeds even the influence of the added weight at ≈50% of the blade length (Table 5.1). This results in a very high loading at around 60-70% of the blade length. When reducing the weight at ≈90% of the blade length and taking off the weight at ≈50% of the blade length, the overload of 1a is still significant at 60% of the blade length. When adding weights stepwise at ≈50% of the blade length, the overload can be reduced as shown with 2a and 3a. A minimum is generated at the position of the added mass.

If additional masses were added at ≈50% of the blade length, the curve could be lowered to the range of the given curve 3d. To avoid the handling of such big masses and to be able to adjust the effect of such masses by just changing parameters at the controller, curve 3d is the result of exciting setup 3 at a lower frequency than the natural frequency of the system. The additional loading at ≈50% of the blade length is generated by a quasi static actuator instead of the acceleration of added masses.

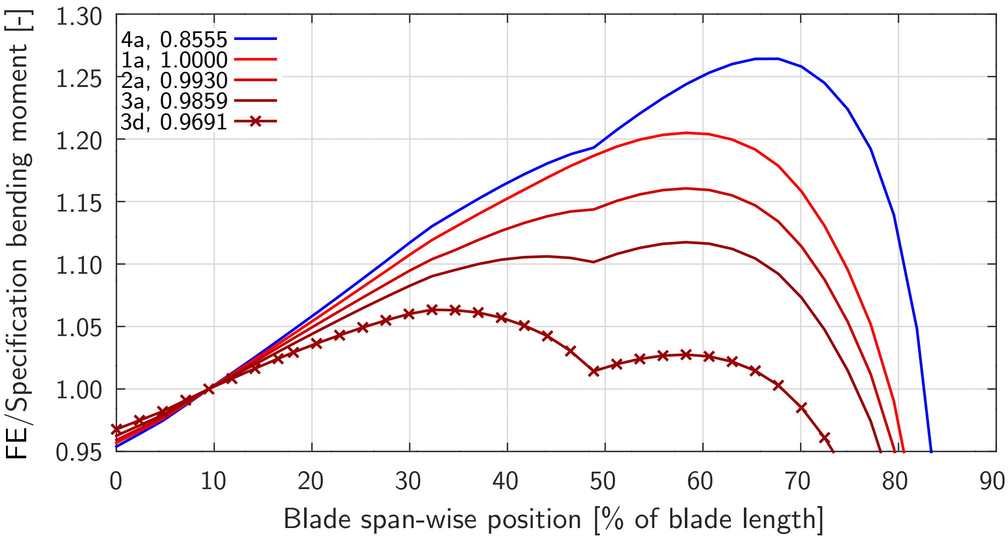

Figure 5.8: Resulting bending moments in relation to the specified bending moments. Simulations performed at the natural frequencies of setups 1, 2, 3 and 4. In the legend, the number of the simulation and each specific test excitation frequency is given.

5.4 FE Analysis of a Biaxially Loaded Blade

Before running an analysis simulating the full BEDEX method, the goal of this section is to prove that the FE analysis is sufficient to represent a biaxial loading of a blade adequately. Subsequently, the FE model of the excitation mechanisms shall be later used in Section 5.5 to simulate the BEDEX method.

The blade test described in Chapter 4 (blade 2 of Table B.1) will be simulated with a transient FE analysis[45]. As described in Chapter 3, the determination of the bending moment of a dynamic fatigue test is complicated resulting in quite high inaccuracies. Therefore, the deflection of the blade tip will be used to compare the FE analysis with the real test measurements.

5.4.1 FE Model

The mechanical setup of the blade test was described in Section 4.1. The blade is almost discretized as described in Section 5.3.1. Instead of BEAM189 elements, the cross-section data is used in combination with BEAM188 elements. Shear deformations of the beam elements are not included.

---

[45] For example in Desmond, White, and Barott (2009), a modal mode approach is used to simulate biaxial tests with satisfying accuracy. Because the BEDEX test does not operate in the 1st flap- and 1st lead-lag-wise natural frequency of the system, a full transient FE analysis was used (also concluded in Park, Park, Lee, Lee, and Lee (2011))

The mass of the blade is included by the density and cross-section parameters of the BEAM188 elements[46]. The setup without air damping elements is shown in Figure 5.9. The discretization of the air damping is performed as described in Section 5.3.1. The FE model including air damping elements is shown in Figure J.1. As described in Section 5.3.1 and Section 5.2, different damping parameters were used. The comparison of the results can be found in Section 5.4.2. The excitation mechanism and the actuators are again discretized with LINK11 elements as described in Section 5.3.1. The FE code is shown in Appendix K.4.

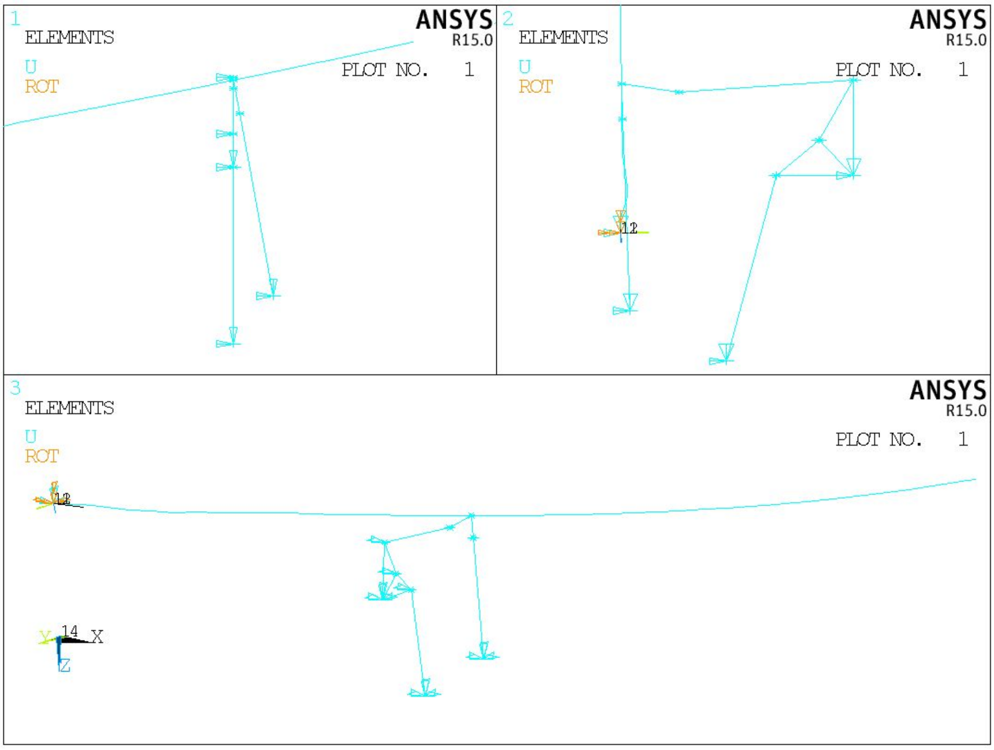

Figure 5.9: FEs model and boundary conditions of the blade and the excitation mechanisms. Top left: Side view; Top right: View from root to tip; Bottom: Overview

Because the mass and the natural frequencies were measured before performing the test with the blade, it is possible to compare these values with the results of a modal analysis of the FE model. The blade mass distribution and absolute mass was adjusted to equal the measured mass by less than ±1kg. The flap- and lead-lag-wise stiffness were adjusted, so that the 1st and 2nd natural frequency of the FE model is equal to measured frequencies to less than ±1/1000Hz.

After tuning the blade FE model as described and including the damping elements, the excitation mechanism was added to the model according to the geometry measured when performing the blade test. Furthermore, the excitation sinusoids for both actuators were included in the FE

---

[46] With increasing experience in modeling a blade in a damped biaxial oscillation, optimized beam elements might be used to include coupling effects as developed in Chortis, Chrysochoidis, and Saravanos (2007).

model using the exact frequencies of the blade test. Only the actuator amplitude and the material damping was adjusted, so that the results are comparable with reality. No change or adjustment of the excitation system, masses, shape of the loading curve or the test frequency was done.

5.4.2 Validation of the FE Simulation

Two different scenarios of air and material damping parameters were used (as described in Section 5.3.1), because it is not known which parameters are correct. Because the biaxial blade deformation could be measured accurately with an optical 3D measurement system, the simulation of this test was performed for an additional scenario of damping parameters, trying to understand which damping parameters describe the complex movement best. Hence, three scenarios were calculated:

1. Assuming quasi-steady air flow conditions: $C_d = 1.4$ and $C_d = 0.2$ for the flap- and lead-lag-wise direction. The material damping ξ_i is lifted, so that the actuator force is comparable to reality ($\xi_i = 0.0407$) Figure 5.10.
2. Assuming unsteady air flow conditions: $C_d = 4.0$ according to Greaves (2013). The material damping ξ_i is lifted so that the actuator force is comparable to reality ($\xi_i = 0.0132$) Figure 5.11.
3. Assuming unsteady air flow conditions: $C_d = 4.0$ according to Greaves (2013). The material damping typically measured for comparable glass-fiber reinforced plastic blades is used ($\xi_i = 0.0015$) Figure 5.12.

The results of all three simulations 1, 2 and 3 are shown in Figure 5.10, Figure 5.11 and Figure 5.12. The displacement of the blade tip is plotted from the measured data of the test and the FE analysis results[47]. For the first two simulations, the material damping was lifted to get representative actuator forces. For simulation 1 (quasi-steady condition), the material damping had to be 27 times of the usual measured value of $\xi_i = 0.0015$. For simulation 2 (unsteady condition), the material damping had to be 9 times of the usual measured value of $\xi_i = 0.0015$. In case of $\xi_i = 0.0015$ at simulation 3 (unsteady condition), the amplitude of the actuator force is only half of what is necessary in reality.

---

[47] To be able to compare both curves, four parameters were adjusted in the FE analysis (amplitudes and mean values). The amplitudes of the flap-wise and lead-lag-wise actuator excitation sinusoids were adjusted, so that the horizontal and vertical displacement range of the FE results is equal to the measured displacements. Because the location of the blade tip before loading the blade had different absolute coordinates for the measured values with regard to the FE results, the whole FE curve was shifted horizontally and vertically to be comparable. These four parameters were adjusted, as they have no influence on the comparability of the two results. This was necessary, as the amplitude parameters used for the hydraulic controller at the real test do not represent the absolute amplitude of the actuator, the amplitude of the *FE actuators* had to be adjusted to hit equal displacements.

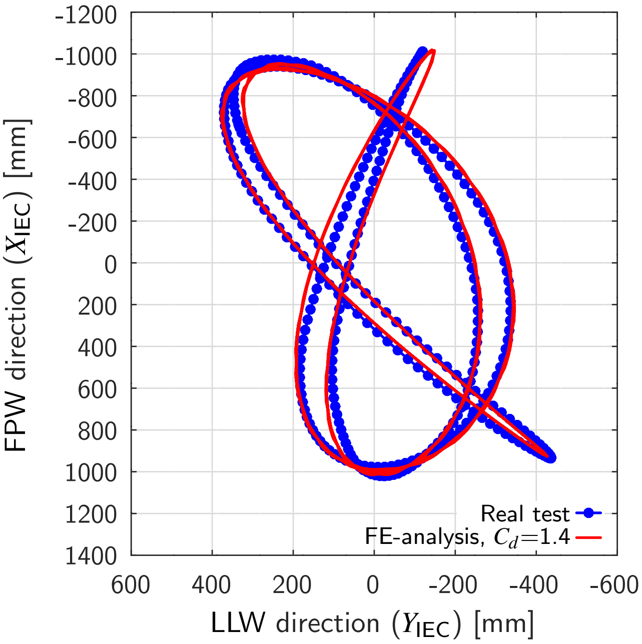

Figure 5.10: Movement of the blade tip when loading the blade at the 1st and 2nd natural frequency (flap- and lead-lag-wise natural frequency). Measured values compared to simulation results (C_d=1.4, $\xi_i = 0.0407$). View from root to tip. The horizontal axis is in Y_{IEC} direction and the vertical axis is in X_{IEC} direction.

Regarding the damping parameters, it can be concluded that simulation 1 represents reality in terms of the blade tip movement most accurately. Having a higher air damping leads to relatively good matching curves as well, but the material damping is still much higher (9 times) than what is usually determined in a free vibration test. Using material damping parameters determined at free vibration tests, even when having the high drag coefficients determined in Greaves (2013), a quite different blade movement in terms of the phase of both directions is present at simulation 3.

As concluded in Section 5.2.2, for the BEDEX simulations the quasi-steady condition with $C_d = 1.4$ and $C_d = 0.2$ is used for the flap- and lead-lag-wise direction.The material damping will be set to $\xi_i = 0.0407$. The large difference to typical material damping parameters must be caused by other damping componats like the joint of the excitation mechanisms or the test-rig itself. Except for small differences, the curves do match quite precisely. Hence, the excitation mechanism and the excitation sinusoids do represent reality sufficiently when using this type of FE discretization. It is assumed that using other geometries of comparable excitation mechanisms will sufficiently represent reality.

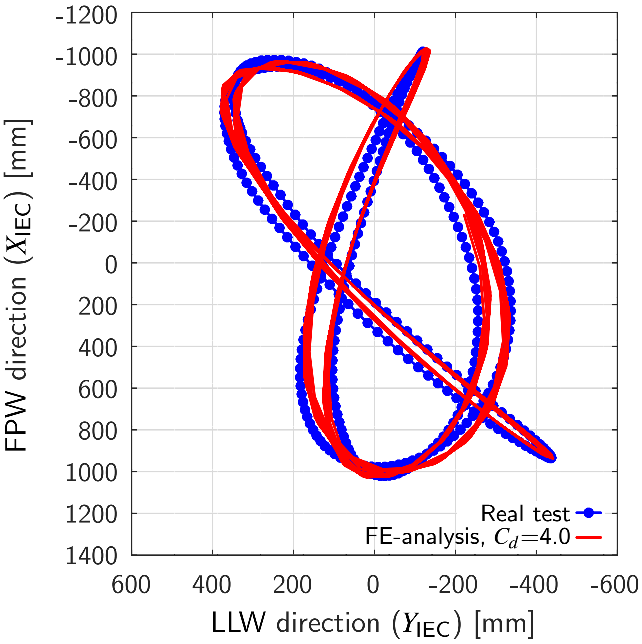

Figure 5.11: Movement of the blade tip when loading the blade at the 1st and 2nd natural frequency (flap- and lead-lag-wise natural frequency). Measured values compared to simulation results (C_d=4.0, ξ_i=0.0132). View from root to tip. The horizontal axis is in Y_{IEC} direction and the vertical axis is in X_{IEC} direction.

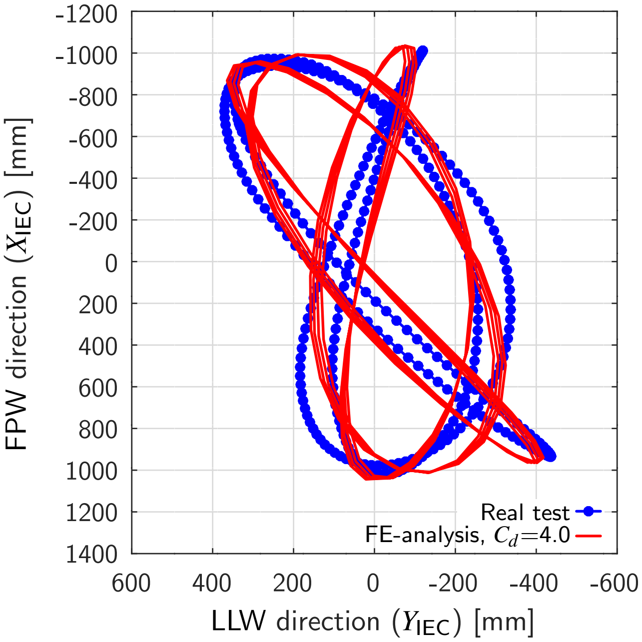

Figure 5.12: Movement of the blade tip when loading the blade at the 1st and 2nd natural frequency (flap- and lead-lag-wise natural frequency). Measured values compared to simulation results (C_d=4.0, ξ_i=0.0015). View from root to tip. The horizontal axis is in Y_{IEC} direction and the vertical axis is in X_{IEC} direction.

5.5 FE Analysis of a BEDEX Test

In this section, an transient FE analysis will be performed to exemplary show the methodology of the BEDEX test method. According to the approach described at the beginning of this chapter, the goal is to shown the BEDEX working principle, even though it has not been possible to perform a real BEDEX test yet.

5.5.1 Analysed Mechanisms

In Figure 5.2, the analyzed setup is shown. The blade of approx. 65m (blade 9 of Table B.1) length (b) is horizontally fixed to a stiff test rig (a)[48] above the strong floor (c). The pressure side of the blade is faced upwards. Two bell crank mechanisms are attached to the blade at ≈50% and ≈80% of the blade length. Each bell crank mechanism (k_v or k_h) consists of a load frame, a push rod connecting the load frame and the leaver arm, an actuator (e_v or e_h) and a translational fixture of the lever arm at the end. The masses of the bell crank structures are located at the load frames (m_2 and m_3) and at the push rod end of the lever arm (m_4) for the horizontal bell crank mechanism (k_h). An additional tuning mass (m_1) is located at ≈90% of the blade length. The advantages of this setup are described in Section 5.1.4.

An optimization of the bell crank dimensions was not performed. It was tried to chose rather large dimensions to minimize secondary influences due to the change of the push rod angle to the blade at biaxial movements. Still dimensions were used which can be achieved in reality. As shown in Figure 5.2, the horizontal bell crank has a 12m long lever arm and a 7m long push rod. The vertical bell crank has a 15m long lever arm and a 7m long push rod. It is assumed that the dimensions at least of the horizontal bell crank structure can be significantly smaller. The goal was to find out, if the loading of the blade is comparable to uniaxial tests with reasonable dimensions of the bell crank system. By optimizing bell crank dimensions and desired test bending moments, the bell crank dimensions can be decreased.

5.5.2 FE Model

To achieve comparable results, the FE analysis described in Section 5.4.1 is used for simulating the BEDEX excitation mechanic. The FEs excluding the air damping elements and boundary conditions are shown in Figure 5.13. The air damping elements are shown in Figure J.3. The FE model of blade 9 Table B.1 is used for this simulation. The FE code is shown in Appendix K.5. In Section 5.2 it was possible to tune this FE blade model nicely to reliable measured data with

---

[48] Figure 5.2 shows a setup for a real test, where a certain angle of the blade to horizontal is necessary to have enough space underneath the blade tip for placing a bell crank structure. Because this does only increase the complexity of the FE analysis, the blade was oriented horizontally at the root. No significant change of the results is expected.

regard to the blade mass and the blade natural frequencies. Looking at the resulting overloads at mid-span, it has to be mentioned that an intense tuning of the BEDEX test to minimize overloads was not performed and has to be addressed in future work (Section 6.3).

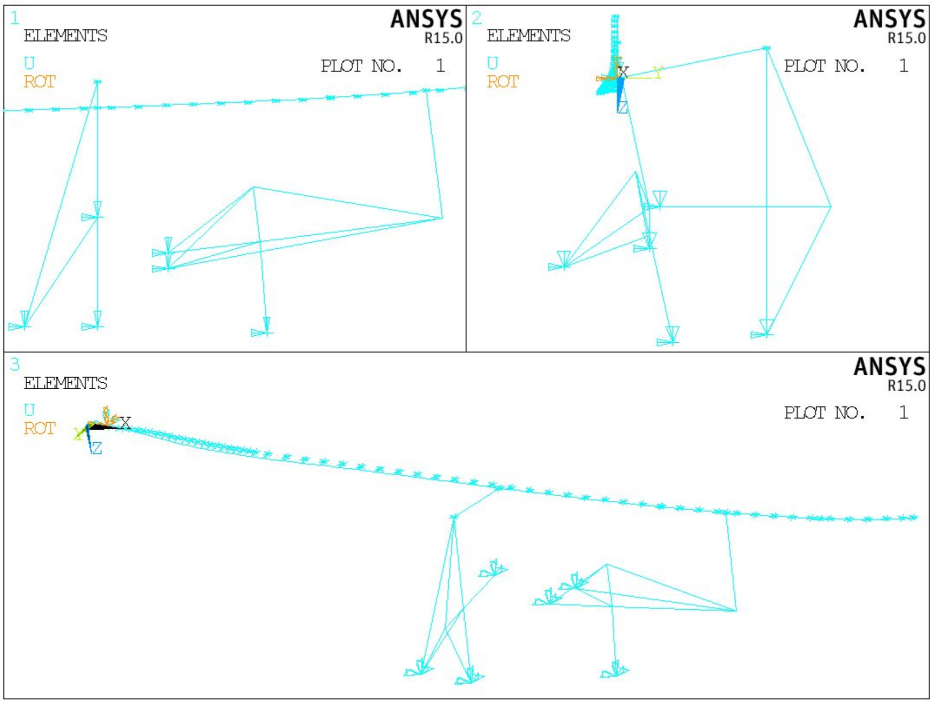

Figure 5.13: FE model of a BEDEX test simulation and boundary conditions of the blade and the excitation mechanisms excluding air damping elements. Top left: Side view of excitation mechanism; Top right: View from the root of the excitation mechanism; Bottom: Overview

5.5.3 Tuning

The mechanical setup described in Section 5.1.4 is used to describe a basic tuning procedure pursuing to the following steps:

1. **Tuning the flap-wise direction with uniaxial loadings:** The minimum mass necessary at ≈90% of the blade length (m_1 of Figure 5.2) was determined to achieve a compromise between the test frequency getting slower and the loading at the tip region getting too low (a mass of 550kg was determined). Additionally, the mass at ≈50% of the blade length (m_3 of Figure 5.2) was defined in such a way that the overload at mid-span is reduced as much as possible (a mass of 3000kg was determined). The test frequency or excitation frequency is the 1st or flap-wise natural frequency of the blade including these two masses. For all BEDEX test excitations, this frequency is used for all actuators (in flap- *and* lead-lag-wise direction).

2. **Tuning the lead-lag-wise direction with uniaxial loadings:** The idea of the BEDEX method is, that all masses necessary to load the lead-lag-wise direction, but not necessarily the flap-wise direction, need to be compensated in order *not* to have an influence on the flap-wise direction. This can be achieved by two methods: A) Additional masses have to be compensated by the AMC method described in Section 5.3. This method allows masses to be placed as far outboard as necessary to achieve a sufficient loading in lead-lag-wise direction. The AMC method is used, because a typical bell crank mechanism can be chosen even though having large deflections of the blade at the mass location. B) At locations where the flap-wise amplitude is lower, additional masses can be attached to the blade by using push rods oriented in lead-lag-wise direction. Additionally, a mechanism supporting the gravity force of the mass, but allowing a movement in lead-lag-wise direction, needs to be used. Several systems are possible to fullfill these requirements. Typical mechanisms are bell crank mechanisms (Malhotra (2010)) or masses on roller tables (Greaves (2013) and Malhotra (2010)). Because a bell crank mechanism was used for this test, a mass (m_4 of Figure 5.2) was attached to the leaver arm of the bell crank (k_h).

   Using both described methods, two additional masses are attached to the blade at ≈50% of the blade length and ≈80% of the blade length, which only apply loads in the lead-lag-wise direction. The oscillating system in lead-lag-wise direction consists of the blade plus the four masses (m_1) to (m_4) shown in Figure 5.2. The tuning of the lead-lag-wise direction can only be performed by changing the two masses (m_2) and (m_4). The masses (m_1) and (m_3) must not be changed, in order not to change the tuning of the flap-wise direction again. Because the excitation frequency is given by the tuning of the flap-wise direction, as explained before, the test loadings of the lead-lag-wise direction have to be performed at exactly this frequency. This does influence the determination of masses (m_2) and (m_4) as well, as a significant dynamic loading in lead-lag-wise direction can only be achieved, if the 1st natural frequency of the blade plus (m_1) to (m_4) in lead-lag-wise direction is close to the defined excitation frequency. When using 1820kg for (m_2) and 6000kg for (m_4), the loading is adequate for a certification blade test and the natural frequency in lead-lag-wise direction is close enough to the defined excitation frequency by the flap-wise direction.

3. **Adjusting the amplitudes at the biaxial loading:** After tuning of the flap- and lead-lag-wise direction, both loadings were applied at the same time to simulate a BEDEX test. Only the amplitudes of the excitation sinusoids were adjusted to achieve the desired loading in both directions. Having two sinusoids to load actuator 1 and 2, the phase of the lead-lag-wise to the flap-wise loading had to be set. Where principally all phases are possible, most likely a phase of 90° to 100° might be used to load the blade in flap- and lead-lag-wise direction exactly one after another[49]. In D. White (2004), an optimized phase of 72° was determined, when the phase of the loading has to be as close as possible to the phase of the loading of the blade at the real turbine. In this work, 100° was used to create

---

[49] The theoretic value of 90° most likely has to be adjusted, because the geometry of each excitation mechanism will lead to a slight shift of the phase between loading sinusoids and blade movement.

a test which matches most closely the usual situation of performing two uniaxial dynamic fatigue tests separately (uniaxial dynamic fatigue tests one after another).

5.5.4 Simulation Results

In Figure 5.14, the resulting bending moments in flap-wise and lead-lag-wise direction of the BEDEX test are plotted as *BEDEX test flap-wise* and *BEDEX test lead-lag-wise*. Both bending moments are given as the quotient of the simulation bending moments over the specified test bending moments for this blade. As mentioned in Section 5.5.3, the loading of the actuator elements determined at the flap-wise and the lead-lag-wise tuning was only adjusted by changing the amplitude. Still, pure sinusoids were used to load the blade in both directions.

To analyze how much the bending moments have changed by loading the flap- and lead-lag-wise bell crank structure at the same time, in Figure 5.14, the resulting bending moments of flap- and lead-lag-wise tuning are plotted as *BEDEX loaded only flap-wise* and *BEDEX loaded only lead-lag-wise*. When comparing the two curves for each test direction, it becomes clear that the loading is almost similar (difference flap-wise $\leq$0.8% , lead-lag-wise $\leq$1.9%). Of course this behavior does change with the bell crank structures decreasing in size. Especially using shorter push rods changes the loading angles significantly. How much of this change still leads to acceptable loadings of the blade needs to be addressed in future work (Section 6.3).

To evaluate the feasibility of the BEDEX test in comparison to two dynamic fatigue tests performed separately, two simulations were used for comparison. Because the flap-wise direction was already simulated and tested, the resulting bending moment curve is used as an example for a uniaxial flap-wise dynamic fatigue test. These results include an optimization of the bending moment by adjusting the location and the weight of added masses. To be able to compare the lead-lag-wise blade loading of the BEDEX test with a uniaxial lead-lag-wise dynamic fatigue test, a separate simulation for this direction was performed. Again, an optimization of the bending moment by adjusting the location and weight of added masses was performed. In Figure 5.15, the four resulting bending moments are plotted over the blade span.

It was tried to use representative uniaxial tests. The time needed for the tests shall be as short as possible. To achieve this, even higher overloads are sometimes accepted. The uniaxial lead-lag-wise dynamic fatigue test is tuned in a way that a minimum amount of added masses is used to perform the test as fast as possible. At the same time, the overload shall usually not exceed 25%. The result is shown in Figure 5.15, the test frequency is 1.539 times higher than the BEDEX test frequency. The overload is just below 25%. Comparing the uniaxial and biaxial lead-lag-wise loadings, the difference of the overload becomes clear. Besides an almost 5% reduction of the maximum overload, the span-wise range of high overloads is also reduced at the BEDEX test. In case the uniaxial test is performed with more added masses and a lower test frequency, the testing time and overloads in lead-lag-wise direction approximate the BEDEX test, but the testing time is increased.

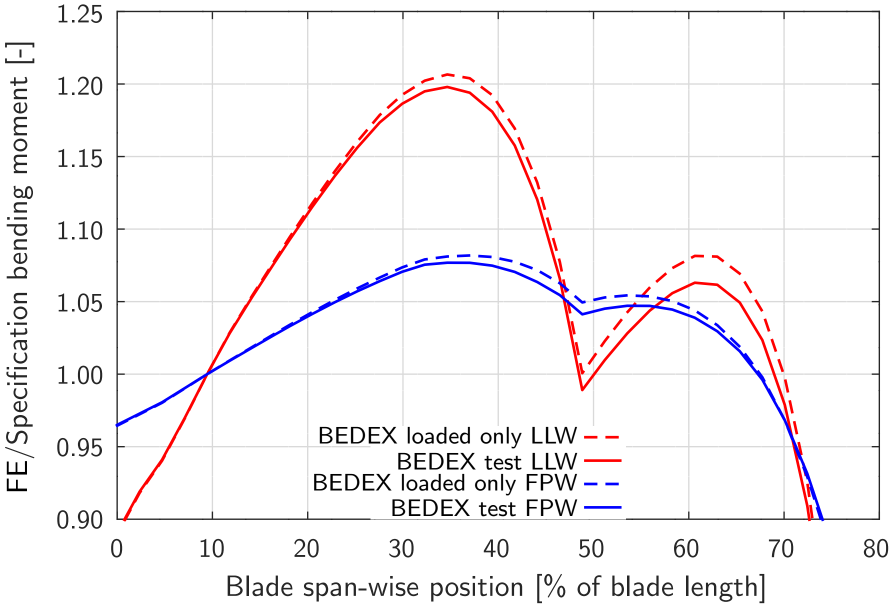

Figure 5.14: Flap- and lead-lag-wise bending moments of a BEDEX test compared with the bending moments if only loading one direction of the same test setup (exciting flap- and lead-lag-wise actuator separately). Applied bending moments in relation to the specified bending moment.

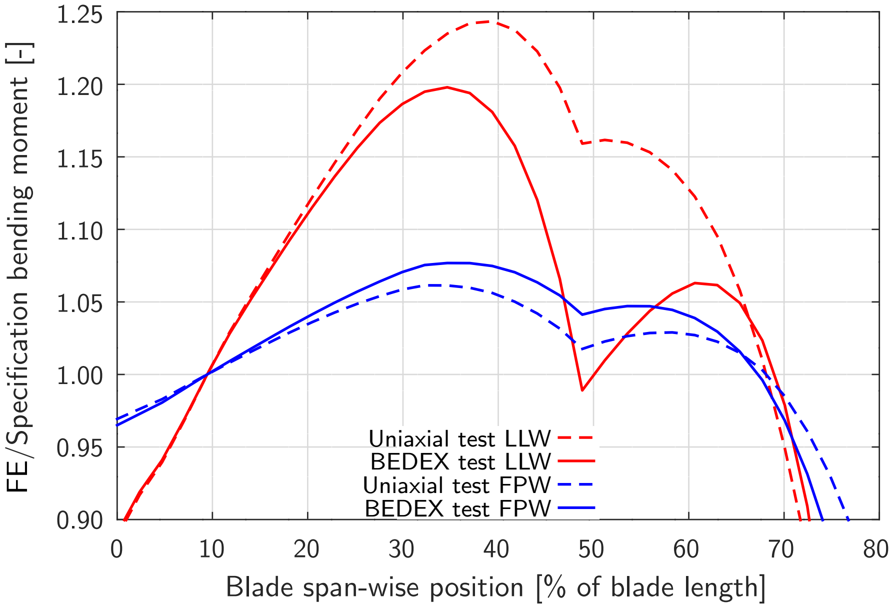

Figure 5.15: Flap- and lead-lag-wise bending moments of a BEDEX test compared with the bending moments if the blade is tested with two standard uniaxial tests. Applied bending moments in relation to the specified bending moment.

The results of the uniaxial flap-wise dynamic fatigue test with the flap-wise direction of the BEDEX test is also shown in Figure 5.15. With $\leq$2.3% difference the bending moments are almost comparable. In this case, the uniaxial test was tuned to have minimum overloads.

To picture the BEDEX movement, in Figure 5.16, the movement of the blade tip is shown for only exciting the flap-wise or lead-lag-wise direction and when exciting the blade according to a BEDEX loading. As explained before, a phase of 100° was chosen, but all other phases can be used as well.

Besides a comparison of the BEDEX loading to *usual* flap- and lead-lag-wise dynamic fatigue tests as shown before, every loading in flap-wise direction, which is possible for a uniaxial dynamic fatigue test, can be achieved with a BEDEX test as well. The testing frequency and therefore the testing time for this direction would be equal. In lead-lag-wise direction *not* every loading can be achieved at a BEDEX test in comparison to a uniaxial dynamic fatigue test, because masses have to be added to bring the 2^{nd} or lead-lag-wise natural frequency of the system down to the 1^{st} or flap-wise natural frequency. On the other hand, additional masses are usually needed in a uniaxial lead-lag-wise dynamic fatigue test anyway to decrease overloads in this direction. Hence, comparing the lead-lag-wise direction for both test methods, either a higher overload has to be accepted or a longer testing time.

5.5.5 Testing Time and Costs of a BEDEX Certification Test

The evaluation performed in this chapter is based on the project management experience of blade tests performed at Fraunhofer IWES. Time and costs are compared for a *standard*[50] test program and the same test when substituting the two separate uniaxial dynamic fatigue tests with one BEDEX test. Three different blade length with a low, medium and a high number of fatigue cycles are used. In Table 5.2, the reduction of time and costs when using a BEDEX test is listed.

According to Table 5.2, the reduction of the time needed for a *full certification test* is around 20%. When comparing BEDEX to a uniaxial test with a large number of flap-wise cycles, the reduction is 30% or more. Of course, the reduction of the *pure fatigue testing* time is higher and can be more than 40%. The reduction of the test cost can be quite different for various testing laboratories, assuming quite different labor, material, energy or maintenance costs. With an estimated reduction of 4% to 13% , a BEDEX test will not be more expensive than two separate uniaxial dynamic fatigue tests.

---

[50] Standard test program includes: 100 strain gauges, five load frames, adapters, measurement of the blade dead weight, natural frequency analysis, four pre-fatigue static tests, two uniaxial dynamic fatigue tests, five calibration tests for each direction, four post-fatigue static tests

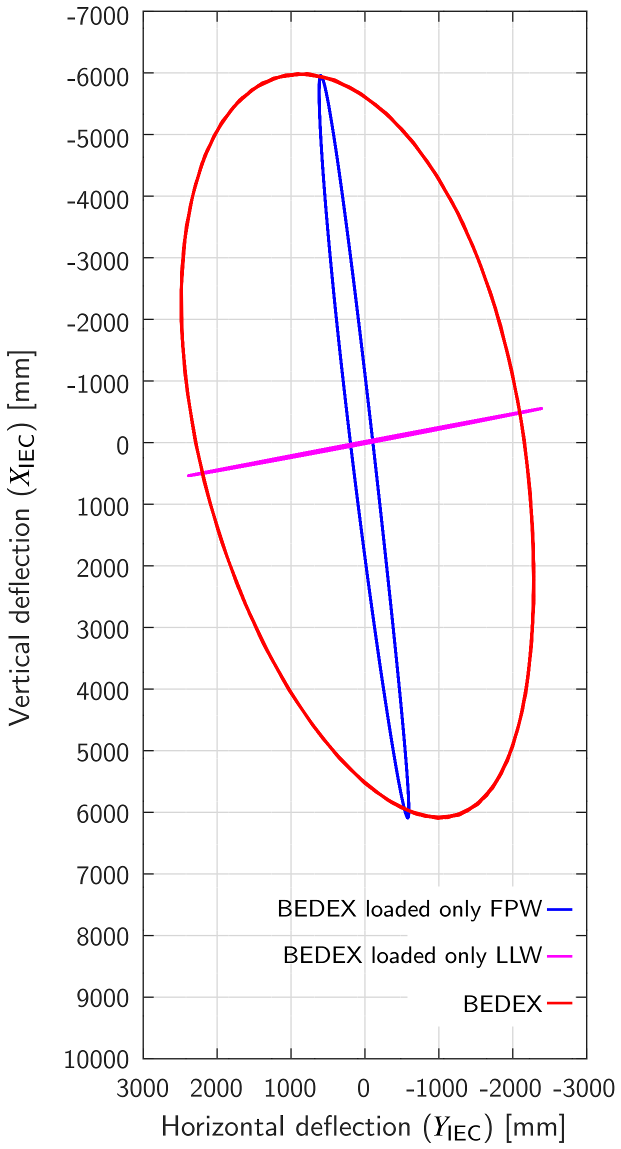

Figure 5.16: Simulated blade tip movement when loading the blade with a BEDEX mechanism in flap- and lead-lag-wise direction separately or simultaneously. View from root to tip. The horizontal axis is in Y_{IEC} direction and the vertical axis in X_{IEC} direction.

Table 5.2: Reduction of time and costs when using a BEDEX test instead of two separate uniaxial dynamic fatigue tests in flap- and lead-lag-wise direction.

Blade length [m]	Cycles flap-wise [-]	Cycles lead-lag-wise [-]	Time full test [%]	Time fatigue test [%]	Cost full test [%]
40	1.00E+06	1.50E+06	-20	-35	-7
40	1.50E+06	3.00E+06	-14	-21	-5
40	3.00E+06	3.00E+06	-27	-37	-11
60	1.00E+06	1.50E+06	-21	-35	-7
60	1.50E+06	3.00E+06	-16	-22	-5
60	3.00E+06	3.00E+06	-29	-39	-11
80	1.00E+06	1.50E+06	-19	-29	-4
80	1.50E+06	3.00E+06	-19	-24	-6
80	3.00E+06	3.00E+06	-34	-42	-13

5.6 Conclusions of AMC and BEDEX Test

By adding masses, the natural frequency in lead-lag-wise direction will be lowered to be equal to the flap-wise direction without these masses. The compensation of the masses in flap-wise direction will be achieved by the developed AMC method: If the excitation of a system is performed at a frequency higher than the natural frequency of the blade including attached masses, the blade oscillates as if such masses are not attached. It is necessary that an actuator is positioned at locations where such compensation shall be performed. How much the masses shall be compensated by the AMC method can be adjusted by varying the excitation frequency. The AMC method also works, if two actuators or bell cranks are used along the blade span. It is beneficial that due to the phase shift between excitation and compensation forces the amplitude of the combined force is often only slightly increased.

When reducing the lead-lag-wise natural frequency to the flap-wise frequency using AMC, a biaxial elliptical dynamic oscillation of the blade can be achieved to test the blade in fatigue (BEDEX). A tuning of the bending moment distribution in span-wise direction is still possible. A minimum of two servo-hydraulic actuators and bell crank structures is needed to perform the test.

Because of the dynamic loading, the energy needed for the test is rather low. A more realistic loading in comparison to two separate uniaxial tests in flap-wise and lead-lag-wise direction is applied, because most areas of the blade cross-sections are loaded adequately for testing. The potential to save testing time in comparison to two uniaxial tests is approximately 20% to 30% of the whole blade test program.

Chapter 6

Conclusions

Due to the good fatigue behavior of glass- or carbon-fiber reinforced plastics, fatigue testing of blades requires significant strain amplitudes and a large cycle number. According to the standards, design assumptions are tested, *not real loads*. Principally, quasi-static and dynamic loadings are suitable for testing blades in fatigue. But with blades growing in length, only dynamic loadings will result in acceptable (low) testing times and costs in industrial applications.

Since the determination of the applied loading of dynamic fatigue tests is currently very inaccurate, optimization methods were developed to reduce inaccuracies and uncertainties by a factor of four, thus staying blow $\pm1.5\%$ for the inner 70% of the blade span. Sometimes, a nonlinear behavior at specific locations of the blade leads to quite inaccurate determination of the applied bending moment as well. A method not requiring additional testing was developed to achieve correct results.

The AMC method was intended to keep the 1st natural frequency (flap-wise direction) unaffected when tuning the 2nd natural frequency of the blade (lead-lag-wise direction) to be close to the 1st natural frequency at a biaxial dynamic fatigue test. Masses attached to the blade, which only influence the 2nd natural frequency, are used to achieve this behavior. The BEDEX test was created, where the blade can be excited dynamically in an elliptical motion. When loading the blade biaxially and elliptically, the flap- and lead-lag-wise direction can be tested at the same time without increasing the test load in comparison to the usual two separate uniaxial dynamic fatigue tests. Furthermore, due to the combined loading of the flap- and lead-lag-wise direction, the most realistic loading is applied to the blade and an optimized phase can be chosen for the test as well. With the intended mechanism, masses for the AMC method can be applied even at the blade tip region, which is not possible in a practical manner using present mechanisms. The blades can then be tested in lead-lag-wise direction to almost any extent in span-wise direction.

Since the blade loading of the BEDEX test is more realistic in comparison to turbine loads, the risk of missing problems in the blade design which occur at the turbine but not in the test, is reduced. As the loading of the blade in the test can now be determined much more precisely, the risk of having an unaware under- or overloading of the blade at the test is reduced significantly. This will help the OEM to avoid an over- or underestimated blade design.

The benefit for the OEM is given by shortening the innovation loop of the blade development, because the overall testing time is reduced by approximately 20% to 30%. The results of the fatigue tests are also earlier available. Adjustments of the blade design can be earlier initiated, which even might change the serial production of blades.

6.1 Contribution to the State-of-the-Art

The most critical inaccuracies and uncertainties of the existing calibration methods were analyzed.

A method to detect and compensate local nonlinear strain over bending moment behavior at specific blade locations was describe. This allows a correction of the linearly determined test bending moment for the nonlinearity just by additional post-processing of the measurement data, but without additional testing.

To take large deflections effects at flap-wise calibration tests into account, a method based on the determination and adjustment of an ideal calibration load angle was developed (OM-I). To further increase the accuracy of the applied calibration test loading, an extended method is developed (OM-II), hanging a calibration mass onto the blade to perform a flap-wise calibration test and a simplified numeric simulation to determine the exact loading along the blade span.

With performing a biaxial dynamic test of a 40m long blade it was shown for the fist time, that a precise and controlled oscillating of the blade at the first flap- and lead-lag-wise natural frequency is possible with directly attached servo-hydraulic actuators.

A loading method was developed allowing a biaxial dynamic *and* elliptical motion of blades. With using favorable control capabilities of servo-hydraulic actuators in combination with a *vertical* bellcrank mechanism, a larger length-wise region of the blade can be loaded appropriately. Disadvantages of either large hall space or the necessity of extremely lightweight bellcrank structures are not limiting the method. A requirement for this method was the development to actively compensate masses attached to the blade with the servo-hydraulically driven bell-crank structures.

6.2 Recommendations

It is recommended to perform the calibration test and the required post-processing for all dynamically performed fatigue tests according to the list below:

1. Determine the uncertainty of the strain gauge measurement with trial loadings for the actual test (Section 3.1.1).
2. Perform a flap- *and* lead-lag-wise calibration test according to Section 2.1.2. The determination of the calibration factors should be performed, using only the zero-load strain and the full-load strain measurement at a calibration test according to Section 3.1.1. As recommended in Papadopoulos et al. (2000), ideally a torsional calibration should be performed

additionally to include the torsional cross-talk terms. Shear forces and axial forces may be neglected.

3. The bending moment should be determined for all combinations of sensors to calculate an average value for each cross-section from all combinations (Section 2.1.2).
4. All strain gauges used for the calibration should be checked against geometric nonlinearities and corrections should be calculated, if required (Section 3.2).
5. Ideally, option (a) of the list below should be used for the flap-wise direction. Otherwise option (b) or (c) apply:
   a) Use the OM-II method for the flap-wise direction with a dead weight loading (Section 3.4.2).
   b) Use OM-I for the flap-wise direction by adjusting the tilt of the test rig and in combination with a dead weight loading.
   c) Use OM-I for the flap-wise direction to optimize the pulling location. (Section 3.4.1).
6. For the lead-lag-wise direction, OM-I should be used (Section 3.4.1).
7. It is recommended to measure the span-wise position of all strain gauges as accurately as possible and to focus on this issue in future work (Section 3.1.2).

Due to a more realistic loading and a significantly decreased testing time, the developed BEDEX test method is recommended. No increase of overloads or costs are expected. Due to the complexity and various tuning possibilities, an adequate FE simulation is recommended in order not to loose any time in the testing laboratory while performing the test.

The most beneficial BEDEX setup determined in this work is shown in Figure 5.2. Just two bell crank systems are needed to have two locations for masses available to tune the lead-lag-wise natural frequency and the lead-lag-wise loading accurately.

Especially if performing segment blade tests in the future, the BEDEX method will save time and energy, but still allows an ideal loading in regard to the test purpose.

With exceeding 100m of blade length, most test halls become to short. To find feasible test options for these long blades, research is performed on testing blades in segments. If the blade is, for example, divided in an inner part (0-65m) and an outer part (40-100m), the BEDEX method might work particularly well to test the inner part biaxially with gaining the described advantages of the method.

6.3 Future Work

In Section 3.2, a method is described how to improve calibration tests if a local nonlinear strain to bending moment behavior occurs at a blade. Test beams showing such behavior should be built and tested for validation. Parallel FE shell models need to be analyzed to learn how far such a behavior is predictable before starting the test.

The OM-II described in Section 3.4.2 was validated against FE models only. Tests need to be performed, where the bending moment of the specimen is exactly known, in order to be able to validate OM-II against reality.

The following tasks should be addressed to optimize the theoretically developed BEDEX test (Chapter 5):

- Development of an optimized bell crank structure with minimal dimensions to reduce purchasing costs and to achieve a better handling in the testing laboratory.
- Analysis of the generator signal for all actuators. Changing the sinusoidal shape might allow smaller bell crank structures or reduce secondary loadings to the blade.
- In D. L. White and Musial (2004), ideal phase angles for a biaxial test were determined to represent a realistic loading of the blade as precise as possible. Because this was only performed for one wind turbine, a general method might be developed to allow such calculation for any wind turbine with a parametric input in order to adjust such analysis to the particular conditions of a specific wind turbine.
- To achieve more representative simulation results when comparing a real test with FE simulation, the material and air damping factors have to be known more precisely. The simulation work of Greaves (2013) needs to be extended and validated with aerodynamic experiments and real blade tests. The determination of air damping factors most likely needs to include the geometric characteristics of each testing laboratory.
- Development of an optimization algorithm to find the ideal BEDEX test setup automatically, including minimized overloads, reduction of the complexity of the setup, minimizing the number of added masses and actuators, increasing the testing frequency to reduce the testing time or minimizing the externally applied shear forces.

Besides optimizing the full-scale testing of blades in order to reduce testing time and improve realism of tests, additional research should be performed by substituting at least parts of the full-scale testing by component testing. More samples can be tested at shorter time (Busmann et al. (2007), Bürkner and van Wingerde (2008)). Comparable to the aerospace industry, in the future more component blade tests and fewer full-length blade tests should be performed for full-scale testing.

A New Approach?

At last, a new approach to determine the material degradation during fatigue tests is presented for consideration: Today the required loading for a rotor blade fatigue test is defined by **bending moment ranges** at specific radial positions. Hence, bending moments have to be measured throughout the test to prove that a sufficient loading was applied. With the need to measure bending moments in dynamic fatigue tests, complex calibaration tests are needed including all challenges discussed in this work.

After all, only strain cycles cause fatigue degradation on the blade material. So the purposed approch would be to define the test loading by **stain ranges** for different areas like spar-caps, trailing egdes and leading edges on specific radial positions.

In this case **absolute strains** need to be measured during the test, compared to the calibration test method where only **relativ strains** need to be measured. Due to the fact that common strain-gauges are too inaccurate to measure absolute strains, there is a need for new strain sensors. If sensores of high accuracy for measuring absolute strains can be developed, all inaccuracies and uncertainties of todays calibration tests will be avoided.

With having SN-lines of spar-caps, trailing egdes and leading edges, the applied fatigue loading can be easily and precisely calculated on-line throughout the test, even when using very complex biaxial blade movements.

References

Aagaard Madsen, B. A., H., & Løgstrup Andersen, T. (2015). Testing of a new morphing trailing edge flap system on a novel outdoor rotating test rig. In *EWEA Annual Conference and Exhibition* (p. 26-30).

Ashwill, T. D. (2010). *Sweep-twist adaptive rotor blade: final project report.* (SAND2009-8037). Sandia National Laboratories.

ASTM, E. .-. (1997). Standard practices for cycle counting in fatigue analysis. *Annual Book of ASTM Standards, ASTM E 1049-85*, *03*(01), 710 – 718.

Bak, C., Zahle, F., Bitsche, R., Kim, T., Yde, A., Henriksen, L., . . . Natarajan, A. (2013). *The DTU 10-MW Reference Wind Turbine.*

Beckwith, J. A., White, D., & Barsotti, D. L. (2013). Development of a dual-axis phase-locked excitation (PhLEX) resonant fatigue test method for wind turbine blades. In *ASME 2013 International Mechanical Engineering Congress and Exposition.*

Böhnisch, H. (1988). *Entwicklung, Bau und Betrieb einer 30/100-kW-Windkraftanlage*. Wiss. Berichtswesen d. DFVLR.

Borst, M. (2012). Knowledge center wind turbine materials and constructions. In *Sandia Blade Workshops.*

Braun, R., & Sayer, F. (2018). *Gemeinsamer technischer Schlussbericht zum Verbundprojekt BladeMaker* (Technical Report). Bremerhaven, Germany: Fraunhofer Institute for Wind Energy and Energy System Technology (IWES).

Bürkner, F. (2014). *Regelung der Ermüdungstests an RB (Einstellung einer servo-hyraulischen Regelung für uni- und bi-axiale Ermüdungstest von Rotorblättern von Windenergieanlagen oder ähnlichen Strukturen)* (Technical Report No. IWES-CO-153-14-01). Bremerhaven, Germany: Fraunhofer Institute for Wind Energy and Energy System Technology (IWES).

Bürkner, F., & Antoniou, A. (2014). *Better Blade - Entwicklung eines optimierten, innovativen Prüfverfahrens zur Zertifizierung von Rotorblättern heutiger und zukünftiger Windenergieanlagen* (Technical Report No. IWES-B-A709011-09 v01). Bremerhaven,Germany: Fraunhofer Institute for Wind Energy and Energy System Technology (IWES).

Bürkner, F., & van Wingerde, A. (2008). Testing of rotor blades of wind turbines. In *9th German Wind Energy Conferenc, DEWEK 2008.* Bremen, Germany.

Bürkner, F., & van Wingerde, A. (2011). Testing of rotor blades. In *Proceedings of the 8th International Conference on Structural Dynamics, EURODYN 2011.* Leuven, Belgium.

Bürkner, F., & van Wingerde, A. (2012). *InnoBladeTeC - Entwicklung neuer Prüfmethodiken und Prüfstände für Rotorblätter und deren Komponenten als wesentlicher Bestandteil des Kompetenzzentrums Rotorblatt* (Technical Report No. IWES-B-A706027-09 v01). Bremerhaven,Germany: Fraunhofer Institute for Wind Energy and Energy System Technology (IWES).

Busmann, H.-G., Kensche, C., Berg-Pollack, A., Bürkner, F., Sayer, F., & Wiemann, K. (2007). Testing of rotor blades. *Dewi Magazin*(30), 5–9.

Castaignet, D., Barlas, T., Buhl, T., Poulsen, N. K., Wedel-Heinen, J. J., Olesen, N. A., ... Kim, T. (2014). Full-scale test of trailing edge flaps on a vestas V27 wind turbine: active load reduction and system identification. *Wind Energy*, *17*(4), 549–564.

Chaviaropoulos, P. K., Politis, E., Lekou, D., Sørensen, N., Hansen, M., Bulder, B., ... Kossivas, T. (2006). Enhancing the damping of wind turbine rotor blades, the dampblade project. *Wind Energy*, *9*(1-2), 163–177. doi: 10.1002/we.183

Chortis, D., Chrysochoidis, N., & Saravanos, D. (2007). Damped structural dynamics models of large wind-turbine blades including material and structural damping. In *Journal of Physics: Conference Series* (Vol. 75).

Desmond, M., White, D., & Barott, W. (2009). Finite element modeling of a dual axis resonant test system for wind turbine blades. In *Proceedings of the ASME 2009 3rd International Conference of Energy Sustainability* (pp. 951–960).

Eder, M. A., Branner, K., Berring, P., Belloni, F., Stensgaard Toft, H., Sørensen, J. D., ... Petersen, T. K. (2015). *Experimental Blade Research-phase 2* (DTU Wind Energy E-0083). Denmark: DTU Wind Energy.

Freebury, G., & Musial, W. (2000). *Determining equivalent damage loading for full-scale wind turbine blade fatigue tests* (Technical Report NREL/CP-500-27510). Golden CO, USA: National Renewable Energy Laboratory (NREL).

Ghorashi, H., & Moetakef-Imani, B. (2016). Development of robust and adaptive controller for blade testing machine. *Renewable Energy*, *85*, 234–247.

Greaves, P. (2013). *Fatigue Analysis and Testing of Wind Turbine Blades* (Unpublished doctoral dissertation). Durham University, UK.

Greaves, P., Dominy, R. G., Ingram, G. L., Long, H., et al. (2011). Evaluation of dual-axis fatigue testing of large wind turbine blades. *Proceedings of the Institution of Mechanical Engineers, Part C: Journal of Mechanical Engineering Science*.

Greaves, P., Prieto, R., Gaffing, J., van Beveren, C., Dominy, R., & Ingram, G. (2016). A novel method of strain-bending moment calibration for blade testing. In *Journal of Physics: Conference Series* (Vol. 753).

Ha, K., Bätge, M., Melcher, D., & Czichon, S. (2019). Development and feasibility study of segment blade test methodology. *Wind Energy Science Discussions*, *2019*, 1–15. Retrieved from https://www.wind-energ-sci-discuss.net/wes-2019-60/ doi: 10.5194/wes-2019-60

Hughes, S. (2008). Wind turbine blade testing at NREL. In *Proceedings of 2008 Wind Turbine Blade Workshop.*

Hughes, S. (2010). Blade testing at NREL's national wind technology center. In *Proceedings of 2010 Wind Turbine Blade Workshop.*

Hughes, S., Musial, W., & Stensland, T. (1999). *Implementation of a Two-Axis Servo-Hydraulic System for Full-Scale Fatigue Testing of Wind Turbine Blades* (Technical Report NREL/CP-500-26896). Golden CO, USA: National Renewable Energy Laboratory (NREL).

IEC-61400-1. (2005). *Wind turbines – Part 1: Design requirements* (Third ed.; International Standard). Geneva, Switzerland: International Electrotechnical Commission.

IEC-61400-13. (2001). *Wind turbine generator systems – Part 13: Measurements of mechanical loads* (First ed.; International Standard). Geneva, Switzerland: International Electrotechnical Commission.

IEC-61400-23. (2001, April). *Wind Turbine Generator Systems – Part 23: Full-scale structural testing of rotor blades* (First ed.; Technical Specification No. IEC TS 61400-23-2001). Geneva, Switzerland: International Electrotechnical Commission.

IEC-61400-23. (2014, May). *Wind Turbine Generator Systems – Part 23: Full-scale structural testing of rotor blades* (- ed.; European Standard). Geneva, Switzerland: International Electrotechnical Commission.

Jansen, L., van Wingerde, A., Kensche, C., Philippidis, P., T.P. Brøndsted, Dutton, A., Nijssen, R., & Krause, O. (2006). *OptiMat Blades - Final report, (OB PC R017) rev. 001* (Technical Report).

Jensen, F., Branner, K., Nielsen, P., Berring, P., Antvorskov, T., Nielsen, M., ... Fergusson, A. (2008a). *Full Scale Test of a SSP 34m box girder 1. Data report.* Denmark: Danmarks Tekniske Universitet, Risø Nationallaboratoriet for Bæredygtig Energi.

Jensen, F., Branner, K., Nielsen, P., Berring, P., Antvorskov, T., Nielsen, M., ... Wedel-Heinen, J. (2008b). *Full Scale Test of a SSP 34m boxgirder 2: Data report.* Denmark: Danmarks Tekniske Universitet, Risø Nationallaboratoriet for Bæredygtig Energi. (Risø-R-1588(EN))

Jensen, F. M. (2008). *Ultimate strength of a large wind turbine blade* (Unpublished doctoral dissertation). Technical University of DenmarkDanmarks Tekniske Universitet, Department of Naval Architecture and Offshore EngineeringInstitut for Skibs-og Havteknik.

Jensen, F. M., Falzon, B., Ankersen, J., & Stang, H. (2006). Structural testing and numerical simulation of a 34m composite wind turbine blade. *Composite structures*, *76*(1), 52–61.

Jensen, F. M., Puri, A. S., Dear, J. P., Branner, K., & Morris, A. (2011). Investigating the impact of non-linear geometrical effects on wind turbine blades Part 1: Current status of design and test methods and future challenges in design optimization. *Wind Energy*, *14*(2), 239–254.

Jensen, F. M., Weaver, P., Cecchini, L., Stang, H., & Nielsen, R. F. (2012). The brazier effect in wind turbine blades and its influence on design. *Wind Energy*, *15*(2), 319–333.

Jørgensen, E., Borum, K., McGugan, M., Thomsen, C., Jensen, F., & Debel, C. (2004). *Full scale testing of wind turbine blade to failure–flapwise loading* (Risø-R-1392 (EN)). Denmark: Forskningscenter Risoe.

Kristensen, O. J. ., & Jørgensen, E. (2003). *Accelerated fatigue testing of LM 19.1 blades* (No. 1358(EN)). Denmark: Forskningscenter Risoe.

Lee, H. G., & Park, J. (2014). Linear relationship of damping ratios in resonance-type fatigue testing of a wind turbine blade. *Wind Energy*, *17*(7), 1119–1122.

Lee, H. G., & Park, J.-s. (2015). Optimization of resonance-type fatigue testing for a full-scale wind turbine blade. *Wind Energy*.

Lekou, D., & Mouzakis, F. (2009). WT load measurements: A comparison between load-based and analytical calibration. *Solar Energy Engineering*, *131*(1), 11005.

Malhotra, P. (2010). *Advanbed Blade Testing Methods for Wind Turbines* (Unpublished master's thesis). Masters Theses 1896, University of Massachusetts, Amherst MA, USA.

Mandell, J. F., & Samborsky, D. D. (1997). *DOE/MSU composite material fatigue database: test methods, materials, and analysis* (Tech. Rep.). Sandia National Labs., Albuquerque, NM (United States).

Melcher, D., Bätge, M., & Neßlinger, S. (2019). A novel rotor blade fatigue test setup with elliptical biaxial resonant excitation. *Wind Energy Science Discussions*, *2019*, 1–17. Retrieved from https://www.wind-energ-sci-discuss.net/wes-2019-84/ doi: 10.5194/wes-2019-84

Nielsen, P. H., Berring, P., Pavese, C., & Branner, K. (2013). *Rotor blade full-scale fatigue testing technology and research* (Tech. Rep.). Denmark: DTU Wind Energy.

Nijssen, R. (2006). *Fatigue Life Prediction and Strenght Degradation of Wind Turbine Blade Composites* (Unpublished doctoral dissertation). Faculty of Aerospace Engineering, Delft University, Delft, Netherland.

Papadopoulos, K., Morfiadakis, E., Chaviaropoulos, P., Foussekis, D., Hamelink, J., Heijdra, J., . . . others (1998). Wind turbine load measurement instrumentation. *European Wind Turbine Testing Procedure Development (SMT4-CT96-2116) report*.

Papadopoulos, K., Morfiadakis, E., Philippidis, T., & Lekou, D. (2000). Assessment of the strain gauge technique for measurement of wind turbine blade loads. *Wind Energy*, *3*(1), 35–65.

Paquette, J., Laird, D., Griffith, D. T., & Rip, L. (2006). Modeling and testing of 9m research blades. In *44th AIAA aerospace sciences meeting* (Vol. 19, pp. 14569–14581).

Paquette, J., van Dam, J., & Hughes, S. (2007). Structural testing of 9 m carbon fiber wind turbine research blades. In *45th AIAA Aerospace Sciences Meeting and Exhibit, Reno, NV.*

Park, J.-K., Park, J.-S., Lee, H.-G., Lee, S.-H., & Lee, W.-K. (2011). Numerical simulation on fatigue test of composite rotor blade for multi-megawatt wind turbine. In *Proceedings of the 18th International Conference on Composite Materials.*

Post, N., & Bürkner, F. (2019). *Fatigue Test Design: Scenarios for Biaxial Fatigue Testing of a 60-Meter Wind Turbine Blade* (Technical Report NREL/TP-5000-65227). Golden CO, USA: National Renewable Energy Laboratory (NREL).

Rosemeier, M., Basters, G., & Antoniou, A. (2018). Benefits of subcomponent over full-scale blade testing elaborated on a trailing-edge bond line design validation. *Wind Energy Science*, *3*(1), 163–172. Retrieved from https://www.wind-energ-sci.net/3/163/2018/ doi: 10.5194/wes-3-163-2018

Rosemeier, M., Berring, P., & Branner, K. (2015). Non-linear ultimate strength and stability limit state analysis of a wind turbine blade. *Wind Energy*.

Sayer, F., Bürkner, F., Blunk, M., van Wingerde, A., Busmann, H., et al. (2009). Influence of loads and environmental conditions on material properties over the service life of rotor blades. *DEWI MAGAZIN*(34).

Sayer, F., Bürkner, F., Buchholz, B., Strobel, M., van Wingerde, A. M., Busmann, H.-G., & Seifert, H. (2013). Influence of a wind turbine service life on the mechanical properties of the material and the blade. *Wind Energy*, *16*(2), 163 – 174.

Schneider, K.-J. (1996). *Bautabellen für Ingenieure* (Vol. 16). Düsseldorf, Germany: Werner-Verlag.

Snowberg, D., Dana, S., Hughes, S., & Berling, P. (2014). *Implementation of a biaxil resonant fatigue test methos an a large wind turbine blades* (Technical Report NREL/TP-5000-61127). Golden CO, USA: National Renewable Energy Laboratory (NREL).

Sutherland, H. J., & Mandell, J. F. (2004a). Effect of mean stress on the damage of wind turbine blades. *Journal of solar energy engineering*, *126*(4), 1041–1049.

Sutherland, H. J., & Mandell, J. F. (2004b). *Updated Goodman diagrams for fiberglass composite materials using the DOE/MSU fatigue database* (Tech. Rep.). Sandia National Laboratories.

Sutherland, H. J., & Mandell, J. F. (2005). The effect of mean stress on damage predictions for spectral loading of fibreglass composite coupons. *Wind Energy*, *8*(1), 93–108.

Westphal, T. (2010). Developements in wind turbine blade fatigue testing. In *Sandia Blade Workshops.*

White, D. (2004). *New Methods for Dual-Axis Fatigue Testing of Large Wind Turbine Blades Using Resonance Excitation and Spectral Loading* (Technical Report NREL/TP-f500-35268). Golden CO, USA: National Renewable Energy Laboratory (NREL).

White, D., Desmond, M., Gowharji, W., Beckwith, J. A., & Meierjurgen, K. J. (2011). Development of a dual-axis phase-locked resonant excitation test method for fatigue testing of wind turbine blades. In *ASME 2011 International Mechanical Engineering Congress and Exposition* (pp. 1163–1172).

White, D., Musial, W., & Engberg, S. (2005). Evaluation of the b-rex fatigue testing system for multi-megawatt wind turbine blades. In *Collection of the 2005 ASME Wind Energy Symposium Technical Papers at the 43rd AIAA Aerospace Sciences Meeting and Exhibit* (pp. 52–65).

White, D. L., & Musial, W. D. (2004). The effect of load phase angle on wind turbine blade fatigue damage. *Journal of solar energy engineering*, *126*(4), 1050–1059.

Williamson, K. (2012). Push and pull–testing wind turbine blades. *Reinforced plastics*, *56*(1), 26–32.

Appendix A

Coordinate Systems

The coordinate systems from IEC-61400-23 (2014) will be used. The chord-wise and rotorwise coordinate system is shown in Figure A.1 and Figure A.2.

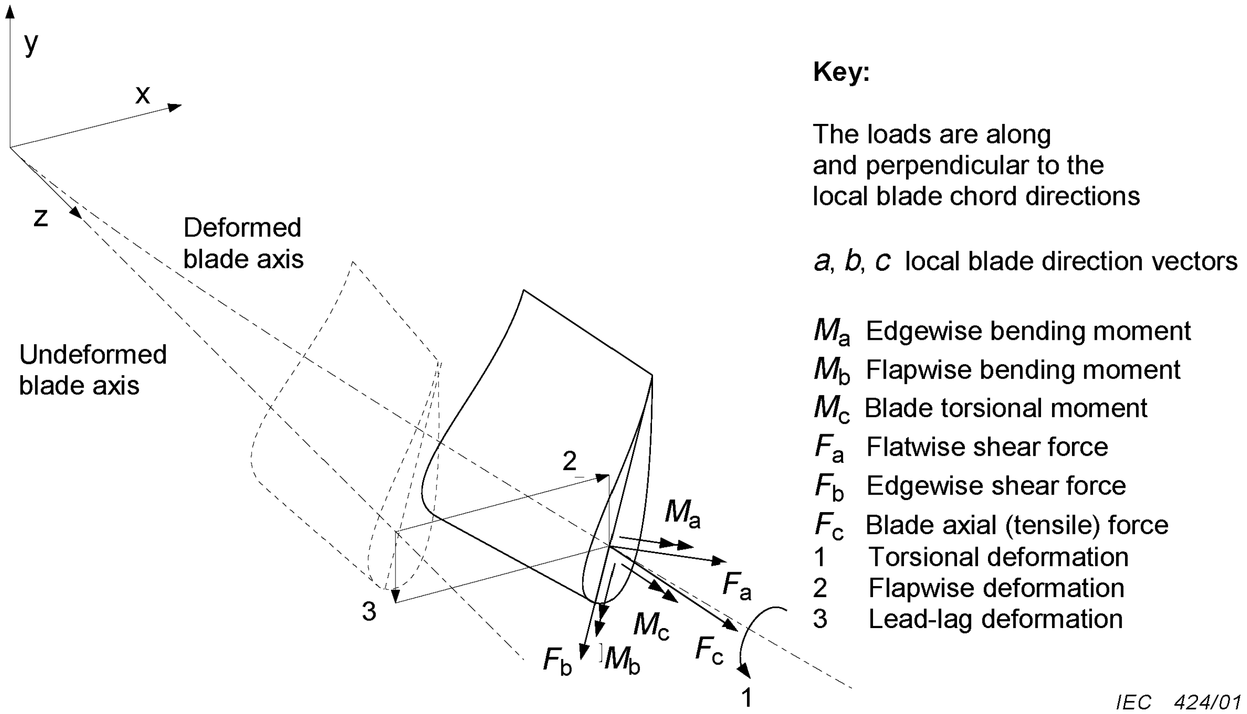

Figure A.1: Chordwise (flat-, edwise) coordinate system, IEC-61400-23 (2014)

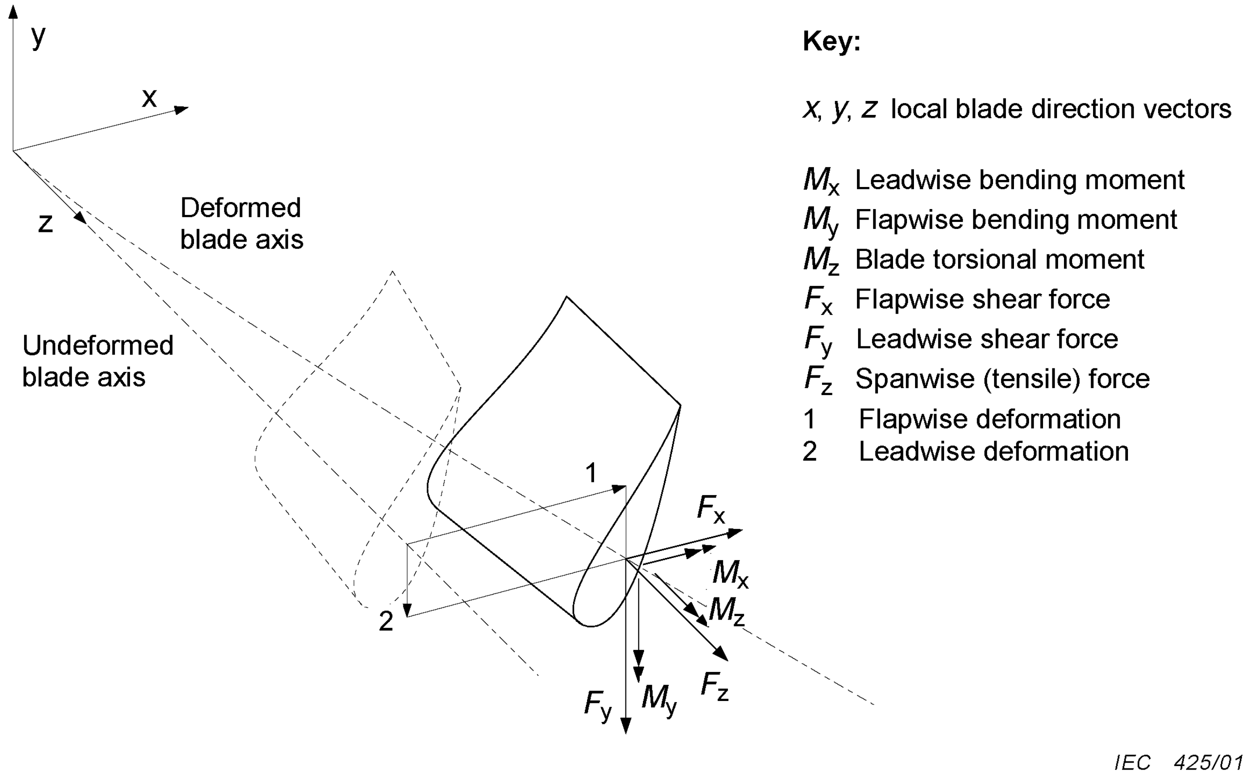

Figure A.2: Rotorwise (flap-, lead-lag-wise) coordinate system, IEC-61400-23 (2014)

Appendix B

Exemplary used Blades

Table B.1: Exemplary used Blades, FE-Models and Test Blade

Number	Approx. Length	FE Model	Test Data	Date of Test	Type of Test	Name
1	40	y	y	01.2015-04.2015	Internal validation	-
2	40	y	y	10.2009-10.2010	Zertification	-
3	40	y	-	-	-	IWT82
4	50	-	y	06.2010-01.2012	Zertification	-
5	55	-	y	11.2011-04.2013	Zertification	-
6	55	-	y	11.2011-08.2012	Zertification	-
7	55	-	y	10.2011-11.2012	Zertification	-
8	65	y	y	08.2013-07.2014	Zertification	-
9	65	y	y	06.2015-01.2016	Zertification	-
10	>80	y	y	10.2012-07.2014	Zertification	-
11	>80	-	y	05.2013-06.2014	Zertification	-
12	>80	y	-	-	-	DTU10MW

Blade 3 was developed within the Blade Maker project (Braun and Sayer (2018)). Version IWT-1-5-82 BladeMaker-Ref10-loop28 blade_db of the blade was used.

Blade 12 was developed within the European InnWind project (Bak et al. (2013)). Reference windt turbine V1p01-1 was used.

Appendix C

Example for Calibration Tests in Flap- and/or Lead-lag-wise Direction

In Figure C.1, four options to calculate a flap-wise bending moment according to Section 2.1.1 are plotted. The exemplary used blade (blade 11 Table B.1) had two shear webs and four spar caps. On each spar cap, one sensor was applied. Highlighted in green, the relative standard deviation is scaled to the right ordinate. With over 15% , the scatter is quite high.

Two strain gauges were applied on each span-wise position at the trailing edge for this blade. Therefore, 12 options are available to calculate the bending moment at each cross-section according to Section 2.1.2 using two different sensors. All possible bending moment lines are shown in Figure C.2.

In comparison to Figure C.1, the scatter of the bending moment is reduced significantly to less than 3% between the root until 27% blade length and to less than 1.2% between 27% to 80% blade length. The scatter of results could be reduced by a factor of five.

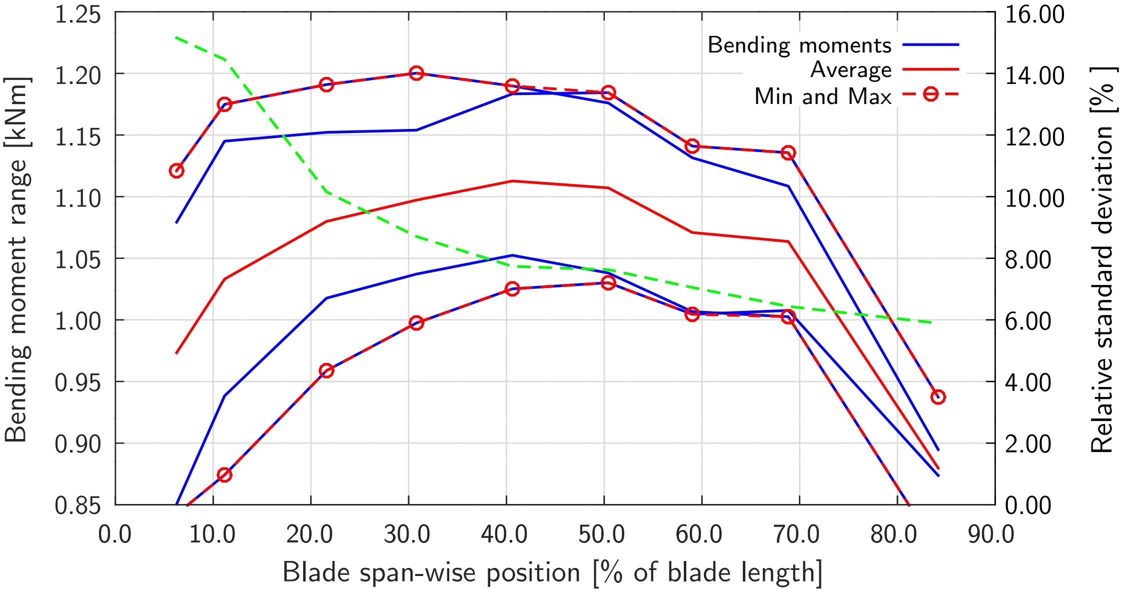

Figure C.1: In blue: Typical resulting test bending moments along the blade span when using 4 different sensors and **no cross-talk terms** for the analysis (according to Section 2.1.1). The bending moment is given as the quotient of test bending moment over the desired bending moment. In red: Average, maximum and minimum of the 4 bending moments per span-wise location. In green: Relative standard deviation in percent scaled to the right ordinate

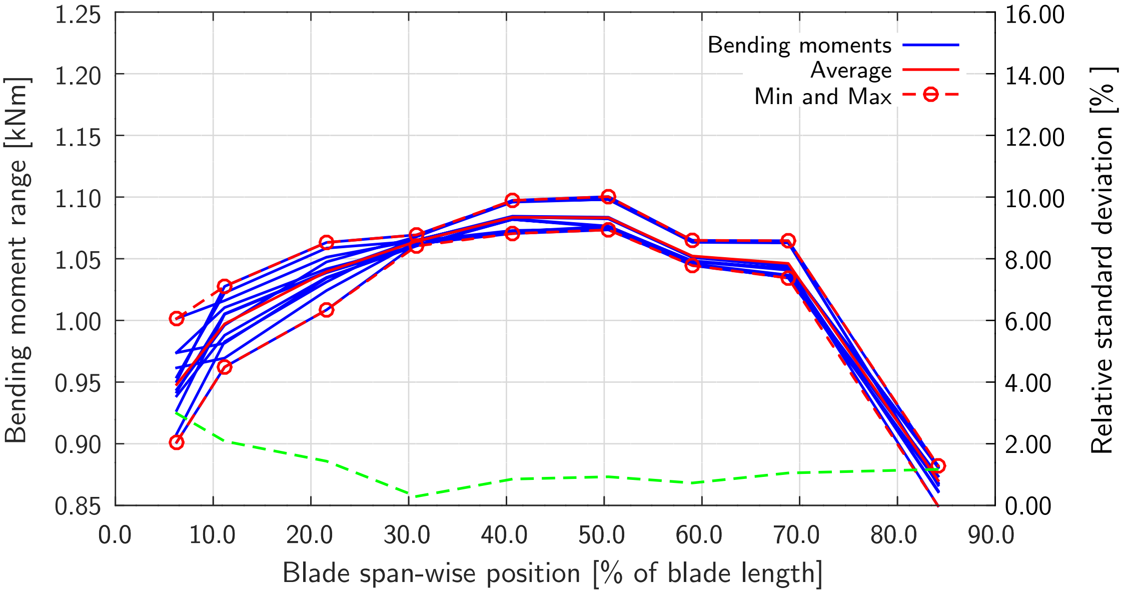

Figure C.2: In blue: Typical resulting test bending moments along the blade span when using 12 different combinations of sensors **with cross-talk** terms for the analysis (according to Section 2.1.2). The bending moment is given as the quotient of test bending moment over the desired bending moment. In red: Average, maximum and minimum of the 12 bending moments per span-wise location. In green: Relative standard deviation in percent scaled to the right ordinate

Appendix D

Verification of the Method to Analyze Nonlinearities

To verify the method described in Section 3.2, in Figure D.1, the bending moments of both options (uncorrected as dotted lines and corrected as solid lines) are plotted for a lead-lag-wise loading. For each option, 4 bending moment lines can be calculated having strain gauges on the suction side, leading edge, pressure side and trailing edge. In this case, a lead-lag-wise dynamic fatigue test was performed, so according to Section 2.1, the leading edge and trailing edge strain can each be corrected with the pressure side or suction side strain.

Comparisons of the uncorrected and corrected bending moments of Figure D.1:

- Where beyond 14.3% blade length all curves are almost identical, the uncorrected bending moment values further inboard diverge by 13.7% . After correcting the curves with the method described in this section, all curves are on a much smaller bandwidth of 3.2% at 1.4% blade length.
- The uncorrected bending moments decrease significantly inboard of 14.3% blade length in comparison to a linear extrapolation as shown in Figure D.2. As this is mechanically impossible, the nonlinear behavior obviously leads to incorrect values inboards of 14.3% blade length. At 14.3 and 25.1% blade length, a bandwidth of 3% [51] to the average bending moment of the uncorrected values is extrapolated to 1.4% blade length. The corrected values are within the extrapolation bandwidth.

Using the purposed method decreases the bandwidth significantly. When correcting the bending moments at sections showing nonlinear behavior, realistic results were determined. With the described results, a verification of the method was performed. A validation of the method was not possible, because the exact bending moment at the root region is unknown for the used example test. This has to be addressed in future work (Section 6.3).

---

[51] This value was exemplarily used as a representative strain gauge uncertainty according to Papadopoulos et al. (2000).

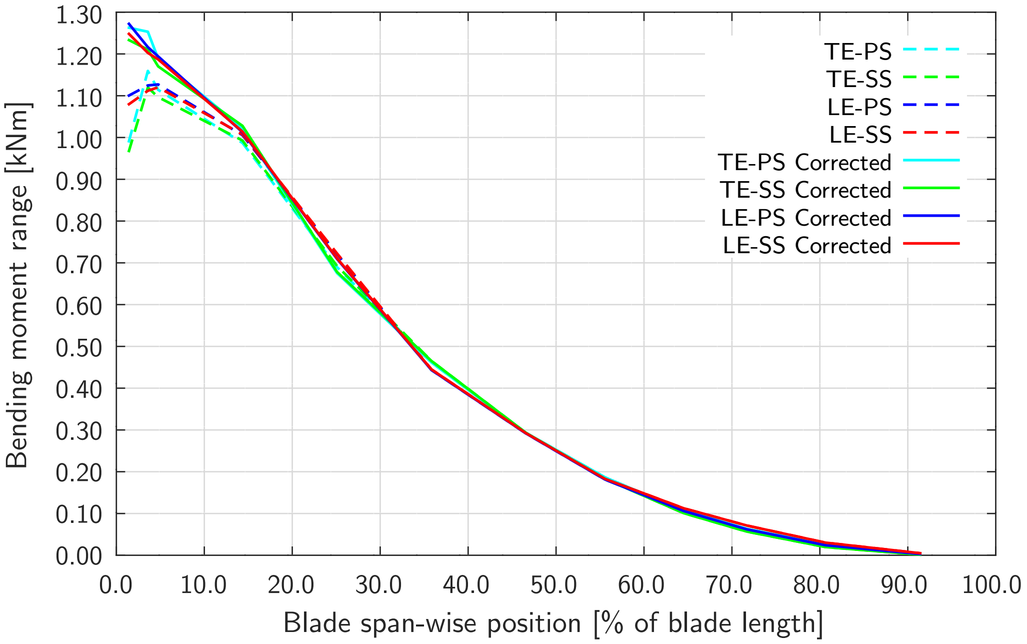

Figure D.1: Normalized bending moments of a lead-lag-wise dynamic fatigue test corrected and uncorrected for nonlinearities plotted over the blade length. Bending moments *not* corrected for nonlinearities plotted in dotted lines and *with* correction in solid lines.

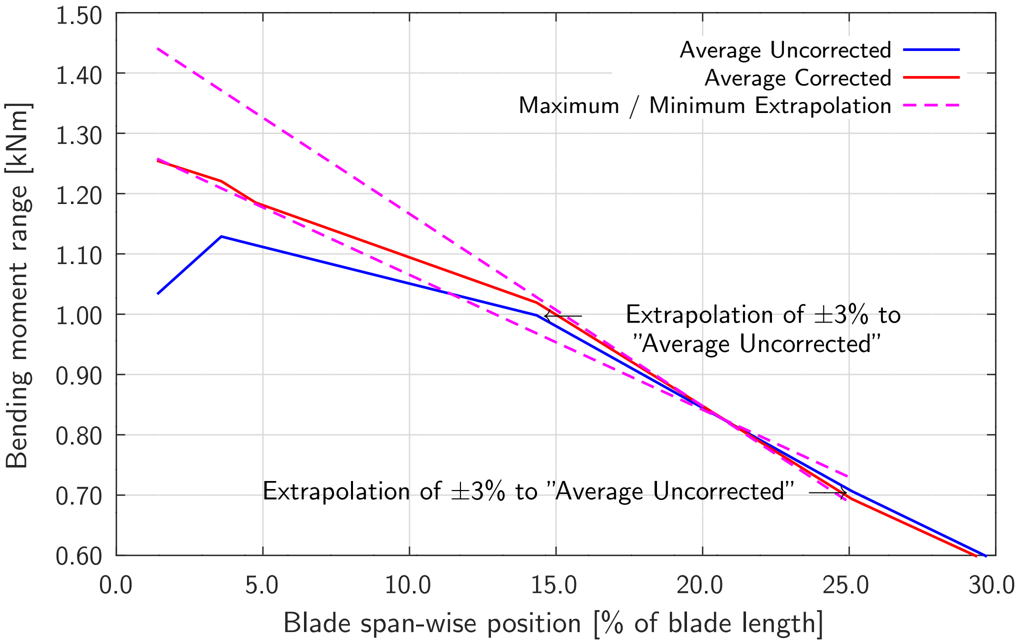

Figure D.2: In magenta: Extrapolation of the average curve based on the four uncorrected options to calculate the bending moment of the lead-lag-wise dynamic fatigue test. The values used to determine the extrapolation were increased and decreased by ±3% to evaluate a bandwidth of results. In red: The average of the corrected four bending moment curves.

Appendix E

Sensitivity to Inaccurate Measurements when Using OM-I

To evaluate the sensitivity of E_{root} and E_{Lc_z} with regard to inaccurate measurements of γ, β, Lc_x and u_z, Equation 3.4 and Equation 3.5 are used with different values (Table E.1 and Table E.2). The maximum uncertainty is still below the uncertainty which shall be reduced. Because rather large uncertainties of the measured parameters lead to only small deviations of the result, a rather stable method is found.

Table E.1: Absolute difference of the error E when using ideal values or measured values with uncertainties for the flap-wise direction. Calculated at the root and at Lc_z using OM-I. For a selected set of uncertainties, the maximum and minimum difference is shown.

Sets [-]	$\pm\gamma$ [°]	$\pm\beta$ [°]	$\pm u_x$ [%]	$\pm u_z$ [%]	max Lc_z [%]	min Lc_z [%]	max Root [%]	min Root [%]
1	1.0	1.0	10.0	10.0	0.66	-0.54	0.47	-0.42
2	1.0	1.0	5.0	5.0	0.66	-0.54	0.37	-0.33
3	1.0	0.5	5.0	5.0	0.48	-0.41	0.37	-0.33
4	0.5	0.5	5.0	5.0	0.31	-0.28	0.23	-0.22
5	0.0	0.5	5.0	5.0	0.15	-0.15	0.09	-0.09
6	0.0	1.0	5.0	5.0	0.31	-0.28	0.09	-0.09
7	0.0	1.0	10.0	10.0	0.31	-0.28	0.19	-0.19

Table E.2: Absolute difference of the error E when using ideal values or measured values with uncertainties for the lead-lag-wise direction. Calculated at the root and at Lc_z using OM-I. For a selected set of uncertainties, the maximum and minimum difference is shown.

Sets [-]	$\pm\gamma$ [°]	$\pm\beta$ [°]	$\pm u_y$ [%]	$\pm u_z$ [%]	max Lc_z [%]	min Lc_z [%]	max Root [%]	min Root [%]
1	1.0	1.0	10.0	10.0	0.14	-0.02	0.05	-0.02
2	1.0	1.0	5.0	5.0	0.14	-0.02	0.05	-0.02
3	1.0	0.5	5.0	5.0	0.09	-0.02	0.05	-0.02
4	0.5	0.5	5.0	5.0	0.05	-0.02	0.02	-0.01
5	0.0	0.5	5.0	5.0	0.02	-0.02	0.00	0.00
6	0.0	1.0	5.0	5.0	0.05	-0.02	0.00	0.00
7	0.0	1.0	10.0	10.0	0.05	-0.02	0.01	-0.01

Appendix F

Numeric Calculation of OM-II

The blade has to be divided in at least 20 elements equally distributed in Z_{IEC} direction. The locations at the end of each element are named *nodes*[52]. The flat-wise (FTW) bending stiffness EI_{FTW} has to be known for each node. The coordinates of each node in Z_{IEC} direction $Ln_{z,prebend}$ and the coordinate of each node in X_{IEC} direction $Ln_{x,prebend}$ has to be known for the undeformed blade (subscript *prebend*). The length of each element l_{el} can be derived with Equation F.1. The index (i) shall stand for the node or element number starting from the root to Lc_z[53] (Figure F.1).

$$l_{el,i} = \sqrt{(Ln_{x,prebend,i+1} - Ln_{x,prebend,i})^2 + (Ln_{z,prebend,i+1} - Ln_{z,prebend,i})^2} \tag{F.1}$$

$l_{el,i}$: Length of element (element i)

$Ln_{x,prebend,i}$: Location (coordinate) of a node in X_{IEC} direction of the undeformed blade (node i)

$Ln_{z,prebend,i}$: Location (coordinate) of a node in Z_{IEC} direction of the undeformed blade (node i)

The angle $\beta_{prebend,i}$ between the pitch axis and the element orientation in the Z_{IEC}-X_{IEC} plane of each element has to be calculated for each element according to Equation F.2.

$$\beta_{prebend,i} = \tan^{-1}\left(\frac{Ln_{x,prebend,i+1} - Ln_{x,prebend,i}}{Ln_{z,prebend,i+1} - Ln_{z,prebend,i}}\right) \tag{F.2}$$

$\beta_{prebend,i}$: Rotation of the blade to the pitch axis of the undeformed blade at the tip-wise end of an element (element i)

The deflection u_{el} is calculated from element to element starting at the root. The geometry is shown in Figure F.1. Two deflections are added, the deflection $u_{el,F_{el}}$ of each element due to the shear force at the tip-wise end of the element (F_{el}) and the deflection $u_{el,M_{el}}$ due to the flap-wise bending moment (M_{el}) at the tip-wise end of each element. Besides the deflection, the angle of each element at the tip-wise end, generated by both loadings, is calculated (β_{el}). Equation F.3

---

[52] Even though a FE calculation is not performed, the blade will be discretized in elements and nodes.

[53] Element 1 starts at node 1 and ends at node 2, etc.

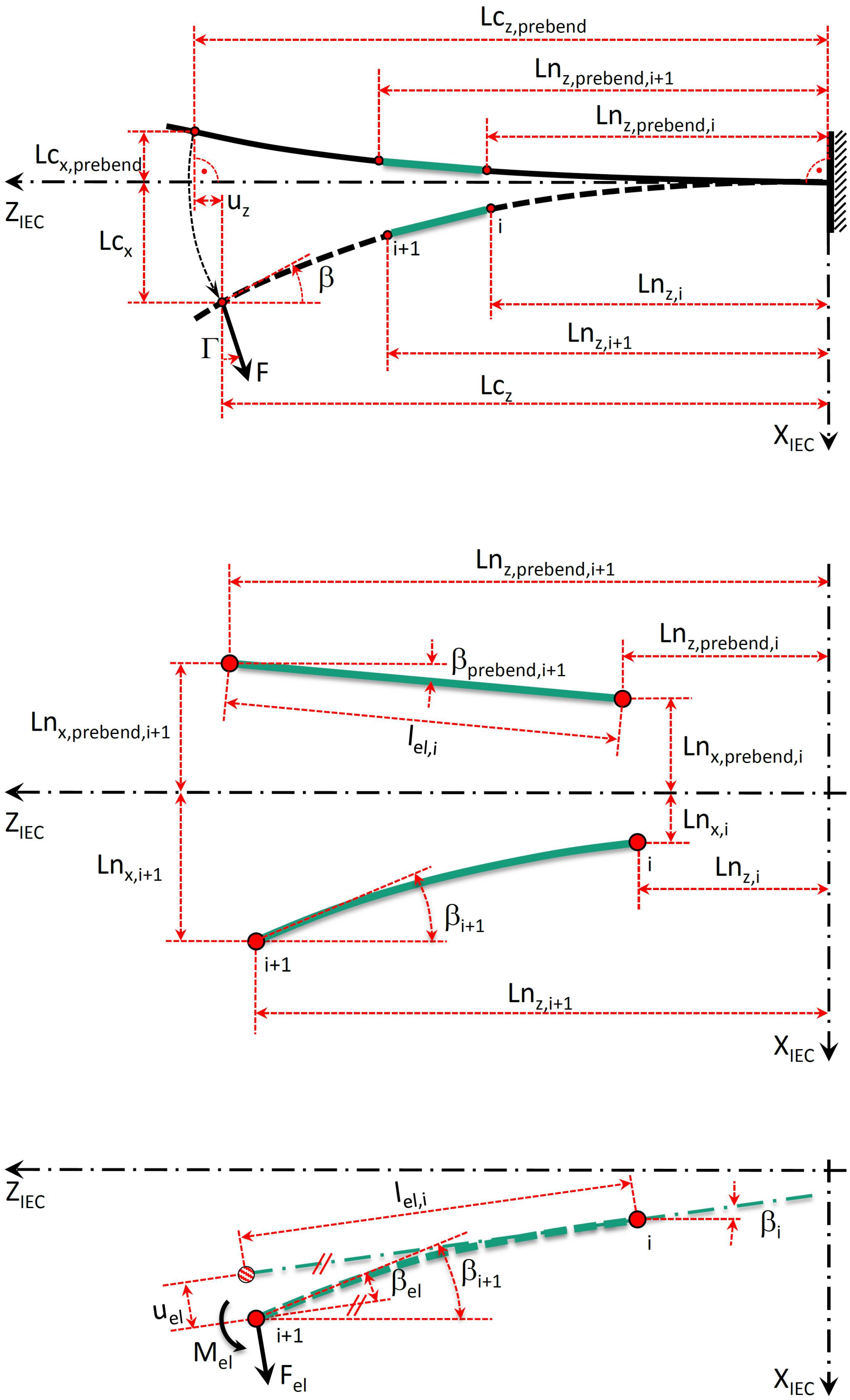

Figure F.1: Geometry of the calculation performed on each element. The deflection u_{el} and rotation β_{el} of the element due to F_{el} and M_{el} is calculated.

to Equation F.6, as described in Schneider (1996), are used according to Figure F.1. For each element, small deflections are assumed (no geometric nonlinearity). For each calculation, the stiffness EI_{FTW} from the node at the *root-wise end* of each element is used.

$$EI_{FTW} \times u_{el,F_{el}} = \frac{F_{el} \times {l_{el}}^3}{3} \tag{F.3}$$

$$EI_{FTW} \times u_{el,M_{el}} = \frac{M_{el} \times {l_{el}}^2}{2} \tag{F.4}$$

$$EI_{FTW} \times \beta_{F_{el}} = \frac{F_{el} \times {l_{el}}^2}{2} \tag{F.5}$$

$$EI_{FTW} \times \beta_{M_{el}} = M_{el} \times l_{el} \tag{F.6}$$

Using Equation F.3 and Equation F.4, the total u_{el} at the tip-wise end of an element is:

$$u_{el} = \frac{F_{el} \times {l_{el}}^3}{3 \times EI_{FTW}} + \frac{M_{el} \times {l_{el}}^2}{2 \times EI_{FTW}} \tag{F.7}$$

Using Equation F.5 and Equation F.6, the total β_{el} at the tip-wise end of an element is:

$$\beta_{el} = \frac{F_{el} \times {l_{el}}^2}{2 \times EI_{FTW}} + \frac{M_{el} \times l_{el}}{EI_{FTW}} \tag{F.8}$$

The goal of OM-II is *not* to calculate the deflections along the blade span as precise as possible, but to use a *simplified* calculation which is precise enough. Hence, simplified and not always geometrically exact approaches will be used.

The deflection of the blade at Lc_z is measured at the calibration test. The numeric simulation will be adjusted by an iterative process (by changing the numeric load F_{num}) to achieve exactly the same deflections. To simplify the calculation, it is assumed that F_{num} is always perpendicular to each element before calculating the deflections [54].

---

[54] Even in case the blade faces upward with $\leq 16°$, this assumption is used. For simplification, the load component of F (at the calibration test) which is parallel to each element is not taken into account at the numeric calculation.

The bending moment at the tip end of each element is calculated according to F_{num} times the span-wise distance between the pulling location $Lc_{z,prebend}$ and the tip-wise node coordinate of each element $Ln_{z,prebend}$ of the undeformed blade. $M_y = F_{num} \times (Lc_{z,prebend} - Ln_{z,prebend})$[55].

Equation F.7 and Equation F.8 can be changed to Equation F.9 and Equation F.10. Again, the index (i) stands for the node number starting from the root for Ln_z, Ln_x, β_{el} and EI_{FTW}. The index (i) stands for the element number starting from the root for l_{el} and u_{el}.

$$u_{el,i} = \frac{F_{num} \times (l_{el,i})^3}{3 \times EI_{FTW,i}} + \frac{F_{num} \times (Lc_z - Ln_{z,prebend,i+1}) \times (l_{el,i})^2}{2 \times EI_{FTW,i}} \tag{F.9}$$

$$\beta_{el,i} = \frac{F_{num} \times (l_{el,i})^2}{2 \times EI_{FTW,i}} + \frac{F_{num} \times (Lc_z - Ln_{z,prebend,i+1}) \times l_{el,i}}{EI_{FTW,i}} \tag{F.10}$$

$u_{el,i}$: Deflection of the tip-wise node of an element (X_{IEC}-Z_{IEC} plane) (element i)

$\beta_{el\,i}$: Rotation of the tip end of an element around the Y_{IEC} axis (element i)

F_{num}: Force used in the numeric calculation of OM-II

$l_{el,i}$: Length of element (element i)

$EI_{FTW,i}$: Bending stiffness of the root-wise end of an element in FTW direction (element i)

Lc_z: Location (coordinate) of the calibration load attachment location in Z_{IEC} direction

$Ln_{z,prebend,i}$: Location (coordinate) of a node in Z_{IEC} direction of the undeformed blade (node i)

$\beta_{prebend,i}$: Rotation of the blade to the pitch axis of the undeformed blade at the tip-wise end of an element (element i) (Equation F.11)

With taking the prebend angles calculated by Equation F.2 into account, Equation F.10 becomes Equation F.11. For node 1, the angle β_0 is equal to $\beta_{prebend,1}$.

$$\beta_i = \beta_{i-1} + \frac{F_{num} \times (l_{el,i})^2}{2 \times EI_{FTW,i}} + \frac{F_{num} \times (Lc_z - Ln_{z,prebend,i}) \times l_{el,i}}{EI_{FTW,i}} + (\beta_{prebend,i} - \beta_{prebend,i-1}) \tag{F.11}$$

---

[55] This is a simplified approach again, as the lever arm will change with the deflecting blade and F is not always perpendicular to the pitch axis. The results show that all simplifications still lead to an acceptable inaccuracy of the results.

The coordinate of each node of the deflected blade is also calculated from element to element, starting at the root. After calculating $u_{el,1}$ (Equation F.9) and β_0 (Equation F.2) for element 1, the coordinates of node 2 can be calculated[56]:

$$Ln_{x,2} = Ln_{x,1} + sin(\beta_0) \times l_{el,1} + cos(\beta_0) \times u_{el,1} \tag{F.12}$$

$$Ln_{z,2} = Ln_{z1} + cos(\beta_0) \times l_{el,1} - sin(\beta_0) \times u_{el,1} \tag{F.13}$$

More generally each coordinate and therefore the deflection curve is calculated according to:

$$Ln_{x,i} = Ln_{x,i-1} + sin(\beta_{i-1}) \times l_{el,i-1} + cos(\beta_{i-1}) \times u_{el,i-1} \tag{F.14}$$

$$Ln_{z,i} = Ln_{z,i-1} + cos(\beta_{i-1}) \times l_{el,i-1} - sin(\beta_{i-1}) \times u_{el,i-1} \tag{F.15}$$

$Ln_{x,i}$: Location (coordinate) of a node in X_{IEC} direction (node i)

$Ln_{z,i}$: Location (coordinate) of a node in Z_{IEC} direction (node i)

β_i: Rotation of the blade to the pitch axis at the tip-wise end of an element (element i)

$l_{el,i}$: Length of element (element i)

$u_{el,i}$: Deflection of the tip-wise node of an element (X_{IEC}-Z_{IEC} plane) (element i)

Once this calculation is performed element by element, all nodal coordinates Ln_z and Ln_x are known for the deflected blade. As mentioned before, the load F_{num} and the stiffness EI_{FTW} have to be evaluated by using an iterative process to achieve that Lc_z is equal to the measured coordinate $Lc_{z,calibrationtest}$ and that β_{Lc_z} is equal to the measured blade angle $\beta_{Lc_z,calibrationtest}$[57]. Where F_{num} can be easily increased and decreased iteratively to find the solution, changing all EI_{FTW} with one single factor does not change angle β_{Lc_z}. The deflection curve will keep the same shape. Only force F_{num} necessary to achieve the correct deflection will change. To change the shape of the deflection curve, EI_{FTW} needs to be changed with different factors along the blade span. Different approaches are possible. In this work, a distribution to change EI_{FTW} is used, which is calculated according to Equation F.16. The power of 5 was used with regard to the curve of EI_{FTW} along the blade span showing almost the same power term. Other power terms are possible, but do not change the results significantly. The factor x$_{iteration}$ is the variable for the iteration.

---

[56] Node 1 is right at the root, where $\beta_0 = \beta_{prebend,1}$, $Ln_{z,1} = 0$ and $Ln_{x,1} = 0$

[57] For example using an Excel spread sheet this can be done by activating the iterative calculation option.

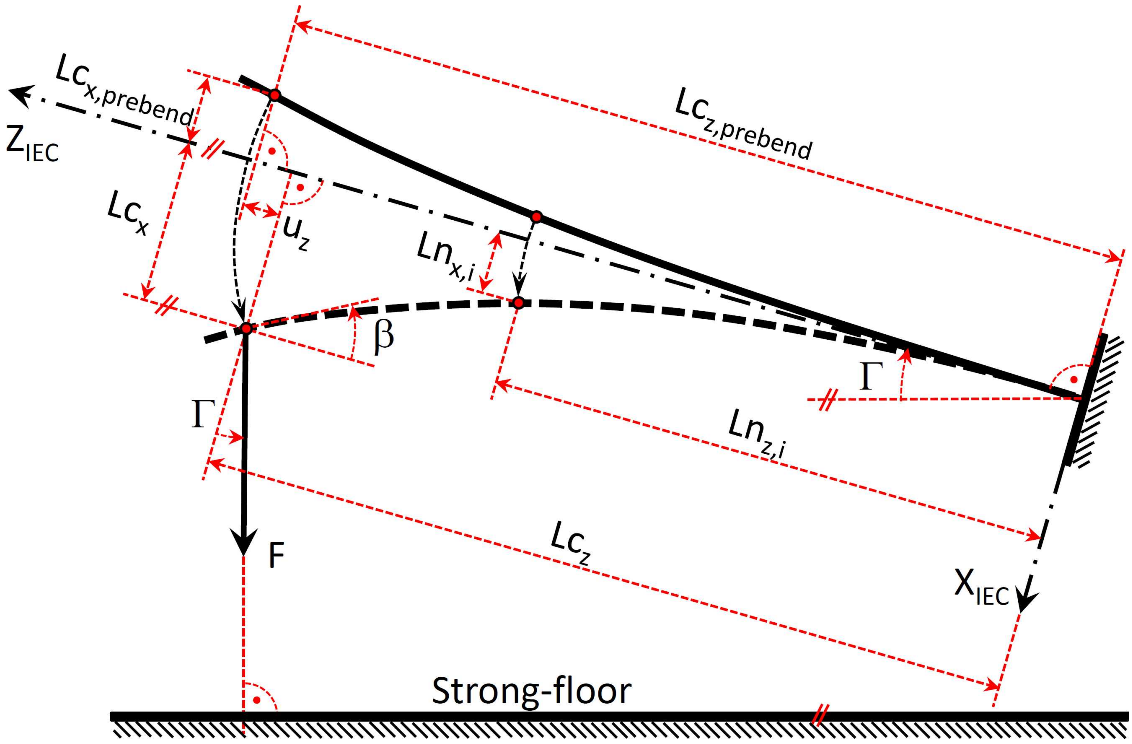

Figure F.2: Geometry of a calibration test using OM-II

$$EI_{new,i} = EI_i \times \left(1 + x_{iteration} \times \left(\frac{Ln_{z,prebend,i}}{Lc_{z,prebend}}\right)^5\right) \tag{F.16}$$

$EI_{new,i}$: Bending stiffness of the root-wise end of an element calculated to be used in the next iteration step (in flat-wise or flap-wise direction), (element i, node i)

EI_i: Bending stiffness of the root-wise end of an element (in flat-wise or flap-wise direction), (element i)

$x_{iteration}$: Variable of the iteration

$Ln_{z,prebend,i}$: Location (coordinate) of a node in Z_{IEC} direction of the undeformed blade (node i)

$Lc_{z,prebend,i}$: Location (coordinate) of the calibration load attachment location in Z_{IEC} direction of the undeformed blade (node i)

Once both iterations converge, the numerically calculated coordinates of the loaded blade are fitted to the calibration test for the blade angle β and the X_{IEC} deflection at $Lc_{z,prebend}$ location. At the root, both curves are identical, as the blade is fixed rigidly to the test rig. The error E is now calculated according to the numerically determined blade coordinates with the blade at full load.

Error E can be described as the quotient of $M_{large-deflected}$ over $M_{un-deflected}$ minus one. Therefore, it can be calculated according to Equation 3.3. As Equation 3.3 was defined for a system where the blade was oriented horizontally, angle γ was the direction of F to vertical. In that case, not a dead weight was used but a fixed pulling location, so that the load direction was not always vertical. In this particular case, the loading is always vertical due to the dead weight used, but the blade root is not horizontal any more, as the test rig might have a certain angle. As shown in Figure F.2, the angle between load and root plane (X_{IEC}-axis) is defined by the same angle of blade root plane to vertical. Therefore, γ is changed to Γ, which is defined to be 0, if the blade is fixed horizontally at the root and positive, if the blade points upwards with the tip[58]. Equation 3.3 becomes Equation F.17:

$$E_{root} = \frac{F \times \cos\Gamma \times (Lc_{z,prebend} + u_z) + F \times \sin\Gamma \times u_x}{F \times Lc_{z,prebend}} - 1 \tag{F.17}$$

Extending Equation F.17 to be used for any span-wise position (i) gives Equation F.18

$$E_i = \frac{F \times \cos\Gamma \times (Lc_z - Ln_{z,i}) + F \times \sin\Gamma \times (Lc_x - Ln_{x,i})}{F \times Lc_{z,prebend} - Ln_{z,prebend,i}} - 1 \tag{F.18}$$

A transformation of Equation F.18 gives Equation F.19:

$$E_i = \; cos\Gamma \times \frac{Lc_z - Ln_{z,i}}{Lc_{z,prebend} - Ln_{z,prebend,i}} + sin\Gamma \times \frac{Lc_x - Ln_{x,i}}{Lc_{z,prebend} - Ln_{z,prebend,i}} - 1 \tag{F.19}$$

E_i: Bending moment difference of calibration tests comparing the loading of an undeformed blade (and a loading perpendicular to the pitch axis) with an deformed blade (and the actual load direction) (node i)

Γ: Calibration load orthogonal to the pitch axis

Lc_z: Location (coordinate) of the calibration load attachment location in Z_{IEC} direction

$Lc_{z,prebend,i}$: Location (coordinate) of the calibration load attachment location in Z_{IEC} direction of the undeformed blade (node i)

Lc_x: Location (coordinate) of the calibration load attachment location in X_{IEC} direction (node i)

$Ln_{z,i}$: Location (coordinate) of a node in Z_{IEC} direction (node i)

$Ln_{z,prebend,i}$: Location (coordinate) of a node in Z_{IEC} direction of the undeformed blade (node i)

---

[58] As explained before, for the numeric determination of the deflection curve, the load F_{num} is always assumed to be perpendicular to the pitch axis, even though there is an angle Γ of $\leq 16°$ present, due to the blade being fixed with this angle to the test rig and a dead weight loading is used. On the contrary, when calculating the bending moment of the deformed blade, the influence of the exact load angle Γ to the pitch axis has to be taken into account.

$Ln_{x,i}$: Location (coordinate) of a node in X_{IEC} direction (node i)

$Ln_{x,prebend,i}$: Location (coordinate) of a node in X_{IEC} direction of the undeformed blade (node i)

When error E is known along the blade span, the bending moment calculated on the undeformed blade can be corrected and used for the determination of the calibration factors. Depending on the calibration method used, the bending moment has to be used in Equation 2.1 or Equation 2.3.

Appendix G

Data Acquisition at a Biaxial Test of a 40m Blade

Data was recorded with an HBM MGC$^+$ Measuring Amplifier System[59] using ML801B multi-channel amplifiers. The multi-channel data acquisition system was used in combination with the HBM "Catman Easy" software.

Strain-gauge Measurement

All over the blade more than 200 strain gauges were applied previously to the performed test. Mainly Vishay ED-DY-500BH-350 with a 4-wire cabling were used to automatically correct the wire resistance. On 13 radii, at least 4 strain gauges were applied at the leading edge, suction side, trailing edge and pressure side to be able to perform a calibration test according to Section 2.1.2. All strain gauges were connected to AP815i connector cards used in the HBM MGC$^+$ System. The bridge factor of the strain gauge is 1 and the gage factor 3.28. Axial strain was recorded (span-wise direction). The transverse sensitivity of these gages is with -0,1% negligible. The absolute uncertainty in the gage factor is ±3% so the strain values recorded have a corresponding uncertainty of ±3% . As the strain measurement was used in combination with a calibration test to determine the bending moments, the uncertainty is much smaller according to Section 3.1.1.

Temperature and Humidity Measurement

PT100 temperature sensors were connected to AP835 cards used in the HBM MGC$^+$ System. The temperature was measured at 2m and 24m span-wise position on the outside of the blade leading edge. A humidity sensor was located at 4m span-wise position.

---

[59] http://www.hbm.com/de/menu/produkte/messelektroniken/labor-pruefstand/

Force Measurement

In the push rod and on top of the pistons of both actuators, HBM force transducers type U5/100kN, U5/160kN and U5/200kN (2mV/V) were located. The calibration tests were performed using the type U5/100kN load cell. The force channel amplifier cards were located in the servo-hydraulic control system from INOVA[60]. All force channels were looped as voltage signals to the HBM MGC$^+$ System using AP401 amplifier cards.

The load cells were checked against an externally DKD calibrated load cell. Several load steps were analyzed with the DKD calibrated load cell and the load cells used in the test connected to one chain. An accuracy of $\leq$0.3% over the entire range of each load cell was determined. The whole chain of electronic devices was validated in total, starting at the load cell via the INOVA system and until the HBM system.

Displacement Measurement

The displacement was measured at 2 locations along the blade span, at the tip and at 81% span-wise position. A prototype AICON 3D MoveInspect HF system[61] was used. The advantage of the system is the high measurement frequency of up to 100Hz in combination with measuring absolute 3-D coordinates. Retro- reflecting target marks have to be applied to the blade. The position of the center of each target mark will be output as Cartesian coordinates in an arbitrary coordinate system and can be transferred into the IEC-61400-23 (2014) blade system. Using 2 digital cameras, the coordinates are determined by triangulation. The cameras itself were calibrated in position with optical marks fixed to the test hall walls. In Bürkner and Antoniou (2014), an absolute uncertainty of the system was roughly analyzed to be around ±3mm for the prototype system. The uncertainty is not taken into account for all further discussions, as movements of $\geq$1m will be analyzed. It is assumed that an accuracy of $\leq$0.3% will not lead to incorrect conclusions.

---

[60] http://www.inovatesting.net/de/

[61] http://www.aicon3d.de/produkte/moveinspect-technology.html

Appendix H

Actuator Forces at AMC

This example describes, how a sinusoidal actuator loading is exciting the blade **and** moving added masses at the same time without a significant change of the force amplitude (comparison of mechanical system 1a and 2a).

An arbitrary displacement of the blade of ±1m (at the location of the attached push rod) and a excitation frequency of 0.5Hz is used. To keep the blade oscillating, a sinusoidal amplitude of 31782N (push rod force 1a) is necessary. To compensate an additional mass, a sinusoidal force of 6190N is necessary[62]. The sum of the two sinusoidal forces is the actuator force to achieve both curves together at the same time. In Figure H.1 all described curves are shown. As a result, the amplitude of the sum of both curves is only increasing by 1.9% compared to the excitation force.

The reason is, that the both curves are out of phase. The phase of the force necessary to compensate the added mass is in phase with the deflection [63]. The phase of the *excitation force* is principally out of phase to the deflection, because the major damping is related to the 2nd power of the velocity. The exact phase relates on the type of damping and the quotient of excitation frequency to natural frequency of the System.

Because the amplitude of the sum of both curves does only slightly increases compared to the excitation force, the necessary increase of the excitation energy and therefore the energy consumption of the test is with +1.9% uncritical.

---

[62] This force is necessary to move the added 900kg at simulation 2a sinusoidal at the displacement and frequency of 2a.

[63] Using the fundamental equations for a spring-mass-system $m \times \ddot{y} = -c \times \dot{y}$ and $y = A \times \sin(\omega_1 \times t + \alpha)$ shows, that the maximum spring force and the maximum displacement is exactly at the same time, because the second derivative of sin is a sin curve again. Therefore, with assuming that the loading of the actuator has to be comparable with the spring force, the sinusoidal load to compensate the mass has to be exactly in phase with the deflection of the blade at the location of the mass.

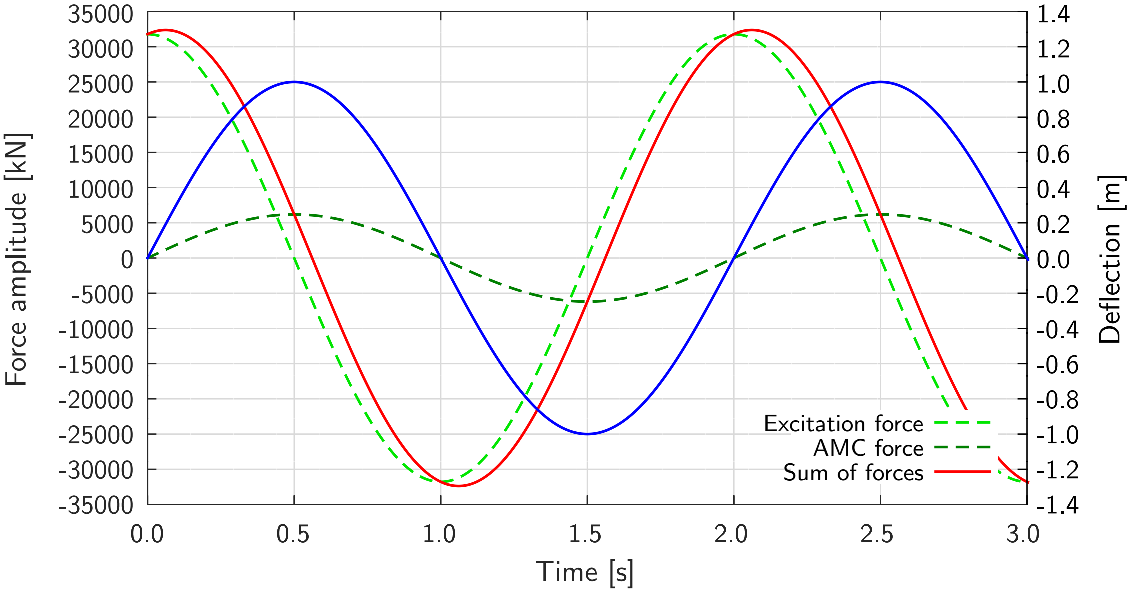

Figure H.1: Example curves for loading the blade when having an AMC besides the excitation of the blade. In blue: Displacement of the load frame of ±1m; In bright green: Excitation force to oscillate the blade against damping; In dark green: Force for accelerating the mass which shall be compensated; In red: Sum of the two green forces.

Appendix I

Actuator and Push-rod Forces AMC

In simulations 1a, 2a and 3a the test is excited at the natural frequencies of each system. The actuator only has to put as much energy into the blade oscillation, as is necessary to keep the oscillation going with the specified amplitude. The air damping and the material damping has to be compensated. According to Table I.1, the maximum actuator force (actuator at 50% Lb) is 63.821N for 1a, 60.250N for 2a and 57.300N for 3a. The excitation force is lowering from 1a over 2a to 3a. This is, because the natural frequency and therefore the excitation frequency is getting lower from 1a over 2a to 3a, which reduces the air damping. Because the bell crank leaver arm has a relation of 1/2, the push rod force is exactly half of the actuator force for 1a and 2a. For 3a the push rod force is higher than 1/2 of the actuator force, because one mass is located directly at the bell crank. Having a mass-spring system in mind, the mass at the bell crank (Figure 5.5, (m_3)) has to be accelerated by the blade which corresponds to the spring. The force necessary to accelerate this mass does increase the push rod force in comparison to 1a and 2a.

For the simulations 1a, 2b and 3c the test is always excited at the natural frequencies of 1a. Like described above, the actuator compensates the air damping and material damping to achieve a constant amplitude of the oscillation. Besides this, the actuator has to move the added masses of 900kg at 2b and additional 900kg at 3c. But when comparing the push rod forces given in Table I.1, the forces can be evaluated as being equal (31.782N at 1a, 31.832N at 2b and 31.253N at 3c[64]). Where the compensation of the additional mass at 2b has to be transmitted by the push rod, the additional mass of 3c is directly attached to the bell crank and will not significantly increase the push rod force. Still, to understand why the force to move the additional mass of 2b (according to the AMC method) is not significantly higher, an example described in Appendix H shall explain this issue. Besides, when comparing the actuator forces of 1a, 2b and 3c, the increasing force to compensate the added mass of 3c is clearly visual (63.821N at 1a, 63.650N at 2b and 65.750N at 3c). What also can be clearly seen here is, that with adding mass to the bell crank structure (m_3) Figure 5.5, this does not lead to a higher loading of the blade but only to a higher actuator force, because the push rod force stays the same going from 1a to 2b to 3c. All attached masses to the bell crank are therefore compensated with a higher actuator force but do have no influence on the oscillating blade.

---

[64] A divergence of at least ±0.5% is given due to a divergence in achieving exactly the same amplitude of the oscillation.

Table I.1: Different mechanical setups used for the FE analysis of the AMC method. The 1st (flap-wise) natural frequency and the test or excitation frequency is given in relation to the natural frequency of setup 1. In column 'Comment' the excitation frequency is explained.

Set-up	**Bell crank**	**Mass 1** (90% Lb)	**Mass 2** (50% Lb)	**Mass 3** (50% Lb)	**NF**	**Test freq.**	**Comment**	**Push-rod** (50% Lb)	**Actuator** (50% Lb)	**Push-rod** (90% Lb)
[-]	[-]	[kg]	[kg]	[kg]	[-]	[-]	[-]	[N]	[N]	[N]
1a	**2**	667	0	0	1.0	1.0	NF of 1	31782	63821	-
2a	**2**	667	900	0	0.993	0.993	NF of 2	30017	60250	-
2b	**2**	667	900	0	0.993	1.0	NF of 1	31832	63650	-
3a	**2**	667	900	900	0.9859	0.9859	NF of 3	29549	57300	-
3b	**2**	667	900	900	0.9859	0.993	NF of 2	29755	60350	-
3c	**2**	667	900	900	0.9859	1.0	NF of 1	31253	65750	-
3d	**2**	667	900	900	0.9859	0.9691	$\leq$NF of 3	32867	59200	-
4a	**1 and 2**	1167	900	900	0.8555	0.8555	NF of 4	-	-	1496
4b	**1 and 2**	1167	900	900	0.8555	0.9859	NF of 3	-	-	76073
5a	**1 and 2**	1167	1800	900	0.8512	0.9859	NF of 3	-	-	75694

In comparison to 1a, in 2b 900kg where added at $\approx 50\%$ span-wise position as shown in Table I.1. With using the excitation frequency and the displacement amplitude from the FE analysis results, a maximum force of 6.190N can be calculated to accelerate 900kg to the desired oscillation[65]. After adjusting the excitation frequency, used in the example of Appendix H (Figure H.1) according to the correct value of simulation 2a, the theoretic phase to have equal amplitudes gives -0.034s. Calculating the phase between the actuator and displacement curve of the FE analysis of 1a and 2a gives -0.06s. Both values are not equal, but close enough to conclude, that the results presented in Table I.1 and therefore the FE analysis performed are reliable.

---

[65] To calculate this force, the second derivative of the equation $y = A \times \sin(\omega_1 \times t + \alpha)$ was used to calculate the maximum acceleration of the oscillating mass. With force is equal to mass times acceleration the maximum spring or actuator force was calculated to 6.190N .

Appendix J

FE Model of a BEDEX Test Simulation

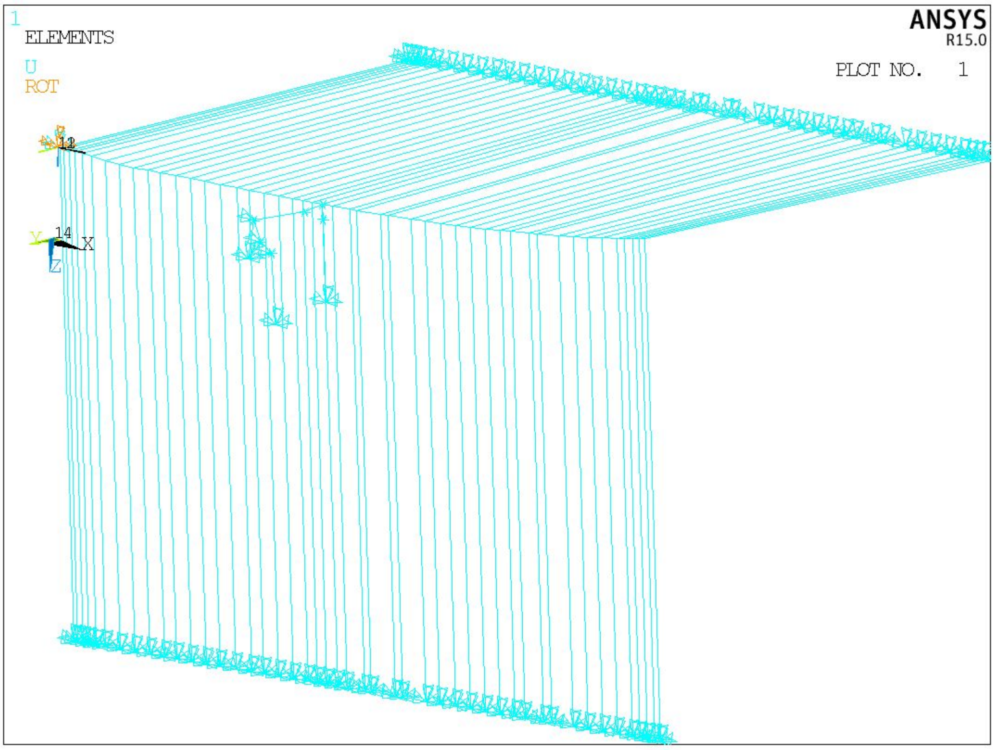

Figure J.1: FEs model to simulate a dynamic uniaxial test, including blade elements, air damping elements, excitation mechanism elements and boundary conditions.

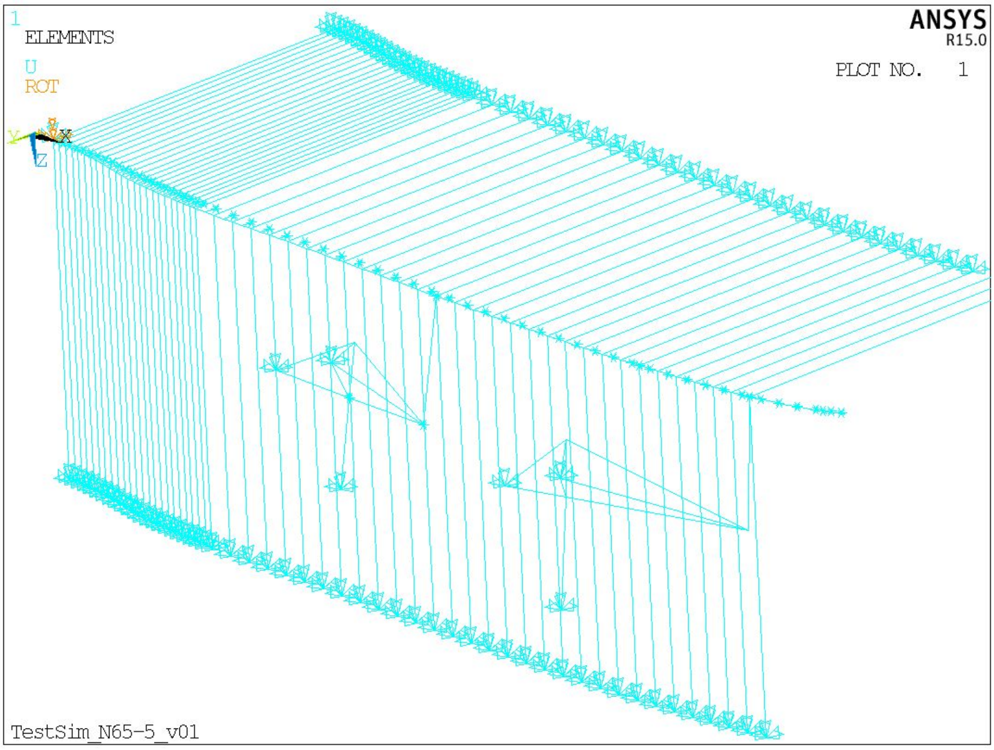

Figure J.2: FEs model to simulate AMC, including blade elements, air damping elements, excitation mechanism elements and boundary conditions.

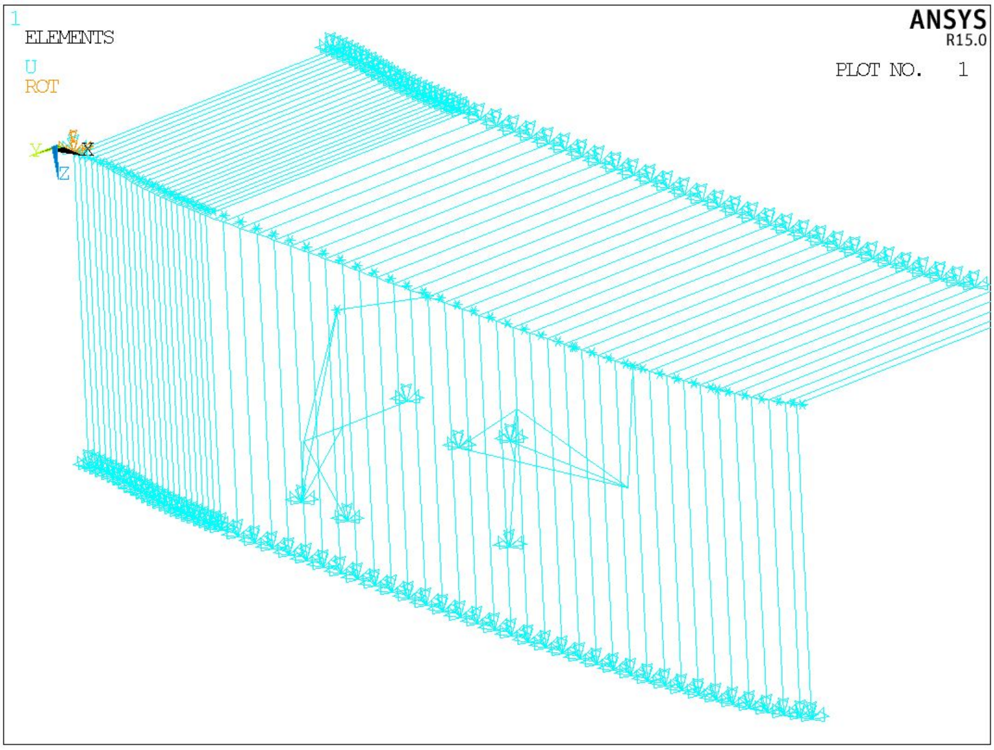

Figure J.3: FEs model to simulate a BEDEX test including blade elements, air damping elements, excitation mechanism elements and boundary conditions.

Appendix K

ANSYS FE Code

K.1 Simulation of Calibration Tests

```
FINISH $ /CLEAR
*DO,aaa,1,2,1   !Flap and lead-lag calc
*DO,bbb,1,9,1   !Distance of loading location
PARSAV,ALL,Doloop,txt

FINISH $ /CLEAR
PARRES,NEW,Doloop,txt

/UNITS,SI $ /TITLE,IWT_82_v01 $ /FILNAME,IWT_82_v01,0 $ /CONFIG,nres,50000

! ---------------------------PREPROCESSOR------------------
/PREP7
NLGEOM,on
ET,1,BEAM188,0,0,3
TYPE,1
LOCAL,11,0,0,0,0,0,0,0

N,11,0,0,0
LOCAL,11 $ N,12,0.87,0,0 $ LOCAL,11,,,,,,-2.23548039267373 $ N,201,0,0,10 $ SECTYPE,12,BEAM,ASEC $
SECDATA,0.32046409,0.15029438,-0.00087714,0.12223735,,0.1338844,0,0,-0.00581781,-0.07100295
SECNUM,12 $ MP,PRXY,12,0.333 $ MP,EX,12,11827719292.9791 $ MP,DENS,12,1264.8317 $ MAT,12 $
EN,11,11,12,201
LOCAL,11 $ N,13,2.1,0,0 $ LOCAL,11,,,,,,11.8285849542089 $ N,202,0,0,10 $ SECTYPE,13,BEAM,ASEC $
SECDATA,0.46795194,0.20943721,0.0033733,0.19897137,,0.26531105,0,0,0.01286741,-0.06726987
SECNUM,13 $ MP,PRXY,13,0.333 $ MP,EX,13,7579132592.12046 $ MP,DENS,13,892.7294 $ MAT,13 $
EN,12,12,13,202
LOCAL,11 $ N,14,3.851,0,0 $ LOCAL,11,,,,,,-21.0746809403823 $ N,203,0,0,10 $ SECTYPE,14,BEAM,ASEC $
SECDATA,0.43930309,0.16609498,0.01041575,0.22789001,,0.32313979,0,0,-0.01160808,-0.08795219
SECNUM,14 $ MP,PRXY,14,0.333 $ MP,EX,14,6250617540.61416 $ MP,DENS,14,649.2957 $ MAT,14 $
EN,13,13,14,203
LOCAL,11 $ N,15,5.6,0,0 $ LOCAL,11,,,,,,-21.8402622895147 $ N,204,0,0,10 $ SECTYPE,15,BEAM,ASEC $
SECDATA,0.40517891,0.12561651,0.01100479,0.19872481,,0.30543553,0,0,-0.06252477,-0.05827533
SECNUM,15 $ MP,PRXY,15,0.333 $ MP,EX,15,5525388525.28134 $ MP,DENS,15,561.6957 $ MAT,15 $
EN,14,14,15,204
LOCAL,11 $ N,16,7.1,0,0 $ LOCAL,11,,,,,,-17.5260975048197 $ N,205,0,0,10 $ SECTYPE,16,BEAM,ASEC $
SECDATA,0.36617053,0.09523621,0.00725024,0.15901014,,0.25095207,0,0,-0.08979408,-0.03174497
```

```
SECNUM,16 $ MP,PRXY,16,0.333 $ MP,EX,16,5202985068.18667 $ MP,DENS,16,628.3239 $ MAT,16 $
EN,15,15,16,205
LOCAL,11 $ N,17,8.851,0,0 $ LOCAL,11,,,,,,-12.0422863841028 $ N,206,0,0,10 $ SECTYPE,17,BEAM,ASEC $
SECDATA,0.32652641,0.06503393,0.0031943,0.12509935,,0.19992193,0,0,-0.01165161,-0.00778522
SECNUM,17 $ MP,PRXY,17,0.333 $ MP,EX,17,5204694468.66488 $ MP,DENS,17,588.8407 $ MAT,17 $
EN,16,16,17,206
LOCAL,11 $ N,18,10.972,0,0 $ LOCAL,11,,,,,,-8.61683331614196 $ N,207,0,0,10 $ SECTYPE,18,BEAM,ASEC $
SECDATA,0.28346712,0.03996997,0.00148226,0.08879967,,0.15383724,0,0,-0.03226039,0.0246043
SECNUM,18 $ MP,PRXY,18,0.333 $ MP,EX,18,5750074999.88006 $ MP,DENS,18,527.2534 $ MAT,18 $
EN,17,17,18,207
LOCAL,11 $ N,19,12.835,0,0 $ LOCAL,11,,,,,,-6.64095888782384 $ N,208,0,0,10 $ SECTYPE,19,BEAM,ASEC $
SECDATA,0.251823,0.02635743,0.00095335,0.06066706,,0.10153665,0,0,-0.10976315,0.05162746
SECNUM,19 $ MP,PRXY,19,0.333 $ MP,EX,19,6306491861.34706 $ MP,DENS,19,491.8184 $ MAT,19 $
EN,18,18,19,208
LOCAL,11 $ N,20,14.6,0,0 $ LOCAL,11,,,,,,-4.4879572486862 $ N,209,0,0,10 $ SECTYPE,20,BEAM,ASEC $
SECDATA,0.2263122,0.01712352,0.00041513,0.04464308,,0.07733957,0,0,-0.12636507,0.07867027
SECNUM,20 $ MP,PRXY,20,0.333 $ MP,EX,20,7227723472.2653 $ MP,DENS,20,546.4446 $ MAT,20 $
EN,19,19,20,209
LOCAL,11 $ N,21,16.36,0,0 $ LOCAL,11,,,,,,-3.02816198326525 $ N,210,0,0,10 $ SECTYPE,21,BEAM,ASEC $
SECDATA,0.20320297,0.01131047,0.00014246,0.03280622,,0.05635382,0,0,-0.1275034,0.10905997
SECNUM,21 $ MP,PRXY,21,0.333 $ MP,EX,21,8044762829.9921 $ MP,DENS,21,499.581 $ MAT,21 $
EN,20,20,21,210
LOCAL,11 $ N,22,17.6,0,0 $ LOCAL,11,,,,,,-2.30452819754742 $ N,211,0,0,10 $ SECTYPE,22,BEAM,ASEC $
SECDATA,0.14436522,0.00646578,0.00005689,0.0197664,,0.04399287,0,0,-0.12554018,0.13598071
SECNUM,22 $ MP,PRXY,22,0.333 $ MP,EX,22,11091668062.4322 $ MP,DENS,22,988.6585 $ MAT,22 $
EN,21,21,22,211
LOCAL,11 $ N,23,19.602,0,0 $ LOCAL,11,,,,,,-1.50207646809197 $ N,212,0,0,10 $ SECTYPE,23,BEAM,ASEC $
SECDATA,0.131449,0.00426745,0.00002322,0.0142569,,0.02519736,0,0,-0.12742273,0.19524152
SECNUM,23 $ MP,PRXY,23,0.333 $ MP,EX,23,12277017702.6832 $ MP,DENS,23,767.7809 $ MAT,23 $
EN,22,22,23,212
LOCAL,11 $ N,24,21.388,0,0 $ LOCAL,11,,,,,,-1.28206469036153 $ N,213,0,0,10 $ SECTYPE,24,BEAM,ASEC $
SECDATA,0.10112062,0.00255146,0.00003741,0.00912519,,0.0189837,0,0,-0.12780889,0.26953299
SECNUM,24 $ MP,PRXY,24,0.333 $ MP,EX,24,15188836856.4196 $ MP,DENS,24,1076.5355 $ MAT,24 $
EN,23,23,24,213
LOCAL,11 $ N,25,23.556,0,0 $ LOCAL,11,,,,,,-1.03697782081842 $ N,214,0,0,10 $ SECTYPE,25,BEAM,ASEC $
SECDATA,0.089194422,0.00166424,0.00004547,0.00685803,,0.01179488,0,0,-0.12510554,0.37150974
SECNUM,25 $ MP,PRXY,25,0.333 $ MP,EX,25,15624289823.8636 $ MP,DENS,25,948.6231 $ MAT,25 $
EN,24,24,25,214
LOCAL,11 $ N,26,25.502,0,0 $ LOCAL,11,,,,,,-0.807393238466541 $ N,215,0,0,10 $ SECTYPE,26,BEAM,ASEC $
SECDATA,0.078275703,0.00113337,0.00003947,0.00520755,,0.00887644,0,0,-0.12449953,0.48110153
SECNUM,26 $ MP,PRXY,26,0.333 $ MP,EX,26,15578877649.9395 $ MP,DENS,26,924.1397 $ MAT,26 $
EN,25,25,26,215
LOCAL,11 $ N,27,27.115,0,0 $ LOCAL,11,,,,,,-0.573153784467293 $ N,216,0,0,10 $ SECTYPE,27,BEAM,ASEC $
SECDATA,0.069402789,0.00080534,0.00003181,0.00429977,,0.00745918,0,0,-0.0977227,0.58764404
SECNUM,27 $ MP,PRXY,27,0.333 $ MP,EX,27,15351986791.1936 $ MP,DENS,27,1013.3313 $ MAT,27 $
EN,26,26,27,216
LOCAL,11 $ N,28,28.459,0,0 $ LOCAL,11,,,,,,-0.357324084879476 $ N,217,0,0,10 $ SECTYPE,28,BEAM,ASEC $
SECDATA,0.058459262,0.00057912,0.00002246,0.00331686,,0.00542549,0,0,-0.11613852,0.68698303
SECNUM,28 $ MP,PRXY,28,0.333 $ MP,EX,28,15174274009.8224 $ MP,DENS,28,1140.7714 $ MAT,28 $
EN,27,27,28,217
LOCAL,11 $ N,29,30.1,0,0 $ LOCAL,11,,,,,,0.155254057590379 $ N,218,0,0,10 $ SECTYPE,29,BEAM,ASEC $
SECDATA,0.050660547,0.00040214,0.00000665,0.00283041,,0.00435787,0,0,-0.10607234,0.81921088
SECNUM,29 $ MP,PRXY,29,0.333 $ MP,EX,29,14178002065.3942 $ MP,DENS,29,960.049 $ MAT,29 $
EN,28,28,29,218
```

```
LOCAL,11 $ N,30,31.6,0,0 $ LOCAL,11,,,,,,0.273340241779967 $ N,219,0,0,10 $ SECTYPE,30,BEAM,ASEC $
SECDATA,0.039812316,0.00025699,0.00000781,0.00228493,,0.00347231,0,0,-0.09219399,0.95600031
SECNUM,30 $ MP,PRXY,30,0.333 $ MP,EX,30,13197026518.1257 $ MP,DENS,30,878.1906 $ MAT,30 $
EN,29,29,30,219
LOCAL,11 $ N,31,32.7,0,0 $ LOCAL,11,,,,,,0.591391938694573 $ N,220,0,0,10 $ SECTYPE,31,BEAM,ASEC $
SECDATA,0.026927166,0.00014982,0.00000121,0.00152724,,0.00254513,0,0,-0.04058329,1.0729398
SECNUM,31 $ MP,PRXY,31,0.333 $ MP,EX,31,15652154407.9314 $ MP,DENS,31,1586.8036 $ MAT,31 $
EN,30,30,31,220
LOCAL,11 $ N,32,34.532,0,0 $ LOCAL,11,,,,,,0.940623364848394 $ N,221,0,0,10 $ SECTYPE,32,BEAM,ASEC $
SECDATA,0.023534891,0.00009651,-0.00000103,0.00116946,,0.00155566,0,0,-0.02958811,1.2794131
SECNUM,32 $ MP,PRXY,32,0.333 $ MP,EX,32,15825501804.9584 $ MP,DENS,32,1304.2041 $ MAT,32 $
EN,31,31,32,221
LOCAL,11 $ N,33,36.602,0,0 $ LOCAL,11,,,,,,0.729723323301177 $ N,222,0,0,10 $ SECTYPE,33,BEAM,ASEC $
SECDATA,0.017437469,0.00004332,0.00000509,0.0007413,,0.00089453,0,0,-0.0106768,1.5419778
SECNUM,33 $ MP,PRXY,33,0.333 $ MP,EX,33,14712925367.7813 $ MP,DENS,33,931.3294 $ MAT,33 $
EN,32,32,33,222
LOCAL,11 $ N,34,37.601,0,0 $ LOCAL,11,,,,,,0.492243523152569 $ N,223,0,0,10 $ SECTYPE,34,BEAM,ASEC $
SECDATA,0.0060641108,0.00000873,0.00000298,0.00022853,,0.00043659,0,0,-0.10336244,1.6972826
SECNUM,34 $ MP,PRXY,34,0.333 $ MP,EX,34,18631059643.5672 $ MP,DENS,34,2560.0078 $ MAT,34 $
EN,33,33,34,223
LOCAL,11 $ N,35,39.251,0,0 $ LOCAL,11,,,,,,0.994754390243804 $ N,224,0,0,10 $ SECTYPE,35,BEAM,ASEC $
SECDATA,0.00099552173,0.00000024,0.00000004,0.00000601,,0.00000692,0,0,-0.03101309,1.937851
SECNUM,35 $ MP,PRXY,35,0.333 $ MP,EX,35,21462774097.357 $ MP,DENS,35,1729.0334 $ MAT,35 $
EN,34,34,35,224
LOCAL,11 $ N,36,39.581,0,0 $ LOCAL,11,,,,,,0.552789369263077 $ N,225,0,0,10 $ SECTYPE,36,BEAM,ASEC $
SECDATA,0.00025764261,0.00000024,0.00000004,0.00000601,,0.0000001,0,0,-0.01227695,1.9969993
SECNUM,36 $ MP,PRXY,36,0.333 $ MP,EX,36,21395527315.9203 $ MP,DENS,36,39752.2619 $ MAT,36 $
EN,35,35,36,225

! ---------------------------LOADING EQUIPEMENT------------
xLoadNode  = 34
xLoadNodeX = 37.601

LOCAL,11,0,0,0,0,0,0,0
*IF,aaa,eq,1,THEN
   *IF,bbb,eq,9,then
      xNode500=-xLoadNodeX
   *ELSEIF,bbb,eq,8,then
      xNode500=-xLoadNodeX/2
   *ELSE
      xNode500=-xLoadNodeX/(11-bbb)
   *ENDIF
   N,500,xLoadNodeX,0,xNode500
*ELSEIF,aaa,eq,2,THEN
   *IF,bbb,eq,9,then
      xNode500=xLoadNodeX
   *ELSEIF,bbb,eq,8,then
      xNode500=xLoadNodeX/2
   *ELSE
      xNode500=+xLoadNodeX/(11-bbb)
   *ENDIF
   N,500,xLoadNodeX,xNode500,0
*ELSE
   /EXIT,NOSAVE
```

```
*ENDIF

ET,500,LINK11,
MP,damp,1000
R,500,0.0,1e4,0

TYPE,500  $ MAT,500  $ real,500
NUMSTR,ELEM,1000
E,500,xLoadNode
FINISH

! ---------------------------SOLUTION STATIC---------------
/SOLU
MDELE,all,all $ D,11,ALL
D,500,Uy,,,,,Ux,uz

ANTYPE,STATIC
NLGEOM,on
SOLCONTROL,on
NROPT,full
AUTOTS,off
OUTRES,all,all $ OUTPR,all,ALL

xTimesteps = 10
xSubsteps  = 5
xFactor    = 1/xTimesteps

*IF,aaa,eq,1,THEN
   xmaxFz=-10874
*ELSE
   xmaxFz=-7700
*ENDIF

! ---------------------------LOADING PHASE-----------------
ACEL,0,0,0
*DO,xTime,1,xTimesteps,1
   KBC,0
   TIME,xTime
   NSUBST,xSubsteps
   SFE,1000,2,pres,1,xmaxFz*xFactor,
   xFactor=xFactor+(1/(xTimesteps))
   SOLVE
*ENDDO
FINISH

! ---------------------------POSTPROCESSING----------------
/INPUT,Post26,txt ! Export Results to Excel

*ENDDO  !Flap and lead-lag calc
*ENDDO  !Distance of loading location
```

K.2 Simulation of a Uniaxial Test

K.2.1 Blade Modeling

```
/prep7
!----------------------------ELEMENT TYPES-----------------
ET,1,BEAM189,0,0,,0,,,,,,,,0
ET,2,MASS21,0,1,0
ET,3,MPC184,1,0

!----------------------------NODES------------------------
NBLOCK,6,SOLID,,...
(3i8,6e16.8)
    1   0   0 ... ... ...
    2   0   0 ... ... ...
    3   0   0 ... ... ...
...
 1001   0   0 ... ... ...
 1002   0   0 ... ... ...
 1003   0   0 ... ... ...
...

!----------------------------ELEMENTS---------------------
EBLOCK,19,solid,,...
(19i8)
  1    1       1    01    0    0    0    0    4    0    1    1     4    2    3
  1    1       1    02    0    0    0    0    4    0    2    4     7    5    6
  1    1       1    03    0    0    0    0    4    0    3    7    10    8    9
...
  1    2    2001     1    0    0    0    0    2    0    2001    3001
  1    2    2002     1    0    0    0    0    2    0    2002    3002
  1    2    2003     1    0    0    0    0    2    0    2003    3003
...
  1    3       1     1    0    0    0    0    2    0    3001    2    3001
  1    3       1     1    0    0    0    0    2    0    3002    5    3002
  1    3       1     1    0    0    0    0    2    0    3003    8    3003
...

!----------------------------SECTIONS---------------------
SECTYPE,1,comb,matrix
CBMX,1, ..., ..., ..., ..., ..., ...,
CBMX,2, ..., ..., ..., ..., ..., ...,
CBMX,3, ..., ..., ..., ..., ..., ...,
CBMX,4, ..., ..., ..., ..., ..., ...,
CBMX,5, ..., ..., ..., ..., ..., ...,
CBMX,6, ..., ..., ..., ..., ..., ...,
...

!----------------------------MASSES-----------------------
*SET,Gewicht(1),... $ *SET,J-xx(i),... $ *SET,J-yz(i),... $ *SET,J-zz(i),...
*SET,Gewicht(2),... $ *SET,J-xx(i),... $ *SET,J-yz(i),... $ *SET,J-zz(i),...
*SET,Gewicht(3),... $ *SET,J-xx(i),... $ *SET,J-yz(i),... $ *SET,J-zz(i),...
```

```
...

*DO,i,1, ...
  r,2000+i,Gewicht(i), Gewicht(i), Gewicht(i), J-xx(i), J-yz(i), J-zz(i)
*ENDDO
FINISH
```

K.2.2 Damper Modeling

```
!----------------------------DECLARATIONS------------------
xDamperLength = 50
xDichte       = 1.25
xCW_Flap      = 1.4
xCW_LeadLag   = 0.2

!----------------------------DAMPER-NODES------------------
*DO,iii,1,xLastDamperNode,3
   *GET,xN_x,NODE,iii,LOC,x
   *GET,xN_y,NODE,iii,LOC,y
   *GET,xN_z,NODE,iii,LOC,z
   N,10000+iii,xN_x,xN_y,xN_z+xDamperLength
   N,20000+iii,xN_x,xN_y-xDamperLength,xN_z
*ENDDO

!----------------------------CORDLENGTH & PROFILEHIGHT-----
*DEL,xCord          $ *DIM,xCord,array,59
*DEL,xProfileHight  $ *DIM,xProfileHight,array,59

xCord(1)=... $ xProfileHight(1)=...
xCord(2)=... $ xProfileHight(2)=...
xCord(3)=... $ xProfileHight(3)=...
...

!----------------------------AREA-FLAP---------------------
*DEL,xAreaFlap $ *DIM,xAreaFlap,array,59
*DO,jjj,1,59,1
   *GET,xN1_x,NODE,jjj*3+1-3,LOC,x
   *GET,xN2_x,NODE,jjj*3+1,LOC,x
   xAreaFlap(jjj)=xCord(jjj)*(xN2_x-xN1_x)
*ENDDO

!----------------------------AREA-LEAD-LAG-----------------
*DEL,xAreaLeadLag $ *DIM,xAreaLeadLag,array,59
*DO,jjj,1,59,1
   *GET,xN1_x,NODE,jjj*3+1-3,LOC,x
   *GET,xN2_x,NODE,jjj*3+1,LOC,x
   xAreaLeadLag(jjj)=xProfileHight(jjj)*(xN2_x-xN1_x)
*ENDDO

!----------------------------DAMPER-ELEMENS-FLAP-----------
*DO,jjj,1,xLastDamperElement,1
```

```
   R,10000+jjj,0,1e-5,0.5*xDichte*xAreaFlap(jjj)*xCW_Flap
   REAL,10000+jjj
   EN,10000+jjj,jjj*3+1-3,10000+jjj*3+1-3
*ENDDO

!----------------------------DAMPER-ELEMENS-LEAD-LAG-------
*DO,jjj,1,xLastDamperElement,1
   R,20000+jjj,0,1e-5,0.5*xDichte*xAreaLeadLag(jjj)*xCW_LeadLag
   REAL,20000+jjj
   EN,20000+jjj,jjj*3+1-3,20000+jjj*3+1-3
*ENDDO
```

K.2.3 Program - Uniaxial Test

```
FINISH
/CLEAR $ /UNITS,SI $ /CONFIG,nres,50000
/TITLE,... $ /FILNAME,...,0

! ---------------------------PREPROCESSOR------------------
xLastBladeNode     = 163
xLastBladeElement  = (xLastBladeNode-1)/3
xLastDamperNode    = xLastBladeNode-3+1
xLastDamperElement = xLastBladeElement
xLastMassElement   = xLastBladeElement

xFpwFact           = 1
xLlwFact           = 1.10

/INPUT,Blade,txt

/PREP7
ET,801,MPC184,1

xExtNode = 163
*GET,xN_x,NODE,xExtNode,LOC,x
*GET,xN_y,NODE,xExtNode,LOC,y
*GET,xN_z,NODE,xExtNode,LOC,z

! ---------------------------EXTRA MASSES------------------
ET,700,MASS21,0,1,0
TYPE,700

R,701,2990,2990,2990,0,0,0
R,702,   0,   0,   0,0,0,0
R,703,   0,   0,   0,0,0,0
R,704,   0,   0,   0,0,0,0
R,705,   0,   0,   0,0,0,0
R,706, 667, 667, 667,0,0,0
R,707,   0,   0,   0,0,0,0
R,708,   0,   0,   0,0,0,0
```

```
REAL,701 $ EN,701,109
REAL,702 $ EN,702,118
REAL,703 $ EN,703,127
REAL,704 $ EN,704,136
REAL,705 $ EN,705,145
REAL,706 $ EN,706,160
REAL,707 $ EN,707,163
REAL,708 $ EN,708,172

FINISH

! ---------------------------MODAL ANALYSES----------------
/SOLU
ANTYPE,MODAL
MODOPT,LANB,10,,,
MXPAND,10
M,all,all
D,1,all
SOLVE
FINISH

! ---------------------------PREPROCESSOR------------------
/PREP7
ET,900,COMBIN14,1,0,0
MP,Damp,50,1e-11
TYPE,900
MAT,50

/INPUT,Damper,txt

! ---------------------------LOADING EQUIPEMENT------------
xLoadNode=109
*GET,xN_x,NODE,xLoadNode,LOC,x
*GET,xN_y,NODE,xLoadNode,LOC,y
*GET,xN_z,NODE,xLoadNode,LOC,z
N,500,xN_x,xN_y,xN_z+10
ET,500,LINK11
MP,damp,1000
R,500,1e2,0,0
TYPE,500 $ MAT,500 $ REAL,500
EN,501,500,xLoadNode
FINISH

! ---------------------------SOLUTION TRANSIENT------------
/SOLU

MDELE,all,all         $ D,1,ALL
NSEL,S,,,10001,1175,3 $ D,all,Uy,,,,,Ux,uz $ NSEL,ALL
NSEL,S,,,20001,2175,3 $ D,all,Uy,,,,,Ux,uz $ NSEL,ALL
D,500,Uy,,,,,Ux,uz

ANTYPE,TRANS
NLGEOM,on
SOLCONTROL,on
```

```
AUTOTS,on

! --------------------------CALCULATION PARAMETERS-------
xFrequy   = 0.4452
xTimeEnd  = 60
xmaxF     = 25000

xTimestep = 0.05
xDELTIM   = 0.025

xALPHAD   = 0
xBETAD    = 0.0045
xKBC      = 1

! -------  ----------------DEFINITIONS------------------
xTy       = 1/xFrequy
PI        = acos(-1)
xTimeIni1 = 1
xTimeIni  = 5

xpZeile   = 6
xKraft    = 0

! --------------------------LOADING PHASE 1--------------
ACEL,0,0,0.0
*DO,xdozeit,0.05,xTimeIni1,0.05
   TIME,xdozeit
   BETAD,0.3
   DELTIM,0.025
   SOLVE
   /INPUT,Post26,txt ! Export Results to Excel
*ENDDO

! --------------------------LOADING PHASE 2--------------
ACEL,0,0,-9.81
*DO,xdozeit,xTimeIni1+0.05,xTimeIni,0.05
   TIME,xdozeit
   BETAD,0.8
   DELTIM,0.025
   SOLVE
   /INPUT,Post26,txt ! Export Results to Excel
*ENDDO

! --------------------------OSZILATION-------------------
zeit   = xTimeIni+xTimestep
steig  = 0
xsteig = 0.005
outres,all,all
*DO,xdozeit,zeit,xTimeEnd,xTimestep
   TIME,xdozeit
   DELTIM,xDELTIM
   BETAD,xBETAD
   KBC,xKBC
   *IF,steig,LT,1,then
```

```
      steig=steig+xsteig
   *ELSE
      steig=1
   *ENDIF
   xKraft=steig*xmaxF*sin((xdozeit-zeit)*2*PI/xTy)
   SFE,501,2,pres,1,xKraft,
   SOLVE
   /INPUT,Post26,txt ! Export Results to Excel
*ENDDO
outres,all,all
FINISH
```

K.3 Simulation of the AMC Method

The blade model of Section K.2.1 is used. The damper code of Section K.2.2 is used.

K.3.1 Program - AMC

```
FINISH
/CLEAR $ /UNITS,SI $ /CONFIG,nres,50000
/TITLE,... $ /FILNAME,...,0

! ---------------------------PREPROCESSOR------------------
xLastBladeNode     = 163
xLastBladeElement  = (xLastBladeNode-1)/3
xLastDamperNode    = xLastBladeNode-3+1
xLastDamperElement = xLastBladeElement
xLastMassElement   = xLastBladeElement

xFpwFact = 1
xLlwFact = 1.10

/INPUT,Blade,txt

xBellCrank32v = 0
xBellCrank58v = 1

/PREP7
ET,801,MPC184,1
! ---------------------------LOADING EQUIPEMENT 2----------
*IF,xBellCrank32v,EQ,1,THEN
   xLPR = 7
   xLBC = 6
   xHOT = 3
   xLOA = 5
   xWOT = 4

   xLoadNode=109
```

```
   *GET,xN_x,NODE,xLoadNode,LOC,x
   *GET,xN_y,NODE,xLoadNode,LOC,y
   *GET,xN_z,NODE,xLoadNode,LOC,z
   xLoadNode1=xLoadNode-2
   *GET,xN1_x,NODE,xLoadNode1,LOC,x
   *GET,xN1_y,NODE,xLoadNode1,LOC,y
   *GET,xN1_z,NODE,xLoadNode1,LOC,z
   xAngl = (xN1_z-xN_z) / (xN_x-xN1_x)
   xAngy = 0.2162

   N,500,xN_x+(xLPR*xAngl),
         xN_y+(xLPR*xAngy),
         xN_z+xLPR
   N,501,xN_x+(xLPR*xAngl)-xLBC,
         xN_y+(xLPR*xAngy),
         xN_z+xLPR+(xLBC*xAngl)
   N,502,xN_x+(xLPR*xAngl)-2*xLBC,
         xN_y+(xLPR*xAngy),
         xN_z+xLPR+(2*xLBC*xAngl)
   N,503,xN_x+(xLPR*xAngl)-xLBC-(xHOT*xAngl),
         xN_y+(xLPR*xAngy)-(xHOT*xAngy),
         xN_z+xLPR+(xLBC*xAngl)-xHOT
   N,504,xN_x+(xLPR*xAngl)-xLBC+(xLOA*xAngl),
         xN_y+(xLPR*xAngy)+(xLOA*xAngy),
         xN_z+xLPR+(xLBC*xAngl)+xLOA
   N,505,xN_x+(xLPR*xAngl)-2*xLBC,
         xN_y+(xLPR*xAngy)-xWOT,
         xN_z+xLPR+(2*xLBC*xAngl)+(xWOT*xAngy)

   ET,500,LINK11
   MP,dens,0
   TYPE,500

   R,500,2.1e11*0.1,0
   REAL,500
   EN,500,500,xLoadNode

   EN,501,500,501
   EN,502,501,502
   EN,503,502,503
   EN,504,503,500
   EN,505,501,503

   EN,507,505,503
   EN,508,505,501
   EN,509,505,500

   R,506,1e2,0,0
   REAL,506
   EN,506,501,504
*ELSE $ *ENDIF

! ---------------------------LOADING EQUIPEMENT 3 ---------
*IF,xBellCrank58v,EQ,1,THEN
```

```
xLPR2  = 5
x1LBC2 = 9
x2LBC2 = 3
xHOT2  = 3
xLOA2  = 5
xWOT2  = 4

xLoadNode2=160
*GET,xN_x2,NODE,xLoadNode2,LOC,x
*GET,xN_y2,NODE,xLoadNode2,LOC,y
*GET,xN_z2,NODE,xLoadNode2,LOC,z
xLoadNode3=xLoadNode2-2
*GET,xN3_x,NODE,xLoadNode3,LOC,x
*GET,xN3_y,NODE,xLoadNode3,LOC,y
*GET,xN3_z,NODE,xLoadNode3,LOC,z
xAng2  = 0.05+(xN3_z-xN_z2) / (xN_x2-xN3_x)
xAngy2 = 0.2162
xAngy1 = 0.05

N,600,xN_x2+(xLPR2*xAng2),
      xN_y2+(xLPR2*xAngy2),
      xN_z2+xLPR2
N,601,xN_x2+(xLPR2*xAng2)- x1LBC2,
      xN_y2+(xLPR2*xAngy2),
      xN_z2+xLPR2+(x1LBC2*xAng2)
N,602,xN_x2+(xLPR2*xAng2)-(x1LBC2+x2LBC2),
      xN_y2+(xLPR2*xAngy2),
      xN_z2+xLPR2+((x1LBC2+x2LBC2)*xAng2)
N,603,xN_x2+(xLPR2*xAng2)- x1LBC2-(xHOT2*xAng2),
      xN_y2+(xLPR2*xAngy2)-(xHOT2*xAngy2),
      xN_z2+xLPR2+(x1LBC2*xAng2)-xHOT2
N,604,xN_x2+(xLPR2*xAng2)- x1LBC2+(xLOA2*xAng2)-xLOA2*xAngy1,
      xN_y2+(xLPR2*xAngy2)+(xLOA2*xAngy2),
      xN_z2+xLPR2+(x1LBC2*xAng2)+xLOA2
N,605,xN_x2+(xLPR2*xAng2)-(x1LBC2+x2LBC2),
      xN_y2+(xLPR2*xAngy2)-xWOT2,
      xN_z2+xLPR2+((x1LBC2+x2LBC2)*xAng2)+(xWOT2*xAngy2)

ET,600,LINK11
MP,dens,0
TYPE,600

R,600,2.1e11*0.1,0
REAL,600
EN,600,600,xLoadNode2

EN,601,600,601
EN,602,601,602
EN,603,602,603
EN,604,603,600
EN,605,601,603

EN,607,605,603
EN,608,605,601
```

```
   EN,609,605,600

   R,606,1e2,0,0
   REAL,606
   EN,606,601,604
*ELSE $ *ENDIF

! --------------------------- SURFACE LOADS ---------------
ET,600,LINK11
MP,dens,0
TYPE,600
xLPR3 = 30
xAng2 = xAng2-0.05
N,650,xN_x2+(xLPR3*xAng2)  ,xN_y2+(xLPR3*xAngy2),xN_z2+xLPR3
R,650,1e7,1e4,0
REAL,650
EN,650,650,160

! ---------------------------EXTRA MASSES------------------
ET,700,MASS21,0,1,0
TYPE,700

R,700,   0,   0,     0,0,0
R,702,   0,   0,     0,0,0
R,704,   0,   0,     0,0,0
R,705,1800,1800,1800,0,0,0
R,706, 667, 667, 667,0,0,0
R,707,   0,   0,     0,0,0
R,708,   0,   0,     0,0,0

*IF,xBellCrank32v,EQ,1,THEN
   REAL,700 $ EN,510,500
   REAL,702 $ EN,512,501
*ELSE $ *ENDIF

REAL,705 $ EN,705,109
REAL,706 $ EN,706,160

REAL,707 $ EN,707,142
REAL,708 $ EN,708,172
FINISH

! ---------------------------PREPROCESSOR------------------
/PREP7
ET,900,COMBIN14,1,0,0
MP,Damp,50,1e-11
TYPE,900
MAT,50
/INPUT,Damper,txt
FINISH


! ---------------------------SOLUTION TRANSIENT------------
/SOLU
```

```
DDELE,all,all $ MDELE,all,all $ D,1,ALL
NSEL,S,,,10001,1175,3 $ D,all,Uy,,,,,Ux,uz $ NSEL,ALL
NSEL,S,,,20001,2175,3 $ D,all,Uy,,,,,Ux,uz $ NSEL,ALL
D,500,Uy,,,,,Ux,uz
D,650,UX,,,,,UY,UZ

*IF,xBellCrank32v,EQ,1,THEN
   D,502,UX,,,,,UY,UZ
   D,504,UX,,,,,UY,UZ
   D,505,UX,,,,,UY,UZ
*ELSE $ *ENDIF

*IF,xBellCrank58v,EQ,1,THEN
   D,602,UX,,,,,UY,UZ
   D,604,UX,,,,,UY,UZ
   D,605,UX,,,,,UY,UZ
*ELSE $ *ENDIF

ANTYPE,TRANS
NLGEOM,on
SOLCONTROL,on
AUTOTS,on

! --------------------------CALCULATION PARAMETERS--------
xFrequy    = 0.45118887
xTimeEnd   = 60
xmaxF2     = 5.00
xmaxF      = -23626
xPhase     = 0
xsteig     = 0.001
xsteigF    = 0.01

xTimestep  = 0.05
xDELTIM    = 0.025

xALPHAD    = 0
xBETAD     = 0.016
xDMPRAT    = 0
xKBC       = 1

! --------------------------DEFINITIONS-------------------
xTy        = 1/xFrequy
PI         = acos(-1)
xTimeIni1  = 0.5
xTimeIni   = 1

xpZeile    = 6
xKraft     = 0
xKraft2    = 0

! --------------------------LOADING PHASE 1---------------
ACEL,0,0,0
*DO,xdozeit,0.05,xTimeIni1,0.05
   TIME,xdozeit
```

```
   BETAD,0.3
   DELTIM,0.025
   SOLVE
   /INPUT,Post26,txt ! Export Results to Excel
*ENDDO

! ---------------------------LOADING PHASE 2---------------
ACEL,0,0,0
*DO,xdozeit,xTimeIni1+0.05,xTimeIni,0.05
   TIME,xdozeit
   BETAD,0.8
   DELTIM,0.025
   SOLVE
   /INPUT,Post26,txt ! Export Results to Excel
*ENDDO

! ---------------------------OSZILATION--------------------
zeit   = xTimeIni+xTimestep
steig  = 0
steigF = 0

*DO,xdozeit,zeit,xTimeEnd,xTimestep
   TIME,xdozeit
   DELTIM,xDELTIM
   ALPHAD,xALPHAD
   BETAD,xBETAD
   DMPRAT,xDMPRAT
   KBC,xKBC

   *IF,steig,LT,1,then
      steig=steig+xsteig
   *ELSE
      steig=1
   *ENDIF

   *IF,steigF,LT,1,then
      steigF=steigF+xsteigF
   *ELSE
      steigF=1
   *ENDIF

   *IF,xBellCrank32v,EQ,1,THEN
      xKraft=steigF*xmaxF*sin((xdozeit-zeit+xPhase)*2*PI/xTy)
      SFE,506,2,pres,1,xKraft
   *ELSE $ *ENDIF

   *IF,xBellCrank58v,EQ,1,THEN
      xKraft2=steig*xmaxF2*sin((xdozeit-zeit-xPhase)*2*PI/xTy)
      SFE,606,1,pres,1,xKraft2,
   *ELSE $ *ENDIF

   xKraft2=steig*xmaxF2*sin((xdozeit-zeit)*2*PI/xTy)
   SFE,650,1,pres,1,xKraft2,
   SOLVE
```

```
   /INPUT,Post26,txt ! Export Results to Excel
*ENDDO
OUTRES,all,all

FINISH
```

K.4 Simulation of a Biaxial Test

```
FINISH
/CLEAR $ /UNITS,SI $ /CONFIG,nres,50000
/TITLE,... $ /FILNAME,...,0

! ---------------------------PREPROCESSOR------------------
/PREP7
ET,1,BEAM188,,0
ET,2,MPC184,1
ET,3,MASS21,0,1,0
ET,4,COMBIN14,1,0,0
ET,5,LINK11

! ---------------------------INPUT BLADE ELEMENTS ---------
PI          = acos(-1)
xRootx      = -0.563
xRooty      = -0.010
xRootz      = -4.592
xRootAngley =  9.975*PI/180
xRootAnglez = -0.1*PI/180

TYPE,1
LOCAL,12,CART,-0.563,-0.01,-4.592,-0.1,0,9.975
N,11,0,...,...
! Element 11
LOCAL,12,CART,-0.563,-0.01,-4.592,-0.1,0  ,9.975 $ N,12,0.125,...,...
LOCAL,11,CART,-0.563,-0.01,-4.592,-0.1,...,9.975 $ N,211,0,0,10
SECTYPE,12,BEAM,ASEC $ SECDATA,...,...,0,...,...,0,0,...,...
SECNUM,12 $ MP,PRXY,12,0.333 $ MP,EX,12,... $ MP,DENS,12,... $ MAT,12
EN,11,11,12,211
! Element 12
LOCAL,12,CART,-0.563,-0.01,-4.592,-0.1,0  ,9.975 $ N,13,0.375,...,...
LOCAL,11,CART,-0.563,-0.01,-4.592,-0.1,...,9.975 $ N,212,0,0,10
SECTYPE,13,BEAM,ASEC $ SECDATA,...,...,0,...,...,0,0,...,...
SECNUM,13 $ MP,PRXY,13,0.333 $ MP,EX,13,... $ MP,DENS,13,... $ MAT,13
EN,12,12,13,212
! Element 13
LOCAL,12,CART,-0.563,-0.01,-4.592,-0.1,0  ,9.975 $ N,14,0.750,...,...
LOCAL,11,CART,-0.563,-0.01,-4.592,-0.1,...,9.975 $ N,213,0,0,10
SECTYPE,14,BEAM,ASEC $ SECDATA,...,...,0,...,...,0,0,...,...
SECNUM,14 $ MP,PRXY,14,0.333 $ MP,EX,14,... $ MP,DENS,14,... $ MAT,14
EN,13,13,14,213
...
```

```
! ---------------------------INPUT DAMPING ELEMENTS--------
/PREP7
TYPE,4
MP,Damp,50,1e-11
MAT,50

LOCAL,12,CART,-0.563,-0.01,-4.592,-0.1,0,12.114
N,312,0.125,,+25 $ N,412,0.125,-25
N,313,0.375,,+25 $ N,413,0.375,-25
N,314,0.750,,+25 $ N,414,0.750,-25
...
R,312,0,0.00001,... $ REAL,312 $ EN,312,12,312
R,313,0,0.00001,... $ REAL,313 $ EN,313,13,313
R,314,0,0.00001,... $ REAL,314 $ EN,314,14,314
...
R,412,0,0.00001,... $ REAL,412 $ EN,412,12,412
R,413,0,0.00001,... $ REAL,413 $ EN,413,13,413
R,414,0,0.00001,... $ REAL,414 $ EN,414,14,414
...

! ---------------------------LOADING EQUIPEMENT------------
xLoadNode=34
! ---------------------------FPW ACTUATOR------------------
*GET,xN_x,NODE,xLoadNode,LOC,x
*GET,xN_y,NODE,xLoadNode,LOC,y
*GET,xN_z,NODE,xLoadNode,LOC,z
N,500,xN_x-tan(xRooty)*0.774,xN_y,xN_z+0.774
N,501,xN_x-tan(xRooty)*4.2,xN_y,xN_z+0.774+4.2
MP,DENS,1,0 $ MAT,1 $ TYPE,2
EN,500,xLoadNode,500

TYPE,5 $ MP,damp,2,1000 $ MAT,2 $ R,501,0,1e2,0
EN,501,500,501

! ---------------------------LLW ACTUATOR------------------
LOCAL,14,CART
*GET,xN_x,NODE,xLoadNode,LOC,x
*GET,xN_y,NODE,xLoadNode,LOC,y
*GET,xN_z,NODE,xLoadNode,LOC,z
N,502,xN_x,xN_y+1.234,xN_z+0.18
N,503,xN_x,xN_y+1.234+3.754,xN_z+0.18-0.25
N,504,xN_x,xN_y+1.234+3.754,xN_z+0.18+2.04-0.25
N,505,xN_x,xN_y+1.234+3.754-1.662,xN_z+0.18+2.04-0.25
N,506,xN_x,xN_y+1.234+3.754-1.662-tan(15*PI/180)*4 ,xN_z+0.18+2.04+4-0.25
N,507,xN_x,xN_y+1.234+3.754-0.742,xN_z+0.18+2.04-0.758-0.25

MP,DENS,1,0 $ MAT,1 $ TYPE,2
EN,502,xLoadNode,502

TYPE,5 $ MP,dens,0 $ R,502,2.1e11*0.1,0
EN,503,502,503
EN,504,503,504
EN,505,504,505
EN,506,503,507
```

```
EN,507,504,507
EN,508,505,507

REAL,501
EN,510,505,506

! ---------------------------EXTRA MASSES------------------
TYPE,3
R,601,652, 652, 652, 0,0,0
EN,601,xLoadNode

R,602,500, 500, 500, 0,0,0
EN,602,500
EN,603,505

R,604,238, 238, 238, 0,0,0
EN,604,502
EN,605,503

R,606,238, 238, 238, 0,0,0
EN,606,507

FINISH

! ---------------------------SOLUTION TRANSIENT------------
/SOLU

MDELE,all,all$ D,11,ALL
NSEL,S,,,312,358,1$ D,all,Uy,,,,,Ux,uz$ NSEL,ALL
NSEL,S,,,412,458,1$ D,all,Uy,,,,,Ux,uz$ NSEL,ALL
D,501,Uy,,,,,Ux,uz
D,504,Uy,,,,,Ux,uz
D,506,Uy,,,,,Ux,uz
D,503,Ux
D,505,Ux
D,507,Ux

ANTYPE,TRANS
NLGEOM,on
SOLCONTROL,on
AUTOTS,on

! ---------------------------CALCULATION PARAMETERS--------
xFrequyv  = 0.81
xFrequyh  = 1.08

xphasev   = (  0/360)*(1/xFrequyv)
xphaseh   = (  0/360)*(1/xFrequyv)
xphasehv  = (-25/360)*(xFrequyv)

xsteigpre = 0.015
xsteig    = 0.005
xTimeEnd  = 100
```

```
xPreloadv =  5000
xPreloadh = 14400

xmaxFv    =-5500.0*0.97
xmaxFh    =-1950.0*0.96
xmaxFhv   =-1*xmaxFh*(2/5)*1.5

xTimestep = 0.05
xDELTIM   = 0.025
xBETAD    = 0.0052
xKBC      = 1

! --------------------------DEFINITIONS------------------
xTyv      = 1/xFrequyv
xTyh      = 1/xFrequyh
xTimeIni1 = 1
xTimeIni  = 5

xpZeile   = 6
xKraftv   = 0
xKrafth   = 0
xKrafthv  = 0

! --------------------------LOADING PHASE 1--------------
ACEL,0,0,0
*DO,xdozeit,0.05,xTimeIni1,0.05
   TIME,xdozeit
   BETAD,0.3
   DELTIM,0.025
   SOLVE
   /INPUT,Post26,txt ! Export Results to Excel
*ENDDO

! --------------------------LOADING PHASE 2--------------
ACEL,0,0,-9.81
steig=0
*DO,xdozeit,xTimeIni1+0.05,xTimeIni,0.05
   TIME,xdozeit
   BETAD,0.8
   DELTIM,0.025
   *IF,steig,LT,1,then
      steig=steig+xsteigpre
   *ELSE
      steig=1
   *ENDIF
   SFE,501,2,pres,1,steig*xPreloadv,
   SFE,510,2,pres,1,steig*xPreloadh,
   SOLVE
   /INPUT,Post26,txt ! Export Results to Excel
*ENDDO

! --------------------------OSZILATION-------------------
zeit  = xTimeIni+xTimestep
steig = 0
```

```
OUTRES,all,all
*DO,xdozeit,zeit,xTimeEnd,xTimestep
   TIME,xdozeit
   DELTIM,xDELTIM
   BETAD,xBETAD
   KBC,xKBC
   *IF,steig,LT,1,then
      steig=steig+xsteig
   *ELSE
      steig=1
   *ENDIF
   xKraftv=xPreloadv+steig*xmaxFv*sin((xdozeit-zeit+xphasev)*2*PI/xTyv)
   SFE,501,2,pres,1,xKraftv,
   xKrafth=xPreloadh+steig*xmaxFh*sin((xdozeit-zeit+xphaseh)*2*PI/xTyh)
   xKrafthv=-1*steig*xmaxFhv*sin((xdozeit-zeit+xphasehv)*2*PI/xTyv)
   SFE,510,2,pres,1,xKrafth+xKrafthv,
   SOLVE
   /INPUT,Post26,txt ! Export Results to Excel
*ENDDO
OUTRES,all,all
FINISH
```

K.5 Simulation of the BEDEX Method

The blade model of Section K.2.1 is used. The damper code of Section K.2.2 is used.

K.5.1 Program - BEDEX

```
FINISH
/CLEAR $ /UNITS,SI $ /CONFIG,nres,50000
/TITLE,... $ /FILNAME,...,0

! ---------------------------PREPROCESSOR------------------
xLastBladeNode     = 163
xLastBladeElement  = (xLastBladeNode-1)/3
xLastDamperNode    = xLastBladeNode-3+1
xLastDamperElement = xLastBladeElement
xLastMassElement   = xLastBladeElement

xFpwFact           = 1
xLlwFact           = 1.10

/INPUT,Blade,txt

xBellCrank32v      = 0
xBellCrank32h      = 1
xBellCrank58v      = 1
```

```
/PREP7
ET,801,MPC184,1

! --------------------------LOADING EQUIPEMENT 1---------
*IF,xBellCrank32h,EQ,1,THEN
   xLPR = 7
   xLBC = 6
   xHOT = 3
   xLOA = 5
   xWOT = 4

   xLoadNode=109
   *GET,xN_x,NODE,xLoadNode,LOC,x
   *GET,xN_y,NODE,xLoadNode,LOC,y
   *GET,xN_z,NODE,xLoadNode,LOC,z
   xLoadNode1=xLoadNode-2
   *GET,xN1_x,NODE,xLoadNode1,LOC,x
   *GET,xN1_y,NODE,xLoadNode1,LOC,y
   *GET,xN1_z,NODE,xLoadNode1,LOC,z
   xAngy = 0.2

   N,800,xN_x,xN_y+xLPR,xN_z-(xLPR*xAngy)
   N,801,xN_x,xN_y+xLPR,xN_z+xLBC
   N,802,xN_x,xN_y+xLPR,xN_z+2*xLBC
   N,803,xN_x,xN_y+xLPR+xHOT,xN_z+xLBC
   N,804,xN_x,xN_y+xLPR-xLOA,xN_z+xLBC
   N,805,xN_x-xWOT,xN_y+xLPR,xN_z+2*xLBC

   ET,800,LINK11,
   MP,dens,0
   TYPE,800

   R,800,2.1e11*0.1,0
   REAL,800
   EN,800,800,xLoadNode

   EN,801,800,801
   EN,802,801,802
   EN,803,802,803
   EN,804,803,800
   EN,805,801,803

   EN,807,805,803
   EN,808,805,801
   EN,809,805,800

   R,806,1e2,0,0
   REAL,806
   EN,806,801,804
*ELSE $ *ENDIF

! --------------------------LOADING EQUIPEMENT 2----------
*IF,xBellCrank32v,EQ,1,THEN
   xLPR = 7
```

```
xLBC = 6
xHOT = 3
xLOA = 5
xWOT = 4

xLoadNode=109
*GET,xN_x,NODE,xLoadNode,LOC,x
*GET,xN_y,NODE,xLoadNode,LOC,y
*GET,xN_z,NODE,xLoadNode,LOC,z
xLoadNode1=xLoadNode-2
*GET,xN1_x,NODE,xLoadNode1,LOC,x
*GET,xN1_y,NODE,xLoadNode1,LOC,y
*GET,xN1_z,NODE,xLoadNode1,LOC,z
xAngl = (xN1_z-xN_z) / (xN_x-xN1_x)
xAngy = 0.2162

N,500,xN_x+(xLPR*xAngl),
      xN_y+(xLPR*xAngy),
      xN_z+xLPR
N,501,xN_x+(xLPR*xAngl)-xLBC,
      xN_y+(xLPR*xAngy),
      xN_z+xLPR+(xLBC*xAngl)
N,502,xN_x+(xLPR*xAngl)-2*xLBC,
      xN_y+(xLPR*xAngy),
      xN_z+xLPR+(2*xLBC*xAngl)
N,503,xN_x+(xLPR*xAngl)-xLBC-(xHOT*xAngl),
      xN_y+(xLPR*xAngy)-(xHOT*xAngy),
      xN_z+xLPR+(xLBC*xAngl)-xHOT
N,504,xN_x+(xLPR*xAngl)-xLBC+(xLOA*xAngl),
      xN_y+(xLPR*xAngy)+(xLOA*xAngy),
      xN_z+xLPR+(xLBC*xAngl)+xLOA
N,505,xN_x+(xLPR*xAngl)-2*xLBC,
      xN_y+(xLPR*xAngy)-xWOT,
      xN_z+xLPR+(2*xLBC*xAngl)+(xWOT*xAngy)

ET,500,LINK11
MP,dens,0
TYPE,500

R,500,2.1e11*0.1,0
REAL,500
EN,500,500,xLoadNode
EN,501,500,501
EN,502,501,502
EN,503,502,503
EN,504,503,500
EN,505,501,503
EN,507,505,503
EN,508,505,501
EN,509,505,500

R,506,1e2,0,0
REAL,506
EN,506,501,504
```

```
*ELSE $ *ENDIF

! ---------------------------LOADING EQUIPEMENT 3 ---------
*IF,xBellCrank58v,EQ,1,THEN
   xLPR2  = 7
   x1LBC2 = 10
   x2LBC2 = 5
   xHOT2  = 3
   xLOA2  = 5
   xWOT2  = 4

   xLoadNode2=145
   *GET,xN_x2,NODE,xLoadNode2,LOC,x
   *GET,xN_y2,NODE,xLoadNode2,LOC,y
   *GET,xN_z2,NODE,xLoadNode2,LOC,z
   xLoadNode3=xLoadNode2-2
   *GET,xN3_x,NODE,xLoadNode3,LOC,x
   *GET,xN3_y,NODE,xLoadNode3,LOC,y
   *GET,xN3_z,NODE,xLoadNode3,LOC,z
   xAng2  = 0.05+(xN3_z-xN_z2) / (xN_x2-xN3_x)
   xAngy2 = 0.2162
   xAngy1 = 0.05

   N,600,xN_x2+(xLPR2*xAng2),
         xN_y2+(xLPR2*xAngy2),
         xN_z2+xLPR2
   N,601,xN_x2+(xLPR2*xAng2)- x1LBC2,
         xN_y2+(xLPR2*xAngy2),
         xN_z2+xLPR2+(x1LBC2*xAng2)
   N,602,xN_x2+(xLPR2*xAng2)-(x1LBC2+x2LBC2),
         xN_y2+(xLPR2*xAngy2),
         xN_z2+xLPR2+((x1LBC2+x2LBC2)*xAng2)
   N,603,xN_x2+(xLPR2*xAng2)- x1LBC2-(xHOT2*xAng2),
         xN_y2+(xLPR2*xAngy2)-(xHOT2*xAngy2),
         xN_z2+xLPR2+(x1LBC2*xAng2)-xHOT2
   N,604,xN_x2+(xLPR2*xAng2)- x1LBC2+(xLOA2*xAng2)-xLOA2*xAngy1,
         xN_y2+(xLPR2*xAngy2)+(xLOA2*xAngy2),
         xN_z2+xLPR2+(x1LBC2*xAng2)+xLOA2
   N,605,xN_x2+(xLPR2*xAng2)-(x1LBC2+x2LBC2),
         xN_y2+(xLPR2*xAngy2)-xWOT2,
         xN_z2+xLPR2+((x1LBC2+x2LBC2)*xAng2)+(xWOT2*xAngy2)

   ET,600,LINK11,
   MP,dens,0
   TYPE,600

   R,600,2.1e11*0.1,0
   REAL,600
   EN,600,600,xLoadNode2

   EN,601,600,601
   EN,602,601,602
   EN,603,602,603
   EN,604,603,600
```

```
   EN,605,601,603

   EN,607,605,603
   EN,608,605,601
   EN,609,605,600

   R,606,1e2,0,0
   REAL,606
   EN,606,601,604
*ELSE $ *ENDIF

! ---------------------------EXTRA MASSES------------------
ET,700,MASS21,0,1,0
TYPE,700

R,700,   0,   0,   0,0,0,0
R,702,   0,   0,   0,0,0,0
R,704,   0,   0,   0,0,0,0
R,705,1800,1800,1800,0,0,0
R,706, 150, 150, 150,0,0,0
R,707,   0,   0,   0,0,0,0
R,708,1600,1600,1600,0,0,0

*IF,xBellCrank32h,EQ,1,THEN
    REAL,810,4500,4500,4500,0,0,0 $ EN,810,800
*ELSE $ *ENDIF

*IF,xBellCrank32v,EQ,1,THEN
    REAL,700 $ EN,510,500
    REAL,702 $ EN,512,501
*ELSE $ *ENDIF

REAL,705 $ EN,705,109
REAL,706 $ EN,706,160
REAL,707 $ EN,707,134
REAL,708 $ EN,708,145
FINISH

! ---------------------------PREPROCESSOR------------------
/PREP7
ET,900,COMBIN14,1,0,0
MP,Damp,50,1e-11
TYPE,900
MAT,50
/INPUT,Damper,txt
FINISH

! ---------------------------SOLUTION TRANSIENT-------------
/SOLU

MDELE,all,all$ D,1,ALL
NSEL,S,,,10001,1175,3$ D,all,Uy,,,,,Ux,uz$ NSEL,ALL
NSEL,S,,,20001,2175,3$ D,all,Uy,,,,,Ux,uz$ NSEL,ALL
```

```
*IF,xBellCrank32h,EQ,1,THEN
D,802,UX,,,,,UY,UZ
D,804,UX,,,,,UY,UZ
D,805,UX,,,,,UY,UZ
*ELSE$ *ENDIF

*IF,xBellCrank32v,EQ,1,THEN
D,502,UX,,,,,UY,UZ
D,504,UX,,,,,UY,UZ
D,505,UX,,,,,UY,UZ
*ELSE$ *ENDIF

*IF,xBellCrank58v,EQ,1,THEN
D,602,UX,,,,,UY,UZ
D,604,UX,,,,,UY,UZ
D,605,UX,,,,,UY,UZ
*ELSE$ *ENDIF

ANTYPE,TRANS
NLGEOM,on
SOLCONTROL,on
AUTOTS,on

! ---------------------------CALCULATION PARAMETERS--------
xFrequy = 0.50303475
xTimeEnd= 60
xmaxF   = -200
xmaxF2  = 0
xmaxF2  = 142000*0.9
xmaxF_h1= 94000*0.89
xphase_h1= (100/360)*(1/xFrequy)
xsteig = 0.001
xsteigF= 0.001
xsteig_h1= 0.001

xTimestep= 0.05
xDELTIM= 0.025

xALPHAD= 0
xBETAD= 0.016
xDMPRAT= 0
xKBC= 1

! ---------------------------DEFINITIONS-------------------
xTy = 1/xFrequy
PI = acos(-1)
xTimeIni1= 0.5
xTimeIni= 1

xpZeile= 6
xKraft= 0
xKraft2= 0
xKraft_h1= 0
```

```
! ---------------------------LOADING PHASE 1---------------
ACEL,0,0,0
*DO,xdozeit,0.05,xTimeIni1,0.05
   TIME,xdozeit
   BETAD,0.3
   DELTIM,0.025
   SOLVE
   /INPUT,Post26,txt ! Export Results to Excel
*ENDDO

! ---------------------------LOADING PHASE 2---------------
ACEL,0,0,0
*DO,xdozeit,xTimeIni1+0.05,xTimeIni,0.05
   TIME,xdozeit
   BETAD,0.8
   DELTIM,0.025
   SOLVE
   /INPUT,Post26,txt ! Export Results to Excel
*ENDDO

! ---------------------------OSZILATION--------------------
zeit   = xTimeIni+xTimestep
steig      = 0
steigF      = 0
steig_h1   = 0

*DO,xdozeit,zeit,xTimeEnd,xTimestep
   TIME,xdozeit
   DELTIM,xDELTIM
   ALPHAD,xALPHAD
   BETAD,xBETAD
   DMPRAT,xDMPRAT
   KBC,xKBC

   *IF,steig_h1,LT,1,then
      steig_h1=steig_h1+xsteig_h1
   *ELSE
      steig_h1=1
   *ENDIF

   *IF,steig,LT,1,then
      steig=steig+xsteig
   *ELSE
      steig=1
   *ENDIF

   *IF,steigF,LT,1,then
      steigF=steigF+xsteigF
   *ELSE
      steigF=1
   *ENDIF

   *IF,xBellCrank32h,EQ,1,THEN
      xKraft_h1=steig_h1*xmaxF_h1*sin((xdozeit-zeit+xphase_h1)*2*PI/xTy)
```

```
      SFE,806,2,pres,1,xKraft_h1
   *ELSE $ *ENDIF

   *IF,xBellCrank32v,EQ,1,THEN
      xKraft=steigF*xmaxF*sin((xdozeit-zeit)*2*PI/xTy)
      SFE,506,2,pres,1,xKraft
   *ELSE $ *ENDIF

   *IF,xBellCrank58v,EQ,1,THEN
      xKraft2=steig*xmaxF2*sin((xdozeit-zeit)*2*PI/xTy)
      SFE,606,2,pres,1,xKraft2
   *ELSE  $ *ENDIF
   SOLVE
   /INPUT,Post26,txt ! Export Results to Excel
*ENDDO
FINISH
```

Falko Bürkner — Curriculum Vitae

I studied Civil and Environmental Engineering at the Technical University of Hamburg-Harburg with the focus on steel and reinforced concrete structures as well as geotechnical engineering. In 2000, I took part in a six-month exchange program at the University of Manchester.

After having worked on harbor and bridge constructions for six months at the technical office of Bilfinger Berger AG, I joined the Ramboll IMS Ingenieurgesellschaft GmbH, located in Hamburg, in 2003. After having worked on harbor constructions and special constructions at the Neumayer Station III[66], a major part of my work was the design of steel and concrete offshore foundations. In 2006, I joined Fraunhofer IWES to work on full-scale tests of wind turbine blades. As a project manager I became responsible for the design of full-scale test rigs. From 2009 on, I established a team to run the full-scale test facilities. In 2011, I became group manager of eleven researchers, working for the newly formed group performing all blade tests at Fraunhofer IWES. I was responsible for the full scope of staff, budget and project acquisition. In 2012, all of the blade and material testing at Fraunhofer IWES was combined in one department. I became the technical head, being responsible for 20 researchers. As a highlight, the department performed the static and cyclic tests of two blades of more than 80m in length. At the end of 2014, I resigned from leading the department to complete my dissertation. Since the start of 2016, I have been working as a Senior Expert at the Innovation for Enercon GmbH on innovative turbine designs.

Working on the design of bridge and harbor constructions, on- and offshore foundations of wind turbines and special constructions like the Neumayer Station extended my experience in the classical engineering sectors of steel, reinforced concrete and geotechnical engineering. With my work on designing full-scale test rigs, I developed my expertise for designing combined steel and reinforced concrete structures to use the advantages of both materials as best as possible, which was necessary for the massive fatigue loads on the test rig. Further experience was gained on servo-hydraulic systems and the mechanical engineering used to design the test equipment. During my work as a project manager for full-scale blade tests and as a project manager for research projects related to this topic, I developed my experience as a test engineer. Additional topics were the controlling of servo-hydraulic actuators, design, testing and non-destructive testing methods of glass- and carbon-fiber reinforced composite structures as well as various kinds of measurement techniques related to testing.

---

[66] https://www.awi.de/expedition/stationen/neumayer-station-iii.html